An Experimental Study of Corrosion for Long Distance Carbon Transportation Pipelines

By

Yong Hua

Submitted in accordance with the requirements for the degree of
Doctor of Philosophy

The University of Leeds
Institute of Functional Surfaces
School of Mechanical Engineering

January 2015

The candidate confirms that the work submitted is his/her own and that appropriate credit has been given where reference has been made to the work of others.

Publication Statement

The candidate confirms that the work submitted is his/her own, except where work which has formed part of jointly authored publications has been included. The contribution of the candidate and the other authors to this work has been explicitly indicated below. The candidate confirms that appropriate credit has been given within the thesis where reference has been made to the work of others.

1. Y. Hua, R. Barker, and A. Neville, Effect of temperautre on the critical water content for general and localised corrosion of X65 carbon steel in the transport of supercritical CO_2. The International Journal of Greenhouse Gas Control, 2014. 31: p. 48-60.

2. Y. Hua, R. Barker, and A. Neville, Comparison of corrosion behaviour for X-65 carbon steel in supercritical CO_2-saturated water and water-saturated/unsaturated supercritical CO2 The Journal of Supercritical Fluids, 2015. 97: p. 224-237.

3. Y. Hua, R. Barker, C. T, M. Ward, and A. Neville, Relating Iron Carbonate Morphology to Corrosion Characteristics for Water-Saturated Supercritical CO_2 Systems. Journal of Supercritical Fluids**,** vol. 98, pp.183-193. 2015.

4. Y. Hua, R. Barker, and A. Neville, Understanding the Influence of SO_2 and O_2 on the Corrosion of Carbon Steel in Water-Saturated Supercritical CO_2. Corrosion, vol. 71, pp.667-683. 2015.

5. Y. Hua, R. Barker, and A. Neville, The influence of SO_2 on the tolerable water content to avoid pipeline corrosion during the transportation of supercritical CO_2, International Journal of Greenhouse Gas Control, vol. 37, pp.412-423. 2015.

Chapter 6 is based on work from publication 1. Chapter 7 is based on work from publications of 2 and 3. Chapter 8 is based on work from publications of 4 and 5.

Yong Hua completed all experimental studies, evaluation of data and preparation of publications. All authors contributed to proof reading of the articles prior to publication. The contributions of Dr. Michael Ward to the work is: use of Focused Ion Beam sample preparation and Transmission Electron Microscopy. The contributions of Dr. Thibaut Charpentier to the work is: the scale kinetics calculations.

Acknowledgements

I would like to express my gratitude to Prof. Anne Neville for all the supervision and encouragement she has provided throughout the course of this work. Without her kind support, insight an passion for engineering, none of this would have been possible.

I am extremely grateful to my colleague Dr. Richard Barker for his invaluable day to day advice. I wish to thanks to my best friend Dr. Simon Hu for his invaluable advice at the beginning of my PHD study.

A big thanks goes to the technical staff, in particular Mark Batchelor for helping me with setting up the whole pressure system.

I wish to thank all my friends in the School of Mechanical Engineering. I would like to thank Michael Ward, Stuart, Ike, Liuquang Yang, Hongyuan Zhao, Yugal, Laura, Thibaut, Mike, James and Chun.

A big thanks goes to my Mum, Dad and Leona Zhang for believing in me and helping me cope with the stress of writing up.

Abstract

This thesis presents results from a systematic study undertaken to establish the influence of sulphur dioxide (SO_2 and O_2) content on the critical water content required to initiate substantial levels of internal corrosion during the transport of supercritical CO_2 for Carbon Capture and Storage (CCS) applications.

An assessment of both the general and localised corrosion behaviour of X65 carbon steel in water-containing CO_2 environments is presented. Firstly, autoclave experiments were conducted in environments where the CO_2 phase was either saturated or under-saturated with water. Such an approach enabled identification of the minimum water content in the system, below which no general or localised attack was observed.

Later, corrosion experiments were performed containing supercritical CO_2 and the presence of 0, 50 and 100 ppm SO_2 with a low level of O_2 (20 ppm). The results highlights that reducing water content is a more favourable option compared to reducing SO_2 content to minimise corrosion in the system as high corrosion rates can be observed in the absence of SO_2 if water content is high enough, but below a minimum water content (~500 ppm), both general and localised corrosion is minimal despite the presence of 100 ppm SO_2.

Analysis of corrosion products formed on the steel surface is performed using X-Ray Diffraction (XRD), Scanning Electron Microscopy (SEM), Energy-Dispersive X-ray spectroscopy (EDX), Transmission Electron Microscopy (TEM), Raman spectroscopy. Only $FeCO_3$ was detected on the surface without SO_2 and O_2, whilst both $FeCO_3$ and $FeSO_3.3H_2O$ were identified on the surface of the carbon steel samples exposed to the environments containing 2 and 100 ppm SO_2 and 20 ppm O_2. The localised corrosion rates were determined by surface profilometry measurement.

The most important observation from this work is that the key degradation mechanism in all experiments was localised corrosion. Not only was the combination of SO_2 and O_2 shown to influence pitting severity, but the pitting rates recorded were nearly one order of magnitude greater than the uniform corrosion rate determined from mass loss measurements. The increase in SO_2 content was shown to influence the shape of pits as well as their overall depth. In particular, the work highlights the importance of adopting a systematic approach when determining pitting behaviour of carbon steels exposed to impure dense-phase CO_2.

Table of Contents

List of Tables

List of Figures

Nomenclature

(alphabetical order)

	Terms	Unit
A_o	Initial surface area	cm^2
A	Total surface area	cm^2
e	Electron. Subscript denotes the charge of the species	
F	Faraday constant	$Cmol^{-1}$
m	Mass loss	g
M	Molecular mass	$gmol^{-1}$
n	Valence number of a particular metal species	
R	Ideal gas constant	$JK^{-1}mol^{-1}$
V_o	Total volume of gas	mm^3
P_o	Reference pressure	bar
P_t	Total pressure	bar
ρ	Steel density	g/L
δ	Corrosion Product film thickness	nm
C	Concentration	mol/L
R_{FeCO3}	Precipitation of $FeCO_3$	mol^2/m^4
T	Temperature	K
t	Temperature	°C
K_{sp}	Solubility of $FeCO_3$	mol^2/L^2
ppm	Parts-per-million, 10^{-6}	
ppmv	Parts-per-million by volume, 10^{-6}	
ppmw	Parts-per-million by weight, 10^{-6}	
ppmb	Parts-per-billion, 10^{-9}	
ppt	Parts-per-trillion, 10^{-12}	

Chapter 1 Introduction

1.1 Background

CO_2 has the greatest negative impact on the observed greenhouse effect, causing approximately 70% of the global warming[1, 2]. There is a growing consensus that global climate change is occurring, and many climate scientists believe that a major cause is the anthropogenic emission of greenhouse gases (GHGs) into the atmosphere in Table 1.1[1].

Table 1.1: Profile by process or industrial activity of worldwide large stationary CO_2 sources with emissions of more than 0.1 $MtCO_2$ per year[1]

Process	Number of sources	Emission ($MtCO_2$ yr-1)
Fossil fuel		
Power	4942	10539
Cement production	1175	932
Refineries	638	798
Iron and steel industry	269	646
Petrochemical industry	470	379
Oil and gas processing	N/A	50
Other	90	33
Biomass		
Bioethanol and Bioenery	303	91
Total	7887	13466

Carbon capture and storage (CCS) is an approach to reduce CO_2 emissions to the atmosphere which has been growing in popularity in recent decades. It requires cost efficient, reliable, and safe solutions for transportation of the separation of carbon dioxide (CO_2) from the capturing source such as power plant, refineries or other industrial plants to the storage sites. This approach would lock up (sequester) the CO_2 for thousands of years. Carbon Capture and Storage (CCS) is recognised as one of the key technologies in terms of carbon dioxide abatement.

1.2 Carbon Capture Technologies

There are four main technologies proposed for CO_2 capture as shown in Fig.1.1. Post-combustion capture applies primarily to coal-fueled power generators that are air fired. Pre-combustion capture applies to gasification plants. Oxy-combustion can be applied to new plants or retrofitted to existing plants, and industry processes[1, 3]. This schematic diagram illustrates the primary routes for carbon capture.

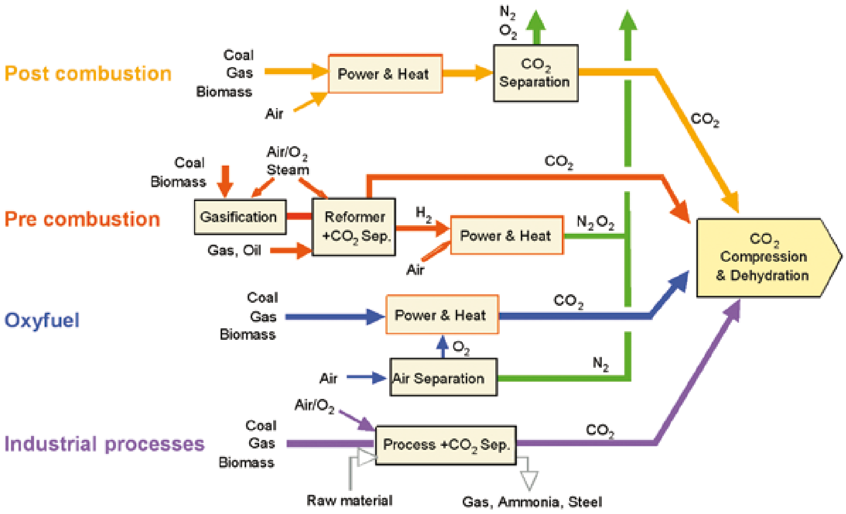

Figure 1.1: CO_2 capture processes[1].

In a post-combustion system, only a small amount of CO_2 is captured from the gas produced by combustion of the fuel with air. The flue gases with CO_2 were injected in a cooled or compressed organic solvent that selectively absorbs the CO_2. High purity CO_2 can then be released from the solution by increasing the temperature or reducing the pressure. Similar separation processes are already used on a large scale to remove CO_2 from natural gas[1, 3].

In a pre-combustion system, the flue gas is converted into gas by heating it with steam and air or oxygen. This conversion produces a gas containing mainly CO_2 with H_2. H_2 can be removed easily which can be used for energy or heat production[1, 3].

In Oxyfuel combustion, the fuel was burned with O_2 (contains 20% of oxygen and a lot of nitrogen) rather than air. The exhaust gas mainly contains water vapour and CO_2. The water vapour is removed by decreasing temperature from the CO_2. However, O_2 is very difficult to remove properly[1, 3].

Several industrial processes (coal gasification or coal gas biomass) used similar CO_2 capture systems[1].

1.2.1 CO_2 separation processes

The technologies are relative to CO_2 separation involving absorption, adsorption, membrane and cryogenic processes. Different types of impurity may be produced depending on the types of power plants, the CO_2 capture technologies and separation processes as shown in Table 1.2.

Table 1.2: Impurity concentrations after different capture methods[4]

Component	Post-combustion	Pre-combustion	Oxy-combustion
Argon, A_r	Trace	<0.05vol%	<5vol%
Methane, CH_4	<100ppmv	<350ppmv	--
Carbon monoxide, CO	<10ppmv	<0.4vol%	Trace
Hydrogen sulphide, H_2S	Trace	<3.4vol%	Trace
Nitric oxides, NO_x	<50ppmv	--	<0.25vol%
Oxygen, O_2	<0.01vol%	Trace	<3vol%
Sulphur oxides, SO_2	<10ppmv	--	<2.5vol%
H2,	Trace	<0.05vol%	<5vol%
N2	<0.17vol%	<0.6vol%	<7vol%
CO2	>99vol%	>95.6vol%	>90vol%

1.3 Transportation

CCS is considered as an effective and promising solution to combat global climate change, receiving significant attention from researchers worldwide. A complete CCS cycle requires safe, reliable and cost effective solutions for the transmission of CO_2 from the capturing facility to the location of permanent storage. The most economically viable option would be a dedicated, extensive pipeline network which transports CO_2 at high pressure in either a liquid or supercritical state[5] (critical point: 31°C and 73.5bar) –at pressures ranging from >5 to > 10MPa, and temperatures ranging from 4°C to 50°C[6].

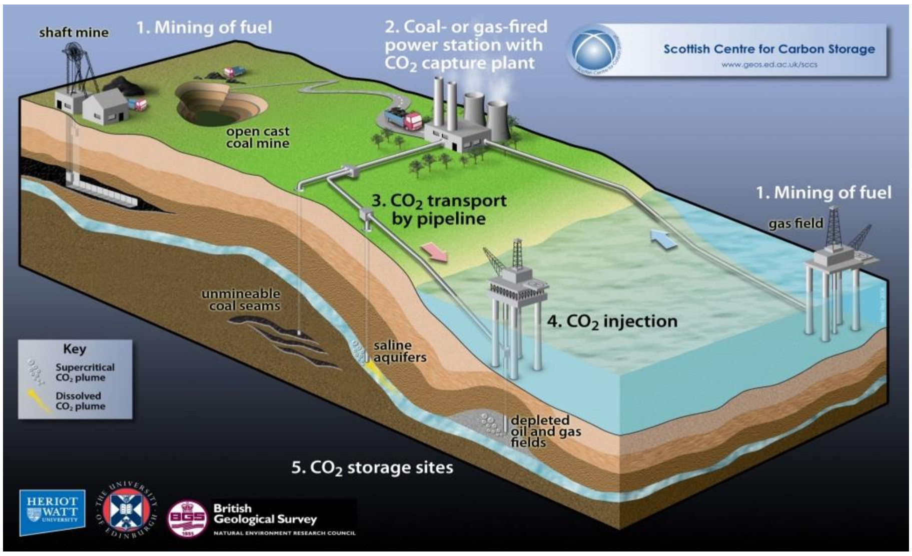

Figure 1.2: Carbon capture and geological storage concept (Image from: http://planetearth.nerc.ac.uk/news/story.aspx?id=932).

The captured CO_2 must be purified before entering the pipelines. A suggestion of the tentative CO_2 quality recommendation (Table 1.3) has been provided by the Dynamis project[7], Alstom[8], IPCC[9], and Kinder Morgan's specification[4]. It can be seen that large variations in the impurities occur because of the process, but the specialised quality should be universal. It can be seen that large variations in these specifications is reasonable as the impurities in the CCS stream will depend on the fuel type, the energy conversion process (post-combustion, pre-combustion or oxy-fuel) and the separation process. In addition, with new capturing technologies, new compounds (impurities) can be formed and higher concentration of impurities can follow the CO_2 phase with unknown effect on corrosion.

There is however no consensus on what the actual target for the maximum water concentration should be when other impurities such as SO_x, NO_x and O_2 are present. It has been argued that full dehydration down to 50 ppm should be applied. This limit has been specified for the first CO_2 pipelines in the USA[10] and for the Snøhvit[11] pipeline in Norway. It is obvious that the additional cost would add into such low water content.

1.4 Deep Underground Geological Storage

A suitable storage should look like a huge underground water-containing rock formation including saline aquifers, depleted oil and gas wells and empty coal seams. The CO_2 storage is normally expected to take place at depths below 800m, resulting in the formation of liquid or supercritical CO_2 phases. At such conditions, the density of CO_2 is close to crude oil (860-900 kg/m^3). Resulting in buoyant forces that tend to drive CO_2 upwards. Consequently, a well-sealed cap rock over the selected storage reservoir is important to ensure that CO_2 remains trapped underground[1].

Table 1.3: CO_2 specifications for transportation[4, 7, 8]

Component	**DYNAMIS**	**IGCC**			**Alstom**		**Kinder Morgan's**
		Post-combustion capture	Pre-combustion capture	Oxy-fuel	Low	High	
CO_2	>95.5 vol%	>95%			>90% (storage)	>95% (EOR)	Minimum 95 %
N_2 / A_r / H_2	< 4 vol % (all non-condensable gasses)	100 ppm	300-6000 ppm	37000 ppm	<4%		Max 4%
O_2	Aquifer < 4 vol%, EOR 100 – 1000 ppm	Include above			<10 ppm (unclear)	<1000 ppm (unclear)	25 ppm
H_2	above	Include above			<4%	<4%	-
H_2o	500 ppm	-			<10 ppm	<600ppm	Max 630 ppm
H_2s	200 ppm	0	100-6000 ppm	0	<10 ppm (H&S)	<15000 ppm (EOR)	Max 50 ppm
CO	2000 ppm	0	300-4000 ppm	0	<100 ppm (H&S)	<40000 ppm (EOR)	-
SO_x	100 ppm	<100 ppm	0	5000 ppm	<100 ppm (H&S)	<1500 ppm (EOR)	Total Sulfur: 86 ppm
NO_x	100 ppm	<100 ppm	0	100 ppm	<100 ppm (H&S)	<1500 ppm (unclear)	-

Note: ppm is parts per million, ppm in mole throughout this project, 1 ppmw water= 2.44 ppmv =2.44 ppm water

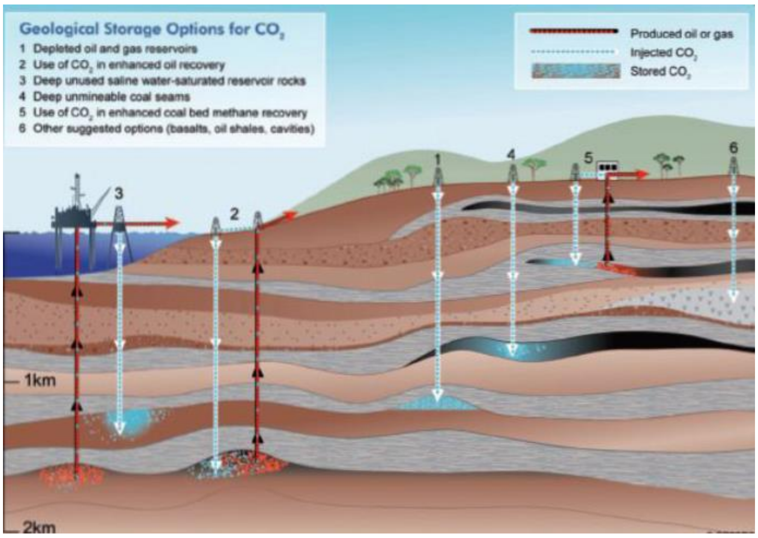

Figure 1.3: Options for storing CO_2 in deep underground geological formations[1].

Deep ocean is not a good option for CO_2 storage, because CO_2 can reduce the pH of ocean, CO_2 can react with sea water, carbonate, and bicarbonate concentrations in sea water may have effected (death) on marine organisms like fish. Instead of saline reservoirs in sedimentary basins can provide suitable geological formations for the safe storage of supercritical CO_2[1, 3]. Table 1.4 shows the existing projects for the geological CO_2 storage.

1.5 Summary

Currently, a large proportion of the research activity in CCS is directed towards the capture and storage phases of the cycle, whilst transportation appears to be an area that has been somewhat left behind. Transportation is an integral part of the CCS process, but it is far behind with most attention given to capture technologies. In tandem with the growing developed economies, the demands for CO_2 to be captured and safely stored is going to be great. This will require the number of CO_2 pipelines to significantly increase, and a few pipelines will need to be close to population centres and such the risks in terms of safety increase and there is an increased urgency to the pipeline integrity.

Carbon steel pipelines are considered to be the most cost effective solution for CO_2 transportation based on their mechanical properties and low cost[12, 13]. During transport, the presence of impurities have to be accurately defined, otherwise will affect pipeline integrity. The level of impurities is important because high impurities will case high corrosion. Experts agree that pipeline failure is normally caused by the internal corrosion and it is difficult to detect. However, the impurity concentrations being reduced to zero will inevitably incur high processing costs. Usually, the existing CO_2 pipelines maintain around 95% CO_2 plus approximately 5% impurities. Defining the consequences in terms of pipeline integrity as a result of certain levels of containment is important to ensure an entire cost effective of CCS process.

Table 1.4: The existing CO_2 storage sites[1]

Project name	**Country**	**Injection start (year)**	**Approximate average daily injection rate (tCO_2 day-1)**	**Total (planned) storage**	**Storage reservoir type**
Weyburn	Canada	2000	3,000-5,000	20,000,000	EOR
In Salah	Algeria	2004	3,000-4,000	17,000,000	Gas field
Sleipner	Norway	1996	3,000	20,000,000	Saline formation
K12B	Netherlands	2004	100	8,000,000	Enhanced gas
Frio	U.S.A	2004	177	1600	Saline formation
Fenn Big Valley	Canada	1998	50	200	ECBM
Qinshui Basin	China	2003	30	150	ECBM
Yubari	Japan	2004	10	200	ECBM
Recopol	Poland	2003	1	10	ECBM
Gorgon (planned)	Australia	~2009	10,000	unknown	Saline formation
Snøhvit (planned)	Norway	2006	2,000	unknown	Saline formation

The compositions of CO_2 mixtures to be transported will depend on the source. CO_2 transport in USA is typically taken from natural sources. However, a few pipelines do transport anthropogenic CO_2. The mixtures from these sources contain, apart from CO_2, typically also, H_2O, O_2, H_2, SO_x, NO_x, H_2S[6, 7].

From a corrosion point of view, the water content is potentially one of the most critical considerations and, as such, is the main focus of this study. It is well known that dry CO_2 does not corrode carbon steel[11], therefore sufficiently drying CO_2 can prevent excessive corrosion rates. However, such a process can be economically impractical. When free water exists, it becomes saturated with CO_2, creating carbonic acid, posing a threat to pipeline integrity. Additionally, the presence of impurities from various sources will pose a risk to the durability of steel pipelines during transport, specifically when the system is contaminated by free water. In addition to water, there is the possibility of the co-existence of acids such as hydrochloric (HCl) and hydrofluoric (HF) depending upon the capture process[7] as well as SO_x, NO_x, H_2S and various other constituents[6, 7, 8].

Currently, the water content for CO_2 pipelines used for enhanced oil recovery (EOR) in the United States is set at a maximum of between 500 and 650 ppm[6, 14] The solubility limit of water in CO_2 over the range of conditions expected for CCS (15-85°C and 73-300 bar), is around 2000ppm before free water precipitation occurs. These calculations are based on the assumption that there are no other additional impurities in the system, which would inevitably influence the solubility limit[14].

No internationally acceptable standards for the specification of CO_2 mixtures exist for pipeline transportation system[15]. Therefore, it is necessary to develop a standard for industry to select the most suitable specification of CO_2 mixtures for safe CO_2 transport.

The focus of this project is directed towards the CO_2-saturated water phase, the water-saturated supercritical CO_2 phase and the under-saturated supercritical CO_2 environment at pressures and temperatures representative of those encountered in CO_2 transport in CCS. Water and SO_2/O_2 as impurities are studied throughout the project. The purpose of this is firstly to determine the susceptibility of carbon steel to the different CO_2-water environments, but also to consider the changes in both general and localised corrosion rates as a function of time to determine whether the rate of growth of surface pits changes over the test duration. Secondly, the main intention of the work is to attempt to relate the corrosion product chemistry and morphology produced in each environment to the extent of surface attack. Thirdly, the focus was to determine the limit of impurities such as H_2O, SO_2 and O_2 at which point significant localised corrosion takes place. Such an approach is adopted through a combination of X-ray diffraction (XRD) measurements, surface profilometry, scanning electron microscopy (SEM) and transmission electron microscopy (TEM).

1.6 Contributions of this research

This work assists in the determination of the operation limitations for safe transport of supercritical CO_2 with impurities such as H_2O, SO_2 and O_2 and helps provide and improve information to establish safe working limits under which acceptable levels of corrosion are observed, both from a localised and general corrosion perspective.

1.7 Objectives of This Study

- To review literature on CO_2 corrosion of carbon steel pipelines to identify the most common types of corrosion that occur, and how these are influenced by operating conditions (such as temperature, pressure, immersion time, and impurities levels);
- To develop a pressurised system and methodology for studying the corrosion issues in CO_2 transportation;
- To study the corrosion scale formed on the metal surface, and to assess both general corrosion and localised corrosion changes under different experimental conditions;
- To characterise the microstructure and composition of corrosion products;
- To determine rates and mechanisms of general and localised corrosion taking place in the presence of impurities;

- To develop a model of CO_2 corrosion in the CO_2 dense phase that can be used to predict rates of corrosion with impurities in a CO_2 pipeline, based on known operating conditions;

1.8 Outline of This Project

Chapter 2 includes all the relevant theories of understands the different corrosion mechanisms and corrosion models.

Chapter 3 is composed of understanding CO_2 pipeline transport and current issues, what cause corrosion, and the mutual solubility of water-CO_2 system, the existing CO_2 pipelines project and regulatory framework for CO_2 transportation – recommended impurities levels, and the last thing is in field data.

Chapter 4 is composed of all the experimental data collected from the literature, which is related to the corrosion behaviour in this SC-CO_2 phase.

Chapter 5 describes the pressure system, the materials used and the preparation, experimental procedures, parameters and test matrices. Surface analysis has been used throughout the project and are described here: the scanning electron microscopy (SEM), Energy-dispersive X-ray (EDX) spectroscopy, the X-ray diffraction (XRD) spectra, transmission electron microscopy (TEM) and profilometry measurement.

Chapter 6 presents the first results to investigate carbon steel exposed to the CO_2-saturated water phase. The effects of temperature, immersion time and pressure on the corrosion behaviour of carbon steel are covered. A discussion of all the results presented, followed by analysis using SEM, XRD. The extent of localised corrosion in each environment taking place was identified using surface profilometry.

Chapter 7 investigates the samples exposed to water-containing (from water-saturated to under-saturated) supercritical CO_2. The study considers the influence of temperature and water content on the corrosion behaviour within the system. The morphology and composition of the corrosion products were identified by using a combination of SEM, XRD and

Transmission Electron Microscopy (TEM) measurements. General corrosion rates were determined through mass loss measurements and in order to determine the localised corrosion taking place, surface profilometry was implemented.

Chapter 8 presents results from measurements of the corrosion rates in supercritical CO_2 with water and gas impurities such as SO_2/O_2. The study considers both the influence of the level of SO_2/O_2 contents, immersion time and water content (from water-saturated to under-saturated) on the corrosion behaviour within the system. The morphology and composition of the corrosion products were identified using SEM, Energy-Dispersive X-ray spectroscopy (EDX), XRD, Raman and Surface Profilometry.

Chapter 9 discusses the main findings of the experiments. A final discussion highlighting the main findings, along with a comparison of experimental studies in literature.

Chapter 10 includes the conclusions and the suggested impurity content for safe CO_2 transportation based on the current experimental data.

Chapter 2 Theory of Corrosion

2.1 Corrosion Theory

Corrosion is defined as the gradual deterioration of materials by chemical or electrochemical reactions within an corrosive environments[16, 17].

In general, corrosion can be classified into a few groups such as high temperature, oxidative and aqueous corrosion. Aqueous corrosion can be known as anodic and cathodic reactions. These phenomenon include more than one process, and for example, iron is exposed to water, there are always two or more chemical reactions which cause corrosion: anodic partial reaction (oxidation of the metal and loss of electrons simultaneously) and the cathodic partial reaction (reduction of the oxidising substance and absorption of electrons simultaneously) at the interface between metal and corrosive medium like water.

2.1.1 Anodic reactions

The most common anodic reaction is the dissolution of metal into the corrosive environments, and at the same time the metal loses electrons. For a typical example when iron is exposed to water, it reacts with the environment to form the oxide; Fe is oxidized to Fe^{2+}.

$$Fe \rightarrow Fe^{2+} + 2e^{-} \qquad 2.1$$

Where 2 is the number of electrons released in the corrosion process and there to be consumed in a cathodic process. Bockris et al[18] suggested the following steps to create Fe^{2+}:

$$Fe + H_2O \leftrightarrow FeOH + H^{+} + e^{-} \qquad 2.2$$

$$FeOH \rightarrow FeOH^{+} + e^{-} \qquad 2.3$$

$$FeOH^{+} + H^{+} \rightarrow Fe^{2+} + H_2O \qquad 2.4$$

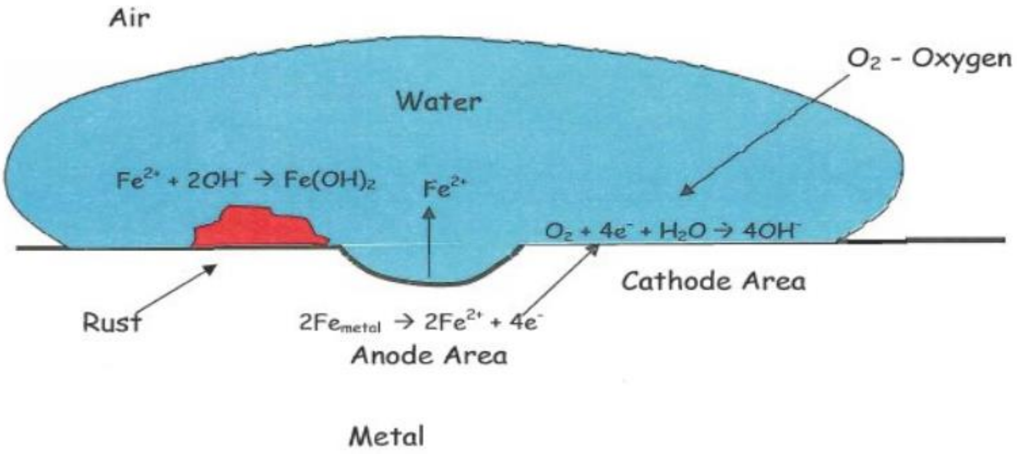

Figure 2.1: Schematic of the corrosion mechanisms for metal in the corrosive environment[16].

2.1.2 Cathodic reactions

Cathodic and anodic reactions are established when sample exposes to solution. Anodic reactions and cathodic activities occur at the same time, namely that the electrons released from the anode are consumed by the cathodic reaction[17]. The cathodic reaction is normally hydrogen evolution or hydrogen ion consumption[19].

$$2H^+ + 2e^- \rightarrow H_2 \qquad 2.5$$

The cathodic reaction depends on the *pH* of the environment. In the neutral or alkaline conditions, i.e., pH=7 or pH>7, the cathodic reaction is normally as the oxygen-reduction or water reduction as shown in 2.6 and 2.7:

$$O_2 + 2H_2O + 4e^- \rightarrow 4(OH)^- \qquad 2.6$$

$$2(H_2O) + 2e^- \rightarrow H_2 + 2(OH)^- \qquad 2.7$$

The overall corrosion reaction can be written as follows:

$$Fe^{2+} + 2OH^- \rightarrow Fe(OH)_2 \qquad 2.8$$

2.2 Types of Corrosion

Corrosion reveals itself in forms that have certain similarities. Many of these forms are not unique but involve mechanisms that have overlapping characteristics that may influence or control initiation or propagation of a specific type of corrosion such as its size, shape and environmental conditions. This project will mainly focus on general corrosion, localised corrosion, and pitting corrosion which has taken place in the CO_2 transportation pipelines.

2.2.1 General corrosion

General corrosion is the most common form of corrosion. General corrosion causes a uniform mass loss of the material, which is characterized by corrosion attack proceeding evenly same rate over the exposed metal area without localised attack. The thickness or mass loss due to corrosion is determined from the weight difference before exposure and after cleaning.

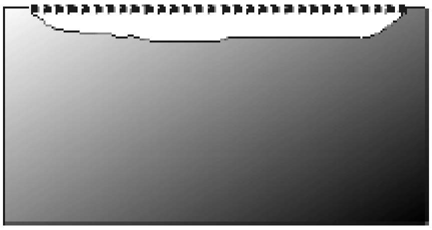

Figure 2.2: Schematic diagram of uniform corrosion (http://corrosion-doctors.org/Forms-Uniform/uniform.htm)

Normally, general corrosion is easier to be predicted and measured. Corrosion failures are not usually caused by general corrosion.

2.2.2 Localised corrosion

Localised corrosion is characterised by high penetration rates at specific sites. Localised corrosion usually takes place at small metal sites where the wetted corrodes at a higher rate while the rest of the surface is subject to a lower attack as shown in Figure 2.3. Work done by Sun and Nesic[20] presents that localised corrosion takes place when partially protective products form on the surface. The rate of corrosion decreases with the existence of protective products, a higher corrosion rate may be obtained from non-productive products. So, the localised corrosion is initiated based on the distribution of the elements in the metal, which can react with corrosive species first.

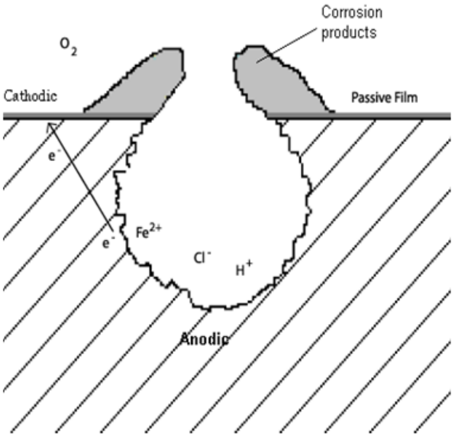

Figure 2.3: Schematic diagram of localised corrosion (http://corrosion-in-rod-pumped-wells.wikispaces.com/Corrosion+Mechanisms+and+Causes).

2.2.3 Pitting corrosion

The most serious and common corrosion in aqueous environments is pitting corrosion, which limits the safe and reliable applications of many alloys in the industries. Pitting corrosion is defined as an extremely localised corrosive attack. Simply stated, pitting is the type of localised corrosion that produces pits, that is, sites of corrosive attack that are relatively small compared to the overall exposed surface. If appreciable attack is confined to a relatively small fixed area of metal acting as an anode, the resultant pits are described as deep. If the area of attack is relatively larger and not so deep, the pits are called shallow. Depth of pitting is sometimes expressed by the term pitting factor. This is the ratio of deepest metal penetration to average metal penetration as determined by the mass loss of the specimen[21, 22, 23].

The pits start at selective areas on the metal surface and follow by the formation of a minute area of an electrolytic cell, which forms an anode, while the cathode is a considerable area of passive metal. The large potential difference characteristic of the anodic-cathodic part results in considerable flow of current with rapid corrosion at the tiny anodic area[23]. The corrosion resistant passive metal surrounding the anode and the activating corrosion products within the pits leads to the tendency of corrosion to penetrate the metal rather than spread all over the surface (Figure 2.4). The pitting shape, size and depth of penetration use to decide the pitting corrosion and rate of pitting (ASTM-46)[24].

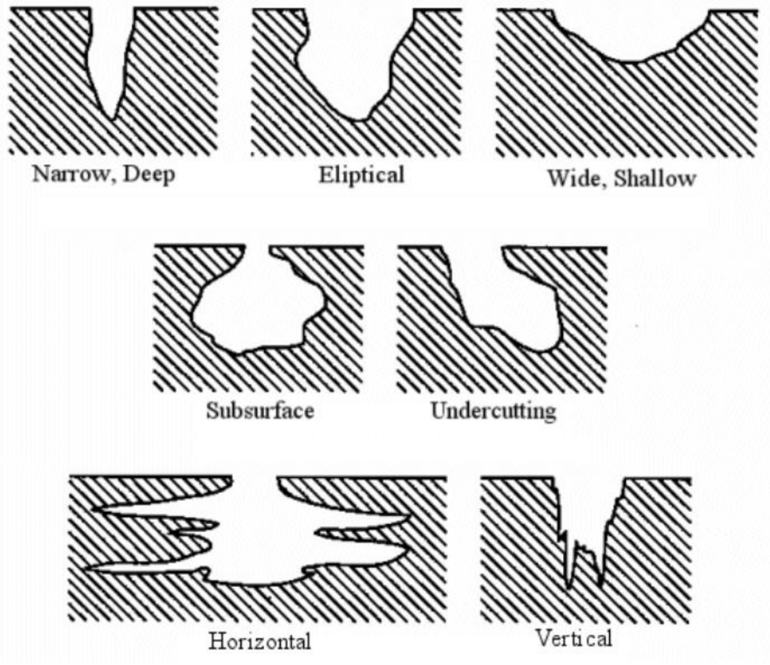

Figure 2.4: Schematic diagram of pitting corrosion (image source: http://www.corrosionclinic.com/types_of_corrosion/pitting_corrosion.htm).

Once pits are initiated, they may continue to propagate or suspend due to their self-sustaining or self-repairing ability. Pit growth is controlled by rate of depolarization at the cathode areas. In the common aggressive environments, the growth is controlled by the amount and availability of dissolved oxygen and ferric chloride[22, 23].

2.3 Mechanisms of CO_2 Corrosion

2.3.1 Chemical reactions

The most common corrosion reactions for CO_2 dissolved in water are discussed by Cole et al[6]. Three series of reactions are capable within steel pipelines which transport supercritical CO_2 when water condenses onto the steel surface. These reactions are:

CO_2 is involved in a sequence of chemical reactions:

- Dissolution of carbon dioxide in water at low CO_2 partial pressures is different from that at high CO_2 partial pressure. Henry's Law used to calculate the solubility constant (K_{sol}, *mol/(L*bar)*) at low CO_2 partial pressure as shown below[25]:

$$CO_{2(g)} \leftrightarrow CO_{2(aq)} \qquad K_{sol} = \frac{C_{CO_2}}{p_{CO_2}} \qquad 2.9$$

$$K_{sol} = \frac{14.5}{1.00258} \times 10^{-(2.27+5.65\times10^{-3}T_f - 8.06\times10^{-6}T_f^2 + 0.075I)} \text{ Molar/bar} \qquad 2.10$$

Where p_{co2} is the partial pressure of CO_2, T_f is temperature in degrees Fahrenheit and C_{CO2} is the concentration of CO_2 in water.

In high pressure CO_2 systems, Henry's law cannot be used due to the relationship between concentration and pressure of CO_2 no longer being linear. The equations from 2.10 to 2.22 are normally used to calculate the non-ideality of the as gas phase[26].

Giving a weak acid, carbonic acid (H_2CO_3):

$$CO_{2(g)} + H_2O_{(l)} \leftrightarrow H_2CO_{3(aq)} \qquad K_{hy} = \frac{C_{H_2CO_3}}{C_{CO_2}} \qquad 2.11$$

The value of the equilibrium constant K_{hy} does not change significantly within the temperature range of 20-100°C, is 0.00258 according to Palmer and Van Eldik's work[27]. This value is applicable for high CO_2 partial pressure.

$$K_{hy} = 2.58 \times 10^{-3} \qquad 2.12$$

Carbonic acid dissociation in water is taken from Duan and Li[28]

$$H_2CO_3 \leftrightarrow H^+ + HCO_3^- \qquad K_{ca} = \frac{C_{HCO_3^-} C_{H^+}}{C_{H_2CO_3}} \qquad 2.13$$

$$InK_{ca} = 233.5159304 - 11974.38348 \cdot T^{-1} - 36.50633536 InT + \\ (-45.08004597 \cdot T^{-1} + 2131.318848 \cdot T^{-2} + 6.714256299 \cdot T^{-1} InT)(P - P_s) + \\ (0.008393915212 \cdot T^{-1} - 0.4015441404 \cdot T^{-2} - 0.00124018735 \cdot T^{-1})(P - P_s)^2$$

Where P is total pressure, P_s is saturation pressure of water and T is temperature in Kelvin. The constant K_{ca} (in molar) can be used reliably from 0 to 100°C and pressure ranges from 1 to 3000 bar[28].

The constant K_{bi} (Bicarbonate anion dissociation, in molar) is taken from[28].

$$HCO_3^- \leftrightarrow H^+ + CO_3^{2-} \qquad K_{bi} = \frac{C_{CO_3^{2-}} C_{H^+}}{C_{HCO_3^-}} \qquad 2.14$$

$$InK_{bi} = -151.1815202 - 0.088695577 \cdot T - 1362.259146 \cdot T^{-1} + 27.79798156 InT - \\ (29.51448102 \cdot T^{-1} + 1389.015354 \cdot T^{-2} + 4.41962584 \cdot T^{-1} InT)(P - P_s) + \\ (0.003219993525 \cdot T^{-1} - 0.1644471261 \cdot T^{-2} - 0.0004736672395 \cdot T^{-1} InT)(P - P_s)^2$$

2.15

Water dissociation (in molar^2) is taken from[28].

$$2H_2O \leftrightarrow H_3O^+ + OH^+ \qquad K_{wa} = C_{H^+} C_{OH^-} \qquad 2.16$$

$$LogK_{wa} = -4.098 - 3245.2 \cdot T^{-1} + 2.2362 \cdot 10^5 \cdot T^{-2} - 3.984 \cdot 10^7 \cdot T^{-3} + \\ (13.957 - 1262.3 \cdot T^{-1} + 8.5641 \cdot 10^5 \cdot T^{-2}) \log \rho_{H_2O} \qquad 2.17$$

Where ρ_{H2O} is the density of water in g/cm^3 and T is temperature in K.

The final stage is the anodic dissolution of iron:

$$Fe \rightarrow Fe^{2+} + 2e^- \qquad 2.18$$

Which can be followed by the precipitation of $FeCO_3$ via a one stage reaction with carbonates, or via a two stage reaction with bicarbonates:

$$Fe^{2+} + CO_3^{2-} \rightarrow FeCO_3 \qquad 2.19$$

$$Fe^{2+} + 2HCO_3^- \rightarrow Fe(HCO_3)_2 \qquad 2.20$$

$$Fe(HCO_3)_2 \rightarrow FeCO_3 + CO_2 + H_2O \qquad 2.21$$

2.3.2 Electroneutrality

Once the concentration of dissolved CO_2 is fixed, according to the equilibrium conditions, the solution cannot have a net charge, an electroneutrality relation is required. Mathematically, it is expressed as[2]:

$$C_{H^+} = C_{HCO_3^-} + 2 \times C_{CO_3^{2-}} C_{OH^-} \qquad 2.22$$

where $C_{H_2CO_3}$, $C_{HCO_3^-}$, $C_{CO_3^{2-}}$, C_{H^+}, and C_{OH^-} are the concentrations (mol/L) of carbonic acid, bicarbonate ion, carbonate ion, hydrogen ion, and hydroxide ion, respectively.

2.3.2 Iron carbonate ($FeCO_3$)

In aqueous environments containing CO_2, corrosion rate and localised corrosion have been shown to be closely linked to the characteristics of the corrosion scale[20]:

$$Fe + 2H_2CO_3 \rightarrow Fe^{2+} + H_2 + 2HCO_3^- \qquad 2.23$$

As dissolution occurs, the pH in the system increases up to the point where the concentrations of Fe^{2+} and CO_3^{2-} ions exceed the solubility limit, enabling precipitation to occur via the one stage reaction in Equation (2.19):

Iron carbonate film growth depends on precipitation rates, R_{FeCO3}; Factors influencing the rate of precipitation of $FeCO_3$ were explained in detail by Hunnick et al[29] who generated the expression in Equation (2.24) to described the precipitation of $FeCO_3$:

$$R_{FeCO_3} = \frac{A}{V} e^{52.4 - \frac{119.8kj/mol}{RT}} K_{sp}(S-1)(1-S^{-1}) \qquad 2.24$$

where R_{FeCO_3} is the rate of precipitation of $FeCO_3$, mol^2/m^4, A is the surface area of the electrode, m^2, V is the solution volume, L, T is the temperature, K, K_{sp} is the solubility product limit, $(mol/L)^2$ and S is the value of super-saturation.

Dugstad et al[30] stated that the driving force for $FeCO_3$ precipitation is determined by the level of supersaturation and in principle, there exist two steps involved in the precipitation processes; nucleation and particle growth. The assumption is made that these two processes are related to the relative supersaturation (S_R):

$$S_R = \frac{Q - Q_{eq}}{K_{sp}} = SS - 1 \qquad 2.25$$

$$SS = \frac{C_{Fe^{2+}} C_3^{2-}}{K_{sp}} \qquad 2.26$$

where Q is the concentration of the solute in mol/L, Q_{eq} is the equilibrium solubility in mol/L, SS is the supersaturation of $FeCO_3$ and K_{sp} is the solubility product for $FeCO_3$ in mol^2/L^2.

Once the product of the Fe^{2+} and CO_3^{2-} concentrations exceed the solubility limit, the formation of crystal $FeCO_3$ at the surface becomes thermodynamically favourable. Saturation of the solution is achieved much earlier in the higher temperature. A significant increase in Fe^{2+} concentration within the bulk solution, resulting in an increase in solution pH (particularly within the electric double layer where Fe^{2+} would be most concentrated, then, an increase in pH has been shown to result in a decrease in corrosion rate. The precipitation film has contributed towards a reduction in corrosion rate by blocking sites on the steel or restricting the transport of corrosive species to the surface.

2.4 Corrosion Models

Many corrosion models were developed for CO_2 corrosion service in the oil and gas industry. The first model was developed by de Waard and Milliams[19] in 1975. This model has been developed further today by many researchers. All the corrosion models can be classified into three groups: empirical models[31, 32, 33, 34, 35, 36], semi-empirical models[37, 38, 39, 40, 41, 42, 43] and mechanistic models[25, 44, 45, 46, 47, 48, 49]. All the models used different mathematical theories, assumptions or dynamic modelling methods.

Table 2.1: Corrosion model classifications

Empirical models	Semi Empirical models	mechanistic models
LIPUCOR	DM 1/2	TULSA
NORSOK	DLM	HYDROCOR
SWEETCOR	DLD	KSC
CORPOS	IFE	OHIO
CBR-TS	CORMED	OLI
	PREDICT	DREAM
	CASSANDRA	MULTICORP
	ECE	WWCORP

2.4.1 Empirical Models

CO_2 corrosion empirical models include LIPUCOR, NORSOK, SWEETCOR, CORPOS and CBR-TS, these models are data driven and rely on measured corrosion rates[31, 32, 33, 34, 35, 36]. The corrosion rates are obtained from the experimental data based on different parameters and variables such as temperature, pressure, velocity, and pH.

An example of the NORSOK model shows below:

$$CR_{NOR} = K_t f_{CO_2}^{0.62} \left(\frac{\tau_w}{19}\right)^{0.146+0.0324\log(f_{CO2})} f(pH)_t \quad 20^\circ C \le T \le 150^\circ C \qquad 2.27$$

$$CR_{NOR} = K_t f_{CO_2}^{0.36} \left(\frac{\tau_w}{19}\right)^{0.146+0.0324\log(f_{CO2})} f(pH)_t \; T = 15^\circ C \qquad 2.28$$

$$CR_{NOR} = K_t f_{CO_2}^{0.62} f(pH)_t \qquad T = 5^\circ C \qquad 2.29$$

Where CR_{NOR} is the corrosion rate in mm/year, K_t is temperature, f_{co2} is the fugacity of CO_2, τ_w is the wall shear stress in Pascal.

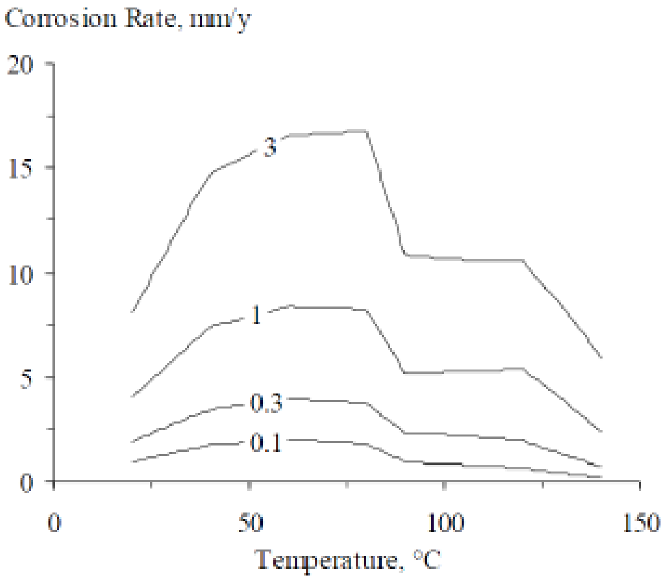

Figure 2.5: An example of calculated corrosion rate prediction from 0.1-3 bars from the NORSOK model[32, 35].

The main problems for empirical models are the limitations when the corrosion rates are to be calculated outside the parameters used for the experimental work. The models need to be updated always and requires recalibration after adding new data.

2.4.2 Semi-empirical models

2.4.2.1 De Waard and Milliams -1975

The most famous semi-empirical model is de Waard and Milliam model[19, 40] which developed it in 1975 based on their experimental work. The corrosion rate is given by:

$$logV_{cor} = 7.96 - \frac{2320}{T+273} - 5.55 \times 10^{-3}T + 0.67logP_{CO_2} \qquad 2.30$$

Where CR is the corrosion rate in mm/year, T is the temperature in K and P_{co2} is the partial pressure of CO_2 (bar).

The corrosion rate is calculated

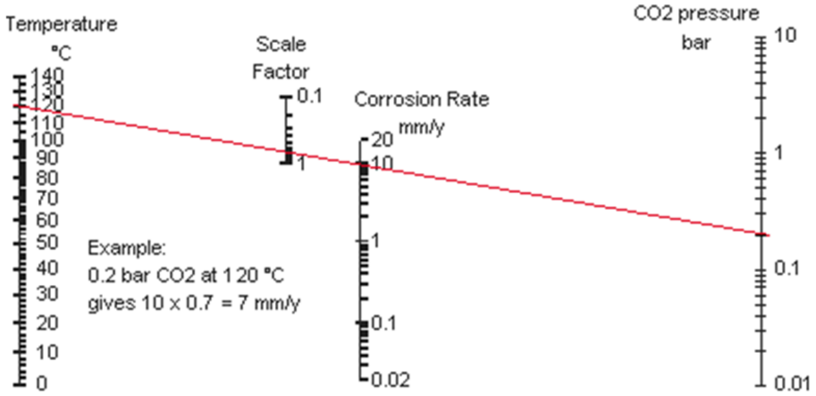

Figure 2.6: An example of calculate corrosion rate from De Waard and Milliams model[19].

This model did not consider the pH effect, only use CO_2 partial pressure and temperature in the equation 2.35. As the pressure increases, it is inaccurate to assume all H^+ ions in the solution come from the dissolution of carbonic acid (such as salt water solution).

2.4.2.2 De Waard and Milliams -1991

In 1991, De Waard and Milliams modified the first model developed in 1975[19]. The new equation for the corrosion rate are shown:

$$log V_{cor} = 5.8 - \frac{1710}{T+273} + 0.67 log f_{CO_2} \qquad 2.31$$

Where f_{co2} is the fugacity of CO_2 (bar).

The core difference of the model uses fugacity of CO_2 rather than CO_2 partial pressure between 1975 and 1991[40]. This model also modified a few factors with an individual equation was proposed for the calculation of each of factors, such as pH, iron concentration, pressure, inhibitor, temperatures and protective scale formation on the surface[40]. Woollam and Hernandez[35] calculated the corrosion rate for the model as shown in Figure 2.7

The main limitation of empirical or semi-empirical models should be when the application is extrapolated outside the experimental range. In such case this can lead to unreliable and sometimes physically unrealistic results[50]. Moreover, predictions made by this model are considered to be worst case scenario, especially under film forming conditions[50].

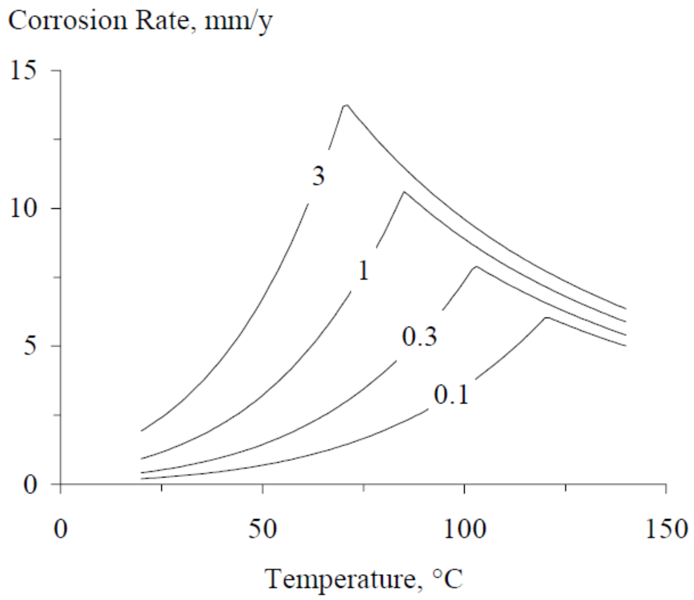

Figure 2.7: An example (Woollam and Hernandez of calculate corrosion rate prediction from 0.1-3 bars from De Waard and Milliams model (1991)[35, 40].

2.4.3 *Mechanistic models*

The mechanistic models do not rely on measured corrosion rates from experimental tests. These models use functions based on limits of corrosion theory. The main problem is that the mechanistic models cannot guarantee the prediction of corrosion rate unless they are validated by experimental data[35]. There are a lot of mechanistic models being used in oil and gas industry as shown in Table 2.2.

Theoretically, mechanistic models are based on the description of the electrochemical processes. When CO_2 dissolves into solution such as water, it will produce H_2CO_3, which then hydrates and dissociates to create HCO_3^- and $CO3^{2-}$. At the same time, the anodic reaction (e.g. Fe^{2+}) will produce on the surface.

The above processes produce a concentration gradient which will lead to molecular diffusion of the species toward and away from the surface.

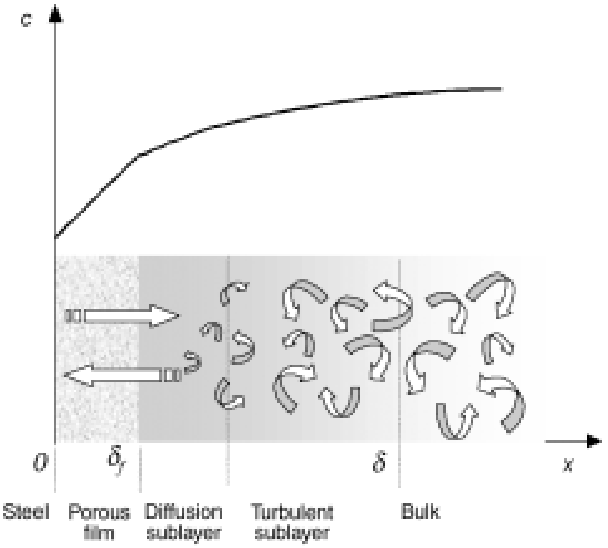

Figure 2.8: A typical concentration profile for a dissolved species[25].

Butler-Volmer equation (2.36) uses to express the electrochemical reactions at the interface between the metal surface and the solution medium.

$$i_{net} = \sum_k i_{0,k} \left\{ e^{\left(\frac{(1-\alpha_k)n_k F(E-E_k^o)}{RT}\right)} - e^{\left(\frac{-\alpha_k n_k F(E-E_k^o)}{RT}\right)} \right\} \qquad 2.32$$

Where $i_{0,k}$ is the k'th electrochemical reaction according to the produced species concentration gradients at the surface. E is the calculated potential.

An example of a mechanistic model developed by Nesic et al[25, 38, 51]; an electrochemical model of CO_2 corrosion is in Equation 2.33. The equation shows the corrosion rate was calculated based on the sum of the cathodic contributions including the hydrogen ions, carbonic acid, water and oxygen are equally that of the anodic contributions including dissolution of iron.

$$i_{H^+} + i_{H_2CO_3} + i_{H_2O} + i_{O_2} = i_{Fe} \qquad 2.33$$

$$CR = \frac{i_{Fe} M_{w,Fe}}{\rho_{Fe} nF} \qquad 2.34$$

Where i_{Fe} is the corrosion current density of the anodic reaction, CR is the corrosion rate in mm/year.

The calculated output i_{corr} required input parameters such as temperature, CO_2 partial pressure, O_2 concentration, flow geometry, pH and materials type.

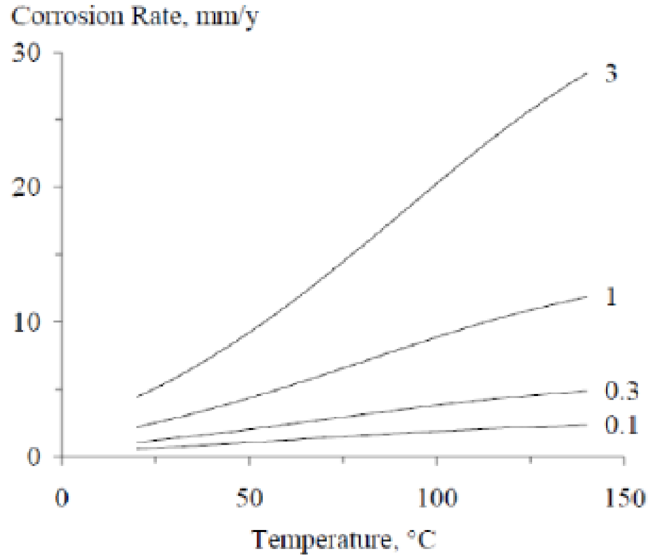

Figure 2.9: Corrosion rates prediction for electrochemical model developed by Nesic et al[25], The plot is from Woollam[35].

The main limitation of mechanistic models are the lack of understanding regarding the interactions between the film formation and corrosion processes at the interface between the steel surface and solution.

2.5 Summary

This Chapter describes the mechanism of CO_2 corrosion, general corrosion and localised corrosion when metal in a CO_2-containing environment.

An appraisal of the empirical, semi-empirical and mechanistic models predict the corrosion rates from literature is presented.

The impact of CO_2 corrosion on low alloy steel has been covered extensively at pressure relevant to oil and gas transport (up to 20 bar)[17]. These models were developed preferentially for service in these conditions. However, less attention has been afforded to work conducted in high pressure CO_2 corrosion systems (up to 100 bar) when CO_2 is the dominant phase, especially in conditions above the critical points of 31°C and 73.8 bar where CO_2 exists as a supercritical fluid. Therefore, these are not applicable to CO_2 transportation were the pressures are above 60 bar.

Chapter 3 Understanding General Supercritical CO_2 Pipeline Transport and Current Issues

3.1 Summary

The current focus of the study includes: properties of gas, liquid and supercritical CO_2, the impurities that cause corrosion, the solubility of water in supercritical CO_2 environments, commercial drivers for CO_2 pipeline projects, the regulatory framework for CO_2 pipelines-recommended impurities levels and the existing corrosion risks in CO_2 transportation.

3.1.1 Pressure and temperature in CO_2 pipelines

Carbon dioxide is usually colorless, and heavier than air as shown in Table 3.1. Efficient transport of CO_2 via pipelines requires that CO_2 be compressed to the liquid or supercritical state[12]. Transport at lower densities (i.e., gaseous CO_2) is inefficient because of the low density of the CO_2 and relatively high pressure drop per unit length. Values for the critical point for pure CO_2 are 31.0°C, 73.8 bar[5]. At temperatures and pressures above this point, CO_2 is present in the supercritical phase. Supercritical carbon dioxide is a fluid state which means it has liquid CO_2 density while it flows like a gas. By operating pipelines at pressures greater than the CO_2 critical pressure of 7.38MPa, temperature fluctuations along the pipeline will not result in the formation of gaseous CO_2 and the difficulties encountered with two-phase flow[5].

CO_2 transportation will usually occur around the temperature (4-50 ºC) and pressure (80-150 bar), respectively. It is critical to avoid presence of CO_2 in two phases during transportation under normal operating conditions[5, 52]. The formation of liquid CO_2 is above 5.1bar. The supercritcal CO_2 forms at or above its the critical point (73.8 bar at 31.1 ºC).

Table 3.1: Specific properties of carbon dioxide

Property	**Unit**	**Value**
Molecular	g/mol	44.01
Critical Pressure	Bar	73.8
Critical Temperature	°C	-56.6
Aqueous Solubility at 25°C, 1 bar	g/l	1.45
Standard (gas) density	Kg/m^3	1.98
Density at critical point	Kg/m^3	467
Liquid density at 0°C, 70 bar	Kg/m^3	995
Sublimation temp. 1 bar	°C	-79
Solid density at freezing point	Kg/m^3	1562
Colour	-	None

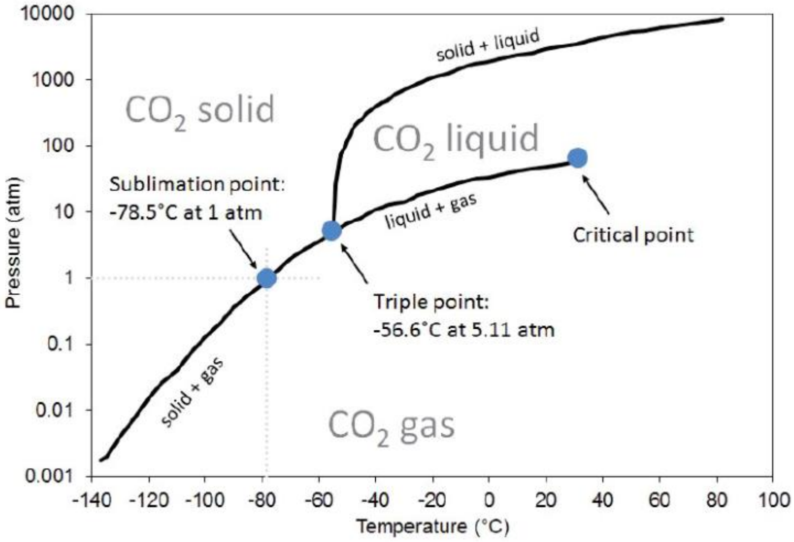

Figure 3.1: CO_2 phase diagram[53].

The lowest temperature that can be expected during normal operation is about 4ºC, as can be deduced from the data in the pipeline Rules of Thumb Handbook[53] because the seawater temperature is typically around 4ºC. The maximum temperature in the transport system is found downstream of the main compressor, where CO_2 exits the final stage at above 30ºC. For normal operation, the pressure ranges in CO_2 pipeline are between 85 and 150 bar onshore and the maximum pressure is 200 bar offshore[54].

3.1.2 Water content

Water plays an important role because carbon steel pipelines are subjected to corrosion deterioration due to the presence of water, which is a significant threat to pipeline integrity. There is no consensus on what the water concentration should be, especially when the impurities such as CH_4, O_2, H_2S, SO_2 NO_2 are considered together[54].

Figure 3.2 shows how the solubility of water decreases on the path from atmospheric pressure to the point where the phase transition from gas to liquid occurs. At the phase transition, there is a sharp increase in solubility, and with increased pressure, the solubility increases even more. It must be noted that this graph applies to pure CO_2. Impurities might increase or decrease the water solubility[54]. A similar CO_2-H_2O model has been done by Spycher et al[26] who calculated mutual solubilities from 12 to 100°C and up to 600 bar.

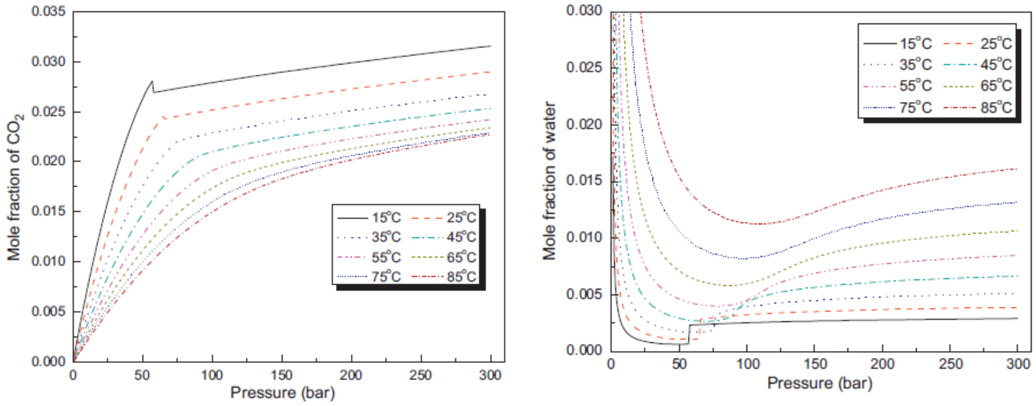

(a) (b)

Figure 3.2: The solubility of CO_2 in water as function of pressure and temperature (a) The solubility of water in CO_2 as function of pressure and temperature (b)[2].

The mutual solubility of CO_2-H_2O calculated using Eq.2.9 to 2.22 are shown in Figure 3.2. The solubility of CO_2 in water increases sharply with rising pressure up to the saturation pressure and at a lesser rate thereafter. However, the solubility of water in CO_2 is high at low pressure, passes through a minimum, and then increases with pressure[2].

Svensson et al[12] looked at issues related to the transport of CO_2 in CCS, and highlighted that some EOR pipelines are run at pressures greater than 100 bar. However, there can be significant drops in pressure and temperature along a line. Eldevik et al[55] showed that the temperature will reduce via heat exchange with the surrounding environment, and the pressure will decrease due to frictional forces during CO_2 transportation. The drop in temperature and pressure would reduce the solubility of water in the CO_2 phase and increase the fluid velocity[2]. If the amount of water was close to the solubility limit at the higher temperature and pressure, formation of an aqueous phase can occur resulting in corrosion of the materials due to presence of CO_2 and the accumulation of impurities during depressurisation can also have a large effect on corrosion of the materials such as carbon steel.

There is no allowable data that shows the mutual solubility of H_2O-CO_2 for varying temperature as a function of pressure combined with impurities such as N_2, H_2S, SO_x and O_2.

3.2 Commercial Drivers for CO_2 Pipeline Projects

Carbon Capture and Storage (CCS) technology would enable the continued use of fossil fuels through the abatement of CO_2, preventing emissions into the atmosphere.

CCS involves capturing CO_2 from large point sources (i.e. power generation, refineries and industrial applications), purified CO_2, compressing it and transporting it to geological reservoirs or depleted oil and gas reservoirs for sequestration or Enhanced Oil Recovery (EOR) purposes.

It is estimated that for the abatement of climate change, approximately 10 or 20 Giga tonnes (Gt) of CO_2 will need to be transported and sequestered in 2050[56]. Dugstad et al[56] estimated that this would require the construction of 3000 twelve-inch (or 1000 twenty-inch) pipelines under the assumption of a flow velocity of 1.5 m/s. They suggested that the only logical choice to achieve such enormous levels of abatement was to have the extensive network constructed from carbon steel.

The transportation of CO_2 has been practiced for over 30 years, and currently, over 6000 km of pipelines exist for EOR purposes. The majority of these pipelines are located in the USA and Canada, with some projects also being undertaken in Norway. The majority of these pipelines transport CO_2 from natural sources; however a few pipelines do transport anthropogenic CO_2.

Although the composition of CO_2 streams is not readily available in the open literature, Table 3.2 provides a summary of information compiled from various sources. CO_2 from natural sources is typically high purity and will require minimal gas treatment prior to injection. Only impurities such as CO_2, N_2, CH_4, H_2O and H_2S are to be expected[57]. Considering the anthropogenic sources, there can be a distinct differences in fluid composition, as the stream can become further contaminated as a result of the presence of flue gas impurities (SO_x, NO_x and O_2 in particular). Regrettably, this is not reflected in the anthropogenic sources listed in Table 1, and it is unclear from the literature from which this was compiled whether this is because these components are not present at all, or the stream was not analysed for these particular compounds.

In Table 3.2, it can be observed that the water content within each CO_2 stream varies from 20 ppm to water-saturated. It is worth noting that if the water content within the CO_2 stream exceeds the solubility limit a separate aqueous phase will exist, inducing corrosion. If such a phase were to form on the pipeline wall, it will invariably become saturated with CO_2, creating carbonic acid (H_2CO_3), lowering the pH of the aqueous phase (to pH ~3.3 at 80 bar) and posing a threat to pipeline integrity[6].

It is also worth pointing out in Table 3.2 that the three anthropogenic sources from gasification plants have the lowest specified water content and the onset of corrosion in the system. The introduction of impurities such as SO_x, O_2, and NO_x from flue gases can pose a significant problem for the transportation of anthropogenic CO_2 streams in terms pipeline integrity when a sufficient level of water is present in the system. Some of these impurities dissolve readily in the aqueous phase at very low water concentrations below the solubility limits reported for pure CO_2[56]. When SO_2, O_2 and water in particular are all present in the system, they can segregate into the aqueous phase forming sulphurous (H_2SO_3) and/or sulphuric acid (H_2SO_4), further lowering the pH and potentially increasing the corrosivity of the environment[56].

Consequently, because of the inherent risk associated with corrosion, companies set their own limits for water content in CO_2 streams. According to Dugstad et al[56], 500 ppm tends to be the accepted limit in the literature, although little reasoning exists behind this specific value. Kinder Morgan set a concentration limit of approximately ~600 ppm[15], whereas Weyburn dehydrated the CO_2 stream down to 20 ppm and the pipelines at Sleipner transport water-saturated CO_2[11].

Surprisingly, there is no general consensus on what the actual allowable water content should be in the transported CO_2 stream.

3.3 In Field Data

Analysis of corrosion rates in field exposures of CO_2 transport pipelines in the US has shown low corrosion rates (0.00025–0.0025 mm/year). 29 leaks were reported from 1986 to 2008[54]. The causes of the incidents for CO_2 pipelines were[5, 60].

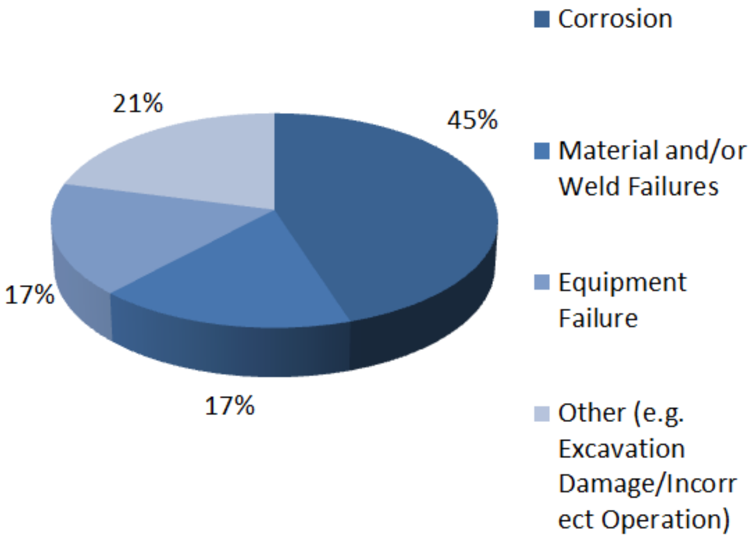

Figure 3.3: DNV – 1986-2008 – in US there were 29 incidents on pipelines transporting dense-phase CO_2[54]

Table 3.2: The impurity levels for the existing CO_2 pipelines

	Canyon Reef Carriers[4, 5, 57, 58]	**Central Basin Pipeline**[4, 57, 59]	**Sheep Mountain**[4, 5, 57]	**Bravo Dome Source**[4, 5, 57]	**Cortez Pipeline**[4, 5, 57]	**Weyburn**[7, 57]	**Jackson Dome**[4]	**Sleipner**[7, 57]	**Snohvit**[4, 11, 57]
Location	USA	USA	USA	USA	USA	USA and Canada	USA	Norway	Norway
Operator	Kinder Morgan	Kinder Morgan	BP	BP	Kinder Morgan	Dakota Gratification Company	Denbury Resources	Statoil	Statoil
Length (km)	225	230	660	350	808	328	295	n/a	153
Capacity (Mt/y)	5.2	11.6	6.3/9.5	7.3	25	5	n/a	1	0.7
Source	Anthropogenic	Natural	Natural	Natural	Natural	Anthropogenic	Natural	Natural	Anthropogenic
CO_2	85-98	98.5	96.8-97.4	99.7	95	96	98.7-99.4	93-96	n/a
CH_4	2-15	0.2	1.7	-	1-5	0.7	0.3	0.5-0.2 total hydrocarbons	n/a
N_2	<0.5	1.3	0.6-0.9	0.3	4	<300 ppm	0.3	3-5 non-condensable	n/a
H_2S	<260 ppm	<26 ppm	-	-	20 ppm	9000 ppm	-	150 ppm	n/a
C^{2+}	-	-	0.3-0.6	-	Trace	2.3	-	0.5-0.2 total hydrocarbons	n/a
CO	-	-	-	-	-	0.1	-	-	n/a
O_2	-	<14 ppm	-	-	-	70 ppm	-	-	n/a
NO_x	-	-	-	-	-	-	-	-	n/a
SO_x	-	-	-	-	-	-	-	-	n/a
H_2	-	-	-	-	-	Trace	-	3-5 non-condensable	n/a
A_r	-	-	-	-	-	-	-	3-5 non-condensable	n/a
H_2O	122 ppm	~650 ppm	315 ppm	-	~650 ppm	20 ppm	420 ppm	Water-saturated	50 ppm

There are no leaks reported from CO_2 pipelines that resulted in injuries to people. However the possibility of the impact of a CO_2 release should be considered, because the density of CO_2 is much higher than air, and will replace air in low-lying areas, and given a significant effect and adverse human to asphyxia. Healthy and safety becomes more important when the other impurities are present such as SO_2, NO_2 and H_2S and these also increase internal corrosion risks. For these reasons, if the number of CO_2 pipelines increase and pass through much more populated areas in future, it will increase the probability of risk**[5]**. The total number of incidents of CO_2 transported pipelines are summarised in Table 3.3 shown that the number of incidents for CO_2 transmission pipelines increases in double in comparison between 1990-2001 and 1994-2013[54].

Table 3.3: A summary the incidents of pipelines[54]

	Natural gas transmission		**Hazardous liquid transmission**		**CO_2 transmission**	
Years	1990-2001	1994-2013	1990-2001	1994-2013	1990-2001	1994-2013
No. of incidents	1287	1891	3035	5897	10	64
No. of incidents/1000 km pipeline/year	0.17	0.19	0.82	1.06	0.32	0.64

Table 3.4 presents typical performance values for removal of flue gas components by SO_x, NO_x and CO_2 control systems. As seen that the impurities contents such as SO_x, NO_x are very high and must be purified before entering the pipelines. A suggestion of the tentative CO_2 quality recommendation has been provided in the Dynamis Project[7], Alstom[8], IPCC[9] and Kinder Morgan's Specification[4] as summarised in Table 1.4 in Chapter 1.

There is no consensus on what the actual target for the maximum water concentration should be. It has been argued that full dehydration down to 50ppmv should be applied. This limit has been specified for the first CO_2 pipelines in the USA[10] and for the Snøhvit[5] pipeline in Norway.

3.4 Regulatory Framework for CO_2 Pipelines – Recommended Impurity Levels

Nonetheless, there are significant differences between the transport of natural CO_2 and that from anthropogenic sources. Flue gas impurities are to be expected and vary depending on the type of capture process, the source and the level of gas treatment applied. Table 3.4 is adapted from the work of Lee et al.,[61] who considered five different scenarios of post processing for a coal-fired power station with different levels of proposed contaminants. The table indicates significant variations in impurity levels depending upon the amount of post processing involved.

Table 3.4: Typical performance values for removal of flue gas components by SO_x, NO_x and CO_2 control systems – adapted from Lee et al.,[61] and Cole et al.,[52]

	Contaminants				
	SO_2	**SO_3**	**NO_2**	**HCl**	**Hg^{2+}**
No contaminant control	0.6-4.4 wt.%	42-579 ppm	24-111 ppm	36-835 ppm	23-261 ppm
SO_2 control by a wet FGD scrubber	337-2403 ppm	21-302 ppm	18-87 ppm	2-44 ppm	2-27 ppm
NO_x control by LNB/SCR	0.6-4.4 wt.%	42-579 ppm	10-44 ppm	36-835 ppm	23-261 ppm
NO_x control by LNB/SCR plus SO_2 control by a wet FGD scrubber	337-2403 ppm	21-302 ppm	7-35 ppm	2-44 ppm	2-27 ppm
NO_x control by LNB/SCR plus SO_2 control by a wet FGD scrubber, and also assuming MEAS-based CO_2 control unit is used to trap CO_2	34-135 ppm	<(21-302) ppm	<(7-35) ppm	<(2-44) ppm	<(2-27) ppb

3.4.1 Purification limits for CCS

Recently, Abbas et al.,[62] summarised the impurity limitations for safe CO_2 transport to geological storage and EOR. Abbas et al.,[62] showed higher allowable SO_x and NO_x concentration of around 200 ppm for geological storage of CO_2 transport as shown in Table 3.5.

3.4.2 Purification limits for EOR

In Table 3.6 the results listed a few unknown reasons when the pipelines contain impurities such as SO_x, NO_x and O_2. Abbas et al.,[62] showed lower allowable SO_x and NO_x concentration of around 50ppm for EOR of CO_2 transport in comparing to that as shown in Table 3.5.

A large variation has been seen in these specifications (Figure 1.4, 3.5 and 3.6). It is unclear from the literature from what the minimum water content can cause significant corrosion take place when SO_x, NO_x and H_2S are present within CO_2 transport shown in table 1.4 3.5 and 3.6. Currently, no CO_2 quality requirements have been decided upon that taken into account these impurities and their effect on corrosion issues.

Table 3.5: Impurities limits for CO_2 transportation for geological storage[62]

Component	**Level (vol% or ppm)**	**Reasons**
CO_2	> 90%[63]	To ensure very high purity of CO_2 and prevention of large amounts of non-condensable
SO_x	<200 ppm[64]	Corrosion and H_2SO_4[64, 65, 66]
O_2	<4% (All non-condensable)[63, 67]	Reacts with oil[64, 66]
N_2	<4% (All non-condensable)[63]	Decrease miscibility (MMP)[64, 66]
A_r	<4% (All non-condensable)[63]	Decrease miscibility and Storage capacity reduction[64, 66]
H_2	<4% (All non-condensable)[63]	Decrease miscibility and Storage capacity reduction[64, 66]
CH_4	<4% (All non-condensable)[63, 67]	Decrease miscibility (MMP)[64, 66]
CO	<4% (All non-condensable)[63]	Storage capacity reduction[64, 66]
H_2S	<1.5%[63]	Potential deposition of sulphur if H_2S is co-injected with SO_x[67]
H_2O	<500 ppm [7, 63]	N.A[7, 62]
NO_x	<200 ppm[67]	Corrosion[64, 65]

Note: 1ppmw water = 2.44ppmv or ppm (in mole) water

Table 3.6: Impurities limits for CO_2 transportation for EOR[62]

Component	**Level (vol% or ppm)**	**Reasons**
CO_2	>95 %[63]	To ensure very high purity of CO_2 and prevention of large amounts of non-condensable
SO_x	<50 ppm[64]	N.A
O_2	<10 ppm (All non-condensable)[63, 67]	Reacts with oil[64, 66]
N_2	<4% (All non-condensable)[63]	Decrease miscibility (MMP)[64, 66]
Ar	<4% (All non-condensable)[63]	Decrease miscibility and[64, 66]
H_2	<4% (All non-condensable)[63]	Decrease miscibility and[64, 66]
CH_4	<2% (All non-condensable)[63, 67]	Decrease miscibility (MMP)[64, 66]
CO	<4% (All non-condensable)[63]	N.A
H_2S	<50 ppm[63]	N.A
H_2O	<50 ppm[63]	N.A
COS	<50 ppm[63]	N.A

Note: 1ppmw water = 2.44ppmv or ppm (in mole) water

Chapter 4 Literature Review for Corrosion Research in High Pressure Conditions

4.1 Materials Used in CO_2 Transportation Pipelines

The material selection in carbon transmission pipelines mainly depends on the corrosion rate. With regards to the transport of CO_2 over moderate distances, carbon steel is the most common material of choice based on its relatively low cost and favourable mechanical properties[55]. However carbon steel is susceptible to corrosion. For the pipeline applications with high contents of water, particularly in some areas which have higher velocities, corrosion-resistant stainless steel (13Cr) to protect the erosion-corrosion problem should be considered[16]. Buit et al[54] point out that economic considerations lead to the use of regular carbon steel, which is commonly used for most pipelines. Corrosion resistant alloys would inhibit corrosion, but would be prohibitively expensive.

4.2 Corrosion Research in Systems of High Pressure Conditions

Experiments in supercritical CO_2-saturated water environments have been performed by a handful of researchers[15, 68, 69, 70, 71]. Cui et al[70] evaluated the corrosion resistance of J55, N80 and P110 steels at a flow velocity of 1 m/s in a simulated oilfield brine saturated with supercritical CO_2 at 82.7 bar through the application of mass loss measurements. The results showed that corrosion rates reduced significantly as a function of time which was attributed to the growth of an uncharacterised surface film on the steel surface as shown in Figure 4.1. The observed film became thicker and more compact over time, offering increased protection to the steel substrate.

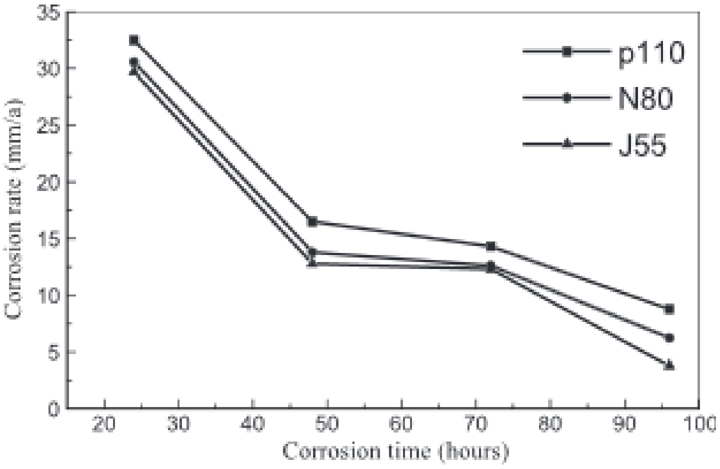

Figure 4.1: Samples exposed to CO_2-saturated water as a function of time[70].

In a later study, Cui et al.,[71] investigated the corrosion resistance of the same three pipeline steels (J55, N80 and P110) in static conditions with a produced supercritical CO_2 water-saturated at 82.7 bar and temperatures of 60, 90, 120 and 150°C. Over 96 hours of exposure as shown in Figure 4.2, mass loss results indicated that corrosion rate reduced with increase in temperature. Compositional analysis of the corrosion products formed indicated that the surface film mainly comprised of $FeCO_3$ and FeOOH. The scales formed at high temperature were observed to be more compact and continuous, and consequently more protective than those witnessed at low temperature.

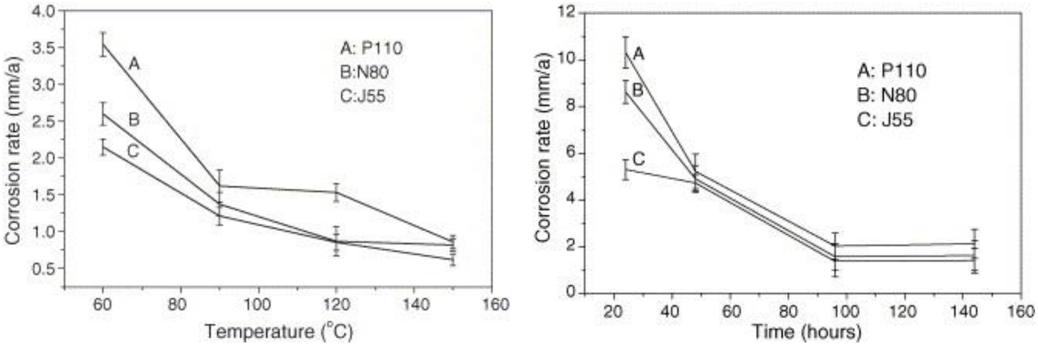

(a) (b)

Figure 4.2: Samples exposed to CO_2-saturated water for 96 hours in (a) different temperatures, (b) immersed time[71].

Wu et al.,[68, 72] studied the growth of corrosion products on carbon steel in a simulated produced water at 82.7 bar and 90 °C through the application of electrochemical impedance spectroscopy. Their results indicated that in such environments, the corrosion rate of the steel reduced significantly over the first 24 hours of testing (~8.6 mm/year) due to the fast formation of a surface corrosion product. The corrosion rate continued to decrease (~1.6 mm/year) with exposure time after 144 hours as the uncharacterised film became thicker and denser.

In a more recent study, Choi et al.,[2] performed corrosion experiments to evaluate the corrosion rate of carbon steel in CO_2-saturated water as a function of pressure (between 40 and 80 bar at 50°C) as shown in Table 4.1. They showed that corrosion rates are over 20 mm/year over a period of 24 hours which was attributed to the low pH in the system (~3.1-3.3)[2] meaning that the solubility of $FeCO_3$ was sufficiently high to prevent the formation of any precipitate on the steel surface.

Table 4.1: Test matrix for corrosion tests[2]

CO_2 Pressure (bar)	O_2 pressure (bar)	Temp (°C)	Time (Hours)	Water	Corrosion Rate (mm/year)	
					General	Localised
40	0	50	24	CO_2-saturated water –(400ml) water added to autoclaves	~20	N/A
60						
80						

Figure 4.3 shows the surface morphologies of the corroded samples in the CO_2-saturated water phase at different pressures. They found that an amorphous layer of corrosion product covered on the surface. It is worth noting that carbon and oxygen were detected within the corrosion product on the steel surface through EDS measurements shown in Figure 4.3 (d)[2].

Uniform corrosion attack (after cleaning) was observed on the surface for the sample exposed to CO_2-saturated water phase at different pressures and 50ºC. Their results showed no localised corrosion on the surface which means that the non-protective Fe_3C film did not initiate localised corrosion[2] as shown in Figure 4.4.

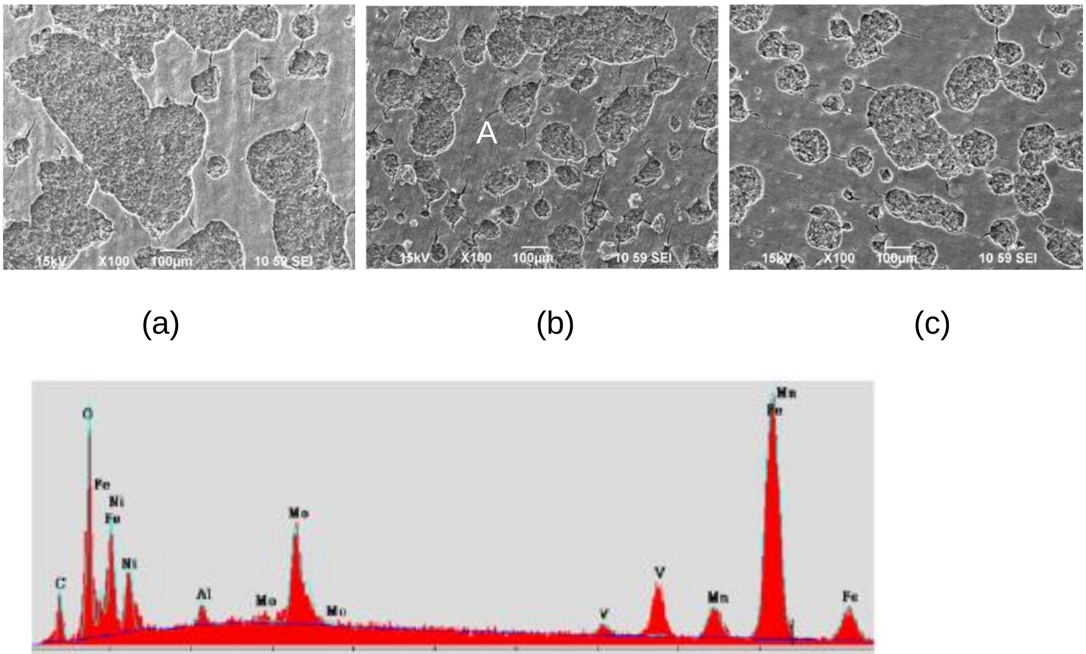

(a) (b) (c)

(area A) in b

(d)

Figure 4.3: SEM image (a, b and c) and EDS spectra (d) of the corroded surface of samples exposed to the CO_2-saturated water for 24 h at 40, 60, 80bar and 50ºC[2].

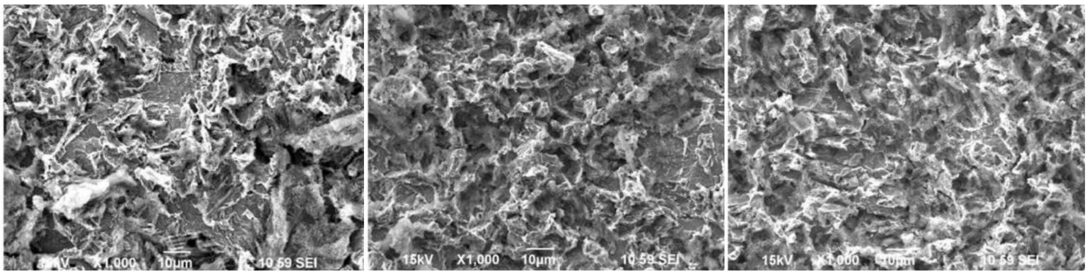

(a) (b) (c)

Figure 4.4: SEM image (a, b and c) spectra of the corroded surface of samples (after cleaning) exposed to the CO_2-saturated water for 24 h at 40, 60, 80bar and 50ºC[2].

Finally, Lin et al.,[73] reviewed the influence of partial pressure on the morphology of corrosion products formed on three materials: N80, P110 and J55 in CO_2-saturated water at pressures between 13.8 and 103.4 bar at 90°C. Under the experimental conditions as shown in Figure 4.5, the largest scale thickness are recorded at 120°C. the thickness reduced with the increasing the temperature between 120°C and 160°C[73].

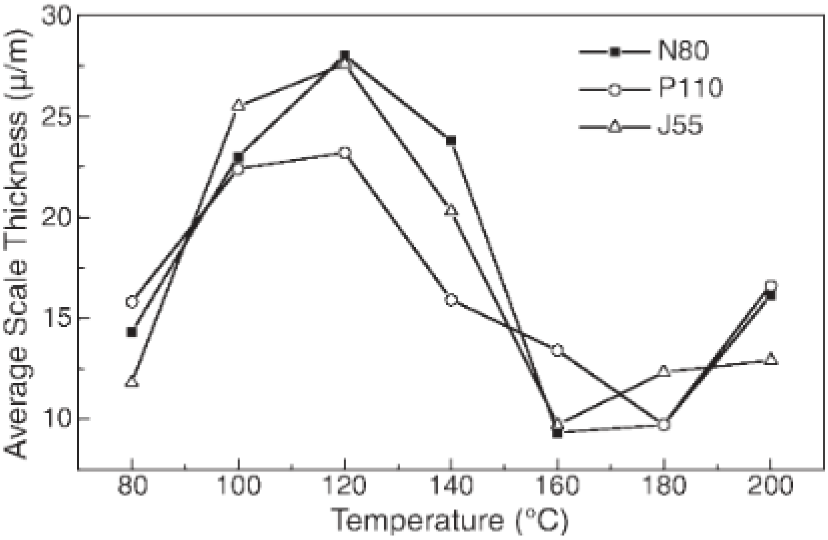

Figure 4.5: The scale thickness change as a function of temperatures[73].

4.3 Corrosion Research in Systems Relevant to of CO_2 Transportation

In the oil and gas field, the dominant phase is either hydrocarbon or water, whilst in CO_2 transport for CCS applications the main process fluid is supercritical CO_2, which contains considerably smaller quantities of water. Therefore, a relative smaller corrosion rate in comparison to that for fully immersed samples is experienced in solution.

4.3.1 Effect of H_2O

The reviewed work is done by Russick et al.,[74] who studied corrosion in supercritical CO_2. They investigated the corrosion of stainless steel (304L and 316) and carbon steel (1018) in pure supercritical CO_2, and water-saturated CO_2 conditions using a CO_2 pressure system as shown in Figure 4.6. Two CO_2 cylinders are used as the CO_2 source, two pneumatic gas booster compressors are used to achieve the supercritical pressure, and the autoclave has the volume of 1.8L. The entire matrix of test conditions are summarised in Table 4.2. They observed that no corrosion occurred in pure supercritical CO_2, only the carbon steel corroded in water-saturated CO_2 condition.

Table 4.2: Test matrix for corrosion tests[74]

	Temperature	Pressure	Water	Time	Corrosion Rate (mm/year)

	(°C)	(bar)	(g)	(Hours)	General	Localised
stainless steel	50	241	0	24	No	N/A
	50	241	40	24	No	N/A
carbon steel	50	241	0	24	No	N/A
	50	241	40	24	Uniform distributed spots covered the surface	N/A

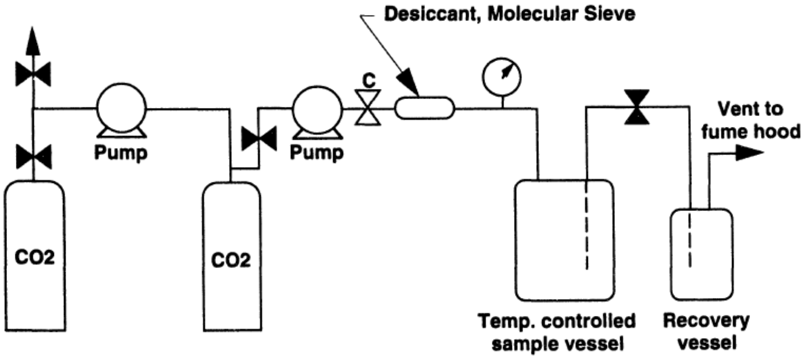

Figure 4.6: Schematic illustration of the CO_2 pressure system used for corrosion testing[74].

Very recently, Choi and Nesic[2] performed some exposure tests in an autoclave (138 bar static autoclave made of stainless steel with 1L volume) and the entire matrix of test conditions are summarised in Table 4.3. They suggest that corrosion rates of steel are around ~0.2 mm/year for the sample exposed to water-saturated supercritical CO_2 phase.

The SEM images of the sample surface were covered by dense, crystalline iron carbonate ($FeCO_3$), and the grain size of $FeCO_3$ decreased with increasing pressure as shown in Figure 4.7(a-c). The EDX spectra showed the corrosion products mainly consisted of iron, carbon and oxygen. This indicates that corrosion can take place in the water-saturated CO_2 phase under high pCO_2 conditions, but the corrosion rate is low (0.2 mm/y) due to the formation of $FeCO_3$ on the steel surfaces[2]. The question here is that it is not clear whether the pits were formed prior to or during the precipitation of the $FeCO_3$ film.

Table 4.3: Test matrix for corrosion tests[2]

CO_2 Pressure (bar)	O_2 pressure (bar)	Temp (°C)	Time (Hours)	Water	Corrosion Rate (mm/year)	
					General	Localised
40	0	50	24	Water-saturated CO_2 –(400ml) water added to autoclaves	~0.2	N/A
60					~0.2	N/A
80					~0.4	N/A

Recent work done by Sim et al.,[75] investigated the localised attack of carbon steel exposed to a supercritical CO_2 environment in which water contamination was deliberately added over the range of 900 to 50,000 ppm at 40°C and 80 bar in 7 days. The entire matrix of test conditions is summarised in Table 4.4.

Their results showed the localised corrosion rates are higher than the general corrosion rate, with an average of ~0.62 mm/y. They also showed the average pitting rate of all samples are not too dissimilar, suggesting that water concentration may only play a minor role on pit growth in a supercritical CO_2 environment. However more detailed work in the future is needed to fully describe pitting kinetics[75].

4.3.2 Effect of H_2O and O_2

In another study by Choi et al.,[15] experiments were conducted to review the influence of O_2 on the corrosion of X65 carbon steel in water-saturated supercritical CO_2 phase. Tests were conducted at 80 bar and 50°C with O_2 partial pressures of 0 and 5.1 bar over durations of 24 hours. The entire matrix of experimental conditions and results are provided in Table 4.5 below. The result indicated that the presence of O_2 inhibited the formation of a protective $FeCO_3$ layer on the steel surface, resulting in a maximum corrosion rate of 1 mm/year at the partial pressure of 3.3 bar.

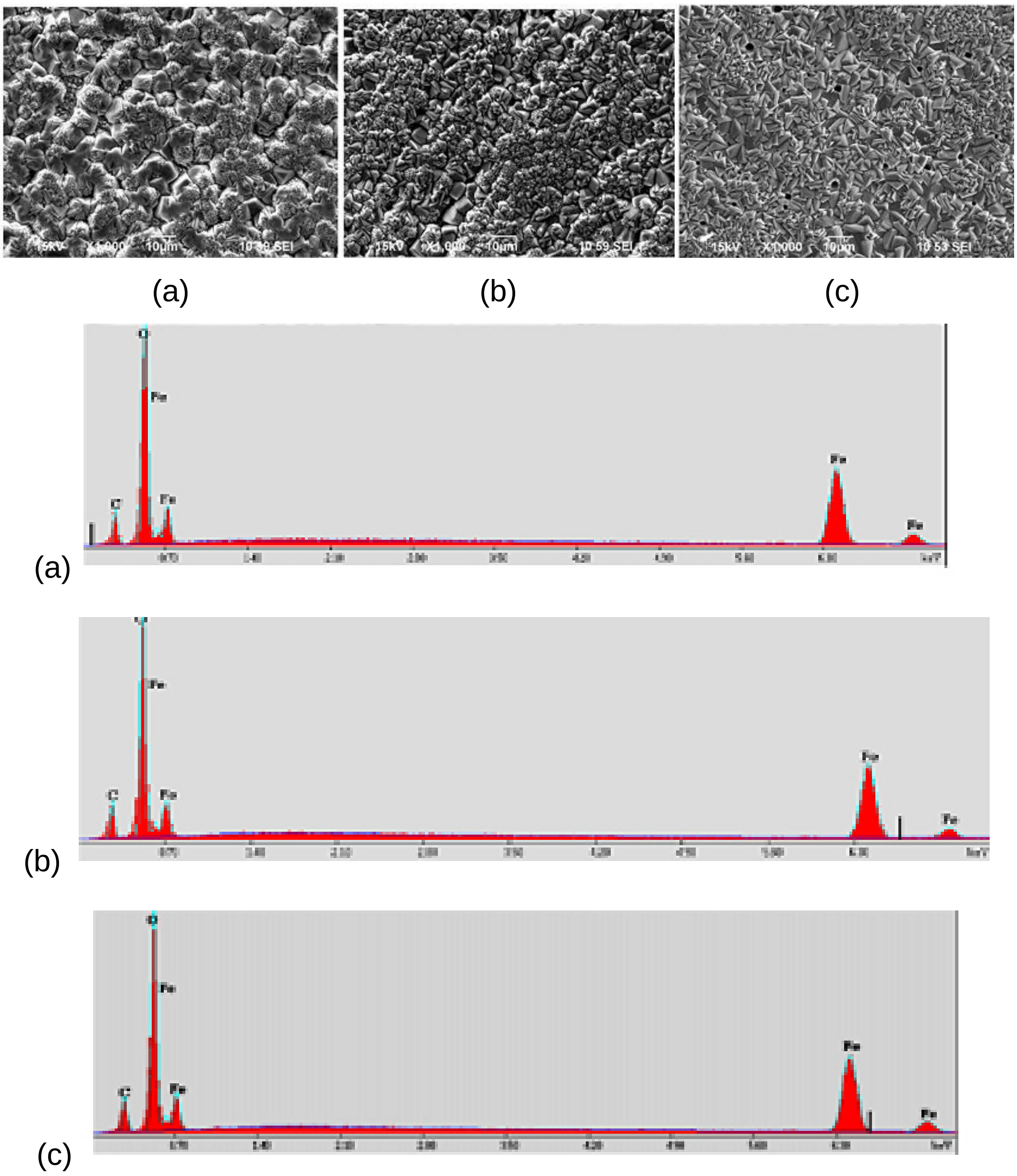

Figure 4.7: SEM images and EDS spectra of the corroded surface of samples exposed to the water -saturated CO_2 phase for 24 h at 40 (a), 60 (b) and 80 (c) bar and 50ºC[2].

When O_2 was added in the system, surfaces were covered by a porous scale; this mainly consisted of iron and oxygen (Figure 4.8 (b)-(d)). This indicates that the addition of O_2 can increase the corrosion rates of carbon steel by inhibiting the formation of protective $FeCO_3$ (Figure 4.8 a) and forming less protective iron oxides[15].

Table 4.4: Test matrix for corrosion tests[75]

CO_2 Pressure (bar)	Temp (°C)	Time (hrs)	Water (ppm)	Corrosion Rate (mm/year)	
				General	Localised
80	40	168	900	~0.08	Av. ~0.22 Max ~ 0.65
			1800	~0.07	Av. ~ 0.30 Max ~ 0.64
			2600	~0.06	Av. ~ 0.22 Max ~ 0.55
			3500	~0.06	Av. ~ 0.22 Max ~ 0.65
			Water-saturated phase (~4500)	~0.08	Av. ~ 0.19 Max ~ 0.50

Table 4.5: Test matrix for corrosion tests[15]

CO_2 Pressure (bar)	O_2 pressure (bar)	Temp (°C)	Time (Hours)	Water (ppm)	Corrosion Rate (mm/yr)	
					General	Localised
80	0	50	24	Water-saturated CO_2 (3400ppm) - 10g water added to autoclaves to ensure saturation	~0.4	N/A
	1.6				~0.6	N/A
	3.3				~1.05	N/A
	5.1				~0.9	N/A

4.3.3 Effect of $SO_2/O_2/H_2O$

When SO_2 and SO_3 are present within the supercritical CO_2 environment, the corrosion mechanism of the carbon steel is changed. SO_2 and SO_3 are expected to play a large role in accelerating corrosion rate and hence reduce the formation of iron carbonate film[14].

Choi et al.,[15, 76] investigated the effect of SO_2 and O_2 on the corrosion of carbon steel in supercritical CO_2 environments as shown in Table 4.6. The addition of 0.8 bar of SO_2 (1%) in the gas phase dramatically increases the corrosion rates of carbon steel from 0.38 to 5.6 mm/y and it increases further to 7 mm/y upon addition of both O_2 (4%) and SO_2.

Figure 4.9 shows the SEM images and EDS spectra of the sample surface after 24 h for 80 bar CO_2/0.8 bar SO_2 and 80 bar CO_2/3.3 bar O_2/0.8 bar SO_2 conditions. The surface was covered by crystalline corrosion products which consisted of iron, sulfur and oxygen[15].

Farelas et al.,[77, 78] explains the effect on the corrosion rate of carbon steel in supercritical/liquid CO_2/SO_2 phase with 650ppm of water for 24 hours. The entire matrix of experimental conditions and results are provided in Table 4.7 below. The corrosion product covered on the surface as shown in Figure 4.10 (a, b).

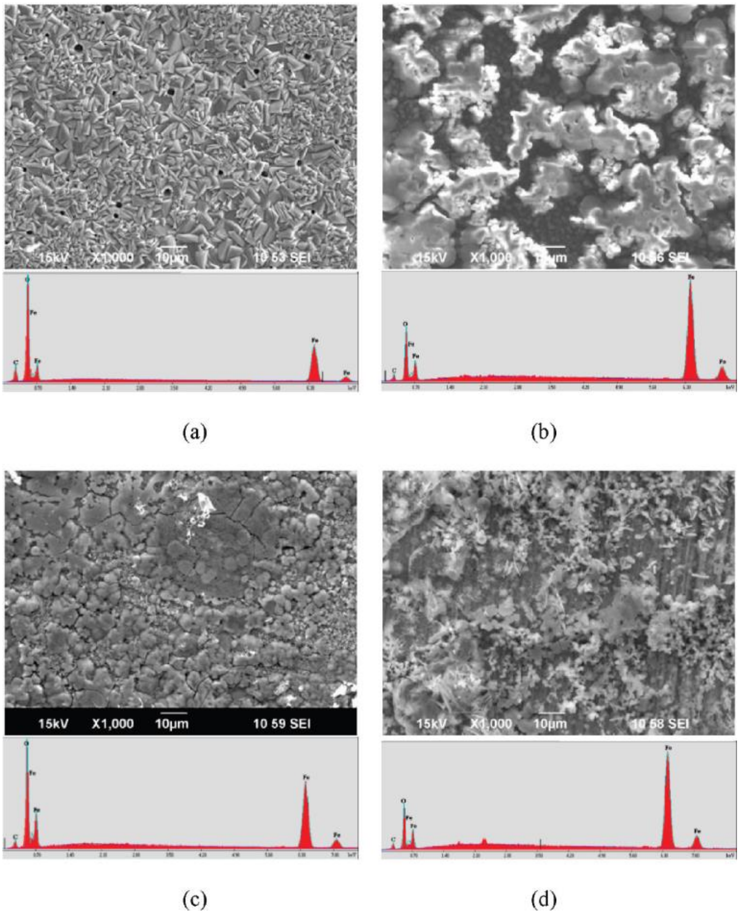

Figure 4.8: SEM image and EDS spectra of the sample exposed in water-saturated CO_2 for 24 h with different O_2 contents: (a) 80 bar CO_2, 50 °C, (b) 80 bar CO_2, 1.6 bar O_2, 50 °C, (c) 80 bar CO_2, 3.3 bar O_2, 50 °C, (d) 80 bar CO_2, 5.1 bar O_2, 50°C[15].

The results showed no significant general corrosion at the surface when the water content was 650 ppm with less than 0.1 % of SO_2. Their results showed that high localised corrosion rates of 2.4 mm/year and 6.8mm/year were obtained in liquid CO_2 conditions with 650 ppm of water as shown in Figure 4.10 (c, d-after cleaning the corrosion products)[78]. Therefore, the question is what would be the localised corrosion in long term experiments?

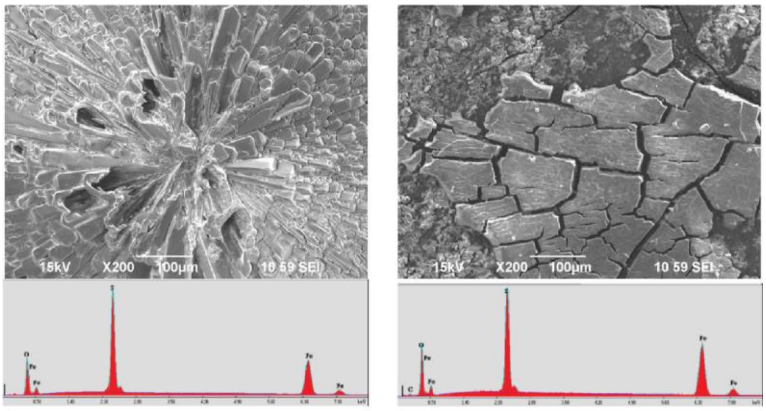

(a) (b)

Figure 4.9: SEM image and EDS spectra of the sample exposed in water-saturated CO_2 for 24 h: (a) 80 bar CO_2, 0.8 bar SO_2, 50 °C, (b) 80 bar CO_2, 3.3 bar O_2, 0.8 bar SO_2, 50°C[15].

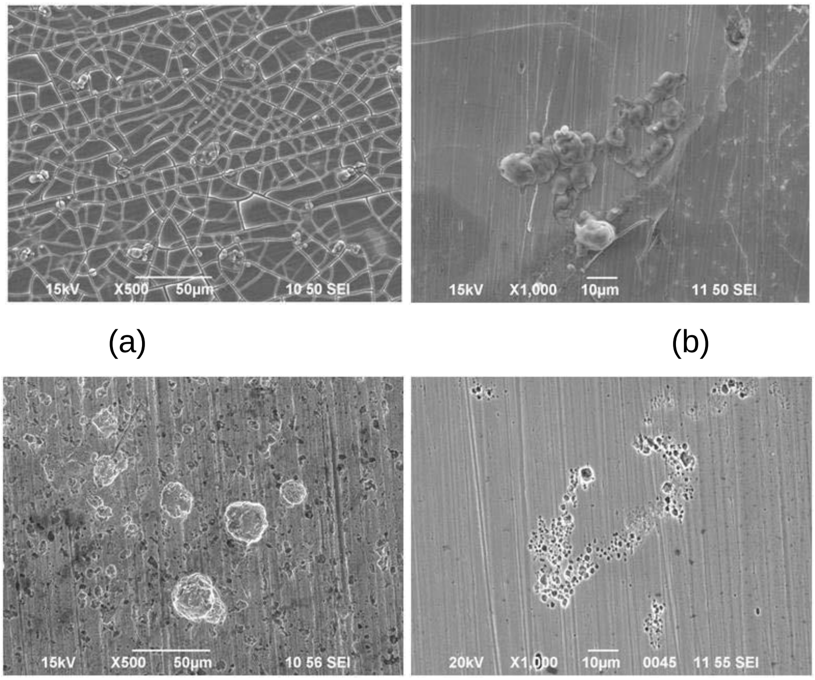

(a) (b)

(c) (d)

Figure 4.10: SEM images of the corroded surface of the samples exposed to the liquid CO_2 for 24 h, at a CO_2 partial pressure of 80 bar, 50°C, before cleaning: (a) 0.1% SO_2, (b) 0.05% SO_2. After cleaning: (c) 0.1% SO_2, (d) 0.05% SO_2[77, 78].

Table 4.6: Test matrix for corrosion tests[76]

CO_2 pressure (bar)	O_2	SO_2	Temp (°C)	Test period	Water content (ppm in mole)	Corrosion Rate (mm/year)	
						General	Localised
80	3.3 bar (4 %)	0.8 bar (1%)	50	24 h	0 ppm	No observed corrosion	N/A
	0	0			Water-saturated CO_2 (~3400 ppm) – 10 g water added to autoclave to ensure saturation	~0.4	N/A
	3.3 bar	0				~1.05	N/A
	0	0.8 bar (1%)				~5.6	N/A
	3.3 bar	0.8 bar (1%)				~7.0	N/A
80	0	0	50	24 h	650 ppm (6% H_2SO_4)	0.032	N/A
	0	0		120h		0.019	N/A
	3.3 bar	0		120 h		0.025	N/A
	0	0.8 bar (1%)		24 h	650 ppm	3.48	N/A
	3.3 bar	0.8 bar (1%)		24 h		3.70	N/A

Dugstad et al.,[56, 79] represented experimental work (Figure 4.11) in small autoclaves with 140-200 ml volume and concluded that corrosion occurred at a very low water concentration (488ppm) when the system was contaminated with SO_2 (2440ppm) as shown in Table 4.8. The surface was covered with a thin corrosion layer as shown in Figure 4.11.

A recent publication[56] showed the corrosion can take place at 25°C and 100bar with 488ppm water, 100ppm SO_2 for 14 days, and the general corrosion rates are recorded as less than ~0.005 mm/year as shown in Table 4.9 below. However, spots are observed on the surface as shown in Figure 4.13 (a-d), the results suggested the localised corrosion rates would much higher than general corrosion rates. However, the localised corrosion rates were not quantified in their work.

Recently, Xiang et al.,[80] investigated the corrosion of X70 steel in water-saturated supercritical CO_2 contaminated with SO_2 and O_2 using a system as shown in Figure 4.14. The system mainly consists of a gas source, pump, rotary autoclave, and waste gas treatment.

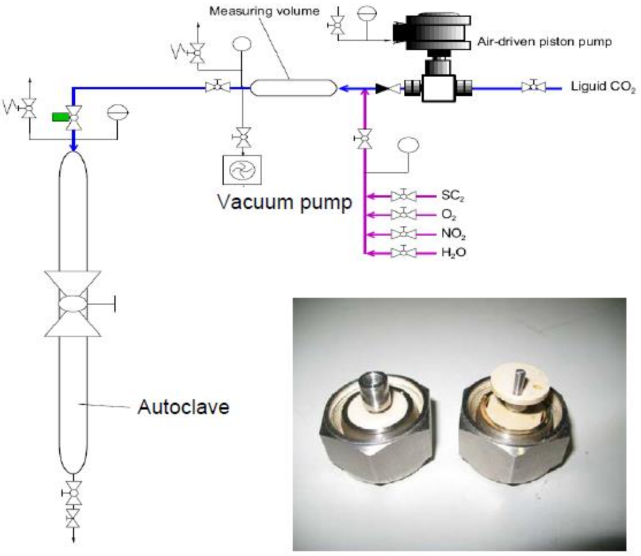

Figure 4.11: Schematic illustration of the test autoclave system used for corrosion experiments[79].

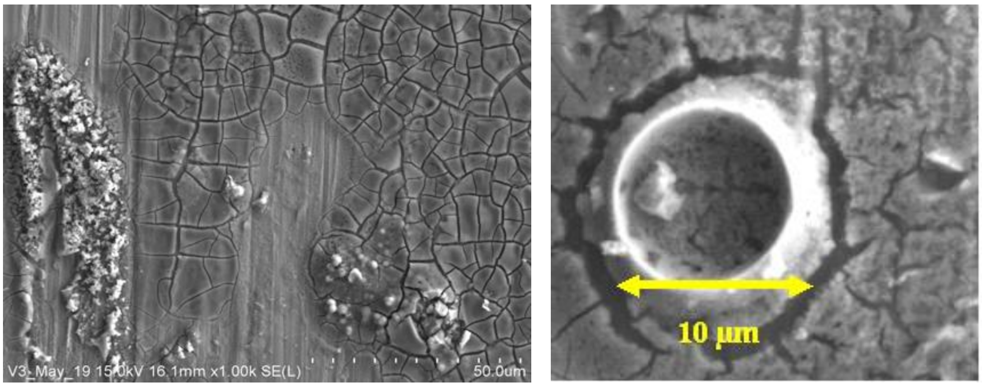

Figure 4.12: The morphology of the surface film formed on the steel sample exposed in liquid CO_2 with 2440ppm SO_2 and 488ppm H_2O[56, 79].

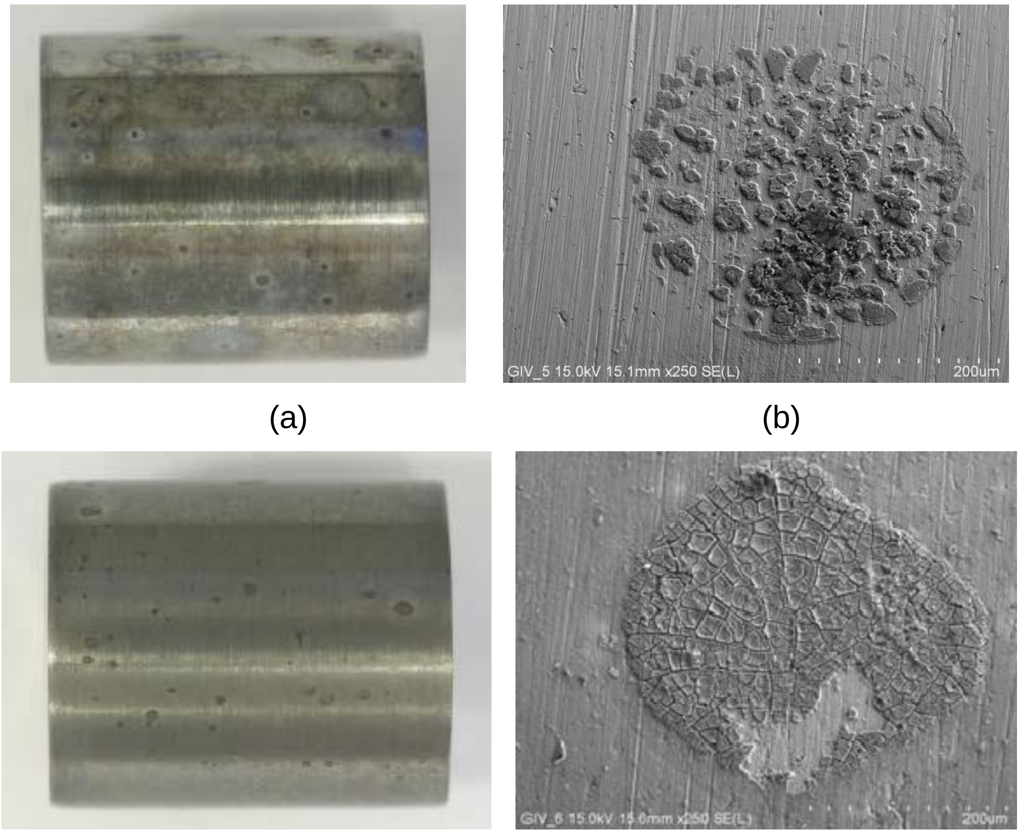

(a) (b)

(c) (d)

Figure 4.13: The morphology of the surface film formed on the steel sample exposed in liquid CO_2 with (a, b) 488ppm H_2O and 344ppm SO_2, (c, d) 1220ppm H_2O and 344ppm SO_2[56].

Table 4.7: Test matrix for corrosion tests[78]

CO_2 pressure (bar)	O_2	SO_2	Temp (°C)	Test period	Water content (ppm in mole)	Corrosion Rate (mm/year)	
						General	Localised
80	0	0	50	24 h	650	0	No attack
		0.08 bar (0.1%)				0.03	No attack
		0.04 bar (0.05%)				0.05	No attack
		0.08 bar (0.1%)	25			0.1	6.8
		0.04 bar (0.05%)				~0	2.4
		0.08 bar (0.1%)				~0.019 (1000 rpm)	No attack
		0.08 bar (0.1%)				~0.013 (1000 rpm)	No attack

Table 4.8: Test matrix for corrosion testing[56]

CO_2 Pressure (bar)	O_2 (ppm)	SO_2 (ppm)	H_2O (ppm)	Temp (°C)	Time (Hours)	Corrosion Rate (mm/yr)	
						General	Localised
100	0	0	1220	20	720	No attack	
	200	0					
	100	200	488		168	~0.01	No attack
	100	1000				<0.01	No attack

Table 4.9: Test matrix for corrosion tests[56]

CO_2 Pressure bar	O_2 ppm	SO_2 ppm	H_2O ppm	Temp °C	Rotation r/min	Time Hours	Corrosion Rate (mm/year)	
							General	Localised
100	0	0	488	25	3	336	No attack	N/A
			1222					
		100	488				~0.005	Spots, Not quantify
							~0.005	
							~0.02	

The samples used in the test were X70 carbon steel. They observed that the corrosion rate increase with increase SO_2 concentration as shown in Table 4.10.

Xiang et al.,[80] presented the surface morphologies of the corroded specimens of X70 steel using SEM under different SO_2 concentrations as shown in Figure 4.15. Results showed that the corroded specimen with 2% SO_2 had a smoother surface than the others, while the specimen with 0.2% SO_2 had many small protrusions on the corroded surface, and that was probably where the anodic corrosion reactions occurred. The samples with 0.7% SO_2 had many cellular shaped corrosion products, this was visible to the naked eye. The XRD spectra showed the corrosion products are hydrates of $FeSO_3$ and $FeSO_4$ and no $FeCO_3$ was observed in their tests. They[80] suggested that the corrosion mechanism of the carbon steel under the conditions of interests may be totally changed due to the presence of SO_2, and the SO_2 is more corrosive than CO_2, even though $FeCO_3$ could be formed, it would dissolve soon. The corrosion products of hydrated of $FeSO_4.4H_2O$ were observed with increase in SO_2 concentration.

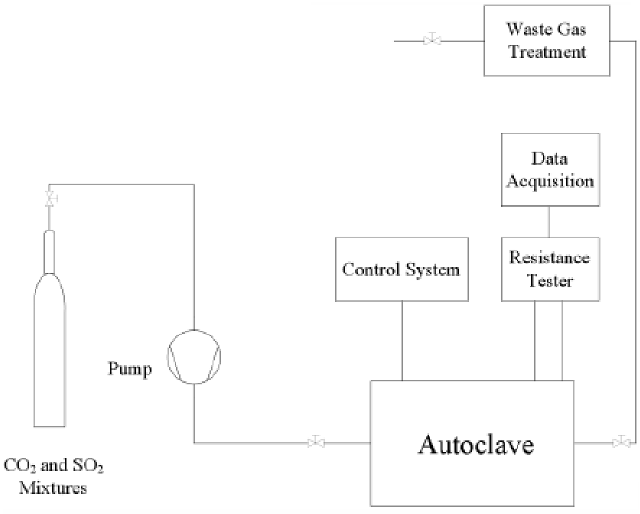

Figure 4.14: Schematic illustration of the test autoclave system used for corrosion experiments[80].

Table 4.10: Test matrix for corrosion testing[80]

CO_2 Pressure bar	SO_2 mol%	O_2 ppm	H_2O ppm	Temp °C	Time hours	Corrosion Rate (mm/yr)	
						General	Localised
100	0.2	1000	Water-saturated CO_2 (~4600 ppm) -6g water added to autoclave to ensure saturated	50	288	~0.2	N/A
	0.7					0.7	
	1.4					~0.85	
	2					~0.9	

More recent work by Xiang et al.,[14] determined the upper limit of moisture content for supercritical CO_2 pipeline transport using the same system as shown in Figure 4.14. The entire matrix of experimental conditions and results are provided in Table 4.11 below. In the experiments, the weight-loss method was applied to measure the corrosion rate of X70 steel exposed to supercritical $CO_2/SO_2/O_2/H_2O$ mixtures for different levels of relative humidity, aiming to explore the critical relative humidity point for X70 steel corrosion under such conditions, which is a crucial point for setting the upper limit of moisture content. The critical relative humidity was estimated to be between 50% and 60% (2750 and 3240 ppm) on the basis of the experimental results.

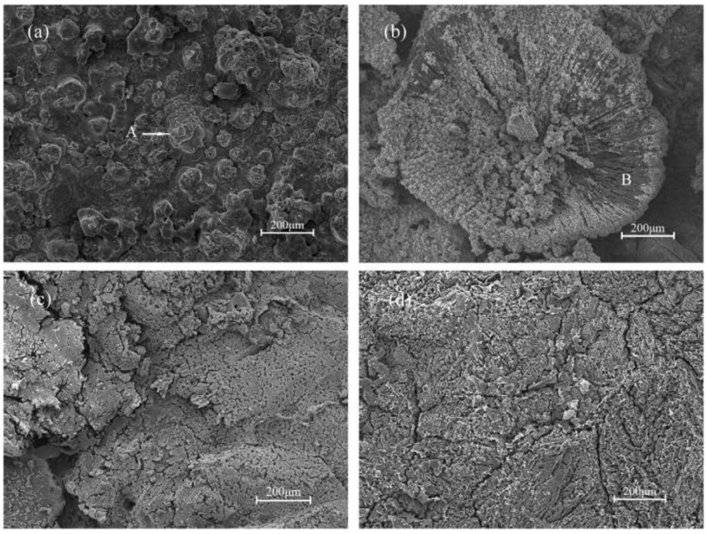

Figure 4.15: SEM scanning images of corroded X70 steel specimens with different SO_2 concentrations. (a) 0.2% SO_2; (b) 0.7% SO_2; (c) 1.4% SO_2; (d) 2.0% SO_2[80].

The SEM images showed that the surface was corroded and covered by corrosion products. The major corrosion products of X70 steel against supercritical CO_2 containing H_2O and certain SO_2 were $FeSO_4$ crystalline hydrate and $FeSO_3$ crystalline hydrate under different relative humidity[14] as shown in Figure 4.16. Again, the localised corrosion rates were not quantified in their work.

Table 4.11: Test matrix for corrosion tests[14]

CO_2 Pressure bar	SO_2 Mol %	O_2 ppm	H_2O ppm	Temp °C	Time Hours	Corrosion Rate (mm/yr)	
						General	Localised
100	2	1000	485	50	120	~0	N/A
			2750			<0.01	
			3240			~0.37	
			3820			~0.82	
			4830			~1.5	
			8740				

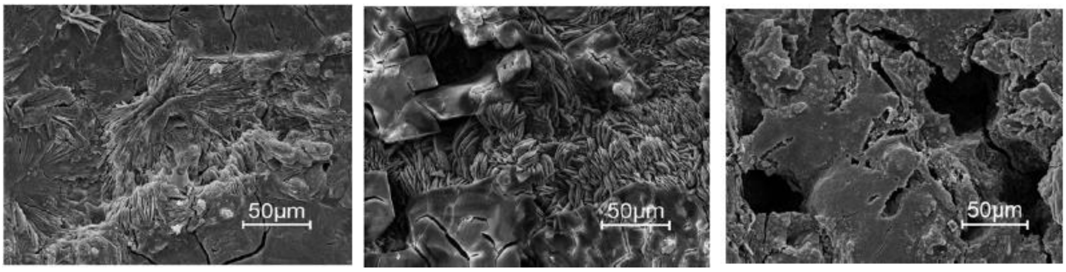

(a) (b) (c)

Figure 4.16: The morphology of the surface products formed on the steel sample exposed with 2mol% of SO_2, 3750 ppm H_2O (a), 4290 ppm H_2O (b), 9000 ppm H_2O (c), 100 bar and 50ºC[14].

4.3.4 Effect of NO_2 and H_2O

Dugstad et al.,[56] performed experiments with different levels of water and NO_2. The entire matrix of experimental conditions and results are provided in Table 4.12 below. The corrosion rates increased to (0.06~1.6 mm/year). The surface of samples were corroded and got a blackish/orange coloured dusty film on the surface (Figure 4.17). The lack of crystals is further supported by XRD measurements.

Table 4.12: Test matrix for corrosion tests[56]

CO_2 Pressure bar	NO_2 ppm	H_2O ppm	Temp °C	Time Hours	Corrosion Rate (mm/yr)	
					General	Localised
100	478	1220	25	240	Uniform ~1.6	N.A
	191	1220		240	Uniform ~0.67	
	191	488		480	Uniform ~0.06	
	96	488		72	Uniform ~0.17	
	191	488	25	168	Uniform ~0.017	

4.3.5 Effect of H_2S and H_2O

McGrail et al.,[81] looked at the corrosion of steel in liquid CO_2 using a Parr reactor vessel (autoclave), both with and without a separate water phase. Initial experiments revealed rapid corrosion when liquid CO_2 (70 bar, 25 °C) was saturated with water as shown in Table 4.13. More controlled corrosion experiments at 998 and 610 ppm of H_2O resulted in visible corrosion of steel after 21 days in the first environment, but no corrosion after 42 days in the latter, which suggests that there is a threshold water content limit at ~600 ppm, above which corrosion will be induced. At this pressure, water solubility is 1100 ppm in CO_2 and thus corrosion would occur in the absence of a separate aqueous phase. McGrail et al.,[81] found that the addition of H_2S (321 ppm) appeared to generate corrosion at a water content lower (408 ppm).

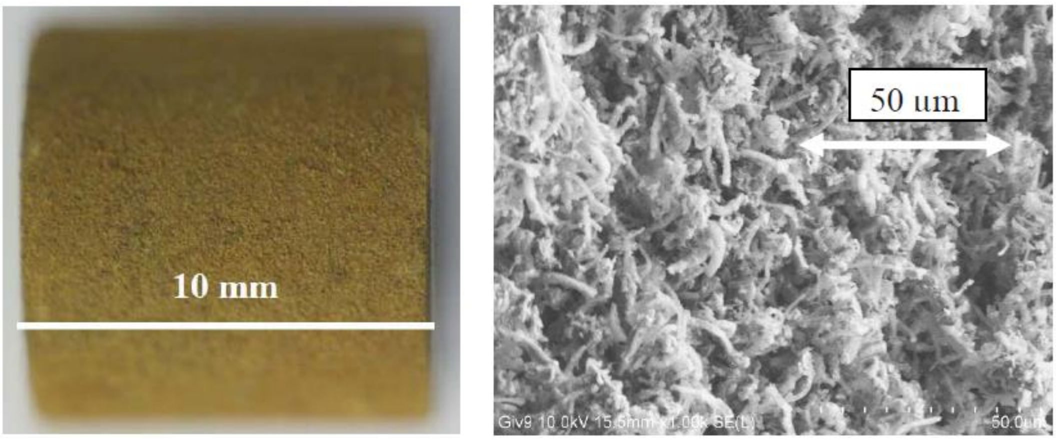

Figure 4.17: The morphology of the surface film formed on the steel sample exposed with 478 ppm NO_2, 1220 ppm H_2O, 100 bar and 25ºC[56].

Table 4.13: Test matrix for corrosion tests[81]

CO_2 Pressure (bar)	O_2 pressure (bar)	Temp (°C)	Time (Hours)	Water (ppm)	Corrosion Rate (mm/yr)
62	0	22	1008	~1500	No attack
			504	~2435	Signs of attack on surface, but not quantified

McGrail et al.,[81] also looked at the corrosion of steel in liquid CO_2 with H_2S as shown in Table 4.14. Figure 4.18 showed the smooth side (a) (prior to testing, one side of the X70 steel coupon was polished as in previous tests with 600 grit SiC paper) and sand blasted side (b), corrosion appears more pronounced towards the bottom of the smooth side, with noticeably less surface alteration towards the top. Horizontal bands of different colors are observable on the upper half of the coupon. In comparison, the sand blasted side of the coupon appears to have undergone extensive, uniform corrosion over the entire surface (Figure 4.18b).

Table 4.14: Test matrix for corrosion tests[81]

CO_2 Pressure (bar)	H_2S pressure (ppm)	Temp (°C)	Time (Hours)	Water (ppm)	Corrosion Rate (mm/yr)
82.2	~783	24	1152	~996	Not quantify

4.4 Summary of Existing Corrosion Research in CO_2 Transportation

To date, the minimum water content is required for regarding the corrosion behaviour of steel pipelines is still not known. This is partly attributed to the difference in operating conditions and stream compositions in CCS pipelines which differ from CO_2-containding fluid transportation in the oil and gas industry where a wealth of CO_2 corrosion literature already exists[41, 82, 83]. For example, in oil and gas transportation, the dominant phase is either hydrocarbon or water, whilst in CO_2 transport for CCS applications the main process fluid is supercritical CO_2, which contains considerably smaller quantities of water.

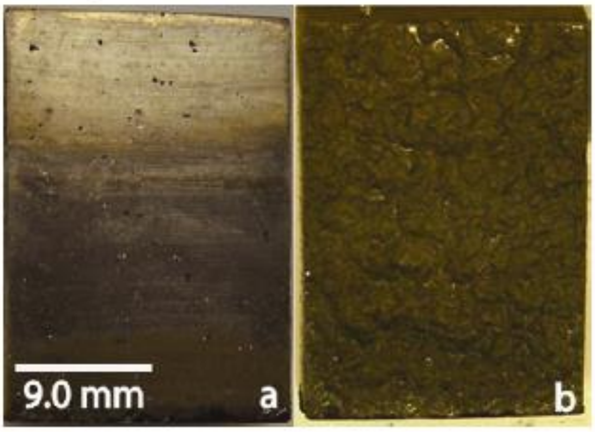

Figure 4.18: Precipitate on X70 steel coupon after 49 days of testing (82 bar CO_2, 321 ppm H_2S, 408 ppm H_2O and 24°C[81]).

Although dry CO_2 in these operating conditions is not corrosive, it is impractical and uneconomic to dry it sufficiently. When free water exists, it becomes saturated with CO_2, creating carbonic acid, posing a threat to pipeline integrity. The presence of impurities from various sources will pose a risk to the durability of steel pipelines during transport, specifically when the system is contaminated by free water. In addition to H_2O, there is the possibility of the co-existence of acids such as hydrochloric (HCl) and hydrofluoric acid (HF) depending upon the capture process[7]. Other potential impurities include SO_x, NO_x and H_2S[53, 75, 77, 81]. The reaction of these impurities with water reduces solution pH, creating an environment that is very aggressive to carbon steels. It is also worth noting that there is currently no generally accepted gas quality specification for CO_2 transportation[7].

In the literature review presented in this section, many researchers have started to investigate corrosion in CO_2 transportation. However, still more experimental data are needed to establish guidelines for the corrosion rates of carbon steel in high pressure dense phase CO_2. Surprisingly, there is no consensus on what the actual allowable water content should be in the transported CO_2 pipelines[56]. This is especially important when localised or pitting corrosion rates are concerned. No systematic study has been conducted currently in literature to attempted to establish whether the same behaviour observed (in terms of the critical water content required to induce corrosion) extends to lower impurity systems (similar to impurity recommended by DYNAMIS[7] and Alstom[56] from a health and safety perspective i.e. < 100 ppm SO_2 content), nor has the corrosion rate been quantified through localised corrosion measurements in such environments. The aim of this project is to fill some of the knowledge gaps in this high pressure corrosion field and to determine the allowable limits of the impurity content such as water, SO_x, NO_x, O_2, etc.

Chapter 5 Experimental Procedure

This chapter describes the methods used in the experimental work. A presented pressurised system as shown in Figure 5.1 was used for this study. This chapter also discusses the material used throughout this research project. The techniques used to analyse the corrosion product morphology and the composition obtained from the sample testing procedures are also described.

Firstly, the material preparation methods are described, followed by the experimental set-up aspects and operating principles of the various gas mixtures. The various surface analysis methods such as Scanning Electron Microscopy (SEM), Energy Dispersive X-Ray (EDX), Transmission Electron Microscopy (TEM) and X-Ray Diffraction (XRD) and surface profilometry are described which were used to evaluate the corrosion products and the localised corrosion mechanisms and rates on the sample surface after testing.

5.1 Material Preparation

Test specimens were machined from carbon steel (API 5L X65) into discs of diameter 25 mm and thickness of 6 mm. The chemical composition of the X65 steel is provided in Table 5.1. Surface preparation consisted of wet-polishing the entire sample to 800 grit silicon carbide abrasive paper, rinsing with distilled water, followed by acetone, high purity ethanol and dried gently with compressed air. Samples were then stored in a desiccator until needed and weighed immediately on an electronic balance to an accuracy of 0.01 mg before suspending inside the autoclave. Two samples were placed within the autoclave for each individual test, generating a total surface area of approximately 28 cm^2 exposed to the solution.

Table 5.1: Elemental composition of X65 steel (wt. %)

C	**Si**	**Mn**	**P**	**S**	**Cr**	**Mo**	**Ni**
0.12	0.18	1.27	0.008	0.002	0.11	0.17	0.07
Cu	**Sn**	**Al**	**B**	**Nb**	**Ti**	**V**	**Fe**
0.12	0.008	0.022	0.0005	0.054	0.001	0.057	Balance

5.2 Autoclave Testing Procedures

Figure 5.1(a) provides a schematic representation of the experimental system layout and Figure 5.1(b) shows a photo of the high pressure autoclaves, respectively. The entire system consists of a 1 litre capacity autoclave, temperature controller, CO_2 cylinder and a series of valves for CO_2 flow control.

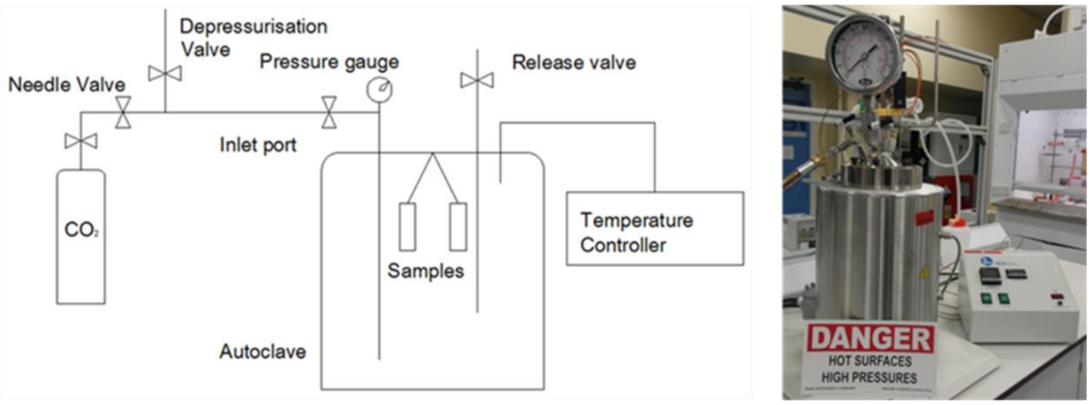

Figure 5.1: (a) Schematic of autoclave setup and (b) photo of high pressure autoclaves.

5.2.1 Supercritical CO_2-saturated water phase

The distilled water used in each experiment was de-aerated by saturating the solution with CO_2 in a separate container for a minimum of 12 hours prior to testing. The specimens were suspended within the autoclave on a non-conducting wire whilst also ensuring they were not in contact with the walls of the cylinder to prevent galvanic effects. The prepared CO_2-saturated water (300ml) was carefully delivered into the autoclave at ambient pressure and temperature and sealed. All lines to the autoclave were purged with CO_2 and evacuated to ensure removal of O_2 within the system. The CO_2 was then transferred into the autoclave and heated and pressurised to the correct temperature and pressure. The starting point of the test is taken from the time at which the autoclave reached the required temperature and pressure. Tests were conducted in static conditions in CO_2-saturated water.

5.2.2 Water-containing supercritical CO_2 phase

In comparison to supercritical CO_2-saturated water, the main difference here is that the amount of distilled water used in the water-containing phase was smaller. The solution preparation methods are the same as before and tests were conducted in static conditions in both water-saturated CO_2 and under-saturated water below the solubility limit (i.e. no free water). According to Spycher et al[26] the saturated water concentration in supercritical CO_2 at 50°C and 80 bar is 3400 ppm whilst the saturated-water concentration at 35°C and 80 bar is 3437 ppm. For under-saturated conditions, between 300 and 2800 ppm water was injected at the start of each test. The prepared CO_2-saturated water was carefully delivered into the autoclave at ambient pressure and temperature and sealed using pipette. All lines to the autoclave were purged with CO_2 and evacuated to ensure removal of O_2 within the system. The CO_2 was then transferred into the autoclave and heated and pressurised to the correct temperature and pressure. The starting point of the test is taken from the time at which the autoclave reached the required temperature and pressure.

5.2.3 Water–containing supercritical CO_2 phase with gas impurities (SO_2, O_2)

A technical grade $SO_2/O_2/CO_2$ mixture was injected into the autoclaves after the certain amount of solution was delivered to the autoclave and removal of O_2 within the initial system. Finally, the CO_2 was then transferred into the autoclave and heated and pressurised to the correct temperature and pressure. The starting point of the test is taken from the time at which the autoclave reached the required temperature and pressure. The entire matrix of test conditions is summarised in Table 5.2.

Table 5.2: Summary of experimental parameters

Parameters	Conditions
Material:	Carbon steel, X65
Corrosion medium:	Supercritical CO_2 with impurities such as H_2O, SO_2, O_2
Temperature:	35°C , 50°C, and 60°C
Pressure:	80bar
Immersion time:	6h, 14h, 24h, 48h, 96h and 168h
Water concentration:	300, 700, 1200, 1770 and 34000 ppm,
SO_2 concentration:	0, 2, 50 and 100 ppm
O_2 concentration:	<1 ppm and 20 ppm

5.3 Mass Loss Testing and Cleaning Procedures

At the end of each test, the specimens were dried thoroughly and photographed. The samples were subsequently weighed and then chemically cleaned to remove all traces of corrosion products before weighing again. The cleaning process consisted of wiping the surface with a cotton pad soaked in Clarke solution (20 g antimony trioxide + 50 g stannous chloride + 1000 ml hydrochloric acid) in accordance with ASTM Standard G1-03[84]. This was followed by rinsing the samples with distilled water, followed by ethanol and drying with compressed air.

$$CR = \frac{87600 \times \Delta m}{\rho \times A \times T} \tag{5.1}$$

Where CR is the corrosion rate of the sample in mm/year, Δm is the mass loss in grams, ρ is the density of the sample in g/cm^3, A is the exposed area in cm^2 , T is the immersion time in hours.

The mass loss due to corrosion was determined from the weight difference before exposure and after cleaning. The corrosion product mass is the difference before and after cleaning, after exposure to the test environment.

5.4 Surface Analysis

The morphology and composition of the corrosion products were analysed by a combination of the scanning electron microscopy (SEM), Energy-dispersive X-ray spectroscopy (EDX), transmission electron microscopy (TEM) and X-ray diffraction (XRD). The forms of corrosion taking place were identified using white light interferometry, which enabled the extent of localised corrosion in each environment to be quantified.

5.4.1 Scanning Electron Microscopy (SEM) and Energy Dispersive X-ray (EDX)

Scanning Electron Microscopy (SEM) was used throughout the project to examine and obtain images of the surface morphology at different exposed time on samples of carbon steel. Energy Dispersive X-Ray (EDX) analysis was used to identify and quantify the elemental composition of the corrosion products on the sample surfaces. These techniques (SEM and EDX) were considered one of the major procedures that were used to conduct throughout the project as shown in Figure 5.2.

SEM was carried out on samples using a Carl Zeiss EVO MA15 SEM to assess coverage and topography of corrosion product. All images were collected at an accelerating voltage of 20 kV and at a working distance of around 8 mm.

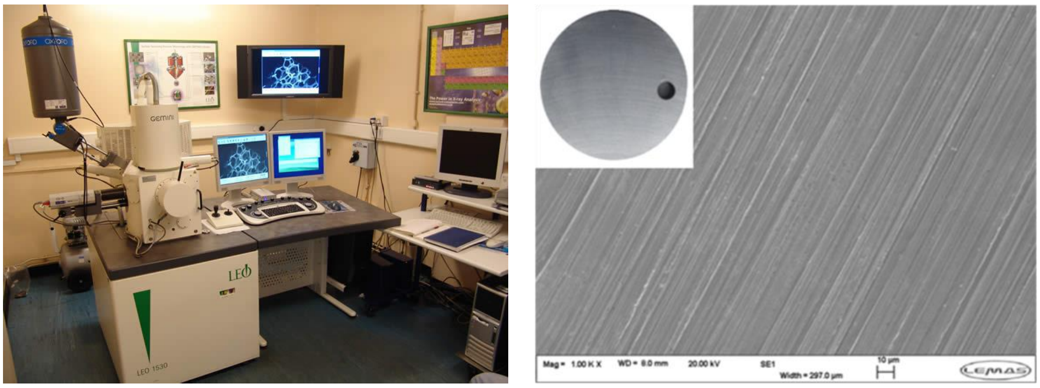

(a) (b)

Figure 5.2: a - Image of SEM/EDX used in this study, b – SEM image of fresh sample surface.

EDX analysis in this study used to analyse the elemental components of the corrosion products and allowing the characterization of the distribution of individual Elements of the corrosion products on the surface as shown in Figure 5.3.

5.4.2 Focused Ion Beam sample preparation (FIB)

Samples were prepared using focused ion beam (FIB, Figure 5.4). The instrument used was a FEI Nova200 dual beam SEM/FIB fitted with a Kleindiek micromanipulator for in situ lift-out. The ion beam was operated at voltages between 30 and 5 kV, and with beam currents between 5 and 0.1 nA. Regions of interest were first coated with a protective layer of platinum before bulk removal of material was performed. Samples were then lifted out in situ, attached to a Cu TEM grid, and then thinned to a final thickness of around 100 nm.

5.4.3 Transmission Electron Microscopy (TEM)

TEM was performed using a FEI Tecnai F20 FEGTEM (200 kV) fitted with a high angle annular dark field (HAADF) detector and a Gatan Orius SC600 CCD camera. In a TEM, Selective Area Electron Diffraction (SAED) used to measure a solid crystal, an example as shown in Figure 5.5.

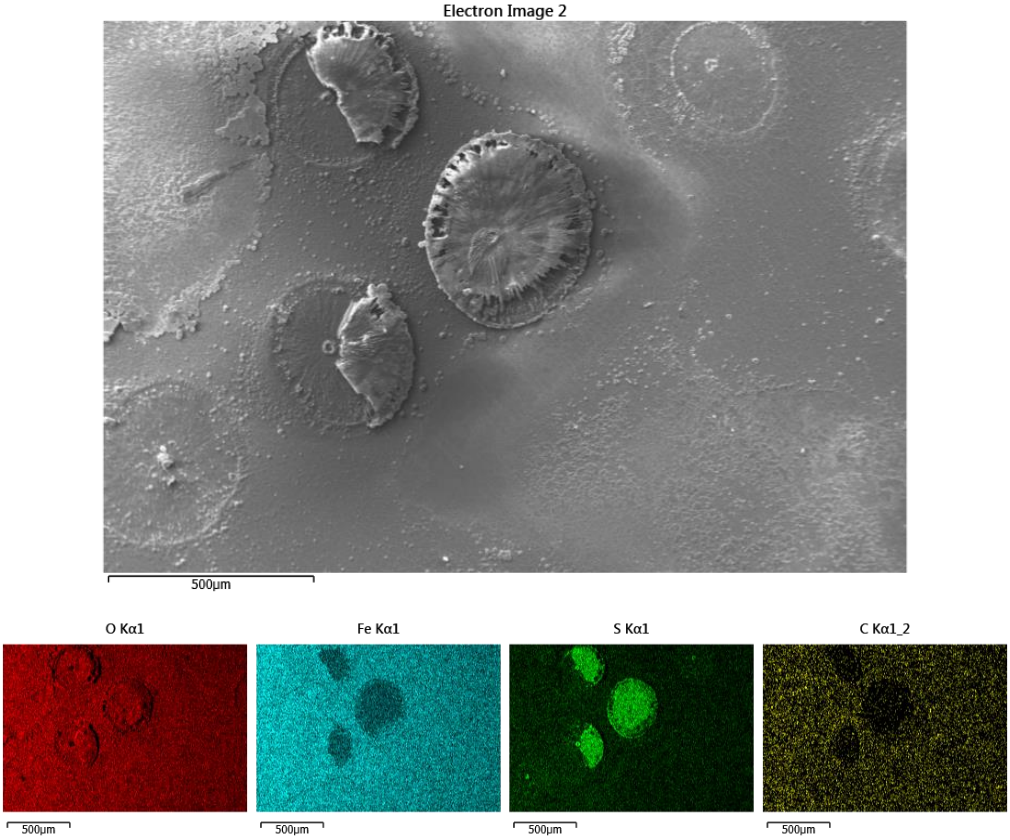

Figure 5.3: Examples of EDX mapping on the surface of X65 carbon steel exposed to SO_2 environments.

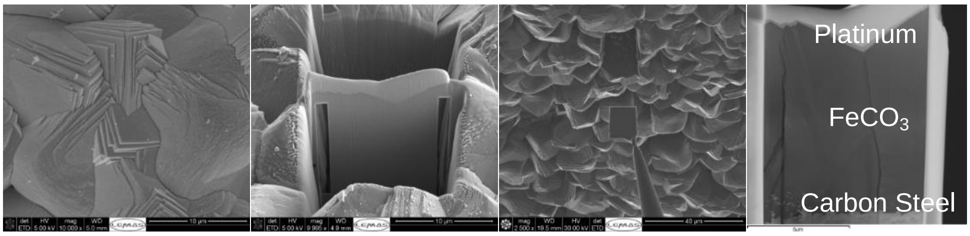

(a) (b) (c) (d)

Figure 5.4: FIB-SEM preparation of TEM section (a) where ion milling was performed on the sample surface prior to Pt deposition, (b) the sections milled away within the surface to produce the TEM sample, (c) FIB prepared section (d) a high-angle annular dark-field image (HAADF) produced in the TEM.

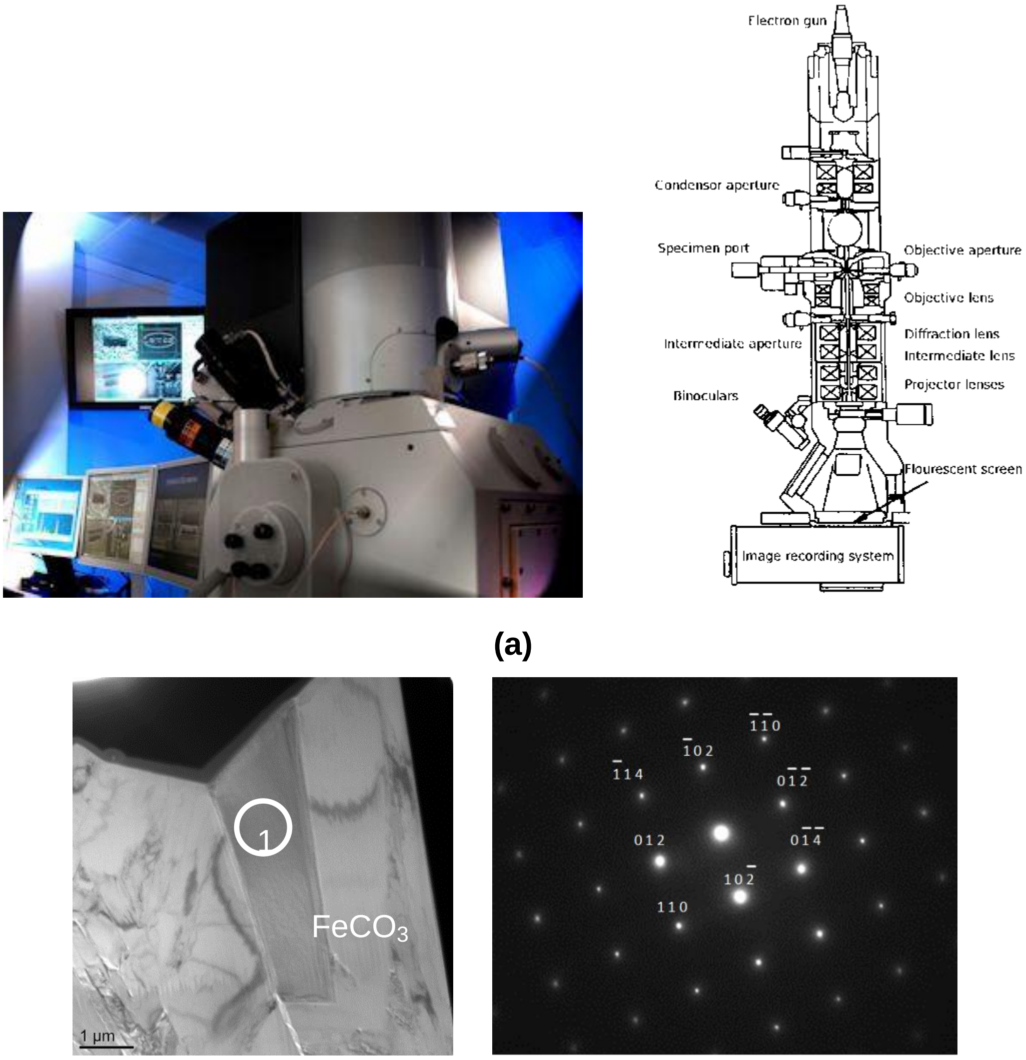

(a)

(b) (c)

Figure 5.5: (a) Image of TEM used in this study and schematically representation (b) Bright field TEM image of area highlighted in Figure 5.4 (c) to indicate the location of the Selected Area Electron Diffraction (SAED) measurement of the solid crystal and (b) the corresponding electron diffraction pattern from Region ①, which produces d-spacing values typical of $FeCO_3$.

5.4.4 Surface profilometry

The profilometry measurements were performed on samples using a NP_{FLEX} 3D Surface Metrology System to quantify localised attack. For each sample, three randomly chosen regions were selected (scanning a 3 mm x 3 mm area at a time). The objective used 2.5X with an approximately 3.5mm working distance. All samples that were analysed by profilometry were first cleaned thoroughly with Clarke’s solution to remove any traces of corrosion product to enable the pits to be accurately quantified. The pit depth analysis was conducted in alignment with ASTM Standard G46-94. The standard stipulates that an average of the 10 deepest pits and the maximum pit depth should be used for pit damage characterisation of the sample area. An example is provided in Figure 5.6.

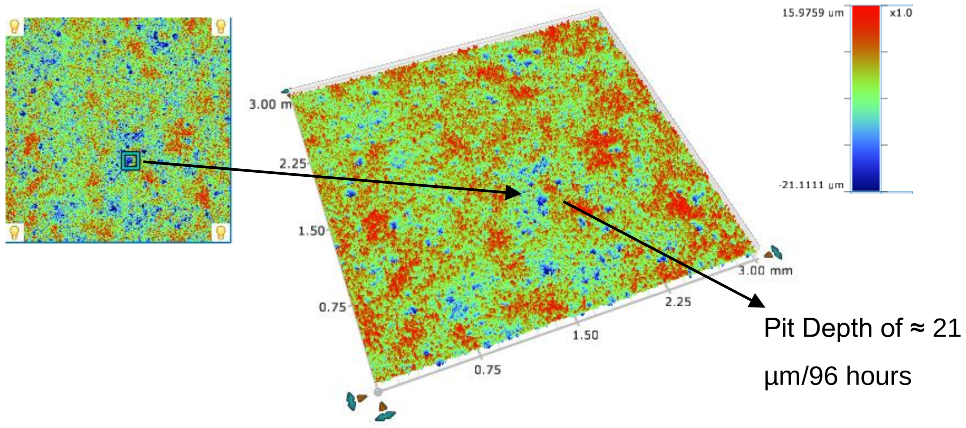

Pit Depth of ≈ 21 µm/96 hours

(c)

Figure 5.6: Examples of 3D profiles of measurable maximum pits on the surface of X65 carbon steel.

5.4.5 XRD measurements

X-ray diffraction (XRD) is one of the common technique for the identification of crystalline structure. This technique is capable to indicate the crystal structure are present or not on the surface.

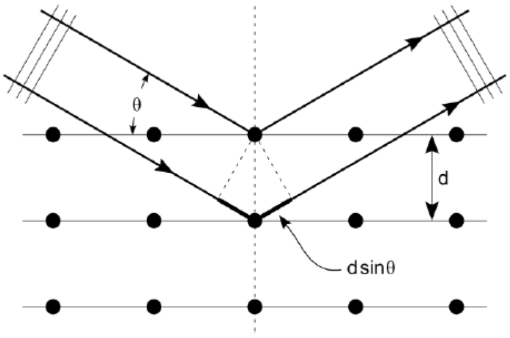

Figure 5.7: Schematic representation of the X-Ray Diffraction techniques.

Where θ is the incident angle, d is the spacing between the diffraction planes, according to Bragg's Law of Diffraction in Equation (2)

$$2d \sin\theta = n\lambda \tag{2}$$

The XRD spectra for each sample was carry out using PANalytical X'pert multipurpose diffractometer (MPD), employing Cu Ka radiation with an active area of 10 x 10 mm programmable di-vergence slits. Scans were performed over a range 2Ɵ= 20 to 80° using a step size of 0.033 per second, with a total scan time of approximately 50 minutes.

5.4.6 Raman spectroscopy

There are two reasons why Raman is used in this study in addition to XRD? Firstly, the use of localised Raman spectroscopy at specific locations on the steel surface confirmed that the corrosion products were indeed $FeCO_3$ or $FeSO_3.3H_2O$. Secondly, the use of Raman spectroscopy to identify if amorphous corrosion products exists (chemical compositions).

Raman spectra were collected by employing 488 nm radiation from an Ar ion laser (1% and 5%). The exposure time for each sample was recorded at between 5 and 30 minutes, with a total scan time of approximately 10 to 50 minutes.

5.6 Summary

This chapter describes the experimental techniques and methods of analysis which are used in a systematic study of general and localised corrosion behaviour in CO_2-containing impurities such as H_2O, SO_2, O_2 conditions at moderate and high pressure. Methods of surface analysis used to conduct a comprehensive investigation on the corrosion products morphology are presented. chemistry and characterise what is happening on the steel surface. Figure 5.8 demonstrates the overall procedure of experimental work throughout the project.

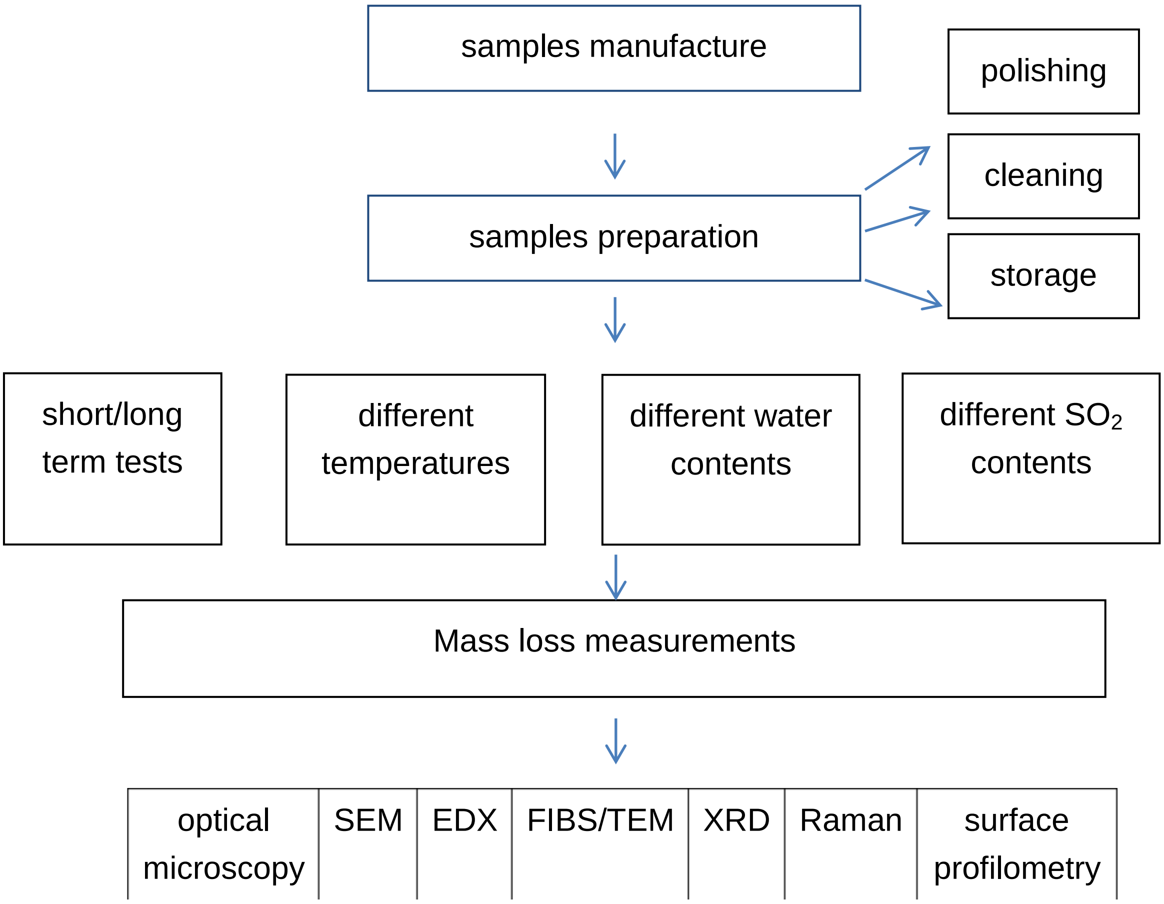

Figure 5.8: Procedures of experimental wok outlined.

Chapter 6 Results of Samples Exposed to Water Saturated With CO_2

6.1 Summary

This chapter presents corrosion results from experiments to assess the behaviour of X65 carbon steel in supercritical CO_2-saturated water conditions at 80 bar and 35, 50 and 60°C respectively, to simulate conditions that may occur in CO_2 transportation if significant amounts of water are present in the pipeline. A detailed assessment of both general and localised corrosion and corrosion product film morphology/chemistry was conducted as a function of time. The entire matrix of test conditions is summarised in Table 6.1.

Table 6.1: Test matrix for corrosion tests

CO_2-saturated water			
Temperature (°C)	Pressure (bar)	H_2O (ml)	Immersion time (hours)
35	80	300	6.5, 14, 24, 48, 96
50			
60			

6.2 Understanding of Corrosion Behaviour of Samples Exposed to Supercritical CO_2-Saturated Water Phase

Figure 6.1 and Table 6.2 show the average corrosion rates recorded over test durations of 14, 24, 48 and 96 hours in 300 ml of supercritical CO_2-saturated water with different temperatures. The water volume to sample surface area ratio in these experiments was 12 cm^3:1 cm^2.

Table 6.2: Corrosion rates of carbon steel in supercritical CO_2-saturated water phase at 80 bar with different temperatures vary as a function of time.

CO_2-saturated water					
Temperature (°C)	Pressure (bar)	H_2O (ml)	Immersion time (hours)	Corrosion rate (mm/year)	SD
35	80	300	6.5	6.95	0.188
			14	5.99	0.215
			24	5.01	0.077
			48	4.28	0.115
			96	2.72	0.132
50			6.5	10.82	0.290
			14	8.33	0.478
			24	6.64	0.320
			48	5.02	0.356
			96	4.13	0.094
60			6.5	11.39	0.222
			14	9.88	0.137
			24	7.72	0.015
			48	5.25	1.007
			96	3.41	0.101

All three conditions shown in Figure 6.1 exhibit a very high average corrosion rate over the initial 6.5 hours. The temperature at 60°C has the highest average corrosion rates of over 11 mm/year compared to those calculated at 50°C and 35°C for the first 6.5 hours. Such high initial corrosion rates were also observed by Zhang et al[85] who conducted mass loss measurements on X65 steel in distilled water saturated with supercritical CO_2 at 95 bar and 80°C.

After 48 hours, there is a difference between the corrosion rates of all three temperatures, suggesting that the difference in temperature would affect the final corrosion rate due to the formation of corrosion product layers. Corrosion rates for all experiments began to reduce very early in the experiment and reached average corrosion rates of 2.72, 4.13, and 3.41 mm/year for the 35°C, 50°C and 60°C over 96 hours of immersion, respectively. A similar decrease in corrosion rate observed in Figure 6.1 was also observed by Zhang et al[85] who ascribed the reduction to the formation of crystalline $FeCO_3$ on the material surface.

It appears that a rapid initial reduction in corrosion rate of low alloy steels over the first few hours of exposure to high pressure CO_2-saturated water is quite a common observation in the literature. Guo et al.,[86] recorded a reduction in corrosion rate of 24 mm/year to 5 mm/year for 2Cr alloy steels exposed to CO_2-saturated formation water at 80^oC and 8 bar between 4 and 32 hours. Additionally, Wu et al.,[68] performed tests using EIS on carbon steel in supercritical CO_2-saturated water at 90^oC and 82.7 bar. The results indicated that after only 4 hours of exposure, the corrosion rate halved from that of the initial corrosion rate recorded. Unfortunately, the magnitude of corrosion rate was not determined from the EIS data and the reduction in corrosion rate was inferred based on the change in the charge-transfer resistance measured. The corrosion rate recorded after 24 hours was (~8 mm/year).

6.2.1 SEM images of the corroded X65 samples exposed to supercritical CO_2-saturated water at 35°C and 80bar

This section relates the corrosion product morphology to the observed changes in corrosion rate for the tests in supercritical CO_2-saturated water at 35°C and 80bar. Considering the SEM images of the specimens provided in Figure 6.2, an iron carbide (Fe_3C) film initially reveals itself on the steel surface over the first 14 hours (Figure 3(a)), which is brought about by the selective dissolution of the ferrite phase within the steel microstructure. Over this period, a slight reduction in corrosion rate is observed from approximately 7 to 6 mm/year based on Figure 6.1. Upon examining the surface of the steel after 48 hours, no visible sign of crystalline $FeCO_3$ was detected on the surface, despite the reduction in corrosion rate.

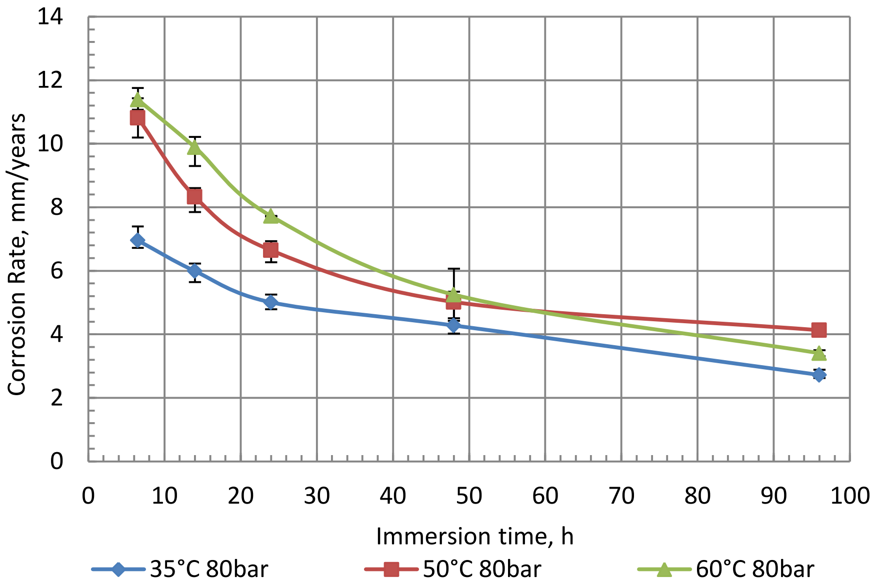

Figure 6.1: Corrosion rates of carbon steel in supercritical CO_2-saturated water phase at 80 bar with different temperatures vary as a function of time.

Upon examining the surface in Figure 6.2, it appears that the Fe_3C network consists of some porous areas, but it also appears that a film with a smudge like appearance begins to form on top of the Fe_3C network. The growth of this film becomes more apparent after 24 hours (Figure 6.2(b)) and becomes very visible after 48 and 96 hours. It is suggested that this film may be an amorphous layer of $FeCO_3$ as no crystalline structure was observed on the XRD spectra after 96 hours in Figure 6.3.

6.2.2 SEM images of the corroded X65 samples exposed to supercritical CO_2-saturated water at 50°C and 80bar

Considering the SEM images of the specimens exposed to supercritical CO_2-saturated water phase at 50°C and 80 bar provided in Figure 6.4. The growth of the similar amorphous film becomes apparent after 14 hours (Figure 6.4(a)) and becomes very visible after 24 hours to that observed at 35°C (Figure 6.2(a and b)).

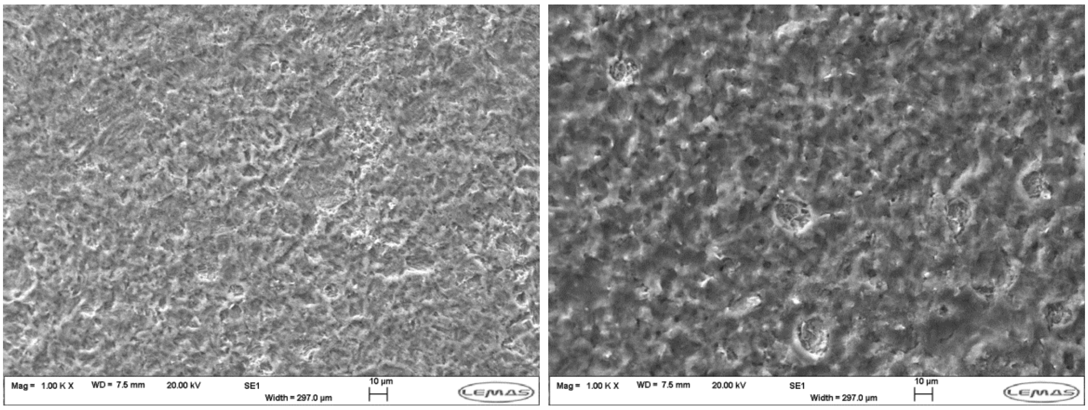

(a) 14 hours **(b) 24 hours**

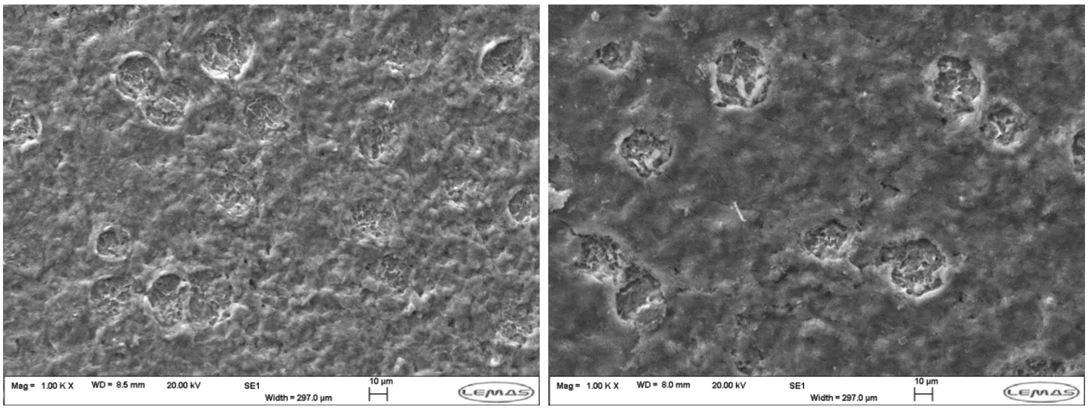

© 48 hours **(d) 96 hours**

Figure 6.2: SEM images of the corroded X65 samples exposed supercritical CO_2-saturated water at 50°C and 80 bar for (a) 14 hours – dissolution of ferrite phase, exposing an Fe_3C network, (b) 24 hours – precipitation of a smudge-like surface layer within/on top of the network, (c) 48 hours – precipitation of a smudge-like surface layer within/on top of the network, and (d) 96 hours – precipitation of a smudge-like surface layer within/on top of the network.

After 48 hours of exposure, the amorphous film becomes clearly visible in the SEM images (Figure 6.4(c)) and $FeCO_3$ crystals begin to precipitate on top of the initially formed ‘inner’ layer. The presence of crystalline $FeCO_3$ is confirmed from the XRD spectra provided in Figure 6.5 after 48 hours. It is worth noting that the XRD analysis of the inner layer after 24 hours did not produce an XRD spectra, suggesting that the film is an amorphous structure.

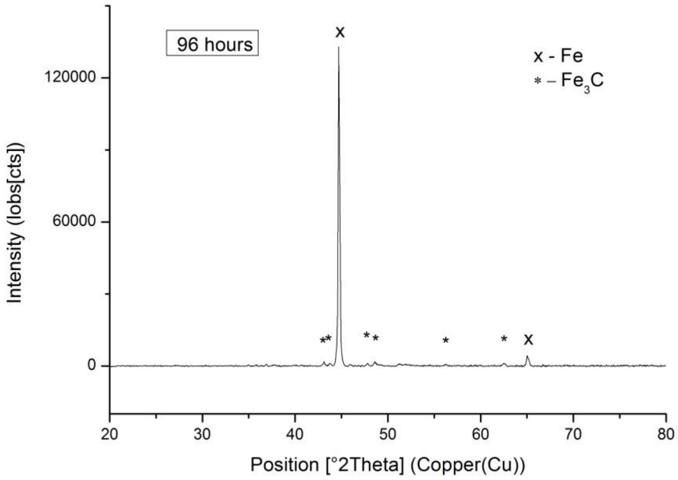

Figure 6.3: XRD spectra of samples in 300 ml supercritical CO_2-saturated water at 35°C, 80bar for 96 hours.

Guo et al.,[86] presented similar findings to those observed here in which $FeCO_3$ crystals were shown to precipitate onto an initially formed inner amorphous $FeCO_3/Cr(OH)_3$ layer for experiments conducted on carbon steel in a brine solution at 80°C and 8 bar. Guo et al.,[86] observed cracking of the inner amorphous layer which was attributed to the dehydration effect during sample preservation for SEM. It is believed that the same dehydration-induced cracking effect can be seen here in Figure 6.4(c), especially considering the fact that Figure 6.4(b) shows no indication of the inner layer cracking and that this particular sample was stored for a shorter period of time within a desiccator. A description of a film with a similar texture has also been made by de Waard et al.,[40] who identified a ‘smudge-like’ $FeCO_3$ film forming on carbon steel in low temperature environments (below 60^oC), albeit at significantly lower pressures.

After 96 hours, Figure 6.4(d) indicates that a crystalline $FeCO_3$ layer has precipitated onto the steel surface, consisting of a number of crystals which measured over 20 µm in width. The composition of the crystals was confirmed from the XRD pattern in Figure 6.5 which produced high intensity peaks relating to $FeCO_3$. An increase in $FeCO_3$ peak intensity and the subsequent reduction in intensity of the Fe peak can clearly be seen in the XRD spectra provided in Figure 6.5 as the corrosion product grows. The growth of the $FeCO_3$ on the surface of the sample is also reinforced by the mass loss measurements provided previously in Figure 6.1.

It is interesting to note that the corrosion rate decreases as a function of time in Figure 6.4. These observations are aligned with Zhang et al.,[85] who conducted tests at 80°C and 95 bar on carbon steel in distilled water over immersion times of 0.5, 7, 23, 48, 96 and 168 hours. Although they observed the $FeCO_3$ layer increasing in thickness from around 10 to over 80 µm between a period of 48 and 168 hours exposure, they too observed no significant change in corrosion rate of the underlying steel, with corrosion rate stabilising at 7.3 mm/year.

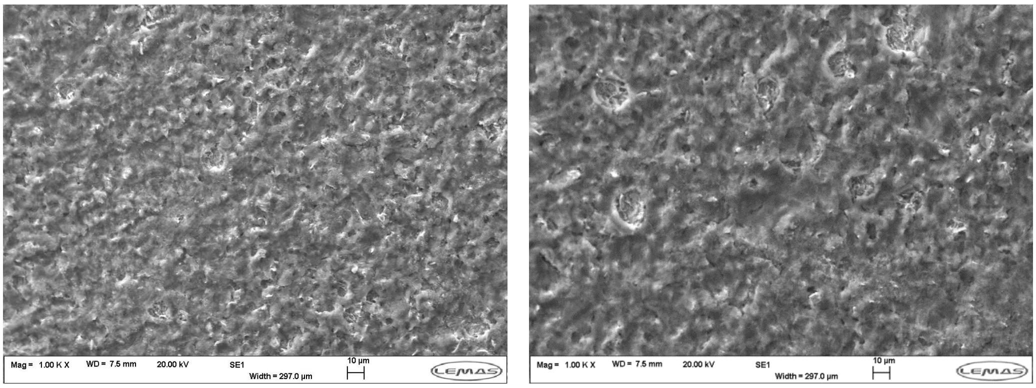

(a) 14 hours **(b) 24 hours**

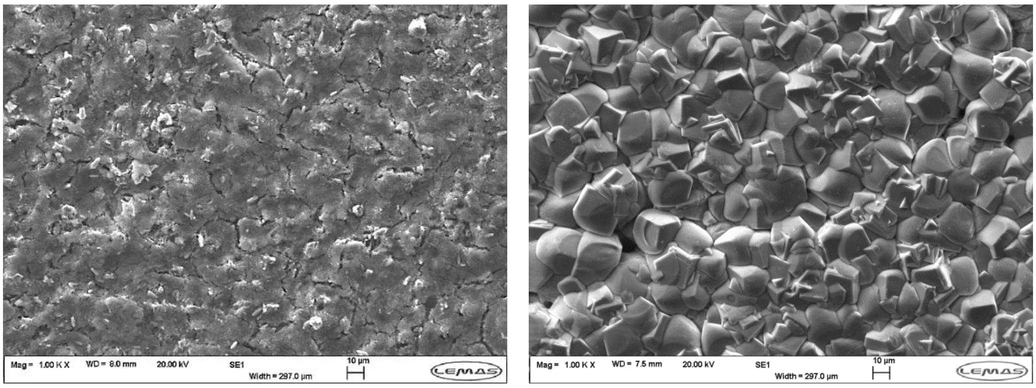

(c) 48 hours **(d) 96 hours**

Figure 6.4: SEM images of the corroded X65 samples exposed supercritical CO_2-saturated water at 50°C and 80 bar for (a) 6.5 hours – dissolution of ferrite phase, exposing an Fe_3C network, (b) 14 hours – precipitation of a smudge-like surface layer within/on top of the network, (c) 48 hours – precipitation of crystalline $FeCO_3$ onto the surface of the inner layer and (d) 96 hours – extensive layer of larger $FeCO_3$ crystals on top of the inner layer.

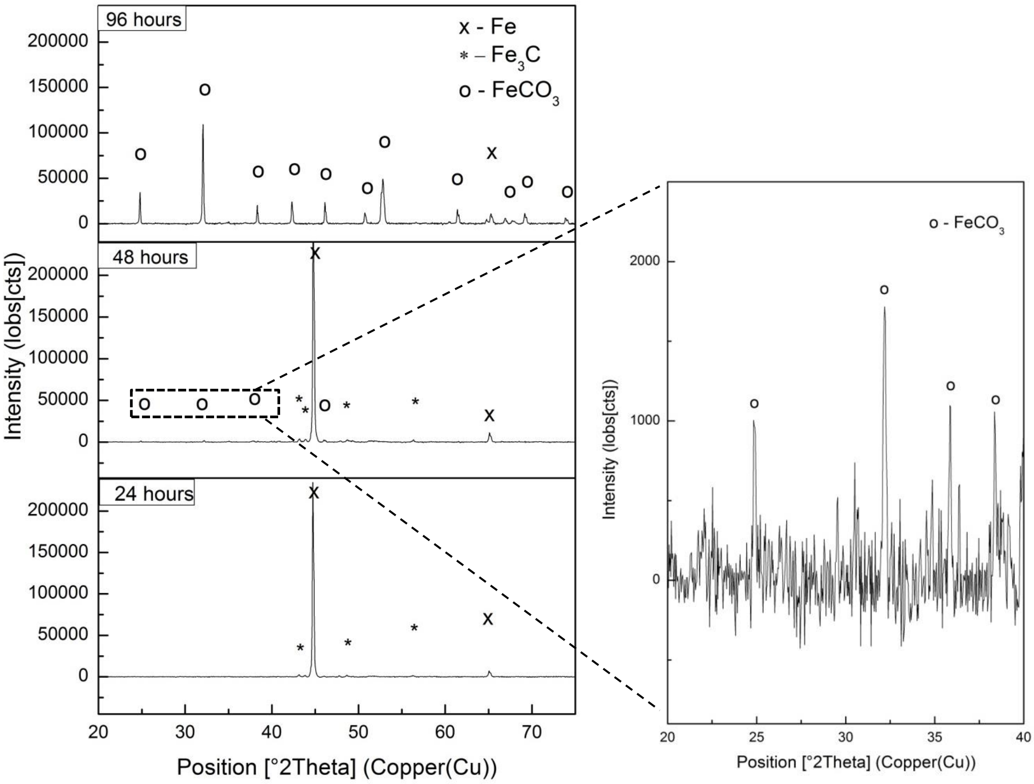

Figure 6.5: XRD spectra of samples in 300 ml supercritical CO_2-saturated water at 50°C, 80bar for 24, 48 and 96 hours.

6.2.2.1 Characterisation of thin film observed in supercritical CO_2-saturated water experiment

It was important to characterise the thin, inner film present on the surface of the steel formed in the supercritical CO_2-saturated water to understand whether it possessed the same morphology as that observed by Guo et al.,[86], as it appears this film is capable of reducing both the general and extent of localised attack on the steel surface.

As discussed previously, after 24 hours of exposure no presence of any crystalline product was found on the steel surface using XRD, suggesting the presence of an amorphous structure.

Consequently, a TEM sample was cut from the steel surface using a FIB and mounted onto a copper grid for further analysis. An SEM image of the cut taken from the sample surface using the FIB can be seen in Figure 6.6(a) with Figure 6.6(b) showing the sample cross-section after thinning to 100 nm. Unfortunately, due to the porous nature of the film, a certain degree of material was removed during the thinning process, however, enough remained for a reliable analysis of the film. Figures 6.6(c) and (d) show high resolution images of the film and the selected area electron diffraction (SAED) pattern of this area is provided in the top right corner of Figure 6.6(d)). The SAED pattern confirmed that the deposit was amorphous in nature.

As a result of the amorphous nature of the deposit, the film could not be identified using SAED. However, an Energy Dispersive X-ray (EDX) elemental analysis of this area (Figure 6.6(e)) indicated that the film comprised mainly of alloying element (molybdenum and chromium) whilst also showing traces of iron, oxygen and carbon. This elemental analysis is extremely similar to that of the amorphous layer observed by Guo et al.,[86] in their studies.

Through the implementation of XPS, Guo and colleagues[86] were able to identify the film as a combination of amorphous $FeCO_3$ and amorphous $Cr(OH)_3$. Similar observation have also been made by Sun et al[87] who also showed that the formation of amorphous $Cr(OH)_3$ occurs with a co-deposition of $FeCO_3$ and such a film is able to significantly reduce the susceptibility of X65 to localised attack.

There is a possibility that the same amorphous film exists here. However, given the limitations of SAED to only fingerprint crystalline species, the compounds comprising amorphous layer could not be fully confirmed. However, a number of areas were scanned using EDX point analysis and found that the Fe:C:O elemental ratio was very close to 1:1:3, which is indicative of the presence of $FeCO_3$. Unfortunately, the presence of $Cr(OH)_3$ could not be confirmed via this technique and its presence could not be confirmed.

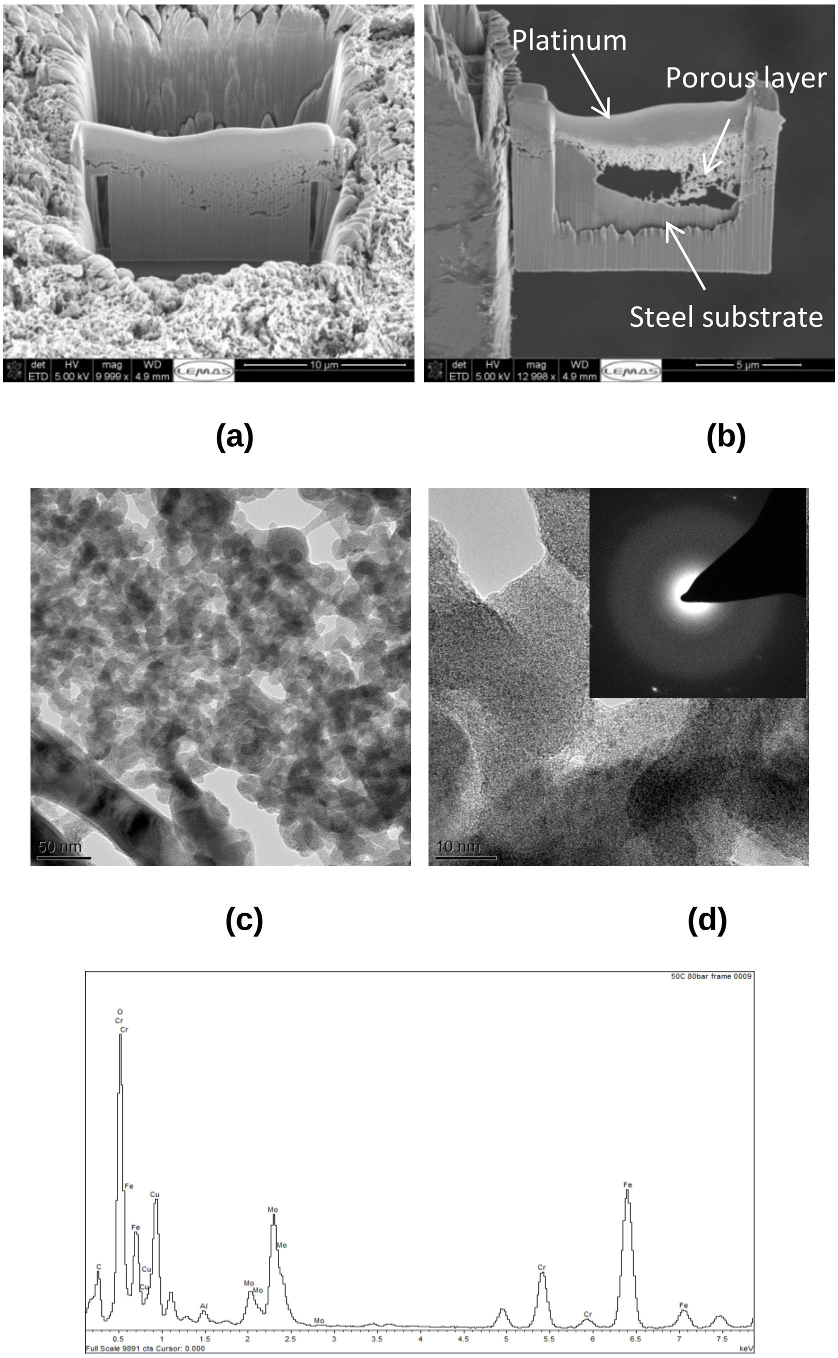

(a) **(b)**

(c) **(d)**

(e)

Figure 6.6: Analysis of X65 sample exposed to 80 bar and 50°C supercritical CO_2-saturated water for 24 hours indicating (a) an SEM image showing the location where the section was milled away using the FIB to produce the TEM sample, (b) fixation of the FIB prepared section to the Cu TEM grid and after thinning, (c) TEM image of the porous film, (d) higher magnification TEM image of porous film, indicating amorphous nature with a corresponding SAED pattern and (e) an EDX result for the amorphous layer from region investigated in (d).

6.2.3 SEM images of the corroded X65 samples exposed to supercritical CO_2-saturated water at 60°C and 80bar

This section relates the corrosion product morphology to the observed changes in corrosion rate for the tests in supercritical CO_2-saturated water at 60°C and 80 bar. Considering the SEM images of the specimens exposed to 300 ml water as a function of time (Figure 6.7), the temperature accelerates the corrosion and precipitation take place on the surface in comparison to that of the samples exposed to 35 and 50 °C and 80 bar.

A similar dense and compact crystal layer (Figure 6.7(c)) was observed faster (at 48 hours) than that for at 50 °C and 80 bar after 96 hours, no crystals were observed at 35°C and 80 bar. Over this period, also a significant reduction in corrosion rate is observed from approximately 12 to 6 mm/year based on Figure 6.1. Previous authors have linked the reduction in corrosion rate over time in these environments to the formation (dense and compact layer) of crystalline $FeCO_3$ which is capable of blocking active sites on the surface of the sample and acting as a diffusion barrier to species involved in the cathodic reaction. This layer can protect sample surface, prevent the corrosion take place further and reduce the corrosion rate. However, upon examining the surface of the steel after 14 hours, no visible sign of crystalline $FeCO_3$ was detected on the surface, despite the reduction in corrosion rate.

6.3 The General Corrosion Rates vs. Localised Corrosion Rates at Different Temperatures

A detailed analysis of all the steel samples exposed to the supercritical CO_2-saturated water phase was conducted using white light interferometry to determine the extent of surface pitting relative to the general corrosion rate measured from mass loss measurements. All samples were analysed after cleaning the surface thoroughly with Clarke's solution to remove any traces of corrosion products. It is worth noting that tests were also performed on freshly ground steel surfaces to ensure that the inhibited acid did not induce surface pitting.

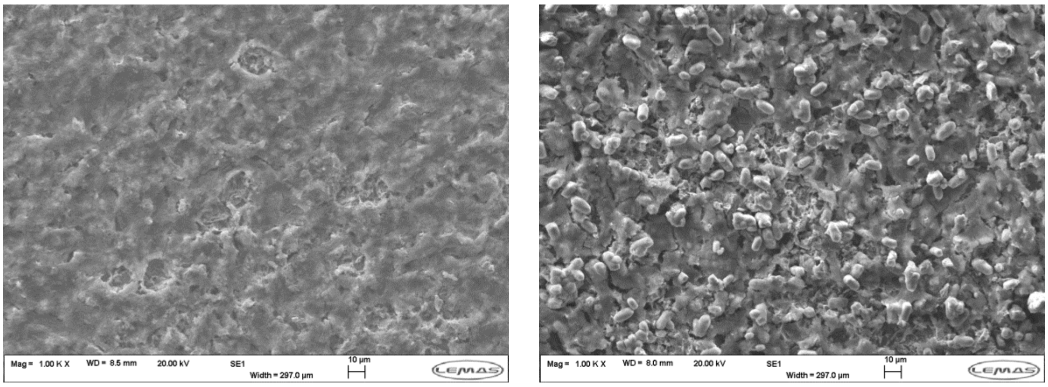

(a) 14 hours **(b) 24 hours**

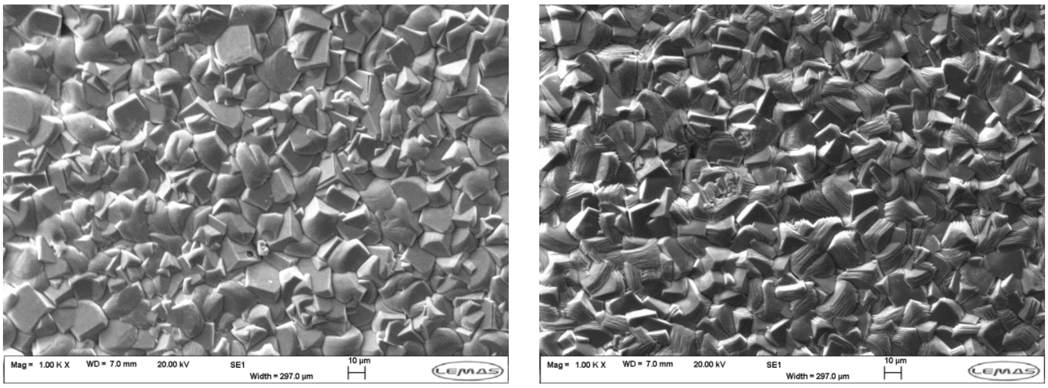

(c) 48 hours **(d) 96 hours**

Figure 6.7: SEM images of the corroded X65 samples exposed supercritical CO_2-saturated water at 60°C and 80 bar for (a) 14 hours – precipitation of a smudge-like surface layer within/on top of the network, (b) 24 hours –precipitation of crystalline $FeCO_3$ onto the surface of the inner layer and (c) 48 hours – extensive layer of larger $FeCO_3$ crystals on top of the inner layer (d) 96 hours – extensive layer of larger $FeCO_3$ crystals on top of the inner layer.

An example of pitting rate and depth as a function of exposure time for the supercritical CO_2-saturated water experiments at 50°C and 80 bar is provided in Figure 6.8. The rate of pit growth on the steel surface begins to noticeably decline after 24 hours of exposure. For example, at the end of the experiment at 50°C, average pit depths on the carbon steel surface were recorded at 16.0 µm (within an error of ±2 µm) when considering the top 10 deepest pits. This depth corresponds to an overall pitting rate of 1.5 mm/year over 96 hours relative to the corroding steel surface. However, from another perspective, between 0 and 24 hours, pit depth increased from 0 to 9.9 µm, corresponding to a pit growth rate of approximately 3.6

mm/year. Conversely, between 24 and 48 hours (where only the ‘inner’ layer was present as shown in Figure 6.4(c)- an inner amorphous layer underneath a top layer of $FeCO_3$ crystals), pit depth increased only from 9.9 to 12.4 µm which is a pit growth of 0.7 mm/year over that period. It is noted that the rate of pitting growth with increasing temperature. Reviewing the results in this manner strongly suggests that the presence of the inner layer in the 300 ml tests is playing a role in inhibiting the propagation of pits. Such observations were also made by Guo et al.,[86] who conducted corrosion tests on X65 and low chromium alloy steels (1-3% Cr) at 8 bar and 80°C in a simulated formation water. Their research showed that in specific tests, an amorphous inner layer (composing of $FeCO_3$ and $Cr(OH)_3$) was produced underneath precipitated $FeCO_3$ crystals. When reviewing the extent of localised corrosion on the surface, Guo et al and colleagues[86] found that the amorphous film showed a strong ability to help prevent localised corrosion. Guo et al.,[86] suggested that piling of large crystals provides a number of free passages for corrosive media which can influence the level of localised attack, whereas the inner layer can cover the entire steel surface and offer an increased level of protection to localised attack.

6.4 Reaction Mechanisms

However, the main question revolves around why an amorphous film is present. Based on the research of Guo et al.,[86], it has been established that a low pH favours the precipitation of an amorphous $FeCO_3$ inner film by changing the relative supersaturation of $FeCO_3$ in the system. Guo et al.,[86] showed that a bulk solution pH below 4.7 was enough to promote the formation of amorphous $FeCO_3$ prior to the deposition of $FeCO_3$ crystals by putting the system into a regime whereby nucleation was more favourable than crystal growth.

As steel corrodes and an equivalent amount of alkalinity are released, according to Equation (6.1):

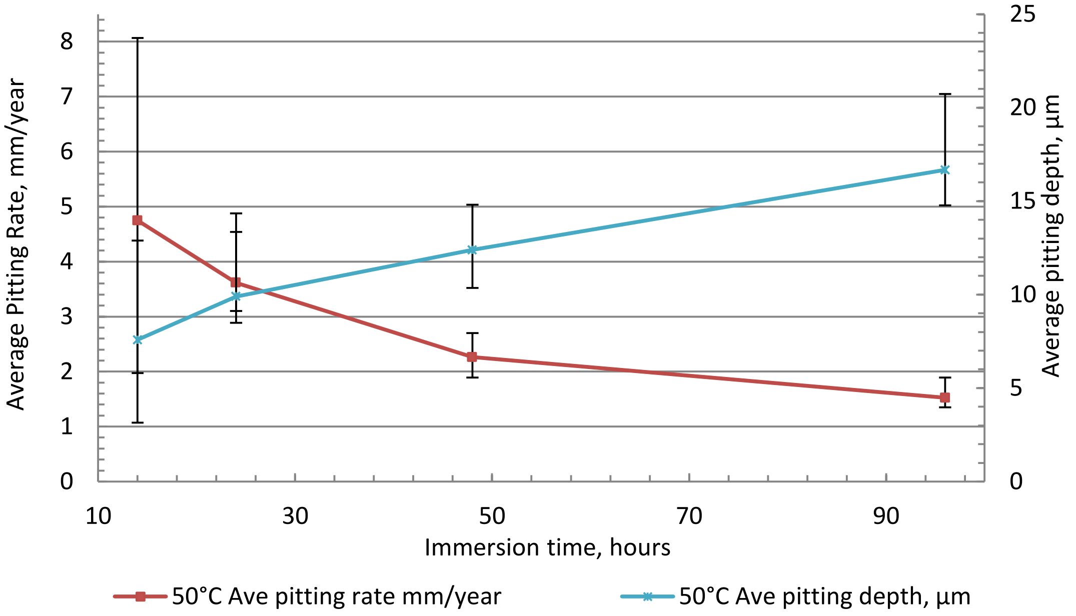

Figure 6.8: Pitting depths of carbon steel in supercritical CO_2-saturated water phase at 80 bar at 50°C as a function of time.

$$\mathrm{Fe} + 2\mathrm{H_2CO_3} \rightarrow \mathrm{Fe^{2+}} + \mathrm{H_2} + 2\mathrm{HCO_3^-} \qquad 6.1$$

As Fe^{2+} and CO_3^{2-} dissolution occurs, the pH in the system increases up to the point where the concentrations of Fe^{2+} and CO_3^{2-} ions exceed the solubility limit, enabling precipitation to occur via the one stage reaction in Equation (6.2)

$$\mathrm{Fe^{2+}} + \mathrm{CO_3^{2-}} \rightarrow \mathrm{FeCO_3} \qquad 6.2$$

When $FeCO_3$ formation begins to exceed the corrosion rate, the pH in the system will start to decline. If precipitation occurs at the same rate as dissolution, the pH will remain stable.

Figure 6.9 presents the mass of corrosion product before and after cleaning the exposed samples (not the total mass loss) measured on the surface of the sample at different temperatures as a function of time. The growth of the corrosion product at 60°C is considerably faster than 35 and 50°C. The temperature here plays an important role. The temperature accelerates all the processes such as electrochemical, chemical and transport involved in corrosion. In the case of the formation of the protective scale at 60°C after

48hours, as the solubility of $FeCO_3$, K_{sp} decreases with an increase of temperature, the increased temperature makes the concentration of $Fe^{2+}$and CO_3^{2-} exceed the solubility faster. In chapter 2, the $FeCO_3$ supersaturation (SS) according to Eq. (2.25 and 2.26) and $FeCO_3$ precipitation rate R_p (Eq. 2.24) increases. The higher temperature, the larger supersaturation SS and the higher precipitation R_p. The formation of $FeCO_3$ becomes faster and has the ability to block active sites on the surface of the sample and act as a diffusion barrier to species (e.g. SEM Images of 60°C in comparison to 50°C and 35°C), thereby, the mass loss reduces due to the dense, compact $FeCO_3$ layers protecting the sample surface. The observations could well be in agreement with Zhang et al.,[85] who related the precipitation of $FeCO_3$ to the reduction of carbon steel corrosion rate in CO_2-saturated water at 90°C in supercritical conditions.

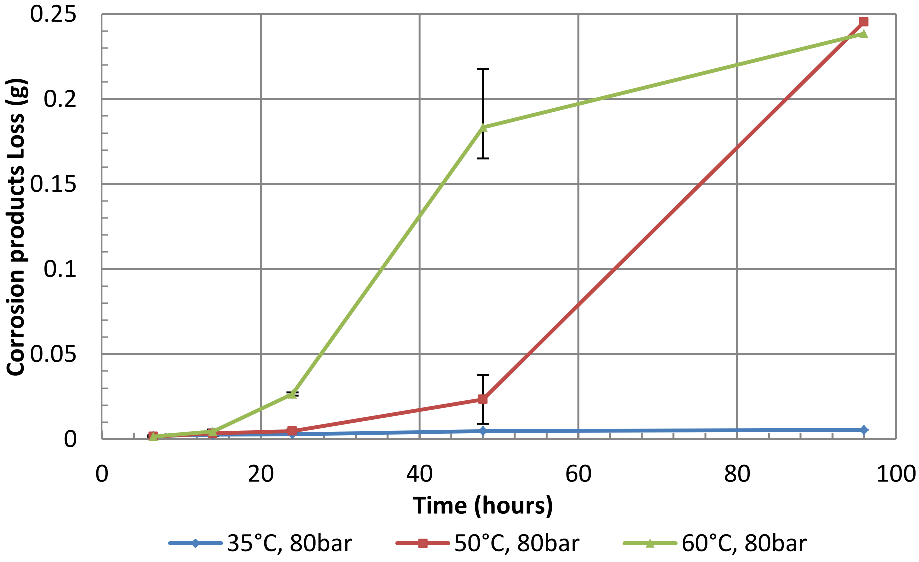

Figure 6.9: The corrosion products loss are corresponding to the iron carbonate precipitation and growth kinetics.

Factors influencing the rate of precipitation of $FeCO_3$ were explained in detail by Hunnik et al.,[29] who generated the expression in Equation (2.24) in chapter 2 to describe the precipitation of $FeCO_3$.

Dugstad[88] stated that the driving force for $FeCO_3$ precipitation is determined by the level of supersaturation and in principle, there exist two steps involved in the precipitation processes; nucleation and particle growth. The assumption is made that these two processes are related to the relative supersaturation as shown in Equation 2.25 and 2.26 in chapter 2.

Once the product of the Fe^{2+} and CO_3^{2-} concentrations exceed the solubility limit, the formation of crystal $FeCO_3$ at the surface becomes thermodynamically favourable. Saturation of the solution is achieved much earlier at higher temperature; hence precipitation on the surface begins earlier in the experiment.

When SS > 1, the nucleation of $FeCO_3$ is initiated. Although nuclei formation is possible at SS > 1, its rate increases rapidly only when a critical supersaturation is exceeded[86]. It is assumed that the rate of both nucleation and particle growth is related to the relative supersaturation[86]. The rate of nucleation is believed to increase exponentially with relative supersaturation (S_R), whilst particle growth varies linearly with S. Consequently, particle growth should occur at low S_R and when S_R is high, particle growth is prevented and a nanocrystalline or amorphous film develops[86].

Ruzic et al.,[89] used this theory to explain the presence of an amorphous inner layer identified under a top layer of dense crystalline $FeCO_3$. They proposed that there was an initial high relative supersaturation at the surface of the sample which led to rapid precipitation where nucleation prevailed, leading to an amorphous $FeCO_3$ film. This process was then followed by a growth phase when S_R was lower. This process produced a dense, crystalline layer on top of the inner layer.

This theory can be used to explain why the presence of the amorphous film under the crystalline structure is prominent on the surface of the sample in tests observed here. Considering that the corrosion rate was initially high (~11 mm/year) and that the solution was static, it is suggested this helped to promote a high concentration of ferrous ions at the surface of the steel. It is proposed that the inner layer develops during the first precipitation stage as a result of accumulation of ferrous ions within the porous network, causing the relative supersaturation to be high enough to allow nucleation to be favoured as opposed to particle growth and leading to an amorphous layer precipitating. Subsequently, once supersaturation at the surface drops due to a decline in corrosion rate, crystal growth becomes more favourable than nucleation and the top crystalline layer nucleates and grows.

The exact same form of behaviour has been suggested by Dugstad et al.,[88] who observed that in low temperature systems a much slower precipitation rate is experienced, resulting in the relative supersaturation becoming very high and leading to a non-crystalline film as shown in Figure 6.10. Consequently, the observations witnessed here are in alignment with the behaviour seen by both Ruzic et al.,[89] and Dugstad et al.,[88].

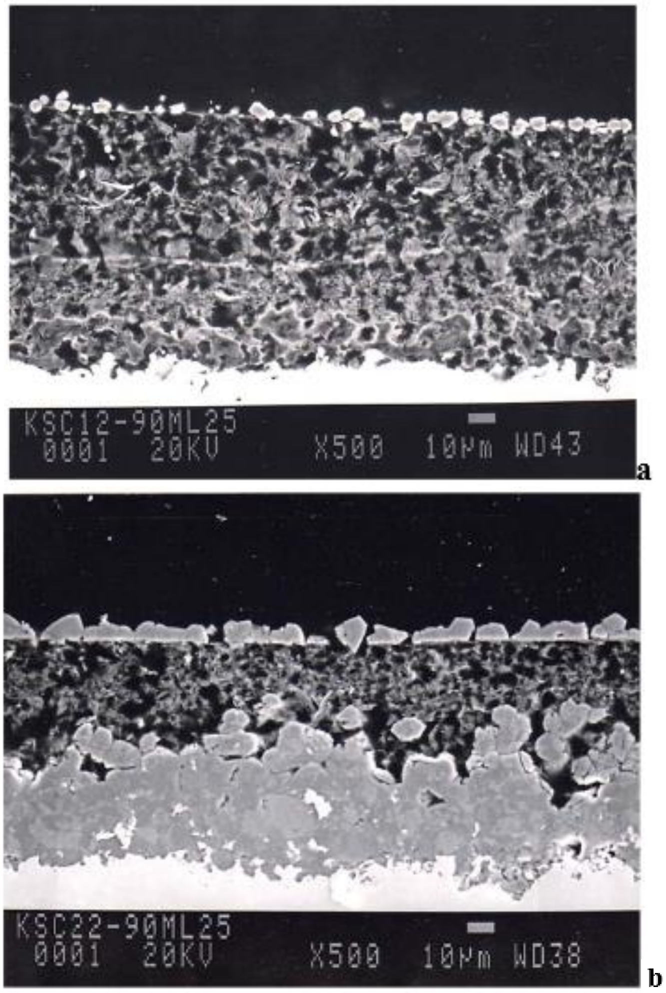

Figure 6.10: Corrosion films formed: a) 40°C, b) 80°C[88].

6.5 Summary

In this chapter, the corrosion behaviour of X65 carbon steel was evaluated in CO_2-saturated water conditions at different temperatures and 80 bar. Findings in this section can be summarised into the following:

- A reduction in corrosion rate was observed with time.
- The corrosion rates of X65 carbon steel were initially high (~10 mm/year).
- The formation of an amorphous film and then subsequently a crystalline $FeCO_3$ film on top was observed on the steel surface.
- The corrosion processes accelerate with increasing temperature.
- The formation of dense and compact crystal $FeCO_3$ layer observed faster at 60°C than that at 50 or 35°C.
- The dense and compact crystal layer at 60°C and 80 bar (after 48 hours) can protect the surface to reduce the subsequent corrosion rates.

Chapter 7 Results of Samples Exposed to Supercritical CO_2 With Water

7.1 Summary

The focus of this section is directed towards understanding the extent of both general and localised corrosion of X65 steel in water-containing CO_2 environments representative of those encountered in CO_2 transport in CCS. The work contributes to literature by providing a detailed comparison between the levels of localised corrosion and general corrosion for CO_2 transport systems, highlighting the importance of accurate localised corrosion measurements. The study also focuses on the role of temperature and how this parameter influences the critical water content in the system i.e. the water content below which no appreciable levels of corrosion are observed. The overall aim of the work is to understand the level of degradation in water-containing CO_2 systems typical of CO_2 transport in CCS. It is hoped that this work may help to establish safe working limits under which acceptable levels of corrosion are observed, both from a localised and general corrosion perspective.

All tests were conducted at a pressure of 80 bar and three stages of testing were conducted, which are outlined below.

The first stage of testing involved considering the effect of immersion time on corrosion behaviour in the water-saturated CO_2 environment. Experiments were conducted over 14, 24, 48 and 168 hours at 35^oC and 80bar to understand the corrosion kinetics and film formation as a function of time in these environments.

The second set of experiments exams the corrosion behaviour of X65 steel in water-containing CO_2 at 50^oC where the water content is below the solubility limit. Water concentrations of 2650, 1600 and 700 ppm (in mole) are considered. These tests are all below the water solubility limit of 3400 ppm determined using the Spycher solubility model[26].

The third set of tests considers the corrosion behaviour at 35^oC at water concentrations of 2800, 1750, 700 and 300 ppm (mole). Again, based on the calculations performed by Spycher et al.,[26], the concentrations are below the solubility limit of 3437 ppm for these specific conditions.

7.2 Water-Saturated Supercritical CO_2 Environments

Figure 7.1(a) indicates that the experimental tests conducted in this research are located well within the supercritical region on the CO_2 phase diagram. The entire matrix for the test conditions is shown in Table 7.1:

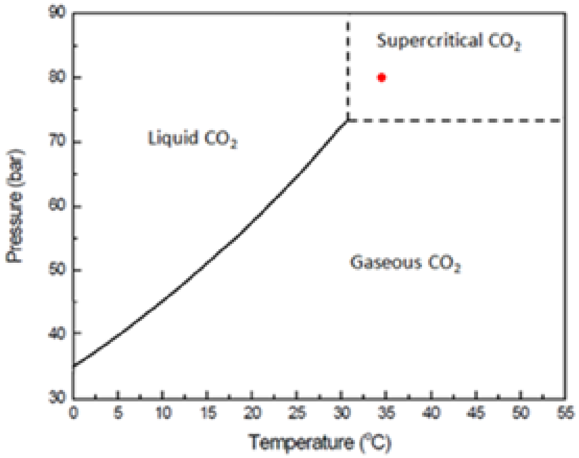

(a)

Figure 7.1: (a) phase diagram for CO_2 highlighting the condition at which the tests were conducted in this work (indicated by the red dot).

Table 7.1: Tests matrix for corrosion tests

Temp. (°C)	**Pressure (bar)**	**H_2O (ppm)**	**Immersion time (hours)**
35	80	Above solubility limit of 3437 ppm through addition of 34000 ppm water	14, 24, 48, 168

The CO_2 properties are accompanied by the mutual solubility of both CO_2 in water and water in CO_2 using the model provided by Spycher et al.,[26]. It can be seen that the density of CO_2 approximately halves as a result of an increase in temperature from 35 to 50°C. Considering that the solubility of water in CO_2 at both 35 and 50°C is very similar on a molar basis (3437 and 3400 ppm, respectively), it can be inferred that because of the difference in CO_2 density, over double the quantity of water can be dissolved into the CO_2 phase per unit volume of the system at 35^oC relative to 50^oC.

Table 7.2: Mutual solubility of water and CO_2 under tested conditions

Temperature, °C	Pressure, bar	CO_2 density, kg/m^3	Water in CO_2, ppm
35	80	489.82	3437
50	80	219.28	3400

7.3 Results of Samples Exposed to Water-Saturated Supercritical CO_2 Phase at 35°C and 80bar

Average mass loss results recorded over a period of 14, 48 and 168 hours are provided in Figure 7.2 for carbon steel samples exposed to water-saturated supercritical CO_2 at 80bar and 35°C. The measurements indicate that the general corrosion rate of the steel samples reduces as a function of time over the test duration. After 14 hours of exposure to the water-saturated environment, the general corrosion rate recorded was 0.11 mm/year, whereas a thickness loss rate of 0.03 mm/year was measured over 168 hours.

Figure 7.3 shows the SEM images and photographs of the sample exposed to the water-saturated supercritical CO_2 phase for different immersion times at 35°C and 80 bar. The samples removed from the autoclave showed signs of discolouration over the entire steel surface after 48 hours. Furthermore, localised patches on the steel surface could be identified in each test, indicating areas were appreciably greater amounts of water had condensed on the steel surface.

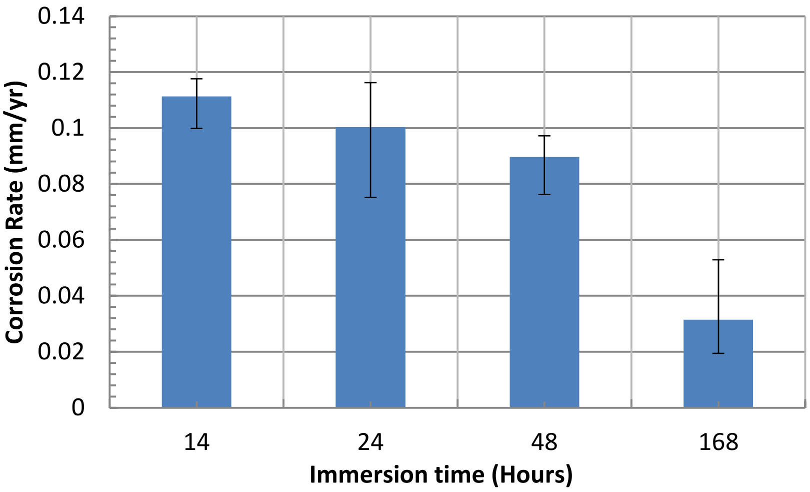

Figure 7.2: General corrosion rates (from mass loss measurements) of carbon steel in the water-saturated supercritical CO_2 phase at 35°C and 80 bar at test durations of 14, 24, 48 and 168 hours. Water content in the CO_2 phase is approximately 3437 ppm.

The presence of $FeCO_3$ crystals was clearly visible under the SEM after 14 hours in the localised darker areas (‘Region A’) of the surface (Figure 7.3(a)). Very little discolouration of the sample was evident in ‘Region B’ and except for areas in which precipitation was obvious, the remaining surface was relatively clean. Figure 7.3(b) shows one small location in Region B where a few deposits of corrosion product were identified. It is worth noting that this image does not fully represent Region B as most of the surface was free from any form of surface deposit. The surface deposits appeared to be a thin, randomly distributed layer of corrosion product which looked to have no form of crystalline structure.

Over time, the crystals situated in Region A appear to grow in size, change in morphology and increase in number (supported by Figures 7.3(b) and (c)). After 168 hours, the $FeCO_3$ crystals situated in Region A form a dense, compact surface layer. Conversely, in Region B, the steel surface becomes more discoloured with time, and the spots of corrosion product begin to grow, but are still quite dispersed. Again, from the SEM images taken, the corrosion product does not have the characteristic shape of $FeCO_3$ crystals.

The nature of the corrosion products in both regions was confirmed as $FeCO_3$ using X-ray diffraction (XRD) measurements. Figure 7.4 shows the localised XRD measurements taken in Region A as a function of time. As the test progresses, the quantity of $FeCO_3$ situated in Region A increases, resulting in the intensity of the $FeCO_3$ peaks (particularly the one situated at 2θ ≈ 32° corresponding to the (104) Miller plane) increasing relative to the main iron peak situated at 2θ ≈ 45° and corresponding to the (110) plane from the ferrite phase in the steel.

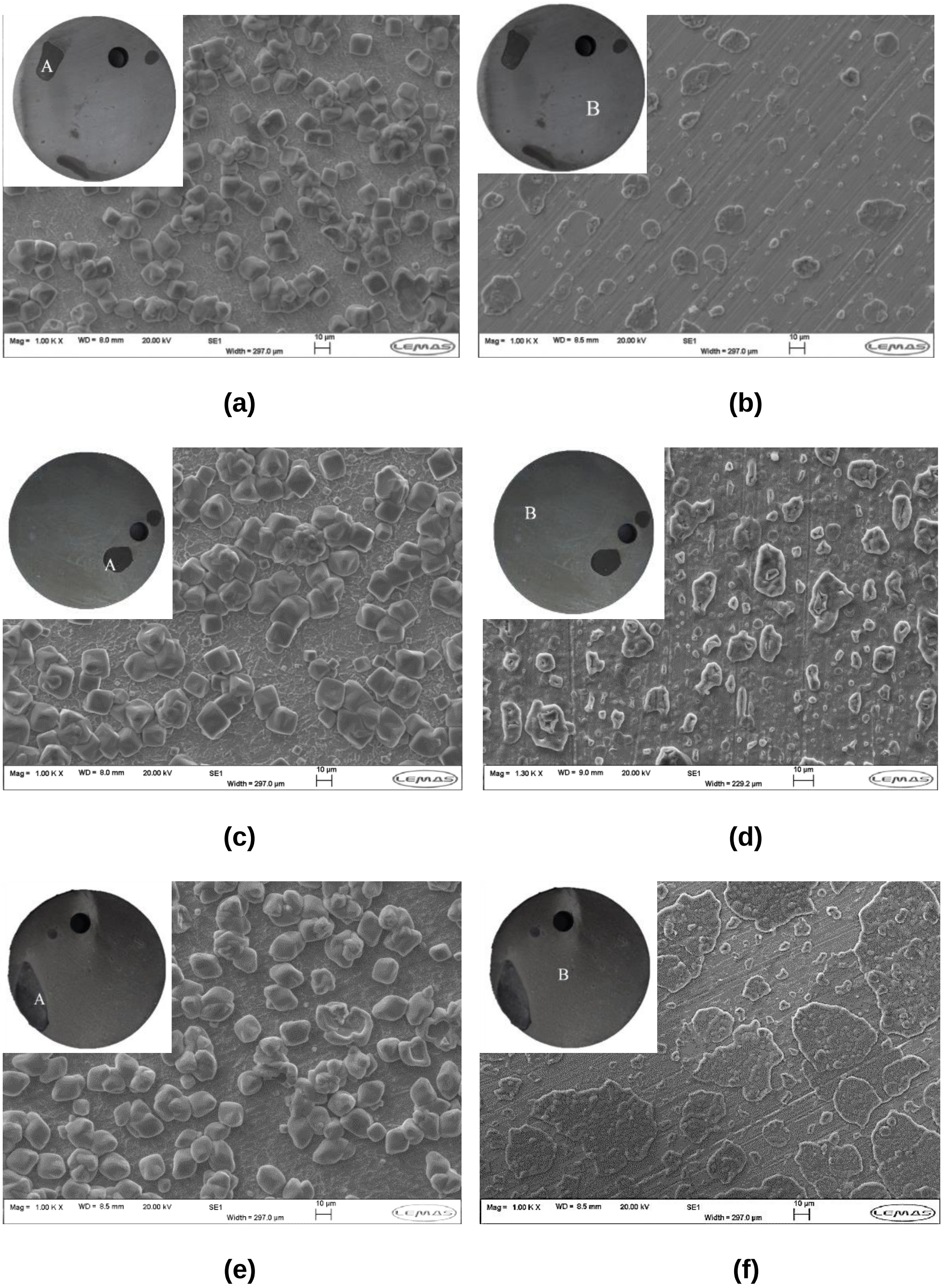

(a) (b)

(c) (d)

(e) (f)

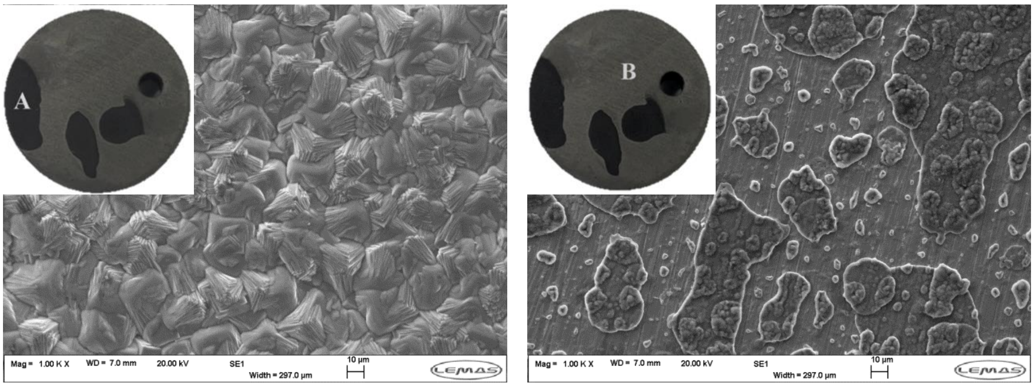

(g) **(h)**

Figure 7.3: SEM images of the corroded samples exposed to water-saturated supercritical CO_2 at 35°C and 80 bar for (a) 14 hours – Region A (b) 14 hours – Region B (c) 24 hours – Region A (d) 24 hours – Region B (e) 48 hours – Region A and (f) 48 hours – Region B (g) 168 hours – Region A and (h) 168 hours – Region B.

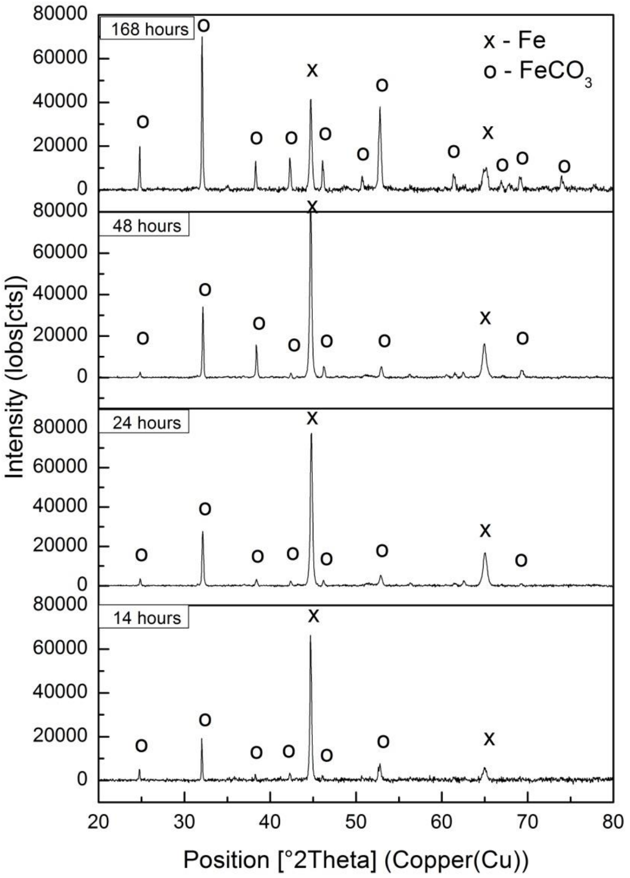

Figure 7.4: XRD spectra of samples exposed to water-saturated supercritical CO_2 phase at 35°C and 80 bar for 14, 24, 48 and 168 hours.

Analysis of the photos and SEM images corresponding to the tests at 35°C suggests that the degradation in the system may be localised and that the general corrosion rates recorded from mass loss measurements may not be a true reflection of the susceptibility of carbon steel to the water-saturated supercritical CO_2 environment. To supplement the mass loss data, surface profilometry measurements were conducted to review the extent of surface pitting and provide an appreciation for any changes in pitting behaviour on the material with time. All samples that were analysed by profilometry were first cleaned thoroughly with Clarke's solution to remove any traces of corrosion product to enable the pits to be accurately quantified. The pit depth analysis was conducted in alignment with ASTM Standard G46-94[24].

It was clear that if different precipitation processes were occurring in Regions A and B, then it is likely that the extent of localised attack in such areas may be different. For parts of the surface representative of Region A, each area was systematically scanned using $3x3mm^2$ sections and the most aggressively attacked areas were used to determine the extent of localised corrosion through consideration of the maximum and average pit depths. For Region B, owing to the large discoloured area, three $3x3\ mm^2$ areas were randomly scanned on the surface. The most severe images in terms of attack where then used to assess the extent of pitting corrosion.

Figure 7.5 and Table 7.5 provide examples of the profilometry measurements taken from the samples exposed to the water-saturated supercritical CO_2 environment at 35°C for 168 hours. The profilometry images are provided in conjunction with the general corrosion rates (from mass loss measurements) and the localised corrosion rates based on the top 10 deepest surface pits identified for both Region A and Region B. Figure 6 indicates that the localised corrosion rates (when considering the entire surface) are approximately one order of magnitude greater than the general corrosion rates. Furthermore, as the test duration approached 168 hours, a significant difference in localised corrosion rates over the two regions becomes apparent. The profilometry results suggests that the localised corrosion rate in Region A remains relatively constant throughout the entire test, whilst in Region B, the pitting rate slows down as a function of time. Profilometry images in Figure 6 also show that the characteristic of pitting are different in Regions A and B. In Region A, the surface pits are much wider, deeper and less in number in contrast to pits in Region B which are high in number and not as wide or shallow. The following section will perform a detailed analysis of the corrosion product in Regions A and B in an effort to relate this to the localised corrosion rates recorded in the system.

7.4 Analysis of corrosion products at 35°C and 48 hours

7.4.1 Region A – visibly darker area, ~10 µm diameter crystals, many areas not compact after 48 hours i.e. areas of low crystal density

The sample exposed to the water-saturated environment at 35°C for 48 hours was selected and taken for further analysis of its corrosion product composition and morphology through the use of Focused Ion Beam (FIB) etching and subsequently, Transmission Electron Microscopy (TEM). Figure 7.6(a) shows a high resolution FIB-SEM image of a selected area within Region A of the sample. Initially, a layer of platinum was deposited onto the chosen area to protect the surface during preparation. Once this was complete, material either side of the section was milled away using a Gallium ion beam. The sample was thinned further and was partially cut free from the bulk material (Figure 7.6(b)) before being removed using a Kleindiek micromanipulator mounted inside the chamber of the microscope and attached to a Cu TEM grid. The cut section was secured in place via Platinum deposition and thinned further using the FIB to reduce the thickness to below 100 nm, enabling it to be electron transparent (Figure 7.6(d)). The sample was subsequently placed in a FEI Tecnai F20 FEGTEM where the high-angle annular dark-field image shown in Figure 7.6(d) was produced. The TEM image illustrates that the $FeCO_3$ corrosion product layer after 48 hours was approximately 10 µm in thickness within Region A.

Selected Area Electron Diffraction (SAED) measurements of the corrosion product were conducted in Region ① of Figure 7.7(a) and the corresponding diffraction pattern is provided in Figure 7.7(b). Indexing of the diffraction patterns from the corrosion layer produced d-spacing values characteristic of $FeCO_3$. The pattern observed in Figure 7.7(b) is suggestive of a single crystal and similar such diffraction patterns (albeit with different crystallographic orientations) could be observed throughout the entire corrosion layer within the TEM sample.

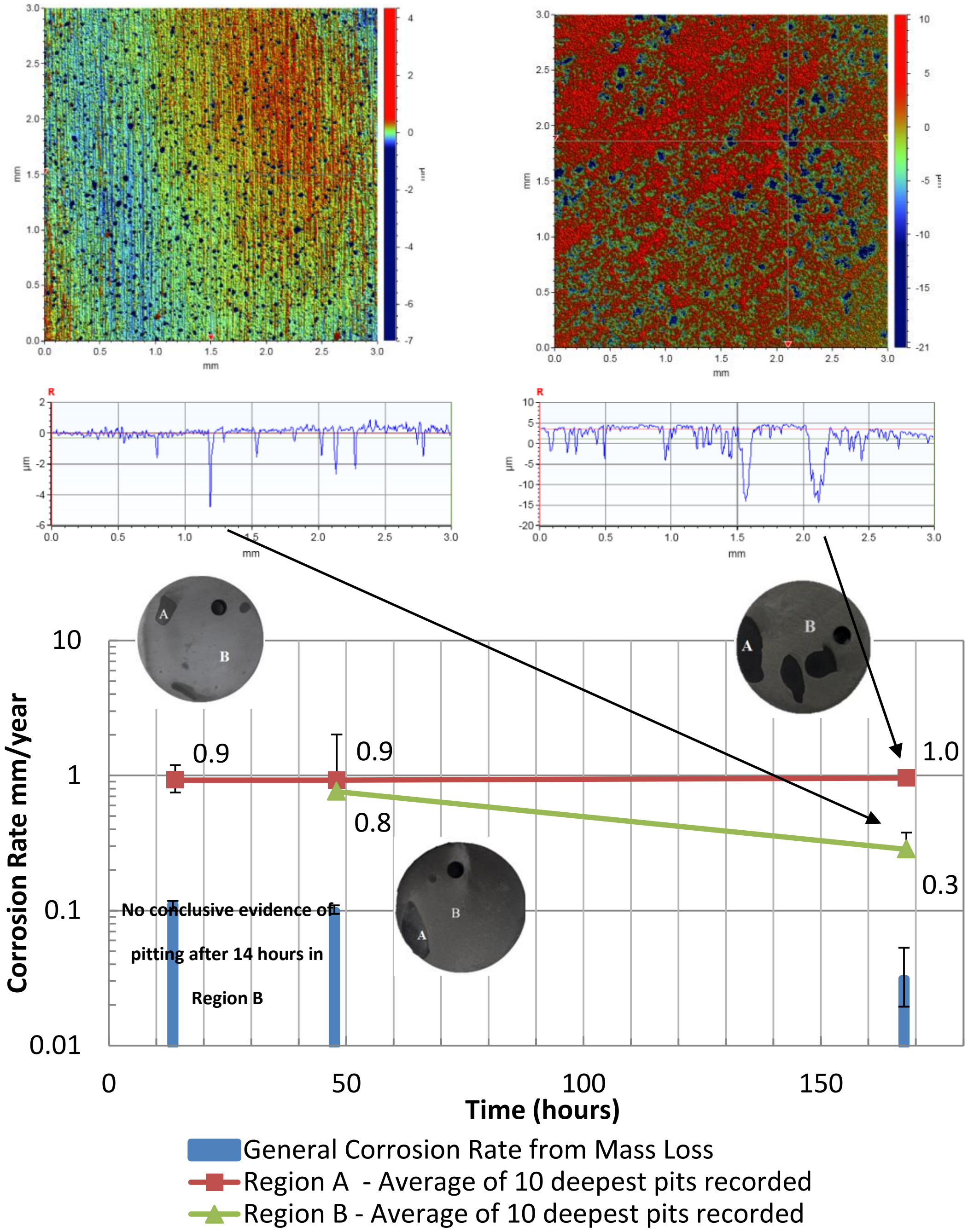

Figure 7.5: Average corrosion rates of carbon steel from water-saturated supercritical CO_2 conditions at 35°C and 80bar for different time periods presented in conjunction with profilometry images of the samples and the average pitting rates (from top 10 pits). Values of average pitting rates are provided in the Figure.

Table 7.3: Corrosion rates of sample exposed to water – saturated supercritical CO_2 phase at 35°C and 80 bar at test duration of 14, 24, 48 and 168 hours

CO_2 pressure (bar)	Temp (°C)	Test period	Water content (ppm in mole)	Corrosion Rate (mm/year)					
				general	**SD**	**Localised-A**	**SD**	**Localised-B**	**SD**
80	35	14 h	Water-saturated CO_2 ~34000 ppm water added to autoclave to ensure saturation	0.11	0.022	0.92	0.149	0	*
		48 h		0.09	0.011	0.92	0.399	0.76	0.041
		168 h		0.03	0.019	0.96	0.058	0.28	0.037

*No measurement can be observed

7.4.2 Region B – discoloured area containing dispersed patches of small, agglomerated crystals

To aid as a comparison with the images in Figure 7.6 from Region A, FIB sectioning and a TEM analysis was also implemented on a selected area within Region B. In a similar process to that described above, the area of interest (Figure 9(a)) was selected and material was milled out either side of the TEM sample (Figure 7.8(b)). Figure 7.8(c) shows the sample after it was attached to the Cu TEM grid and subsequently thinned down. The dark-field image in Figure 7.8(d) coupled with the SEM images observed previously shows a more compact film in Region B in comparison to Region A. The thickness of the film in this selected area was measured at between 2 and 3 µm.

Further analysis of the TEM slides indicated a small surface deposit at the very interface of the $FeCO_3$ crystals and the steel substrate as shown in Figure 7.9(b). Figure 7.9(a) is an image of the deposit in relation to the surrounding surface corrosion product, with Figure 7.9(b) providing an image at higher magnification. It can be observed that $FeCO_3$ crystals appear to be initiating and growing from this site on the surface. The HAADF image provided in Figure 7.9(c) shows the point of initiation more clearly.

Subsequent SAED patterns were retrieved from Regions ② and ③ identified within Figure 7.9(c) and are provided in Figures 9(d) and (e), respectively. Indexing of both patterns yielded d-spacing values indicative of $FeCO_3$. The pattern observed in Figure 7.9(d) suggested the presence of a single crystal within the region analysed. However, the pattern produced from Region ③ in Figure 7.9(e) produced ringed diffraction patterns suggesting a nano-polycrystalline material. It is highly plausible that this polycrystalline region was the initiation point for further crystal growth from the surface. Such an initiation point was not observed within Region A, although there is no evidence to suggest such an initiation point does not exist in this region as well.

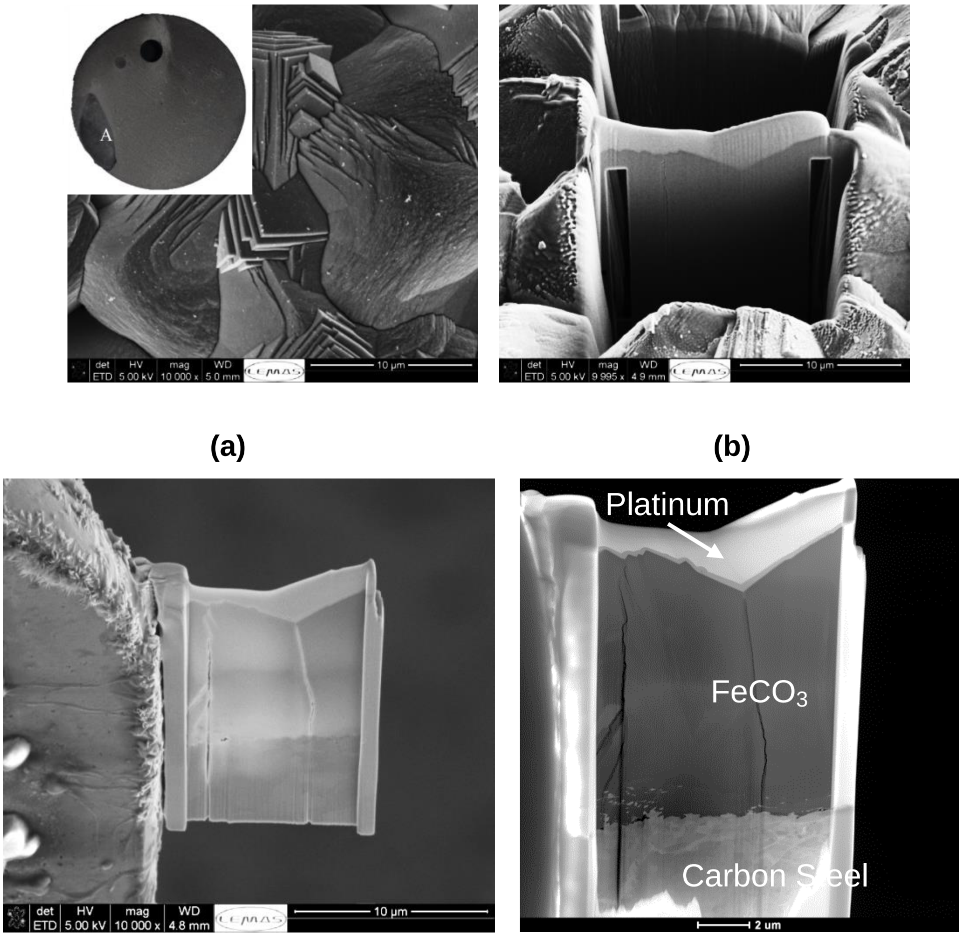

(a) **(b)**

(c) **(d)**

Figure 7.6: High resolution FIB-SEM images of Region A (35°C sample) after 48 hours, indicating (a) where ion milling was performed on the sample surface prior to Pt deposition, (b) the sections milled away within the surface to produce the TEM sample, (c) fixation of the FIB prepared section to the Cu TEM grid and the final thinning of the sample (d) a high-angle annular dark-field image (HAADF) produced in the TEM.

One way of explaining the difference in $FeCO_3$ can be related to the extent of water which condensed onto the steel in each location. In Region A, a significant amount of water has condensed onto the steel surface relative to Region B, resulting in a visibly darker surface. In Region B, much smaller water droplets have condensed on the steel and have left the surface discoloured. Through comparison between the two areas, Region A will have a greater level on condensed water on the surface and inevitably, it will take longer for the surface film of water to become saturated with water. In contrast, Region B will have a smaller water volume to surface area ratio and consequently, the solution on the surface will become saturated with

Fe^{2+} much faster. The two regions on the surface will therefore display different precipitation kinetics; Region A will display slower precipitation of $FeCO_3$, which leads to larger crystals and consequently, a thicker corrosion product film (~10 μm) whilst Region B will display faster precipitation kinetics, resulting in smaller, more compact crystals with a thinner layer (2-3 μm).

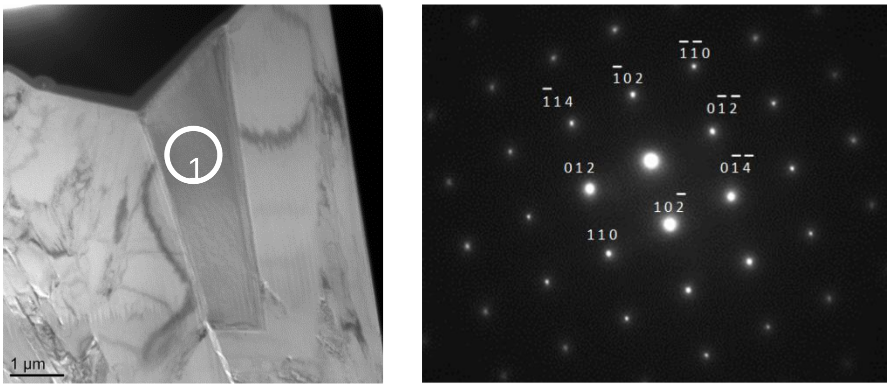

(a) **(b)**

Figure 7.7: (a) Bright field TEM image of area highlighted in Figure 7.6 (c) to indicate the location of the Selected Area Electron Diffraction (SAED) measurement of the corrosion product film in Region A and (b) the corresponding electron diffraction pattern from Region ①, which produces d-spacing values typical of $FeCO_3$.

Interestingly, the two corrosion products precipitating on the steel surface in Regions A and B appear to have had an influence on the corrosion mechanisms taking place. In terms of the general corrosion rate, a reduction in material dissolution rate is recorded as a function of time which can be related to the presence of $FeCO_3$ on the steel surface. Numerous authors have reported the ability of $FeCO_3$ to block activate sites on the steel surface and act as a diffusion barrier to electrochemically active species involved in the charge-transfer processes associated with CO_2 corrosion.

Table 7.4 summarises the main observations from the results obtained, comparing the surface morphology of the corrosion products with the pitting corrosion characteristics in Region A and Region B.

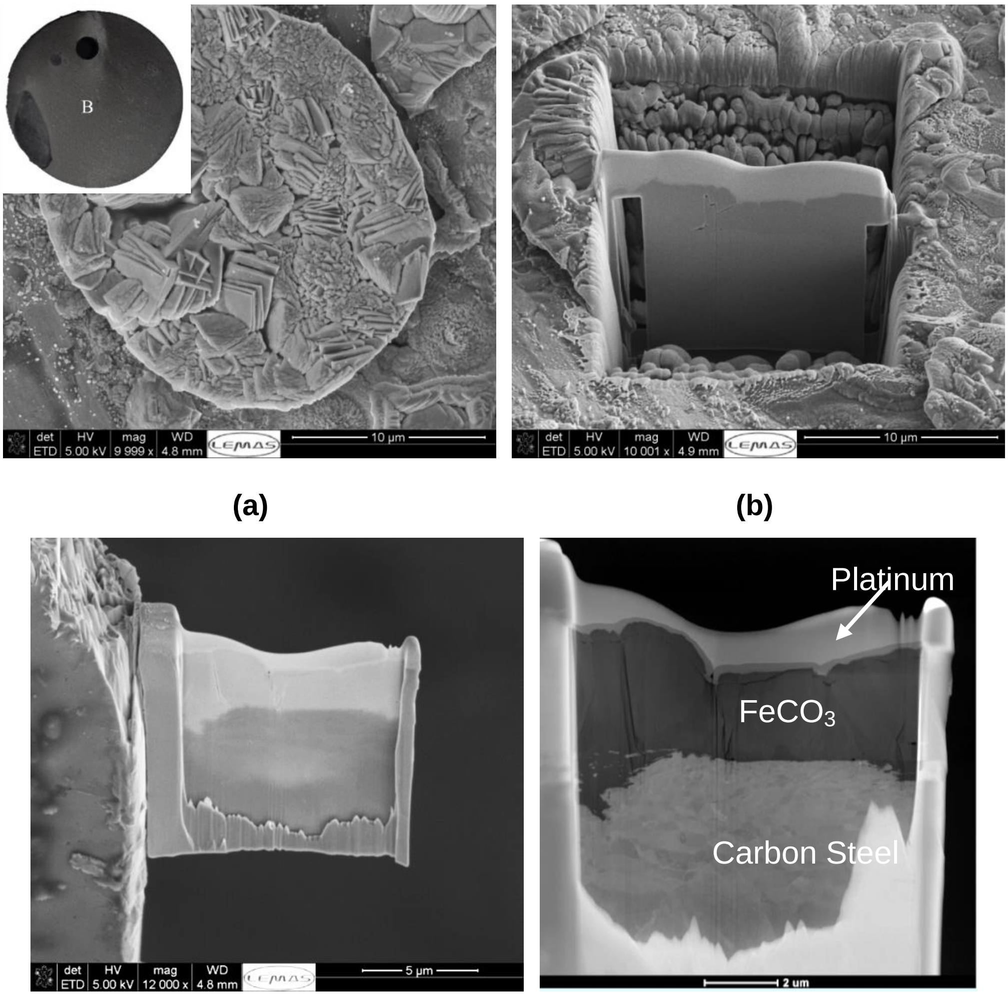

(a) (b)

(c) (d)

Figure 7.8: High resolution FIB-SEM images of Region B (35°C sample) after 48 hours, indicating (a) where ion milling was performed on the sample surface, (b) the sections milled away to produce the TEM sample, (c) the prepared TEM sample after thinning and (d) a high-angle annular dark-field image (HAADF) produced in the TEM.

7.5 Results of Sample Exposed to Water-Containing Supercritical CO_2 Phase at Different Temperatures

The entire matrix of test conditions are summarised in Table 7.5. According to Spycher et al.,[26], the saturated water concentration in supercritical CO_2 at 50°C and 80 bar is 3400ppm whilst the saturated-water concentration at 35°C and 80 bar is 3437ppm. In order to ensure the water-saturated supercritical CO_2 condition, 3.4g of water was introduced to the autoclave for the water-saturated test (10 times the saturation limit). For under-saturated conditions, between 300 and 2800 ppm water was injected at the start of each test.

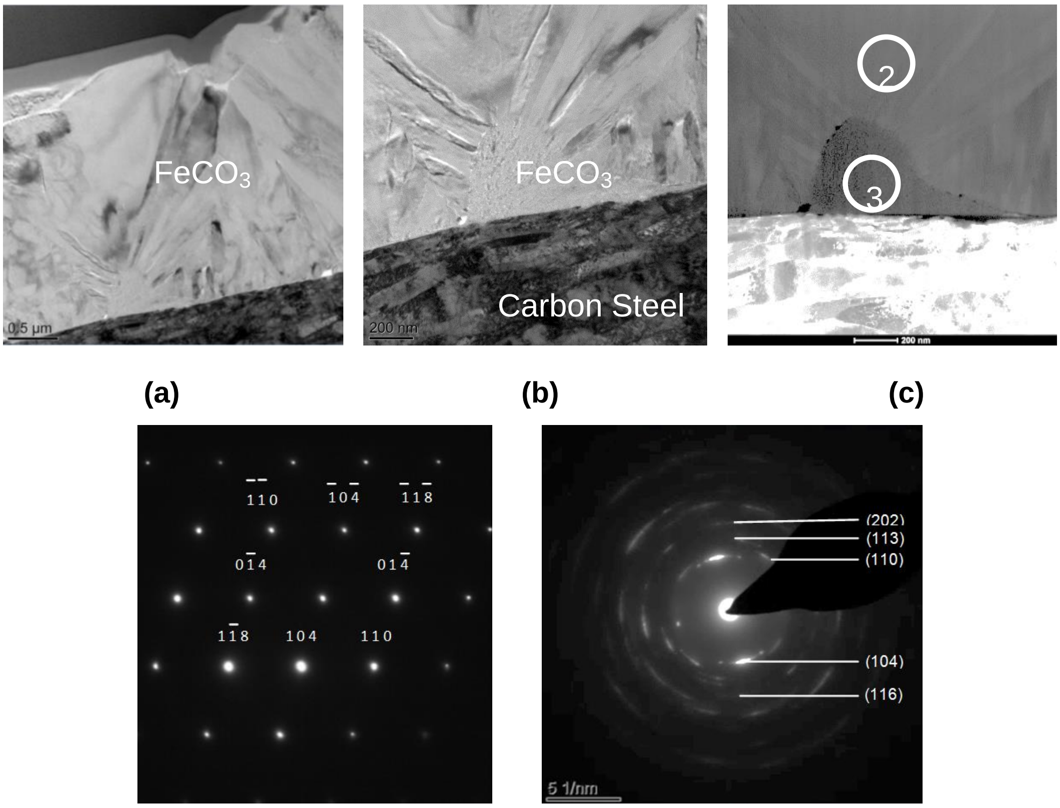

(a) (b) (c)

(d) (e)

Figure 7.9: (a) TEM image of $FeCO_3$ corrosion product film in Region B, (b) increased magnification of corrosion product cross-section, showing the nano-polycrystalline initiation point for subsequent crystal growth, (c) a high-angle annular dark-field image (HAADF) of the nano-polycrystalline deposit indicating the points where SAED patterns were obtained, (d) the electron diffraction pattern corresponding to Region ②, which produces d-spacing values typical of $FeCO_3$ an shows the presence of a single crystal and (e) the electron diffraction pattern corresponding to Region ③, which produces d-spacing values typical of $FeCO_3$ and shows the region as polycrystalline.

Tests in water-saturated supercritical CO_2 phase described previously revealed that corrosion of carbon steel can take place at the surface at both 35 and 50^oC. However, considering the real conditions during the transport of supercritical CO_2 in pipelines, water content tends to be below the solubility limit. Therefore, it is also important to study the behaviour of carbon steels when exposed to under-saturated conditions in the supercritical CO_2 phase.

Table 7.4: Summary and comparison of corrosion product morphology in relation to Region A and Region B on steel surface

Test Conditions	35°C, 80 bar, water-saturated CO_2	
Location on Sample	Region A	Region B
Corrosion Product (XRD/SAED)	$FeCO_3$	$FeCO_3$
Visible Differences	Dark surface deposit	Discoloured surface
Crystal Size and Morphology (SEM)	Cubic crystals with rounded edges and vertices dispersed on the surface. Crystals were in excess of 10 µm in diameter.	Agglomeration of multiple crystals compact together to produce a thin corrosion product film. Each 'patch' of corrosion product on the surface consisted of number $FeCO_3$ crystal platelets stacked on top of one another to produce a compact structure with crystals smaller than 2 µm in width
Corrosion Product Thickness (TEM)	~10 µm	~ 2-3 µm
General Corrosion Behaviour	Corrosion rate reduced from 0.11 to 0.03 mm/year from 14 to 168 hours	
Localised Corrosion Behaviour	Stable pitting rate at 0.9-1.0 mm/year over 168 hours	0.8 mm/year pitting rate after 48 hours, but decreased to 0.3 mm/year over 168 hours
Pit Morphology	High aspect ratio (pit depth/width)	Low aspect ratio (pit depth/width)

7.5.1 Results of samples exposed to under-saturated supercritical CO_2 phase at 50^oC

Figure 7.10 shows the measured corrosion rates of samples exposed to the water-saturated supercritical CO_2 phase in comparison to the under-saturated conditions at 50°C and 80 bars for immersion times of 48 hours. They consist of tests at water contents of 2650, 1600 and 700 ppm. No corrosion rate was observed for water content below 1600 ppm. This is supported by the image in Figure 8(a) which shows the carbon steel sample after 48 hours exposure. The surface was completely clean and no signs of corrosion or discolouration were observed.

Table 7.5: The experimental matrix of the samples exposed to water-undersaturated supercritical CO_2 at 35°C and 80 bar

Under-saturated conditions at 50°C			
Temperature, °C	Pressure, bar	H_2O (ppm)	Immersion time, h
50	80	2650	48
50	80	1600	48
50	80	700	48
Under-saturated conditions at 35°C			
Temperature, °C	Pressure, bar	H_2O (ppm)	Immersion time, h
35	80	2800	48
35	80	1770	48
35	80	700	48
35	80	300	48

As the water content was increased to 2650 ppm, the average general corrosion rate reached 0.014 mm/year. SEM images of the sample surface provided in Figure 7.11(b) and (c) indicate that corrosion products were detected on the surface of the sample, confirming that corrosion had taken place. At the saturation limit (3400 ppm), corrosion rate increased further to above 0.02 mm/year as stated previously and as shown in Figure 7.

The important point to note from this set of tests are that corrosion can take place in conditions where the water content is below the solubility limit i.e. when there is no free water in the system. However, the results also suggest that the current requirement for water content to be below 500[7] ppm in the CO_2 pipeline would be sufficient too much for the prevention of corrosion in the supercritical CO_2 environment at an operating temperature of 50°C.

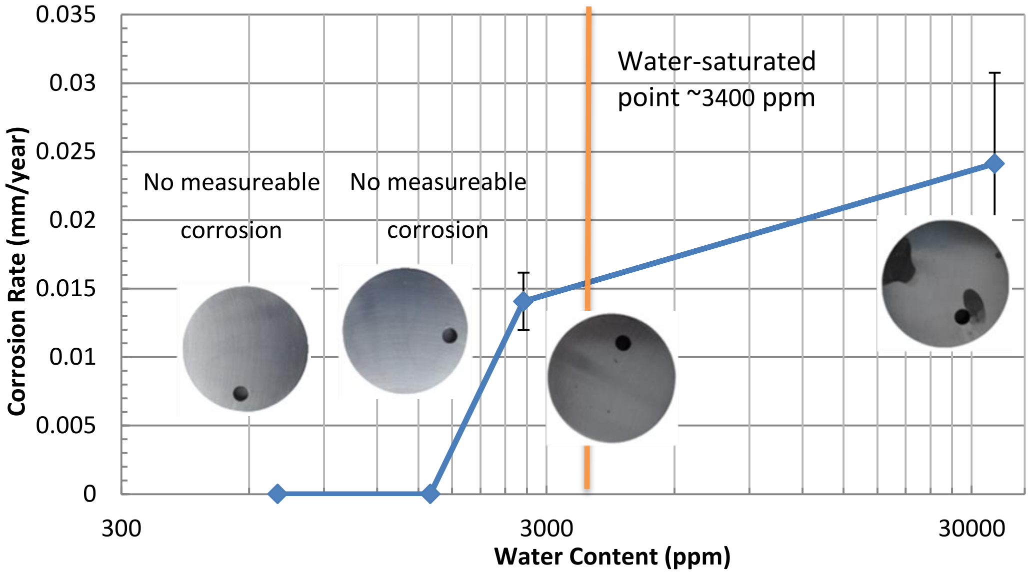

Figure 7.10: Average corrosion rates of carbon steel from water-saturated supercritical CO_2 down to under-saturated conditions at 50°C and 80bar for 48 hours.

7.5.2 Results of samples exposed to under-saturated supercritical CO_2 phased at 35^oC

Figure 7.12 shows the measured corrosion rates of samples exposed to the water-saturated supercritical CO_2 phase in comparison to the under-saturated conditions at 35°C and 80 bars for immersion times of 48 hours. Immediately, through comparing Figures 7.10 and 7.12, it was clear that corrosion was recorded at every concentration of water tested down to 300 ppm at 35^{o}C, whereas no corrosion was measured below 1600 ppm at 50^{o}C. From this perspective, the molar concentration limit of 650 ppm would not be sufficient to completely prevent corrosion in the system at 35^{o}C, although corrosion rates would be very small at this concentration (i.e. below 0.02 mm/year). Sim et al.,[75] performed similar tests at 80 bar and 40°C for 168 hours. They introduced water at concentrations of 900 to 3500 ppm and found that corrosion rates averaged between 0.06 and 0.08 mm/year, showing similarity with the results presented in Figure 7.12 which were conducted at a temperature only 5°C lower.

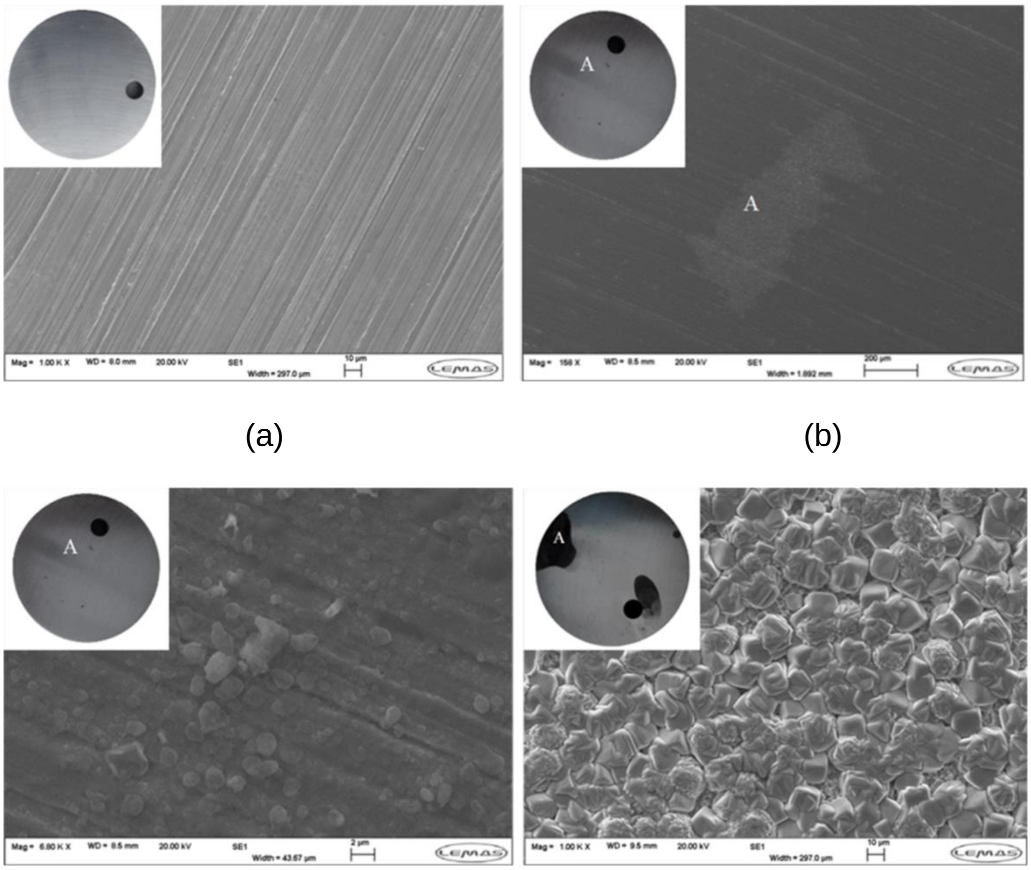

(a) (b)

(c) (d)

Figure 7.11: SEM images of samples exposed to supercritical CO_2 phase containing (a) 1600 ppm water, (b) 2650 ppm water, (c) 2650 ppm water at closer magnification and (d) water-saturated supercritical CO_2 at 50°C and 80 bar after 48 hours.

Despite a mass loss being measured for the coupon exposed to 300 ppm water in supercritical CO_2 at 35°C, no indication of corrosion could be detected on the SEM over the regions scanned (Figure 7.13(a)). As the quantity of water in the system was increased up to 1770 ppm, signs of corrosion became more apparent as corrosion products became more visible on the surface (Figures 7.13(a)-(d)). Based on the mass loss results in Figure 9, a water content of 2800 ppm marks the transition point in terms of general corrosion behaviour from a low corrosion rate of 0.03 mm/year (at 1770 ppm) to a considerably higher corrosion rate (relatively) of over 0.1 mm/year in water-saturated supercritical CO_2 phase. The regions of localised attack observed on the sample surface showed clear signs of $FeCO_3$ crystals in the presence of 2800 ppm (Figure 7.13(e)) and water-saturated supercritical CO_2 (Figure 7.13(f)) as a result of the increased level of material dissolution in this area where the water has condensed, relative to other regions of the sample surface.

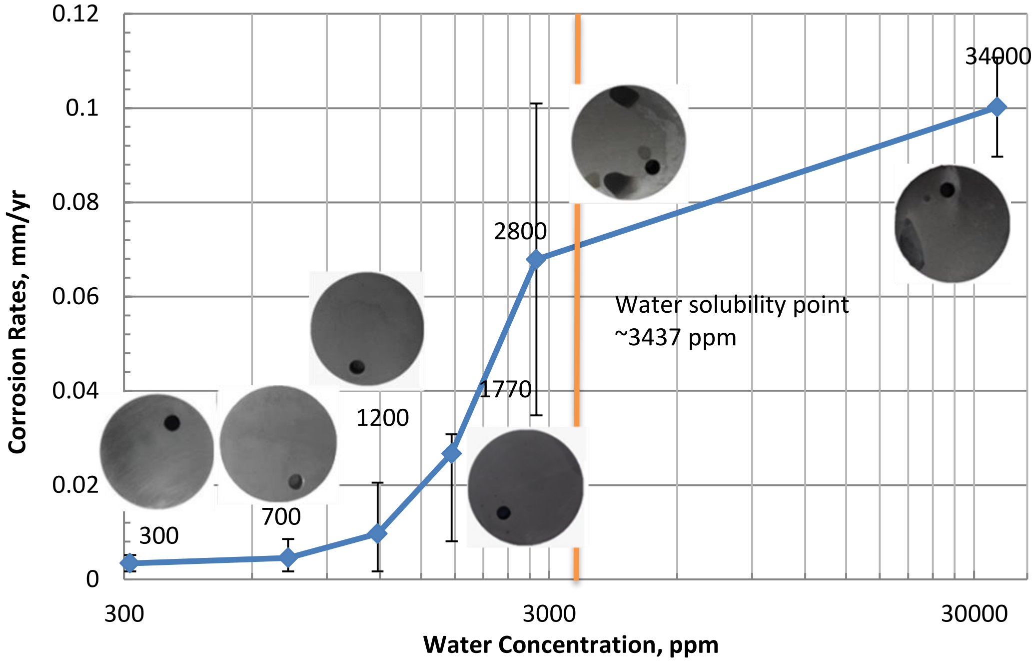

Figure 7.12: Average corrosion rates of carbon steel from water-saturated supercritical CO_2 down to under-saturated conditions at 35°C and 80bar for 48 hours.

7.5.3 Localised corrosion vs. general corrosion behaviour

It is clear from analysing photographs of the samples in the water-saturated supercritical CO_2 phase and the under-saturated conditions that the corrosion in the system, particularly in higher water content environments can be quite localised. There is a suggestion that the 'general' corrosion rates calculated from mass loss measurements may not be an accurate reflection of the detrimental effect the water concentration may be having in terms of metal penetration. Therefore, in addition to the mass loss measurements, surface profilometry was conducted to review the extent of surface pitting in comparison to the general corrosion rate.

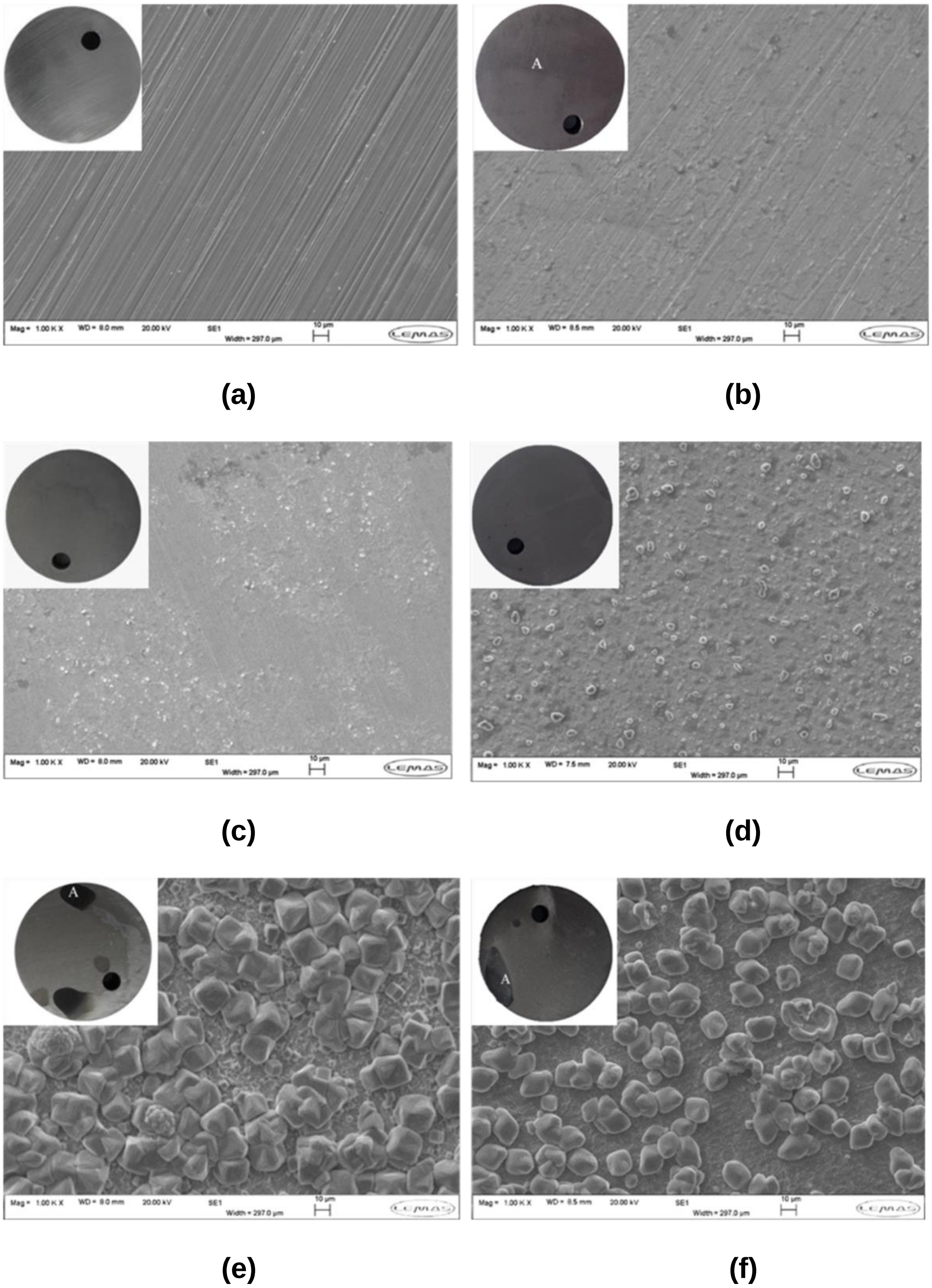

(a) (b)

(c) (d)

(e) (f)

Figure 7.13: SEM images of sample exposed to supercritical CO_2 phase containing (a) 300 ppm water, (b) 700 ppm water (c) 1200 ppm water, (d) 1770 ppm water, (e) 2800 ppm and (f) water-saturated supercritical CO_2 at 35°C and 80bar after 48 hours.

Figure 7.14 and Table 7.6 provide examples of the profilometry measurements taken of the samples subjected to the water-containing supercritical CO_2 at 50°C and 80 bar. The profilometry images are provided in conjunction with the general corrosion rates (from mass loss measurements) and the localised corrosion rates (both maximum and average) calculated from the top 10 measured pit depths. Figure 7.14 indicates that the level of pitting attack on the steel surface is over an order of magnitude greater than the general corrosion rate, showing that localised corrosion represents a real threat to the integrity of carbon steel pipelines involved in transporting water-containing supercritical CO_2 if the water content is substantial enough. The results show that if the water content is at 1600 ppm or below, then no corrosion (general or localised) will be observed. However, if the water content is increased to 2650 ppm, then the average pitting rate reaches 0.2 mm/year (maximum of 0.4 mm/year), despite the water content being below the solubility limit of 3400 ppm. When the CO_2 is completely saturated with water at 50^oC, the average pitting rate was 1.4 mm/year (maximum of 2.6 mm/year), in comparison to the general corrosion rate of 0.02 mm/year. The results highlight the importance of understanding and quantifying the localised corrosion rates in these systems to ensure pipeline integrity.

Figure 7.15 provides examples of the profilometry measurements taken of the samples subjected to the water-containing supercritical CO_2 at 35°C and 80 bar along with the general and localised corrosion rates. The reduction in temperature from 50 to 35^oC resulted in corrosion being observed at a much lower water concentration of 300 ppm, but no localised attack was detected on the surface. At the water contents from 700 ppm up to water-saturated conditions, the average pitting rate increased steadily with water content from 0.3 mm/year (max of 0.8 mm/year) to 0.9 mm/year (max of 2.0 mm/year). When localised corrosion was recorded, the rates or attack were over an order of magnitude greater than the general corrosion rates, just as with tests at 50^oC. Again, these results illustrate that localised corrosion is a concern in supercritical CO_2 transport when the system is contaminated with water. Additionally, the tests at 35^oC show that even when the water content is below the maximum set in the US of between 500 and 650 ppm, pitting rates can reach 0.3 mm/year with only water present as the impurity.

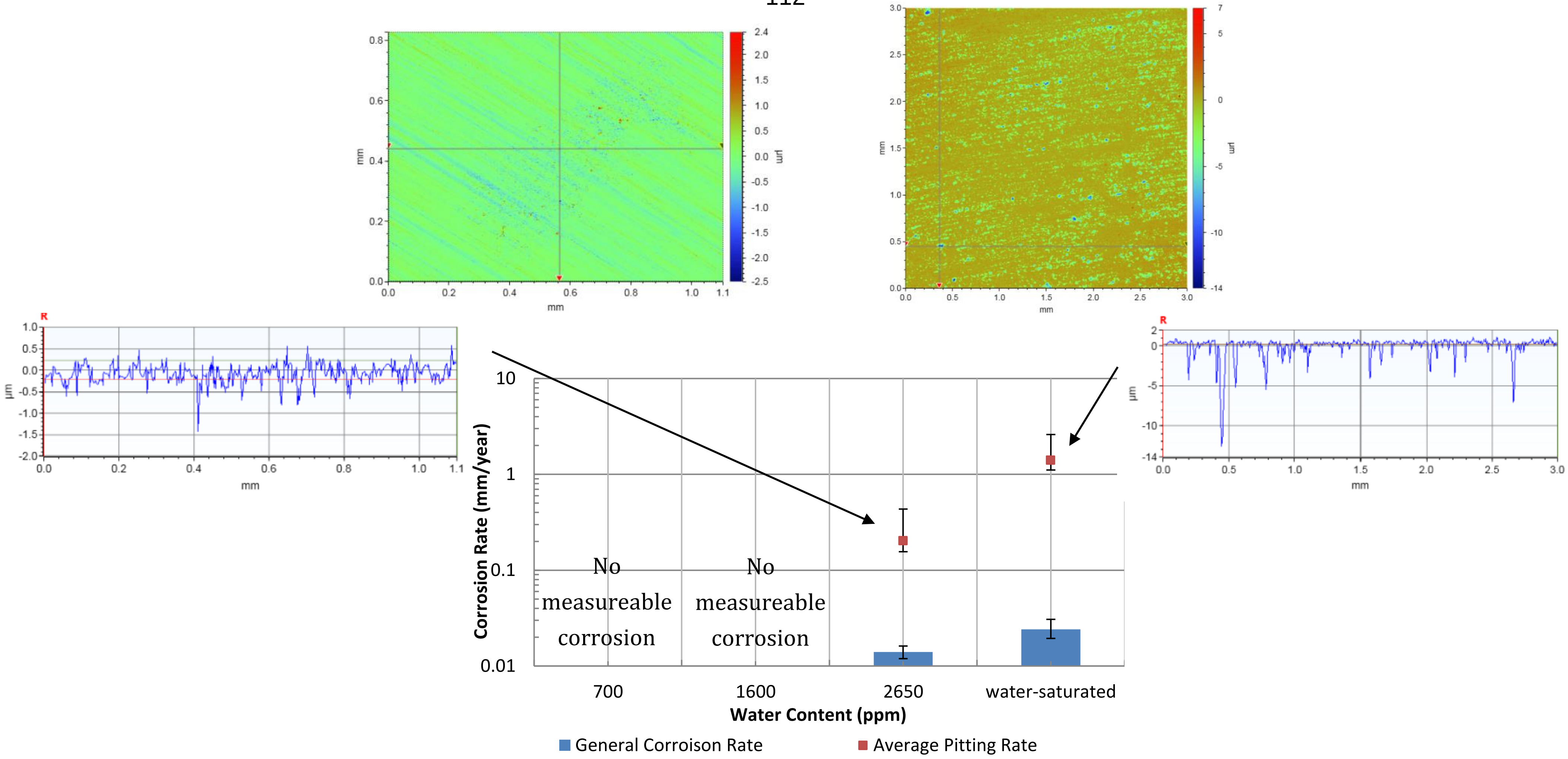

Figure 7.14: Average corrosion rates of carbon steel from water-saturated supercritical CO_2 down to under-saturated conditions at 50°C and 80bar for 48 hours presented in conjunction with profilometry images of the samples and the maximum and average pitting rates. Values of maximum pitting rates are provided on the Figure.

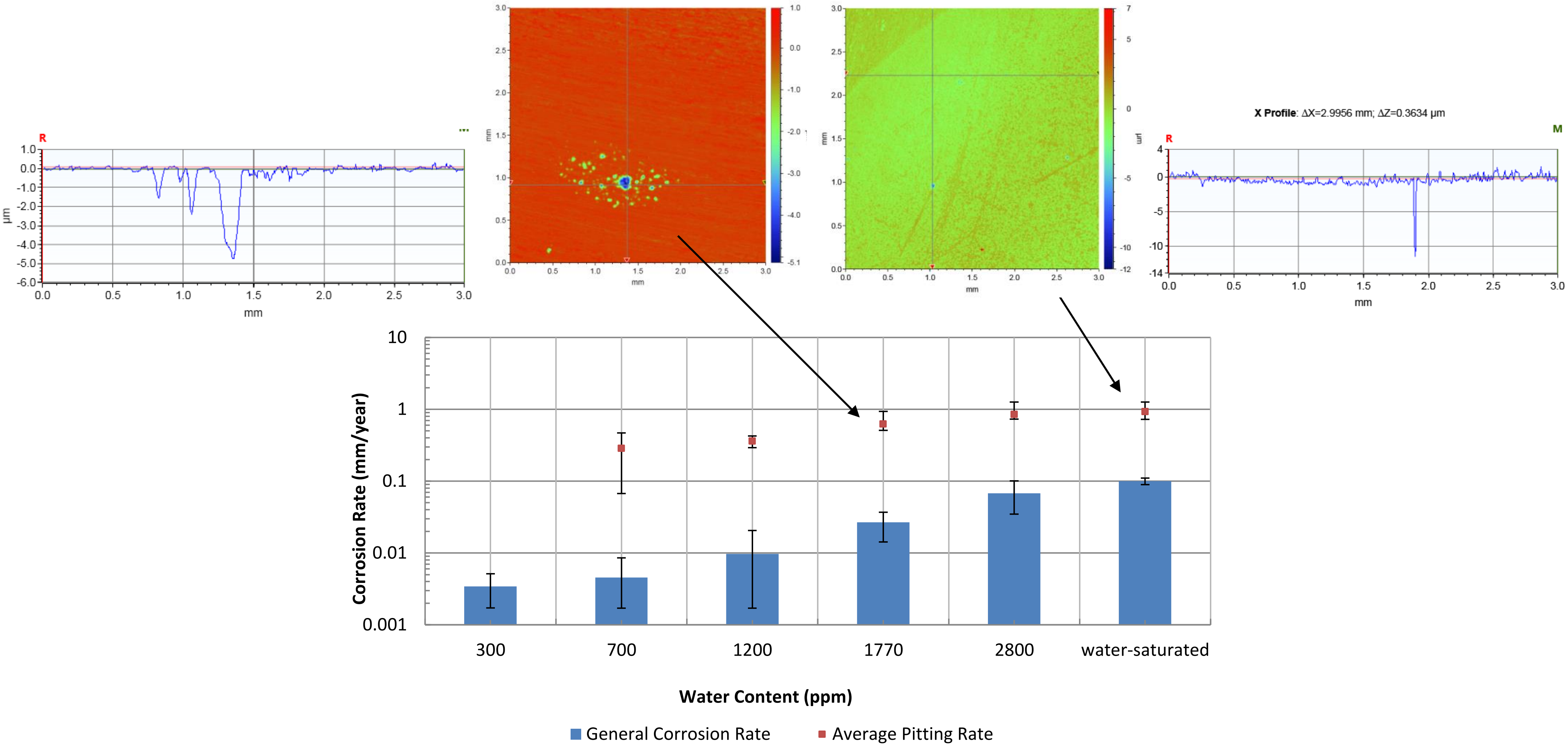

Figure 7.15: Average corrosion rates of carbon steel from water-saturated supercritical CO_2 down to under-saturated conditions at 35°C and 80bar for 48 hours presented in conjunction with profilometry images of the samples and the maximum and average pitting rates. Values of maximum pitting rates are provided on the Figure.

Table 7.6: Corrosion rates of sample exposed to water - containing CO$_2$ phase

CO$_2$ pressure (bar)	**Temp (°C)**	**Test period**	**Water content (ppm in mole)**	**Corrosion Rate (mm/year)**			
				general	**SD**	**Localised**	**SD**
80	35	48 h	300 ppm	~0.003	0.001	0	*
			700 ppm	~0.005	0.003	~0.29	0.299
			1200 ppm	~0.01	0.009	~0.36	0.034
			1770 ppm	~0.03	0.011	~0.62	0.121
			2800 ppm	~0.07	0.033	~0.85	0.061
			Water-saturated CO$_2$	~0.09	0.011	~0.92	0.399
	50		700 ppm	0	*	0	*
			1600 ppm	0	*	0	*
			2650 ppm	~0.014	0.002	~0.20	0.024
			Water-saturated CO$_2$	~0.02	0.006	~1.99	0.310

*No measurement can be observed

7.6 Summary

In this chapter, the corrosion behaviour of X65 carbon steel was evaluated in water-containing supercritical CO$_2$ conditions at different temperatures and 80 bar. Findings in this section can be summarised into the following:

- In the water-saturated CO$_2$ environment, two very different types of corrosion behaviour were observed at temperatures of 35^{o}C and 80 bar.
- In the water-saturated CO$_2$ environment at 35°C and 80 bar. Larger volumes of water had condensed onto the steel surface in Region A, resulting in large FeCO$_3$ crystals (10 μm in diameter) forming in Region A.
- Conversely, Region B were covered with ‘patches’ of agglomerated FeCO$_3$ crystal platelets (2-3 μm thickness).
- In the water-saturated CO$_2$ environment at 35°C and 80 bar. The localised corrosion rates remained constant at ~1.0 mm/year in Region A over the 168 hours test duration. The localised pitting rate reduced from 0.8 to 0.3 mm/year in Region B.

- In the water-saturated CO_2 environment, the level attack was localised at 50°C and 80 bar, with approximately 90% of the surface showing no signs of corrosion after 48 hours.
- The rate of pitting became more severe with increasing water content for both temperatures.
- In under-saturated tests at 50°C, no corrosion was observed at a water content of 1600 ppm and below, whilst a measureable corrosion rate was recorded for 300 ppm water addition at 35°C (0.005 mm/year).
- In all tests performed, the level of localised attack was over an order of magnitude higher than the general corrosion rate calculated.

Chapter 8 Results of Samples Exposed to Water-Containing Supercritical CO_2 with SO_2/O_2

8.1 Summary

The purpose of this chapter is firstly, to determine the susceptibility of carbon steel to water-containing supercritical CO_2 environments in the absence and presence of SO_2 (2, 50 and 100ppm) with and without O_2 (0 and 20ppm) by determining the general and localised corrosion rates through the implementation of the mass loss method and surface profilometry. And to find the minimum water content required for corrosion to occur when SO_2 and O_2 are present. Secondly, a systematic study is conducted in an attempt to relate the corrosion product chemistry and morphology produced in each environment to the extent of surface attack. Such an approach is adopted through a combination of X-ray diffraction (XRD) measurements, surface profilometry measurement, and scanning electron microscopy (SEM). Table 8.1 provides information on the entire set of tests conducted.

8.2 Mass Loss Results of Water-Saturated Supercritical CO_2 Phase with Different Levels of SO_2 With or Without O_2

8.2.1 Corrosion tests in water-saturated supercritical CO_2 phase with 2 ppm SO_2 (with and without 20 ppm O_2)

The effect of 2 ppm SO_2 on the corrosion rate of X65 steel in the presence and absence of 20 ppm O_2 in the water-saturated supercritical CO_2 phase is shown in Figure 8.1. The corrosion rate of X65 in the absence of both SO_2 and O_2 (i.e. in solely water-saturated supercritical CO_2) at 35°C and 80 bar is also provided as a reference point. It can be observed that the addition of 2 ppm SO_2 in the gas phase increases the corrosion rate of X65 by 40% from 0.1 mm/year to 0.14 mm/year. The addition of 20 ppm O_2 resulted in no significant change in corrosion rate from the system already containing 2 ppm SO_2, an increase in corrosion rate from the system containing no SO_2 or O_2.

Table 8.1: Test matrix for corrosion experiments

Temp. (°C)	Pressure (bar)	H_2O (ppm)	SO_2 (ppm)	O_2 (ppm)	Immersion time (hours)
35	80	Water-saturated (3437 ppm in CO_2 phase through addition of 34000 ppm water)	0	0	48
			2	0	
			2	20	
			50	0	
			50	20	
			100	0	
			100	20	

It is important to note from Figure 8.1 that only 2 ppm SO_2 is required to promote a change in the level of degradation at the steel surface. SEM images of the corroded steel surfaces from tests performed in the water-saturated environment in the absence and presence of 2 ppm SO_2 and 20 ppm O_2 are provided in Figures 8.2, 8.3 and 8.4. All steel samples exposed to the water-saturated environment became discoloured and two distinctly different corroded areas became apparent which are referred to as Regions A and B and are identified within each of the SEM images.

With reference to the X65 samples exposed to water-saturated supercritical CO_2 in the absence of SO_2 and O_2, Region A consisted of large cubic $FeCO_3$ crystals (Figure 8.2(a)), whilst Region B consisted of patches of much smaller platelet type crystals (Figure 8.2(b)). The morphology of the observed crystals are discussed in detail within Chapter 7, where they are verified as $FeCO_3$ crystals through application of selected are a electron diffraction (SAED) measurements. Figure 8.6 provides an XRD spectra for the surface which indicates that the only crystalline corrosion product identified on the steel surface was $FeCO_3$. EDX analysis was also performed on the surface regions identified in Figures 8.3(a) and (b) and indicated that Fe, C and O were the only elements identifiable within the corrosion product on the X65 surface in this particular experiment. Figures 8.2(c) and (d) provide higher magnification images of the steel surfaces to indicate the difference in crystal structure within each area.

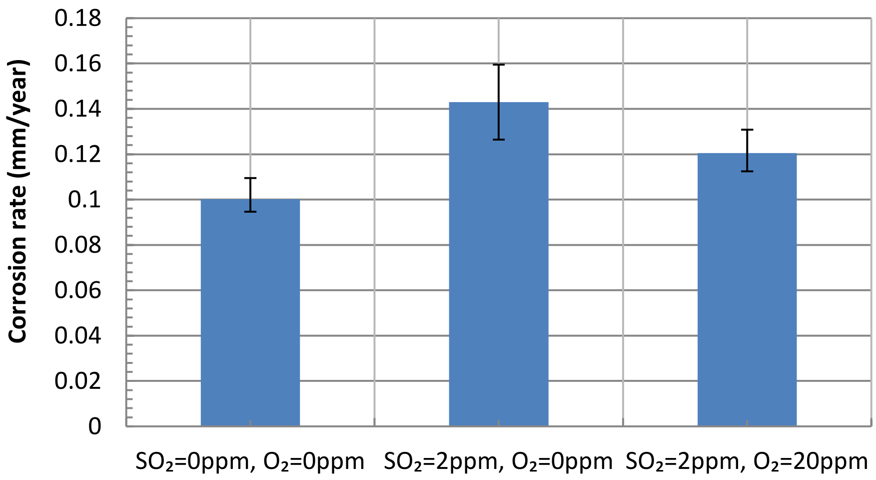

Figure 8.1: Corrosion rates of carbon steel in the water-saturated supercritical CO_2 phase at 80 bar and 35°C for an immersion time of 48 hours. Impurities considered are SO_2 (0 and 2 ppm) and O_2 (0 and 20 ppm).

The addition of 2 ppm SO_2 to the test environment still resulted in the formation of $FeCO_3$ crystals on the steel surface (as shown in XRD spectra in Figure 8.5). No other crystalline compounds were detected on the surface from the XRD spectra. Again, two distinct regions on the steel surface were identified after immersion in the test solution. Region A (Figure 8.3(a)) and Region B (Figure 8.3(b)) both showed the presence of $FeCO_3$ crystals, however, the introduction of 2 ppm SO_2 changed the morphology of the crystals from that of the system where no SO_2 was introduced. The crystals observed in Region A in the presence of 2 ppm SO_2 (Figure 8.3(a)) exhibited a globular structure as opposed to the rounded cubic structure observed without the presence of SO_2. In Region B (Figure 8.3(b)), patches of agglomerated $FeCO_3$ crystals were again visible on the steel surface.

Interestingly, despite XRD not identifying any crystalline products other than $FeCO_3$ on the steel surface, EDX analysis of both Regions A and B (Figures 8.3(a) and (b)) detected the presence of sulphur on the steel surface, which will be discussed later.

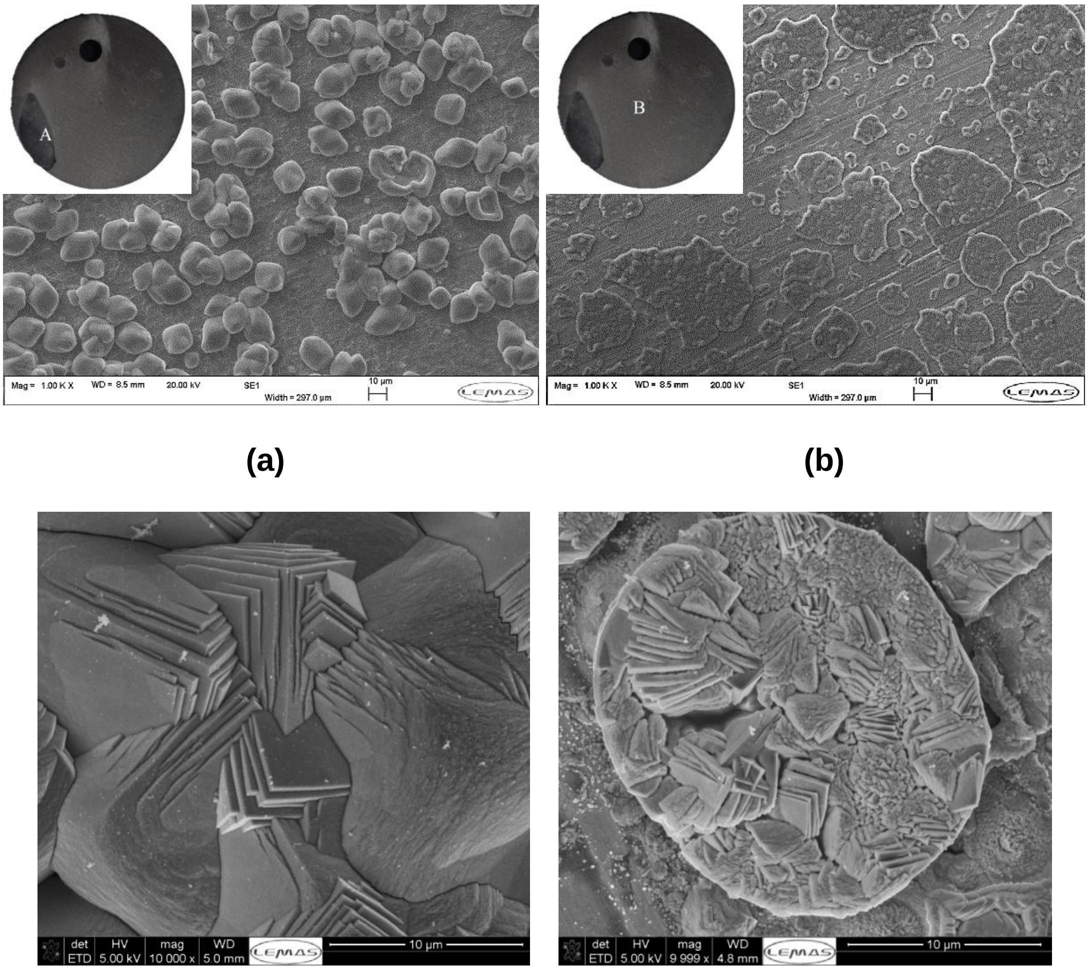

(a) **(b)**

(c) **(d)**

Figure 8.2: SEM images of the X65 corroded samples exposed to water-saturated supercritical CO_2 at 35°C for 48 hours (0 ppm SO_2 and 0 ppm O_2) in (a) Region A at x1000 magnification, (b) Region B at x1000 magnification, (c) Region A at x10,000 magnification and (d) Region B at x10,000 magnification.

The surface morphology of X65 when exposed to both 2 ppm SO_2 and 20 ppm O_2 was similar to the sample exposed to only 2 ppm SO_2 in both regions A and B. $FeCO_3$ crystals were visible in both regions (as shown in Figures 8.4(a) and (b)) and EDX measurements of the surface again indicated the presence of sulphur on the steel surface, despite no sulphur compounds being detected using XRD.

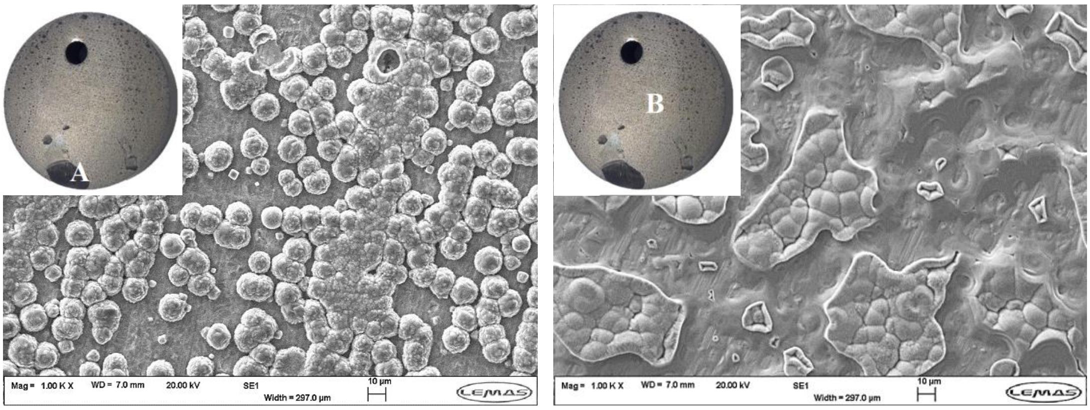

(a) **(b)**

Figure 8.3: SEM images of the X65 corroded samples exposed to water-saturated supercritical CO_2 at 35°C for 48 hours (2 ppm SO_2 and 0 ppm O_2) in (a) Region A at x1000 magnification, (b) Region B at x1000 magnification.

Consequently, the tests performed at a SO_2 content of 2 ppm indicate that the presence of 20 ppm O_2 has no significant effect on the film morphology not the corrosion rate of the steel surface.

8.2.1.2 Analysis of sulphur compound detected on steel surface

The previous section identified the presence of sulphur on the surface of X65 in environments containing both 2 ppm SO_2 and 2 ppm SO_2 with 20 ppm O_2. Figure 8.6 provides an EDX map of Region A from the steel surface exposed to 2 ppm SO_2 and 20 ppm O_2. The image indicates high levels of sulphur are detected at the surface in the interstitial spaces between the $FeCO_3$ crystals.

The combined use of FIB-SEM and TEM allowed a cross section to be extracted from this particular sample and enabled the interface between the $FeCO_3$ crystals and the steel surface to be examined. Figure 8.7(a) indicates the location from which the TEM sample was produced. Figure 8.7(b) shows the sample after it was attached to the Cu TEM grid and subsequently thinned.

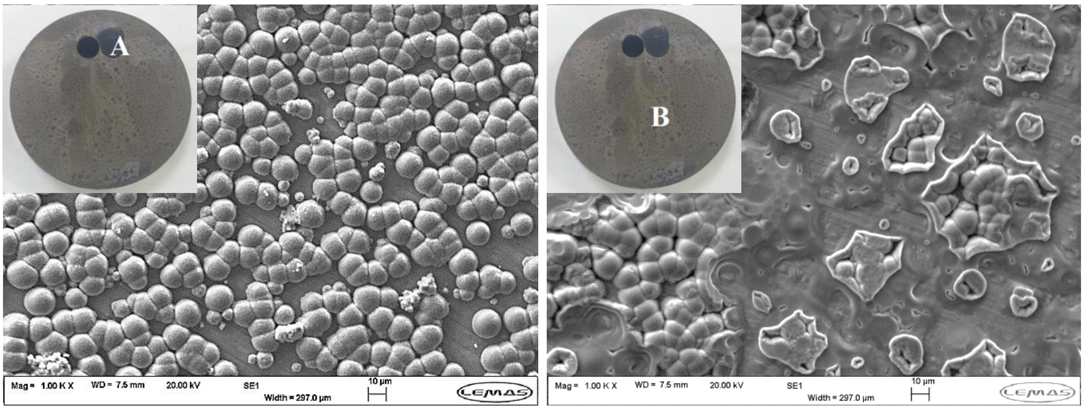

(a) **(b)**

Figure 8.4: SEM images of the X65 corroded samples exposed to water-saturated supercritical CO_2 at 35°C for 48 hours (2 ppm SO_2 and 20 ppm O_2) in (a) Region A at x1000 magnification, (b) Region B at x1000 magnification.

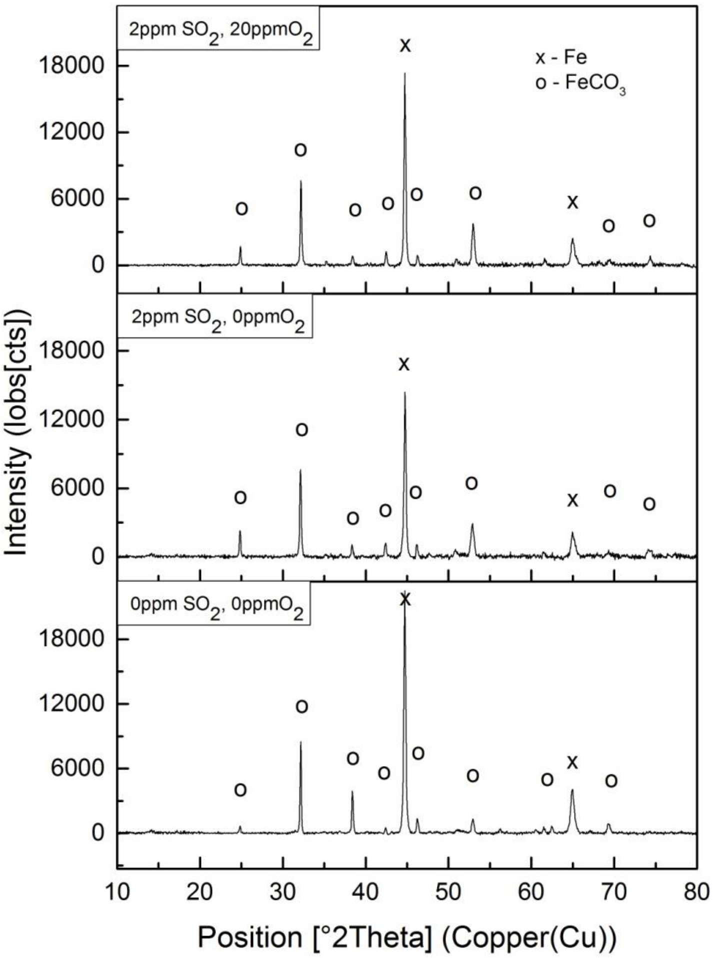

Figure 8.5: XRD spectra of samples exposed to water-saturated supercritical CO_2 phase at 35°C and 80 bar containing different concentration levels of SO_2 (0 and 2 ppm) and O_2 (0 and 20 ppm) impurities.

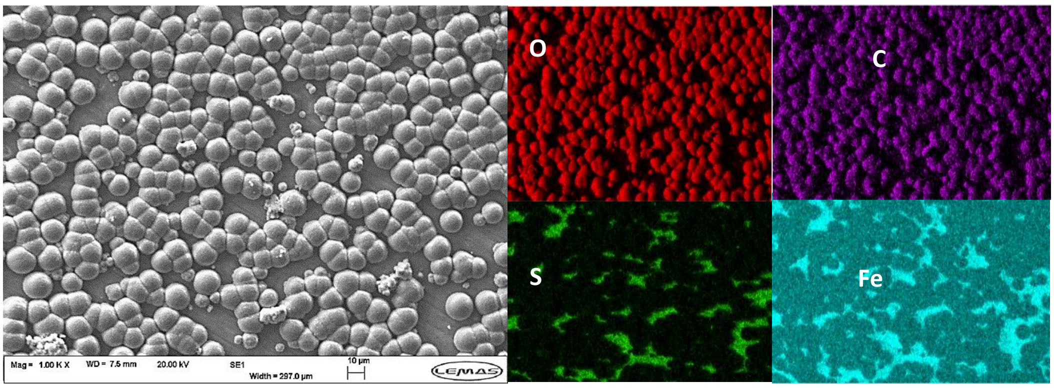

Figure 8.6: EDX map of Figure 5(a) implemented in the SEM indicating areas rich in iron, carbon, oxygen and sulphur.

Further analysis of the TEM sample (provided in Figure 8.8) indicated that the presence of SO_2 had influenced the direction crystal growth. Figure 8.8(a) shows the radial growth of the crystals which has resulted in the globular crystal morphology observed in the top view SEM images in Figures 8.3(a) and 8.4(a). Electron diffraction images also provided in Figure 8.8(a) both index to $FeCO_3$ and demonstrate that the structure becomes nano-polycrystalline closer to the surface of the steel (and the nucleation point of the crystal) and crystal sizes becomes larger towards the outer edge of the crystalline agglomeration.

Upon closer inspection of the interface between the $FeCO_3$ crystals and the steel substrate in Figure 8.8(b), a layer approximately 200 nm thick was visible. The accompanying electron diffraction image of this region in Figure 8(b) confirmed that this layer is amorphous. Figure 8.8(c) shows a high magnification image of the layer, which also shows no indication of crystallinity.

An EDX map of the TEM sample was performed and is provided in Figure 8.9. The map indicated that this layer was also rich in sulphur. The images confirm that the sulphur-containing layer is not only present on the surface in the interstitial spaces between the $FeCO_3$ crystals, but it also exists underneath the crystals themselves, effectively covering the entire surface. Regrettably, the nature of the film could not be identified using the techniques available within the TEM. However, the images clearly show the involvement of SO_2 in the degradation process despite only being present at a low concentration of 2 ppm.

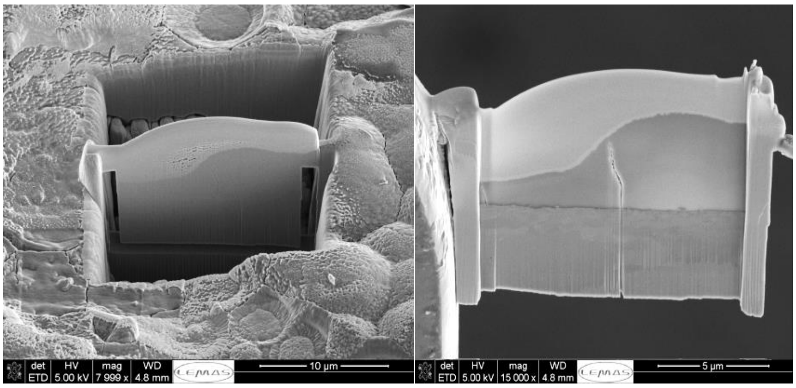

(a) **(b)**

Figure 8.7: SEM images of X65 steel surface after exposure to water-saturated supercritical CO_2 at 35°C and 80 bar containing 2 ppm SO_2 and 20 ppm O_2 for 48 hours indicating (a) the location where ion milling was performed on the sample surface and (b) the prepared TEM sample after thinning.

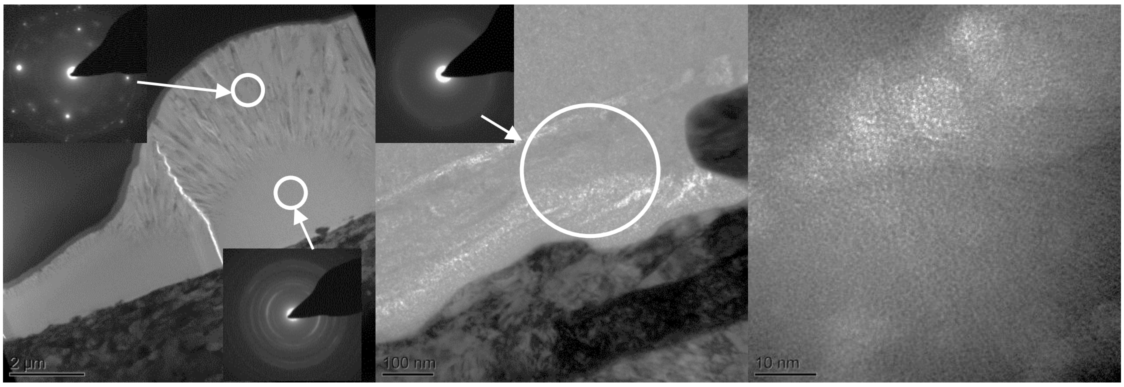

(a) **(b)** **(c)**

Figure 8.8: (a) Bright field TEM image of cross-section extracted from sample shown in Figure 8 along with corresponding electron diffraction measurements of the $FeCO_3$ corrosion product, (b) higher magnification image and accompanying electron diffraction image of amorphous, sulphur containing film and (c) increased magnification of sulphur-containing film, depicting the amorphous nature of the film.

Regrettably, the implementation of Raman spectroscopy was unable to identify the film as no response was observed on the produced spectra for sulphur-containing compounds. However, elemental ratios extracted from point EDX measurements of the film did suggest the presence of $FeSO_3$ or $FeSO_4$, but, $FeSO_4$ was present or not could not be confirmed.

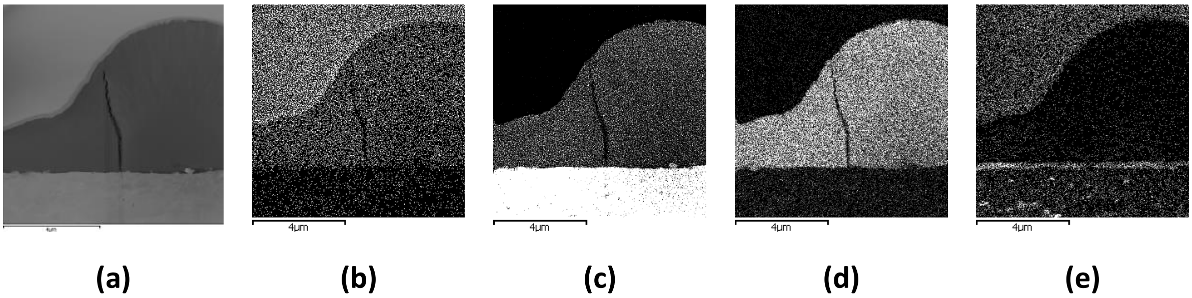

Figure 8.9: EDX mapping implemented within the TEM (a) TEM image and areas rich in (b) carbon, (c) iron, (d) oxygen and (e) sulphur.

8.2.2 Corrosion tests in water-saturated CO_2 phase with 50 ppm SO_2 (with and without 20 ppm O_2) and with 100 ppm SO_2 (with and without 20 ppm O_2)

The effect of 50 ppm SO_2 on the corrosion rate of X65 steel in the presence and absence of 20 ppm O_2 in the water-saturated supercritical CO_2 phase is shown in Figure 8.10. Again, the addition of 20 ppm oxygen to the system had no significant influence on the degradation rate according to mass loss measurements in the system. Corrosion rates in the presence of 50 ppm SO_2 in water-saturated environments reached 0.37 mm/year regardless of the presence of 20 ppm O_2 in the system. Maintaining oxygen concentration and increasing SO_2 content to 100 ppm increased corrosion rate further to 0.72 mm/year.

In comparison to the tests performed in Figure 8.10, Xiang et al.,[80] investigated the corrosion behaviour of carbon steel in water-saturated supercritical CO_2 environments with 0.2, 0.7 and 1.4 mol.% (1 mol% = 10000 ppm) of SO_2 and 1000 ppm of O_2 at 100 bar and 50°C for 288 hours. They obtained a general corrosion rates of between approximately 0.2 mm/year and 0.9 mm/year which are similar to those recorded in this study, despite the SO_2 content used by Xiang et al.,[80] being considerably higher. A suggested reason for such behaviour could be attributed to the fact that tests performed in this work are conducted in static conditions whilst Xiang et al.,[80] performed their experiments in a rotating autoclave at 120 rpm. It is suggested that the presence of flow within the system has the potential to reduce the amount of water condensed onto the steel surface and subsequently minimises the level of corrosion.

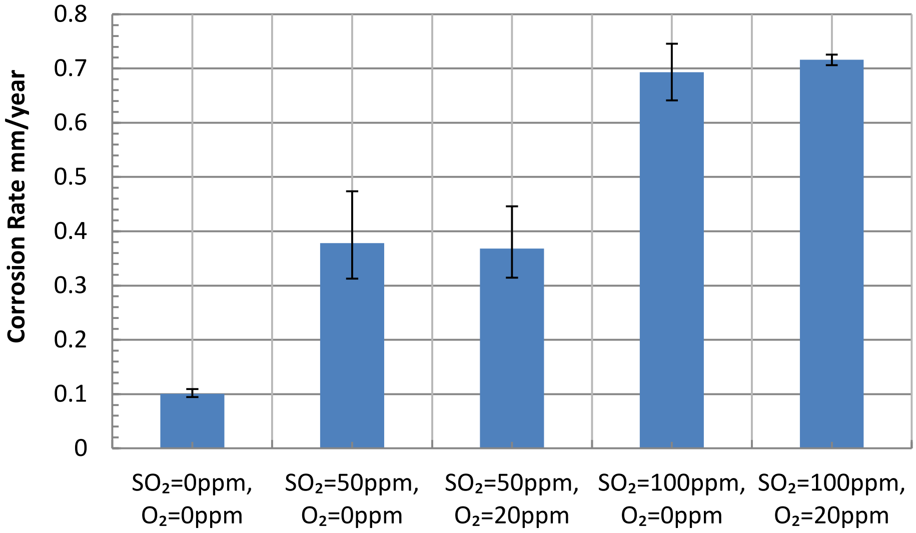

Figure 8.10: Corrosion rates of carbon steel in the water-saturated supercritical CO_2 phase at 80 bar and 35°C for an immersion time of 48 hours. Impurities considered are SO_2 (0, 50 and 100 ppm) and O_2 (0 and 20 ppm).

Such observations were made by Farelas et al.,[78] who demonstrated that the presence of flow at 1000 rpm reduced corrosion rates by around an order of magnitude in some instances compared to static experiments. Tests were performed at 80 bar in both liquid (25°C) and supercritical (50°C) conditions with the addition of 650 ppm water and 0.08 bar (1 mol%) SO_2. General corrosion rates reduced from 0.03 to 0.02 mm/year in supercritical conditions, but from 0.1 to 0.01 mm/year in liquid CO_2 as a result of changing from static to dynamic conditions. Such observation suggest that the presence of flow is capable of reducing the level of water accumulation on the steel surface, thereby reducing the corrosion rate in the system compared to that of stagnant conditions.

8.2.2.1 Corrosion product morphology and composition

Figure 8.11 depicts SEM images of the sample surfaces after exposure to the water-saturated environment containing 50 and 100 ppm SO_2. Samples exposed to 50 ppm SO_2 with 20 ppm O_2 (Figure 8.11(a)) produced columnar crystals on the surface which possessed high levels of sulphur. XRD spectra of the steel surface shown in Figure 8.12 indicated the presence of hydrated iron sulphite ($FeSO_3{\cdot}3H_2O$), which is believed to be attributed to these particular crystals. Additionally, a cracked film was also present of the steel surface which also contained sulphur, iron and oxygen as shown in the EDX maps present in Figure 8.11(a).

In the system without the presence of O_2, no columnar crystals matching those observed in Figure 8.11(a) were observed. Figure 8.11(b) indicates that the cracked, sulphur-containing layer is still apparent, but the only visible crystals using SEM were ones which match the globular morphology of those observed when $FeCO_3$ was detected in the tests involving 2 ppm SO_2. In fact, these particular globular $FeCO_3$ crystals were observed on both samples surfaces exposed to 50 ppm SO_2 with and without O_2 and were also apparent on the XRD spectra in both instances.

The increase in SO_2 content to 50 ppm produced samples which were visibly more corroded than tests performed at the lower SO_2 concentration. The sample surfaces in Figures 8.11(a) bear a striking resemblance to those observed by Choi et al.,[15] in tests performed in water-saturated CO_2 at 80 bar and 50°C with 0.8 bar SO_2. Choi et al.,[15] detected the presence of hydrated iron sulfite ($FeSO_3{\cdot}3H_2O$) on the steel surface and no indication of $FeCO_3$ according to their Raman spectra. However, the lower content of SO_2 (50 and 100 ppm in the presence of 20 ppm O_2) used in the experiments within this work compared to that of by Choi et al.,[15] have resulted in the co-presence of both $FeCO_3$ and $FeSO_3{\cdot}3H_2O$ as shown in the XRD spectra presented in Figure 8.12 and later the use of localised Raman spectroscopy at specific locations on the steel surface confirmed are $FeCO_3$ and $FeSO_3.3H_2O$ and are provided in Figure 8.21.

Interestingly, XRD spectra shown in Figure 8.12 reveal that the lack of oxygen in the system prevented any significant formation of crystalline $FeSO_3$ as it could not be detected using XRD. This experiment was repeated several times, and crystalline $FeSO_3$ was not detected in any of the experiments at 50 ppm SO_2 in the absence of oxygen. The observations in the XRD spectra support the lack of $FeSO_3$ crystals on the steel surface as this particular crystal morphology could not be detected.

The addition of 100 ppm SO_2 with or without 20 ppm O_2 produced higher degradation rates for the X65 steel. The observed corrosion product morphology on both surface were very similar to that for the system containing 50 ppm SO_2 and 20 ppm O_2. Figure 8.11(c) and (d) indicates the presence of both the cracked, sulphur-containing film, as well as the columnar $FeSO_3$ crystals. The XRD spectra provided in Figure 8.12 again confirms the presence of crystalline $FeSO_3 \cdot 3H_2O$ on the steel surface. From detailed SEM observations, it became evident that as SO_2 content in the system increased, the relative ratio between hydrated $FeSO_3$ and $FeCO_3$ on the steel surface became much greater. Interestingly, the formation of crystalline $FeSO_3$ was observed using XRD with 100 ppm SO_2 in the absent of O_2. Literature[80] also suggest that increasing the SO_2 content to even higher concentration such as 0.2 mol% (1 mol% ≈10000 ppm) completely eliminates any traces of $FeCO_3$ on the steel surface. These observations suggests that the presence of very small quantities of SO_2 has the ability to completely change the corrosion mechanism in the system. The results suggest that SO_2 has the ability to take the leading role in the corrosion process even at low concentrations.

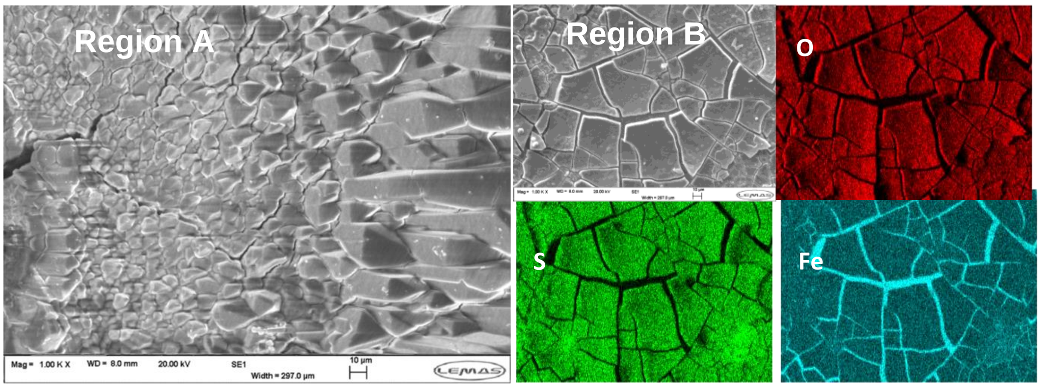

(a)

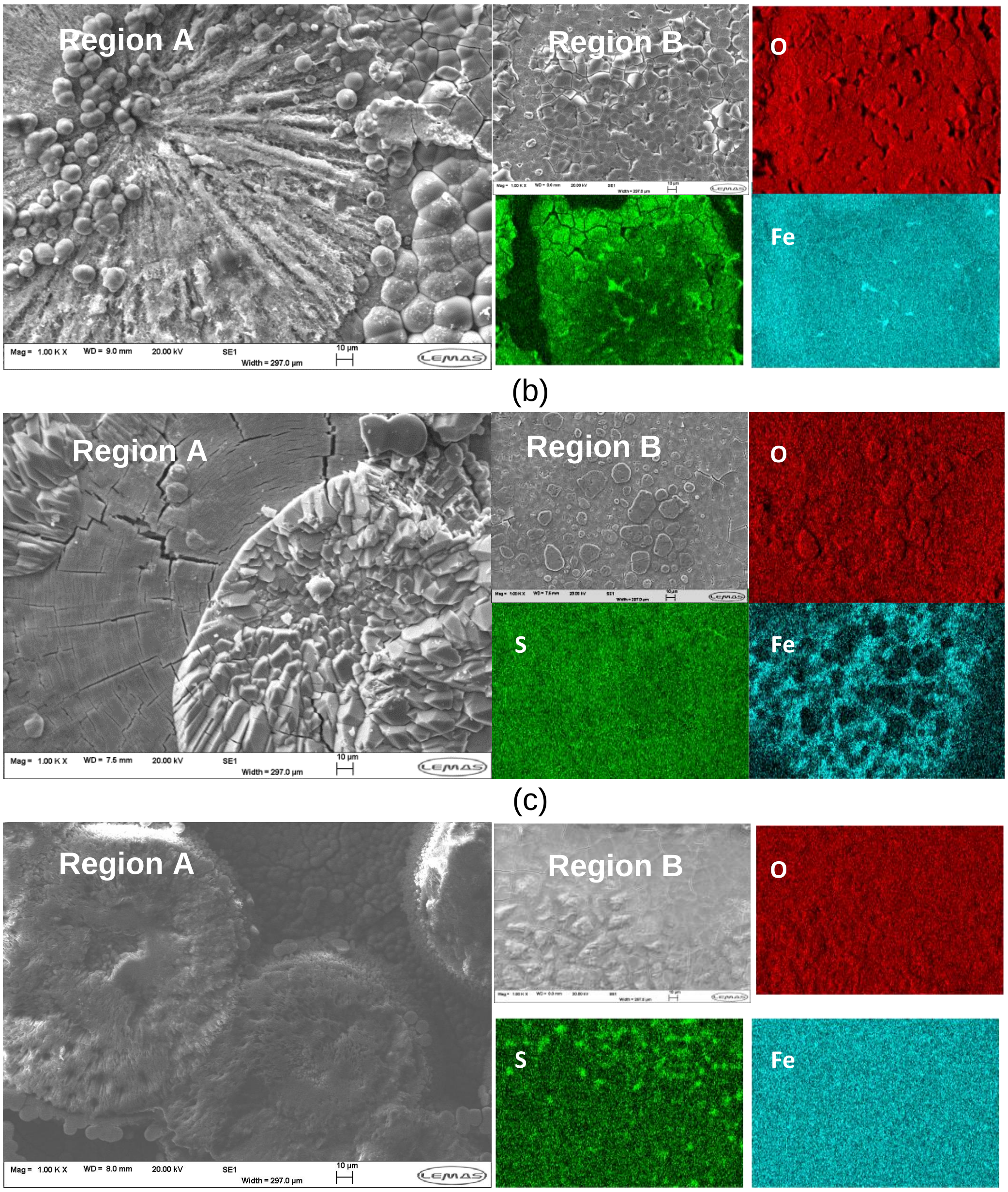

(b)

(c)

(d)

Figure 8.11: (a) SEM images and EDX maps of X65 sample surface after exposure to water-saturated supercritical CO_2 at 35°C and 80 bar containing 50 ppm SO_2 and 20 ppm O_2, indicating areas rich in iron, oxygen and sulphur, (b) SEM images and EDX maps of X65 sample surface after exposure to water-saturated supercritical CO_2 at 35°C and 80 bar containing 50 ppm SO_2 and 0 ppm O_2, indicating areas rich in iron, oxygen and sulphur, (c) SEM image of X65 sample surface after exposure to water-saturated supercritical CO_2 at 35°C and 80 bar containing 100 ppm SO_2 and 20 ppm O_2 (d) SEM image of X65 sample surface after exposure to water-saturated supercritical CO_2 at 35°C and 80 bar containing 100 ppm SO_2 and 0 ppm O_2.

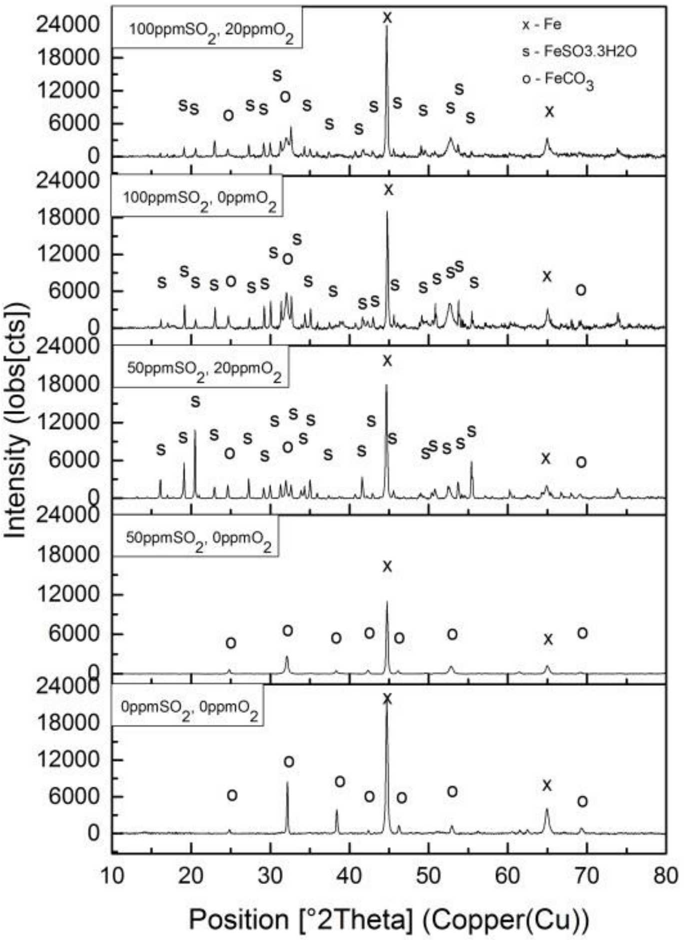

Figure 8.12: XRD spectra of samples exposed to water-saturated supercritical CO_2 phase at 35°C and 80 bar containing different concentration levels of SO_2 (0, 50 and 100 ppm) and O_2 (0 and 20 ppm) impurities.

8.2.3 Comparison of general and localised corrosion behaviour between all environments

Figure 8.13 and Table 8.2 provide examples of the profilometry measurements from samples exposed to the water-saturated supercritical CO_2 environment at 35°C and 80 bar with various concentrations of SO_2 and O_2 present in the system. The profilometry images are provided in conjunction with the general corrosion rates (from mass loss measurements) and the localised corrosion rates based on the top 10 deepest surface pits identified in alignment with ASTM Standard G46-94[24]. Figure 8.13 indicates that the localised corrosion rates are approximately one order of magnitude greater than the general corrosion rates recorded through mass loss measurements. The localised corrosion rate increases from 0.9 mm/year to 1.7 mm/year from the system containing no SO_2/O_2 to that containing 100 ppm SO_2 and 20 ppm O_2. These results to a certain extent are in alignment with the observation of Farelas et al.,[78], who performed experiments in liquid CO_2 at 25°C and 80 bar containing 650 ppm water and also observed localised corrosion rates significantly higher than the general values recorded from mass loss measurements. Mass loss measurements after 24 hours of exposure revealed general corrosion rates of 0 and 0.1 mm/year in the presence of 0.05 and 0.1% SO_2, respectively. However, implementation of surface profilometry measurement indicated localised corrosion rates of 2.4 and 6.8 mm/year, respectively. Both the work presented in this publication and the results of Farelas et al.,[78] indicated that mass loss results can be misrepresentative in terms of the threat posed to carbon steel in impurity containing dense phase CO_2.

Again, there is no significant evidence to suggest that the presence of O_2 inhibits or accelerates the level of localised attack in these particular environments at a concentration of 20 ppm.

8.3 Replenishing of Impurities and the Limitations of Closed System Testing

Regrettably, one of the issues associated with experiments in closed systems with low impurity concentrations is that significant levels of depletion can occur in the system over the course of the experiment. Dugstad et al.,[8] stated that less that 5% of the added impurities in the NO_X and SO_x experiments before the corrosion rate slows down. They also stated that the difference in impurity concentration at start up and when the experiment is terminated is considerably larger than that estimated from purely the mass loss of the steel samples. Such an observation was attributed to a multitude of factors which include immobilisation of the impurities (corrosive phase becoming trapped in dead legs) as well as reactions between different impurities in the system.

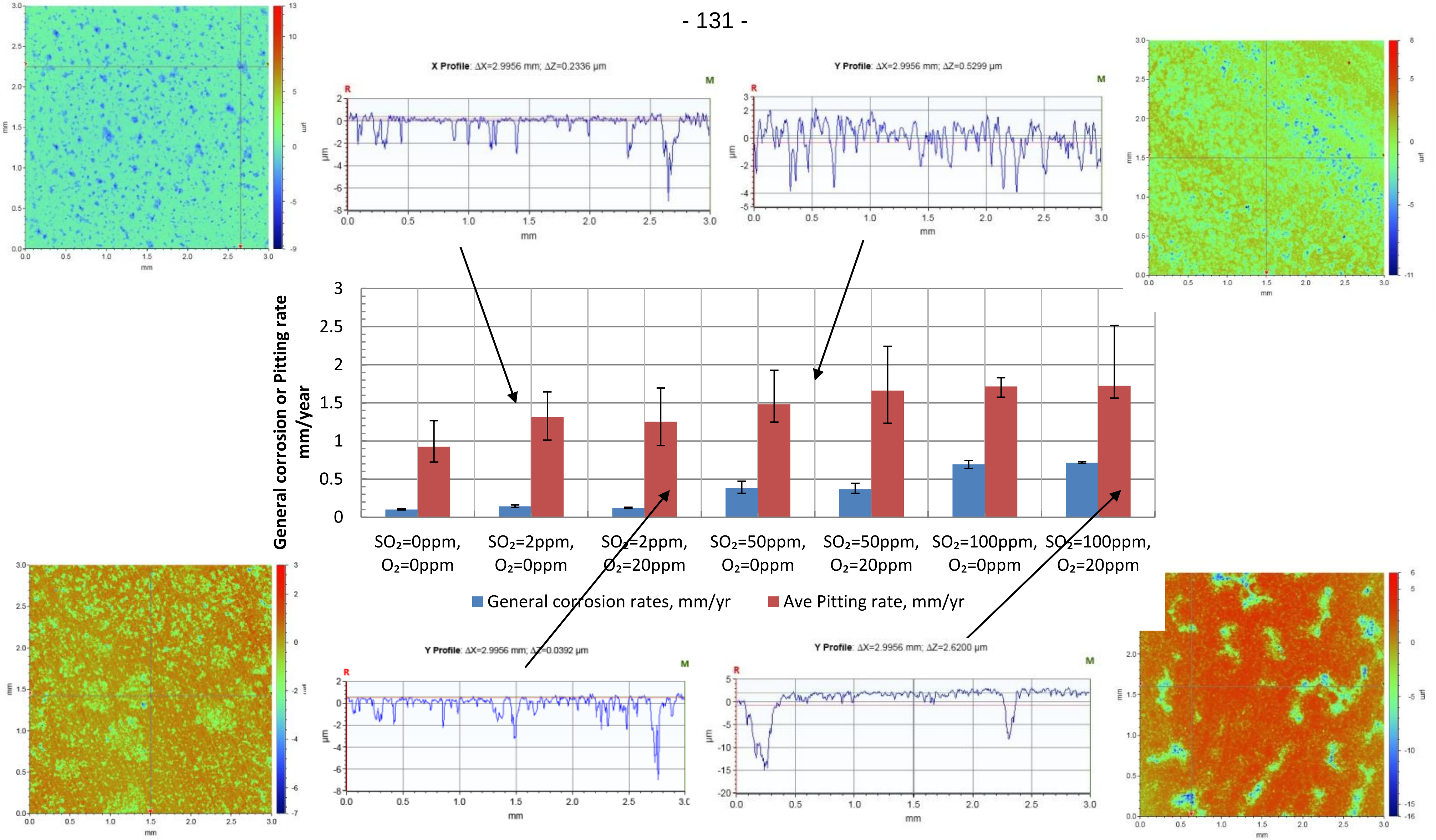

Figure 8.13: Average general corrosion and pitting rates of carbon steel in water-saturated supercritical CO_2 environments mixed with varying concentrations of SO_2 and O_2 at 35°C and 80 bar for 48 hours presented in conjunction with profilometry images of the samples.

Table 8.2: Corrosion rates of sample exposed to water-saturated CO_2 phase with SO_2/O_2 as impurity

CO_2 pressure (bar)	**O_2 content**	**SO_2 content**	**Temp (°C)**	**Test period**	**Water content (ppm in mole)**	**Corrosion Rate (mm/year)**			
						general	**SD**	**Localised**	**SD**
80 bar	0	0 ppm	35	48	Water-saturated CO_2 ~34000 ppm water added to autoclave to ensure saturation	0.09	0.011	0.92	0.399
		2 ppm				0.14	0.022	1.31	0.180
		50 ppm				0.38	0.069	1.48	0.241
		100 ppm				0.70	0.072	1.72	0.069
	20 ppm	2 ppm				0.12	0.008	1.26	0.264
		50 ppm				0.37	0.069	1.66	0.405
		100 ppm				0.72	0.014	1.72	0.282

Based on the observations of Dugstad et al.,[8] it can be questioned as to whether the conditions analysed in this work reflect the worst case scenario in terms of attack. To investigate this effect of depletion of SO_2 and O_2 concentrations during the tests, a series of tests performed in the previous section were extended to 96 hours. A selection of these tests were left for 96 hours, whilst other tests the solution was evacuated and replenished after 48 hours, enabling the effect of replenishing impurities on the corrosion rate to be observed.

Table 8.3 indicates the tests performed in this additional section. Again, an assessment of the corrosion products (using XRD) and the general and localised pitting behavior (using mass loss and profilometry, respectively) was performed.

8.3.1 Mass loss results

Mass loss results are provided in Figure 8.14 for carbon steel samples exposed to water-saturated supercritical CO_2 at 80 bar and 35°C with and without replenishing impurities. It is clear that replenishing the SO_2 and O_2 results in a greater corrosion rate. For the system containing 50 ppm SO_2 and 20 ppm O_2 corrosion rate increased from 0.27 to 0.39 mm/year by replenishing the solution, whilst the corrosion rate in the system containing 100 ppm SO_2 and 20 ppm O_2 increased by 30% from 0.50 to 0.65 mm/year.

Figure 8.15 provides the SEM images and EDX mapping of the samples surface exposed to water-saturated supercritical CO_2 environments with and without replenishing 50 ppm SO_2 and 20 ppm O_2 over 96 hours. Although difficult to tell from discrete SEM images, general observations of the surfaces indicated that there was very little difference in the morphology of the corrosion products on the steel surfaces, despite their being a number of different crystal structures observed on the steel surface. The EDX map of the entire surface shows high levels of sulphur are detected where the crystals formed on the surface.

In terms of the XRD analysis of the samples, an increase in relative intensity between $FeSO_3$ and $FeCO_3$ was observed as a result of replenishing the test solution. The increase in relative intensity indicates a higher quantity of $FeSO_3$ on the surface relative to $FeCO_3$. A much greater response from the XRD was observed from the sample exposed to the replenished solution, suggesting a greater quantity of corrosion product on the steel surface, which coincides to a certain extent with the increase in corrosion rate which would essentially supply more Fe^{2+} ions in to the aqueous solution for precipitation of corrosion products to occur.

Table 8.3: Test matrix for corrosion experiments

Temp. (°C)	**Pressure (bar)**	**H_2O (ppm)**	**SO_2 (ppm)**	**O_2 (ppm)**	**Immersion time (hours)**	
					Total	**Add SO_2/O_2**
35	80	Water-saturated (3437 ppm in CO_2 phase through addition of 34000 ppm water)	50	20	96	No replenished
						Replenished after 48 hours
			100			No replenished
						Replenished after 48 hours

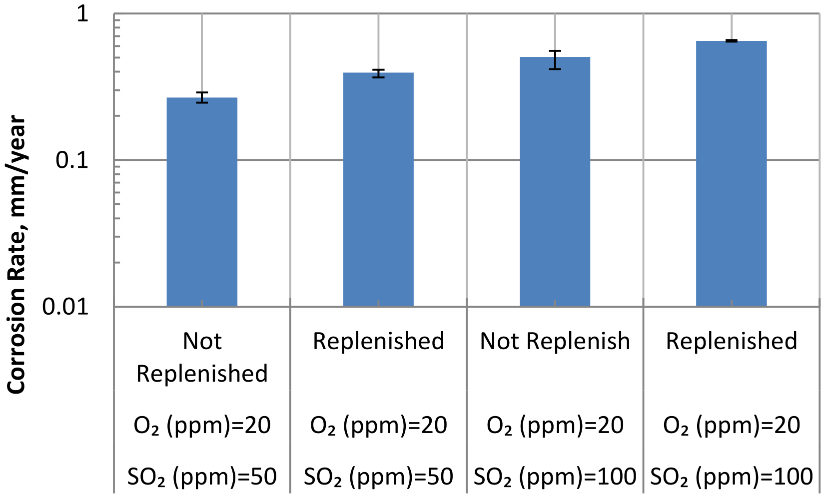

Figure 8.14: Corrosion rates of carbon steel in the water-saturated supercritical CO_2 phase at 80 bar and 35 for an exposure time of 96 hours, containing SO_2 (50 and 100 ppm) and O_2 (0 and 20 ppm), with an without impurity replenishment.

Figure 8.17 provides examples of the profilometry measurements taken from the samples exposed to the water-saturated CO_2 environment at 35°C and 80 bar containing various concentrations of SO_2 and O_2 with and without replenishing the impurities over 96 hours. The profilometry images are provided along with the general corrosion rates in Figure 8.18 (from mass loss measurements) and the localised corrosion rates based on the top 10 deepest surface pits identified (from surface profilometry).

Figure 8.18 and Table 8.4 indicate that the localised corrosion rates in the presence of 50 ppm SO_2 and 20 ppm O_2 over 96 hours increase on average as a result of replenishing the test fluid. Changing the solution after 48 hours resulted in average pitting rates of 1.3 mm/year in contrast to 1.0 mm/year. Similar observations occurred in the system containing 100 ppm SO_2 and 20 ppm O_2 where an increase from 1.1 to 1.5 mm/year was recorded through changing the solution. However, it is important to note that although the maximum and average pit depths as a result of solution replenishment did increase, the error bars in pit depths across the top 10 deepest pits do overlap, indicating this may not be a significant difference in pitting rate.

What is evident, is the significant difference in general corrosion rate between the two systems which clearly demonstrate the limitations of implementing a closed system to obtain reliable quantitative corrosion rate data relating to the transport of impurity-containing supercritical CO_2.

When comparing the 96 hour tests where the solution is replenished in Figure 8.18 with those of the 48 hour experiments in Figure 8.7, the results show no significant change in general corrosion rate between 48 and 96 hours, with the corrosion rates stable at 0.37-0.39 and 0.65-0.70 for the 50 ppm and 100 ppm SO_2 tests, respectively. However, when considering the tests where the solution is not replenished, the results indicate that the general corrosion rates reduce by around half between 48 and 96 hours, which is not the case according to the solution replenished experiments. These results give the perception that the $FeSO_3$/$FeCO_3$ film is offering significant protection to the steel surface, where in reality, very little protection appears to be offered by the $FeSO_3/FeCO_3$ layer based on the replenished fluid experiments.

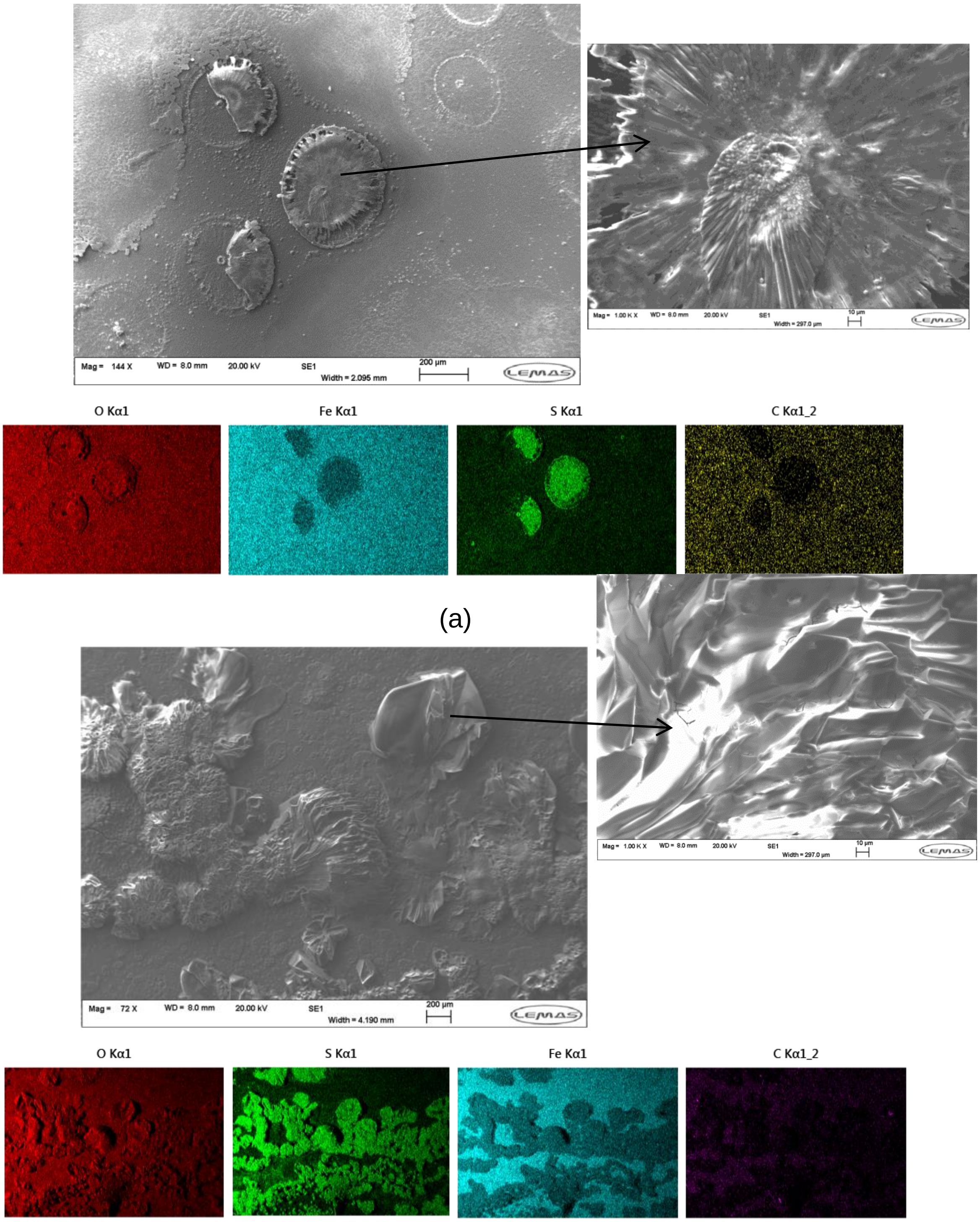

(a)

(b)

Figure 8.15: SEM/EDX images of the corroded samples exposed to water-saturated supercritical CO_2 at 35°C and 80 bar (a) without and (b) with replenishing 50 ppm of SO_2 and 20 ppm of O_2 for 96 hours after 48 hours.

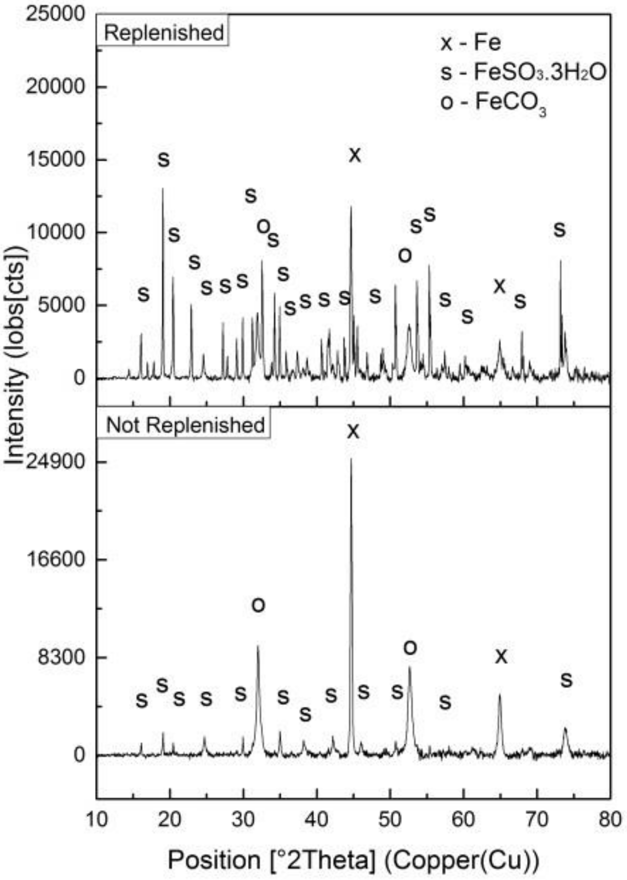

Figure 8.16: XRD spectra of samples exposed to water-saturated supercritical CO_2 phase at 35°C and 80 bar for 96 hours with and without replenishing 50ppm of SO_2 and 20ppm of O_2 after 48 hours.

Interestingly, comparing pitting rates in Figures 8.13 and 8.18, considering the average and maximum pit depths recorded, the pitting rate reduces as a function of time regardless of whether the system fluid is replenished or not.

8.4 Results of Sample Exposed to Water-Containing Supercritical CO_2 Phase at Different SO_2 Contents

In section 8.1, 8.2 and 8.3, it is noting that if the water content within the CO2 steam exceeds the solubility limit a separate aqueous phase will exist, including corrosion. According to Dugstad et al.,[8], 500 ppm tends to be the accepted limit in literature, although little reasoning exists behind this specific value. Kinder Morgan set a concentration limit of approximately ~600 ppm[76], whereas Weyburn dehydrate the CO_2 stream down to 20 ppm and the pipelines at Sleipner transport water-saturated CO_2[90]. Consequently, the research presented in this section has two key goals; firstly, to determine the influence of SO_2 contents typical of the CO_2 stream on the susceptibility of carbon steel to corrosion in supercritical environments both under-saturated and saturated with water, SO_2 and O_2; and secondly, to determine the role that SO_2 content plays on influencing the 'critical' water content where below which, no appreciable levels of corrosion are observed. The complete matrix of tests performed within this project is provided in Table 8.3, outlining the variations in water content that were also assessed.

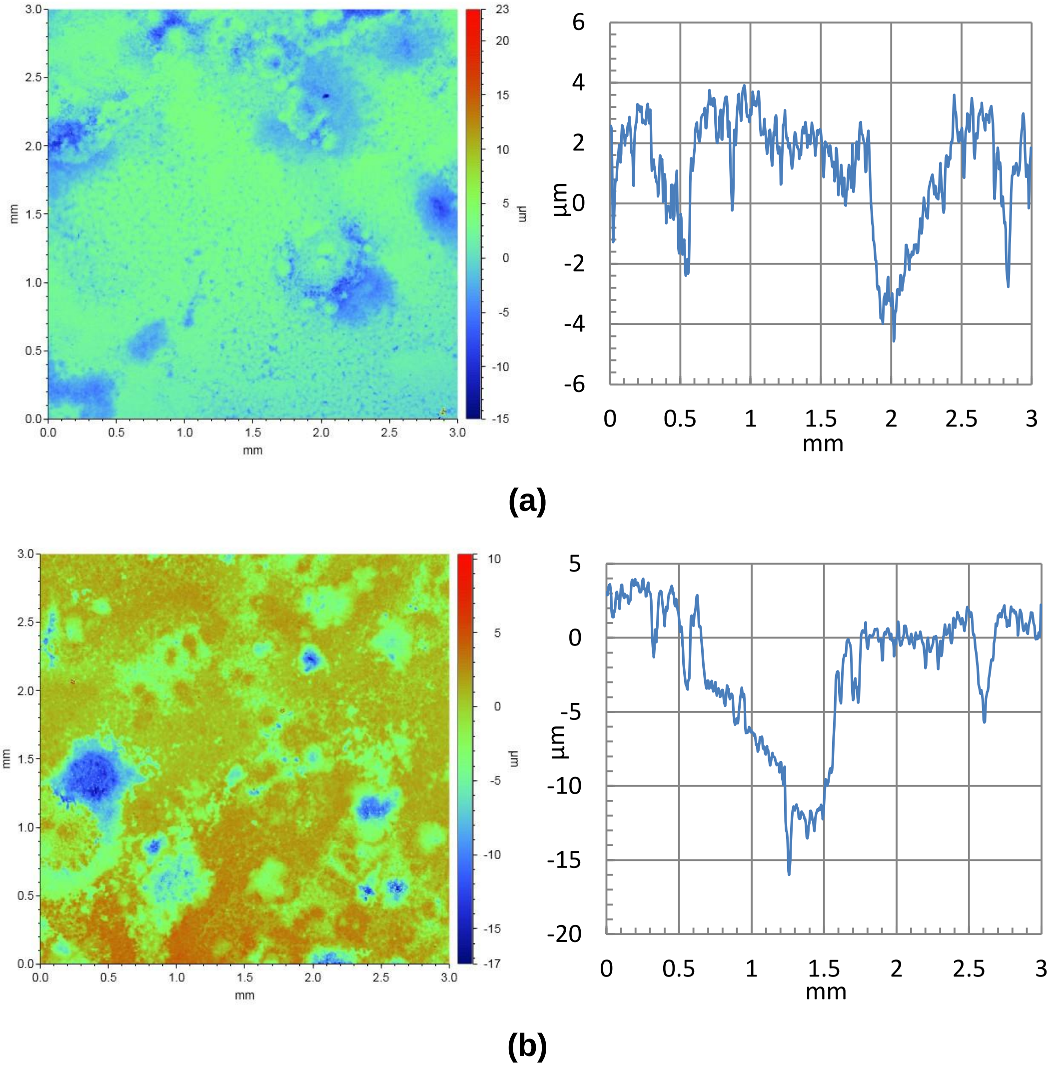

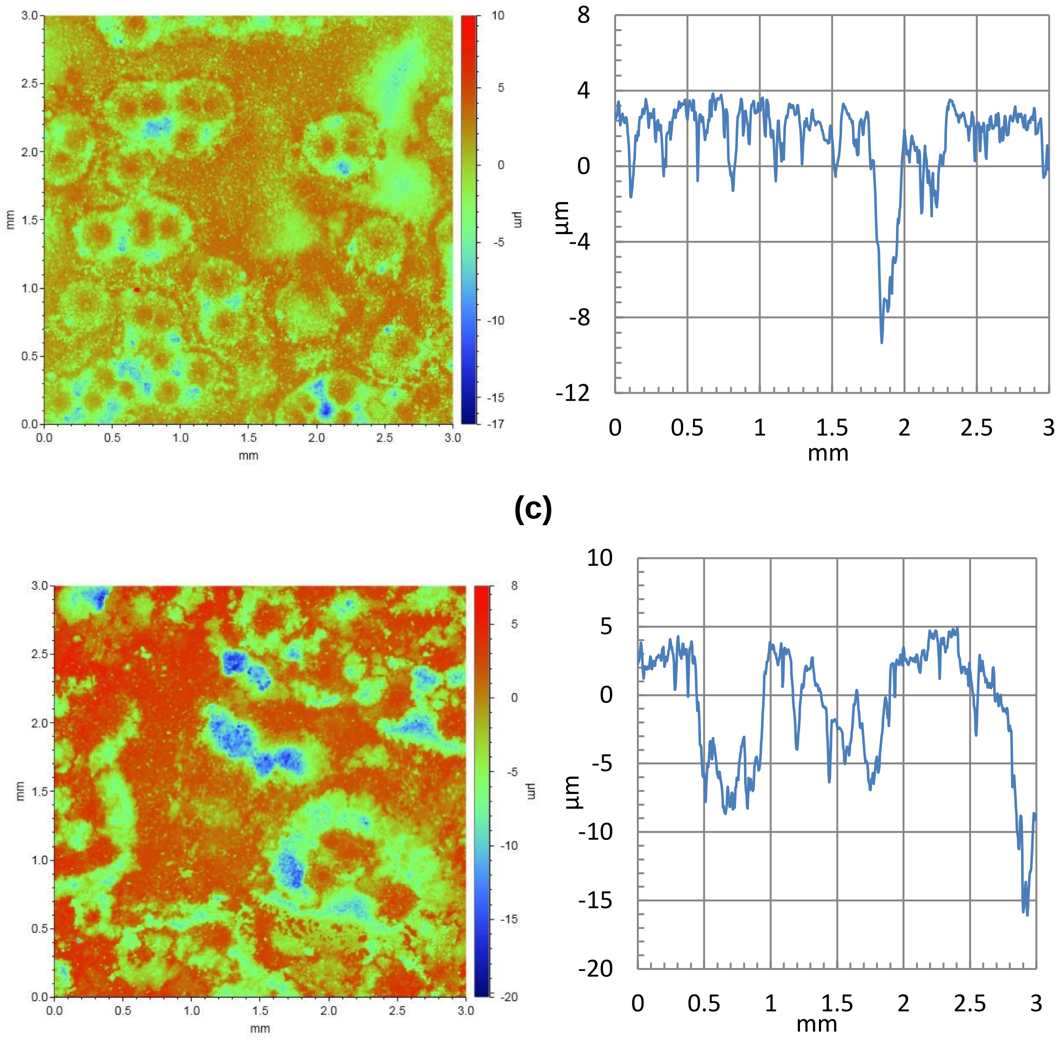

(c)

(d)

Figure 8.17: 3D and 2D profilometry images of X65 carbon steel exposed to water-saturated supercritical CO_2 environments containing varying concentrations of SO_2 and O_2 at 35°C and 80 bar for 96 hours with or without replenishing solution after 48 hours (a) 50 ppm SO_2 and 20 ppm O_2 – solution not replenished (b) 2 ppm SO_2 and 20 ppm O_2 – solution replenished (c) 50 ppm SO_2 and 20 ppm O_2 - solution not replenished and (d) 100 ppm SO_2 and 20 ppm O_2 – solution replenished

8.4.1 Mass loss results

Figure 8.19 shows the measured corrosion rates of samples exposed to the water-saturated supercritical CO_2 phase in comparison to the under-saturated conditions at 35°C and 80 bar mixed with 0, 50 and 100 ppm of SO_2 and 20 ppm of O_2 for immersion times of 48 hours. From Figure 8.19, it is clear that corrosion is observed at every concentration of water considered at 35^{o}C, whereas the corrosion rates were very small below a water content of 700 ppm at 35^oC in all the tests considered (<0.005 mm/year). The tests at 35^oC shown that when the water content is close to the maximum set in the US of between 500 and 650 ppm, averaged corrosion rates can reach 0.005 mm/year with water, SO_2 and O_2 present as the impurities. From this perspective, the molar concentration limit of 500 or 650 ppm[8] would not be sufficient to completely prevent corrosion in the system at 35^oC, although general corrosion rates would be very small in such circumstances (i.e. below 0.005 mm/year). As the quantity of water in the system was increased up to 1770 ppm, corrosion rates became greater. Based on the mass loss results in Figure 8.19, the general corrosion behaviour from a corrosion rate of 0.1 mm/year (without SO_2 and O_2) to a relatively higher corrosion rate of over 0.37 mm/year (50ppm of SO_2 and 20 ppm of O_2), then increased up to 0.71 mm/year (100ppm of SO_2 and 20 ppm of O_2) in water-saturated supercritical CO_2 phase.

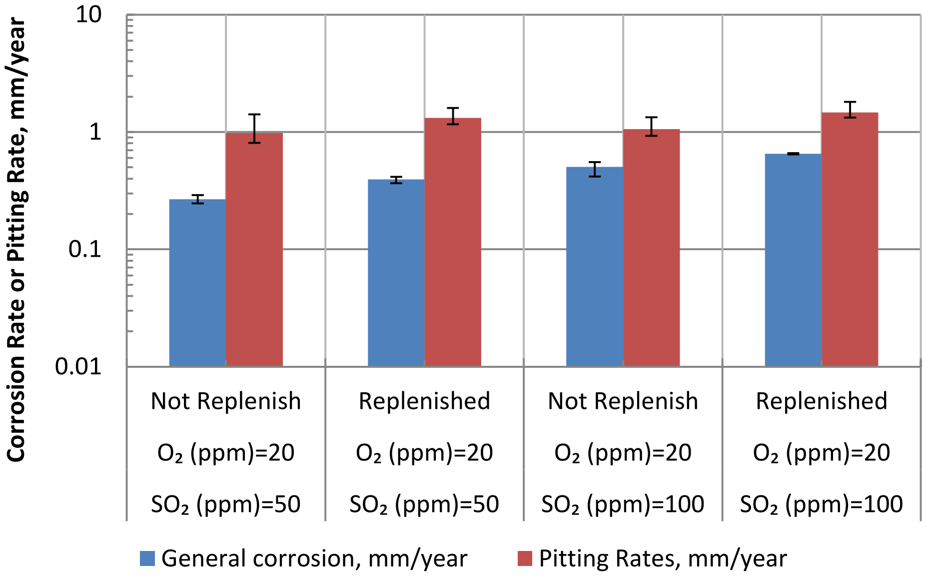

Figure 8.18: Average localised corrosion rates of carbon steel in water-saturated supercritical CO_2 environments with replenishing different level of SO_2 and O_2 at 35°C and 80bar in conjunction with average general corrosion rates.

Table 8.4: Corrosion rates of samples exposed to water-saturated supercritical CO_2 phase containing SO_2 (50 and 100 ppm) and O_2 (0 and 20 ppm), with or without impurity replenishment.

CO_2 pressure (bar)	**O_2 content**	**SO_2 content**	**Temp (°C)**	**Water content (ppm in mole)**	**Temp (°C)**		**Corrosion Rate (mm/year)**			
					Total	**Add SO_2/O_2**	**general**	**SD**	**Localised**	**SD**
80 bar	20 ppm	50	35	Water-saturated CO_2 ~34000 ppm water added to autoclave to ensure saturation	96	No replenished	0.266	0.022	0.981	0.169
						Replenished after 48 hours	0.395	0.026	1.318	0.128
		100				No replenished	0.504	0.075	1.057	0.142
						Replenished after 48 hours	0.651	0.008	1.468	0.155

8.4.2 Analysis of corrosion product morphology and composition

Figure 8.20 presents the scanning electron microscopy (SEM) images of the corroded X65 steel samples exposed to a selected number of conditions tested in the matrix in Table 8.5. Images of the steel surface exposed to 700 ppm water showed minimal signs of corrosion on the steel surface. As water content increased, the quantity of visible corrosion product became noticeably larger.

In the system exposed to supercritical CO_2 without the presence of SO_2 or O_2, an increase in water content resulted in the formation of cubic crystals on the steel surface. These crystals were confirmed as $FeCO_3$ through the implementation of XRD in Chapter 7.

Table 8.5: Test matrix for corrosion experiments

Under-saturated CO_2					
Temperature (°C)	**Pressure (bar)**	**H_2O (ppm)**	**SO_2 (ppm)**	**O_2 (ppm)**	**Immersion time (hours)**
35	80	Water-saturated (3437 ppm in CO_2 phase through addition of 34000 ppm water)	0, 50, 100	20	48
		1770			
		1200			
		700			
		300			

The introduction of 50/100 ppm SO_2 and 20 ppm O_2 into the system resulted in the corrosion product morphology on the steel surface changing dramatically. The presence of SO_2 initiated the formation of a thin, sulphur-containing compound (Figures 8.20 (e), (f), (h) and (i)) across the steel surface, whilst at higher water contents, the presence of columnar crystals were also observed (Figures 8.20 (f) and(i)) which also possessed a high sulphur content. The XRD spectra for the sample exposed to the water-saturated environments containing 50 and 100 ppm SO_2 provided in Figure 8.21 confirmed that the sulphur-containing crystals were hydrated iron sulphite ($FeSO_3{\cdot}3H_2O$). The presence of $FeCO_3$ was also detected on the steel surface, and such crystals proved to locate on the surface using a combination of SEM, XRD and Raman spectral in Figure 8.20, 8.21 and 8.22.

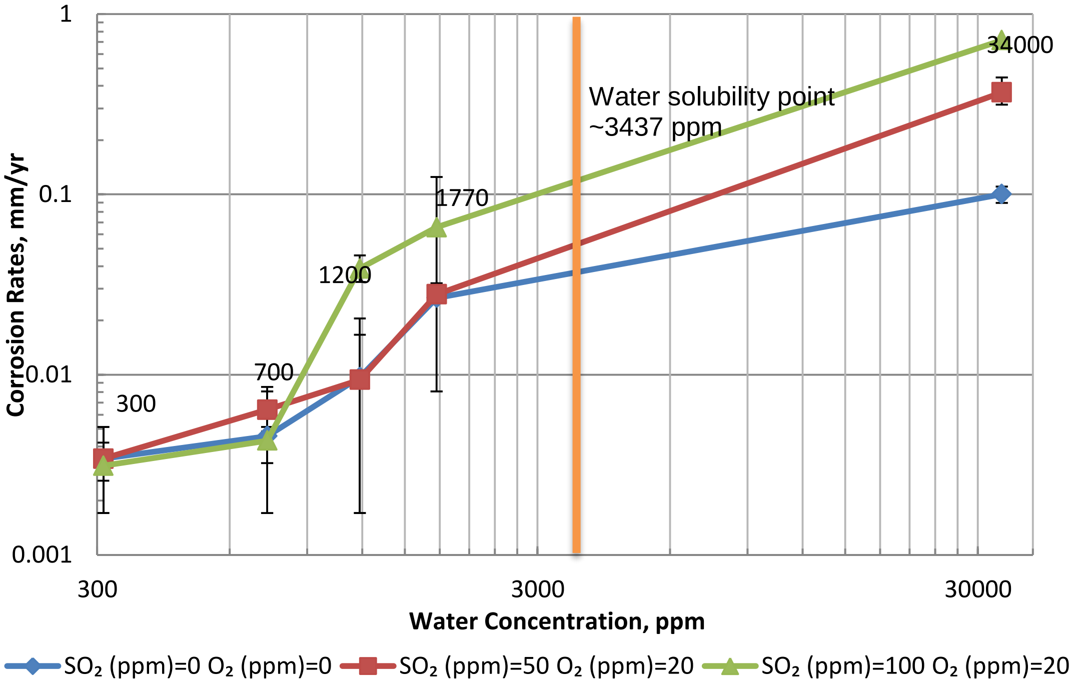

Figure 8.19: Corrosion rates of carbon steel in the water under-saturated supercritical CO_2 phase at 80 bar and temperatures of 35°C and at test durations of 48 hours. SO_2 in the gas phase are approximately 0, 50 and 100 ppm and O_2 is 20 ppm.

The use of localised Raman spectroscopy at specific locations on the steel surface (Figure 8.22(a)) confirmed that the globular crystals were $FeCO_3$ and that the columnar crystals were $FeSO_3{\cdot}3H_2O$(Figure 8.22(b)). The strongest Raman peak observed at 1085 cm^{-1} over the globular crystals in Figure 8.22(a) is representative of $FeCO_3$. Other peaks corresponding to the CO_3^{2-} are located at 735 cm^{-1} and 1500 cm^{-1}.

The strongest Raman peak observed from the scan over the globular crystals exists at 954 cm^{-1} for crystal $FeSO_3$ and the vibrational wavenumbers between ~3200 and 3400 cm^{-1} are related to the degree of hydration. Such $FeSO_3$ crystals are consistent with Choi et al.,[15] who performed carbon steel exposed to water-saturated CO_2 containing 1% (1% ~ 10000 ppm) SO_2 at 50°C and 80 bar. They found the presence of $FeSO_3$ on the surface using Raman spectroscopy. The tests performed here have shown that the lower SO_2 content (50 and 100 ppm) used in this study resulted in the co-presence of $FeCO_3$ and $FeSO_3.3H_2O$ on the steel surface.

8.4.3 Localised corrosion rates

Figure 8.23 and Table 8.6 provide examples of the profilometry measurements taken of the samples subjected to the water-containing supercritical CO_2 at 35°C and 80 bar along with the localised corrosion rates.

Figure 8.24 plots the overall results shown that localised corrosion rates can become appreciably high (in excess of 1 mm/year) if enough water is present in the system, even in the absence of SO_2/O_2.

In all three environments evaluated, corrosion rates exceeded 0.1 mm/year at a water content of 700 ppm. Only tests performed at 0 and 300 ppm water produce no measureable localised attack on the steel surface. Interestingly, the most significant increase in pitting rate was observed between 1200 and 1770 ppm, whilst the largest increase in general corrosion was from 1770 ppm to water-saturated conditions.

8.4.4 Consumption of impurities

One final point to note is that one of the issues associated with experiments in closed systems with low impurity concentrations is that significant levels of depletion can occur in the system over the course of the experiment. Based on the assumption that 1 mole impurity (water or SO_2) reacts with 1 mole Fe, the consumption of impurities can be estimated from the sample corrosion rate. In terms of estimating the consumption of SO_2, the calculation requires the assumption that all corrosion is attributed to SO_2 and not carbonic acid. With this in mind, the rate of consumption of SO_2 and water is shown in Figure 8.25.

Figure 8.25 indicates that significant consumption of the SO_2 occurred in tests where the water content was high (high corrosion rates). This poses the distinct possibility that the corrosion rates recorded from mass loss measurements and surface profilometry did not provide a ‘worst case scenario’ corrosion rate in terms of CO_2 pipeline transportation.

As water content is reduced, the reduction in corrosion rate of the X65 steel results in the calculated loss of SO_2 in the system declining significantly. Below a water content of 700 ppm, the consumption of SO_2 was below 3%. Therefore, confidence can be held in the accuracy of the critical water contents established to minimise localised corrosion as at low water contents, the level of depletion of impurities is considerably lower.

In a publication by Dugstad et al.,[91] it was stated that the actual consumption of impurities had been studied in autoclave experiments by IFE. They suggested that typically, the consumption of less than 5% impurities was sufficient to influence the corrosion rate. Consequently, understanding the consumption of impurities in closed systems is imperative in order to define acceptable CO_2 specifications with the utmost confidence.

8.5 Summary

In this chapter, the corrosion behaviour of X65 carbon steel was evaluated in water-containing supercritical CO_2 environments containing various concentrations of SO_2 (0-100 ppm) and O_2 (0-20 ppm) representative of CO_2 transport in CCS. Findings in this section can be summarised into the following:

- The presence of 20 ppm oxygen did not significantly change the degradation rate in all the tests considered.
- The presence of 2 ppm SO_2 is capable of influencing the degradation process and changing $FeCO_3$ morphology.
- Increasing SO_2 up to 50 and 100 ppm with 20 ppm O_2 resulted in presence of $FeSO_3.3H_2O$ on the steel surface in conjunction with $FeCO_3$.

- As SO_2 concentration increased, the ratio of $FeSO_3$ to $FeCO_3$ also increased.
- The quantity of O_2 in the system was not substantial enough to cause an appreciable level of formation of crystal $FeSO_4$.
- The localised attack became more prominent with increasing SO_2 and water content.
- The localised corrosion rate was an order of magnitude greater than the general corrosion rate calculated from mass loss measurement.
- In under-saturated tests at 35^{o}C and 80 bar, a measureable general corrosion rate was recorded for 300 ppm water addition at 35^{o}C (0.003 mm/year) in the presence of SO_2 up to 100 ppm.
- In under-saturated tests at 35^{o}C and 80 bar, no localised corrosion was observed at a water content of 300 ppm and below.

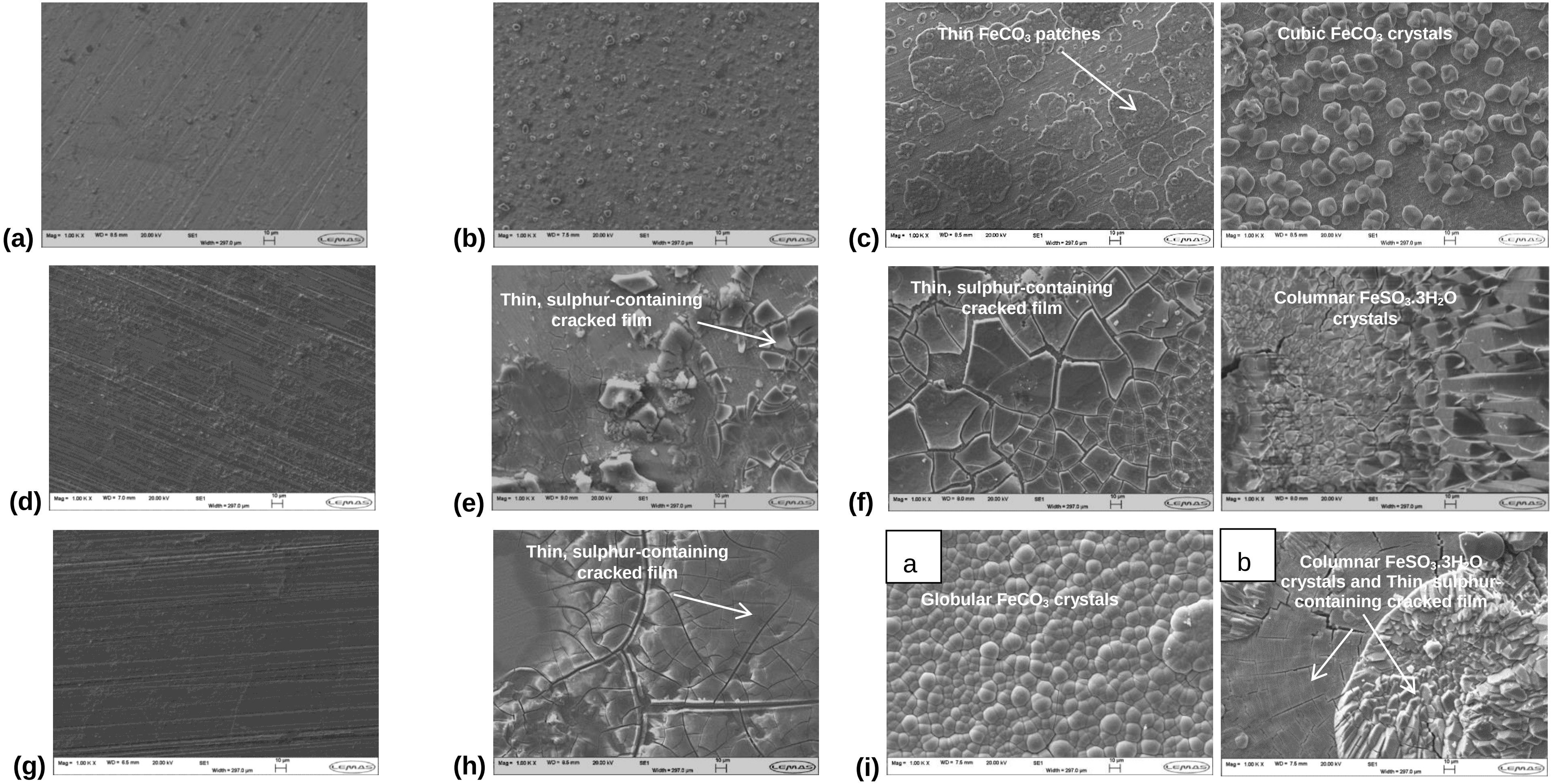

Figure 8.20: SEM images of the X65 corroded samples exposed to under-saturated and water-saturated CO_2 at 35°C and 80 bar for 48 hours in the presence of various concentrations of impurities; (a)-(c) 0 ppm SO_2 and 0 ppm O_2 in the presence of 700, 1770 and 3437 ppm (water-saturated) water, respectively; (d)-(f) 50 ppm SO_2 and 20 ppm O_2 in the presence of 700, 1770 and 3437 ppm (water-saturated) water, respectively; (g)-(i) 100 ppm SO_2 and 20 ppm O_2 in the presence of 700, 1770 and 3437 ppm (water-saturated) water, respectively.

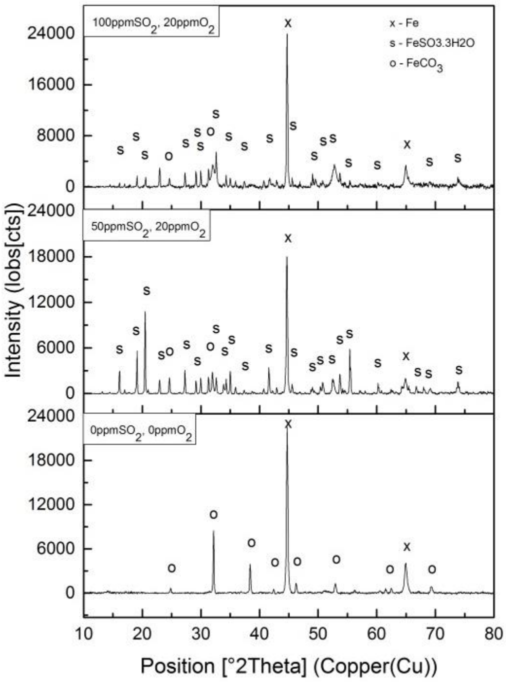

Figure 8.21: XRD spectra of samples exposed to water-saturated supercritical CO_2 phase at 35°C and 80 bar containing different concentration levels of SO_2 (0, 50 and 100 ppm) and O_2 (0 and 20 ppm) impurities.

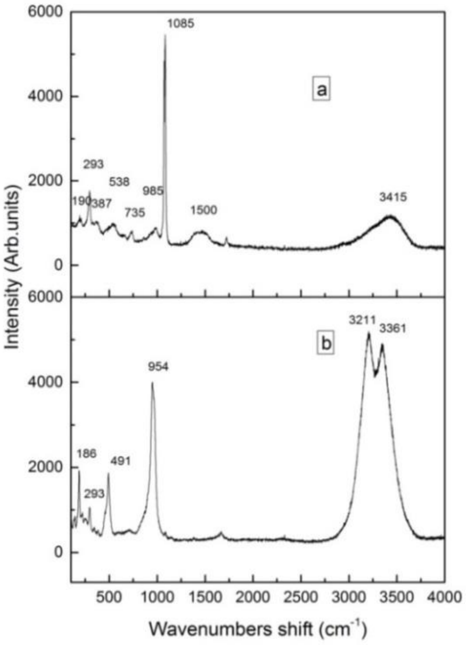

Figure 8.22: Raman spectral of samples exposed to water-saturated supercritical CO_2 phase at 35°C and 80 bar containing 100 ppm SO_2 and 20 ppm O_2 impurities according to SEM images in Figure 8.20(i, a and b).

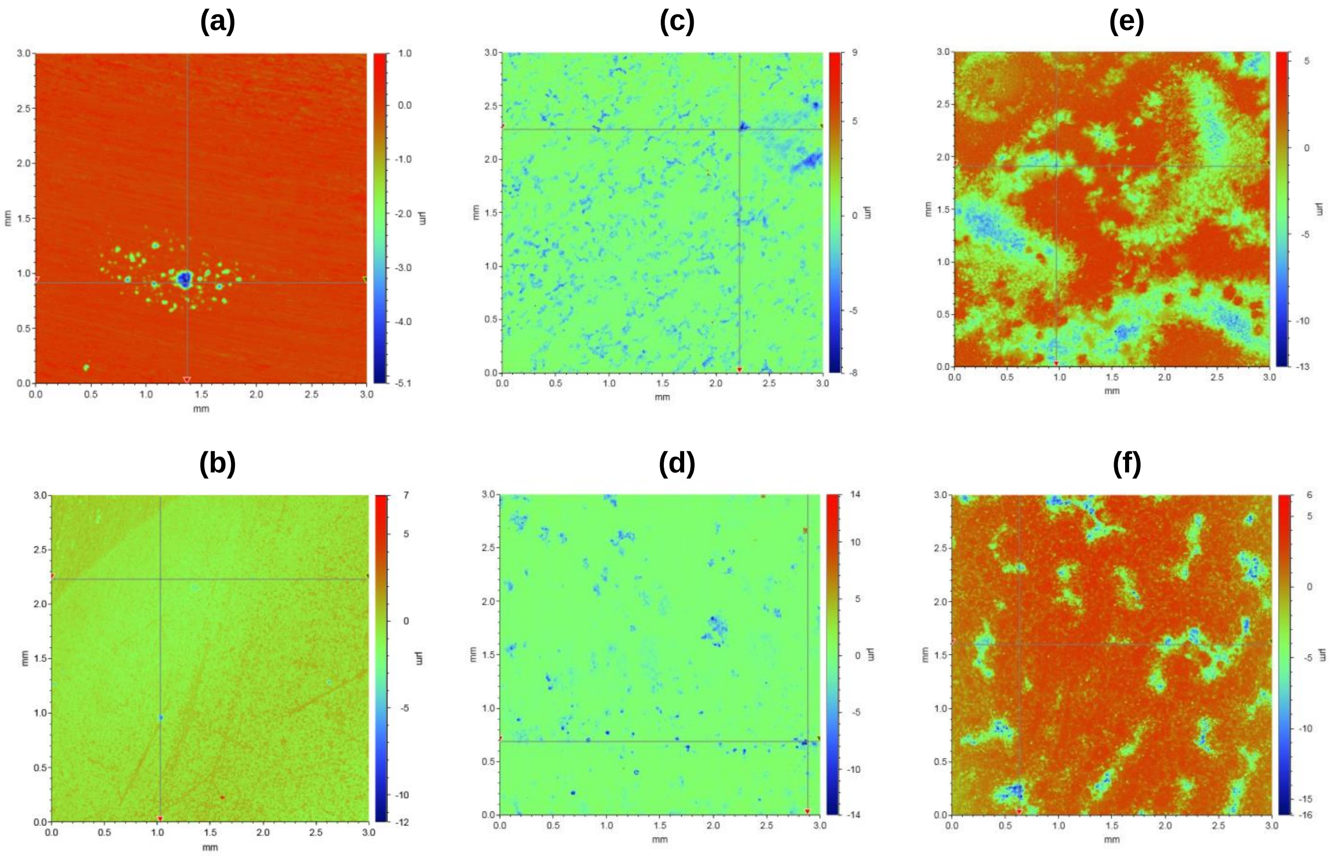

Figure 8.23: Example profilometry images of X65 steel surfaces after removal of corrosion products (a) 0 ppm SO_2, 0 ppm O_2, 1770 ppm water, (b) 0 ppm SO_2, 0 ppm O_2, water-saturated, (c) 50 ppm SO_2, 20 ppm O_2, 1770 ppm water, (d) 50 ppm SO_2, 20 ppm O_2, water-saturated, (e) 100 ppm SO_2, 20 ppm O_2, 1770 ppm water, (f) 100 ppm SO_2, 20 ppm O_2, water-saturated. All tests were performed at 35°C and 80 bar for 48 hours in supercritical CO_2.

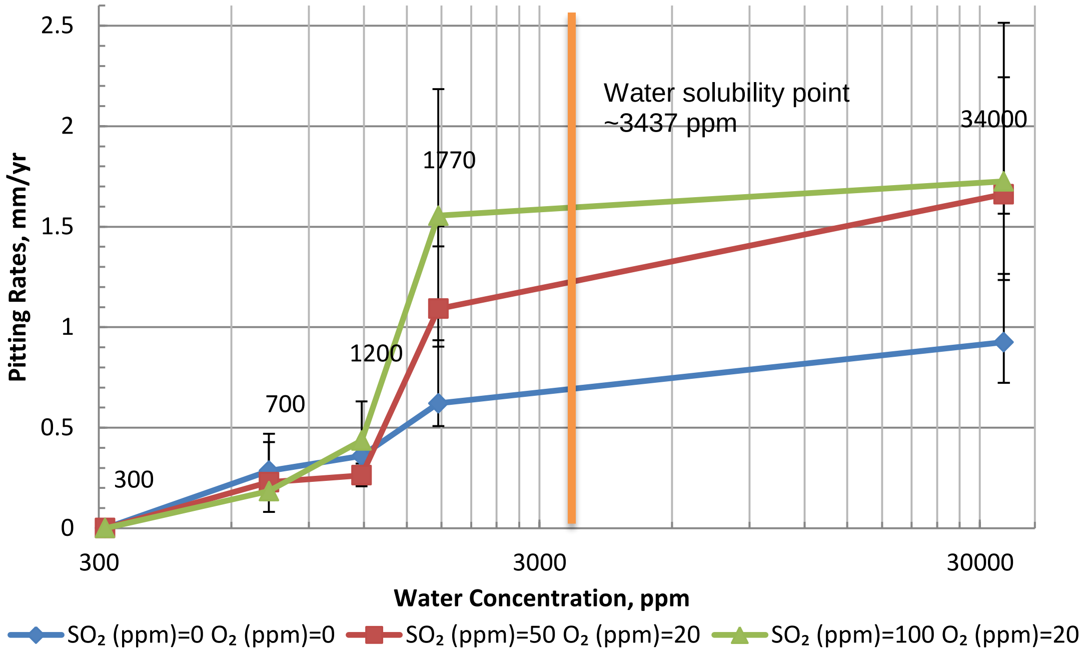

Figure 8.24: Surface profilometry images of carbon steel from water-saturated supercritical CO_2 and under-saturated supercritical CO_2 at 35°C and 80 bar with 0, 50 100ppm of SO_2 and 20ppm O_2 for 48 hours presented.

Table 8.6: Corrosion rates of sample exposed to water-containing CO_2 phase with SO_2/O_2 as impurity

CO_2 pressure (bar)	O_2 content	SO_2 content	Temp (°C)	Test period	Water content (ppm in mole)	Corrosion Rate (mm/year)			
						general	SD	Localised	SD
80	0	0	35	48	300 ppm	~0.003	0.001	0	*
					700 ppm	~0.005	0.003	~0.29	0.299
					1200 ppm	~0.01	0.009	~0.36	0.034
					1770 ppm	~0.03	0.011	~0.62	0.121
					Water saturated CO_2 (~3437 ppm)	~0.09	0.011	~0.92	0.399
	20	50			300 ppm	~0.003	0.002	0	*
					700 ppm	~0.006	0.005	~0.22	0.145
					1200 ppm	~0.01	0.007	~0.26	0.041
					1770 ppm	~0.03	0.002	~1.09	0.163
					Water saturated CO_2 (~3437 ppm)	~0.37	0.069	~1.66	0.405
		100			300 ppm	~0.003	0.002	0	*
					700 ppm	~0.004	0.001	~0.18	0.016
					1200 ppm	~0.04	0.007	~0.44	0.138
					1770 ppm	~0.07	0.051	~1.55	0.231
					Water saturated CO_2 (~3437 ppm)	~0.72	0.014	~1.72	0.282

*No measurement can be observed

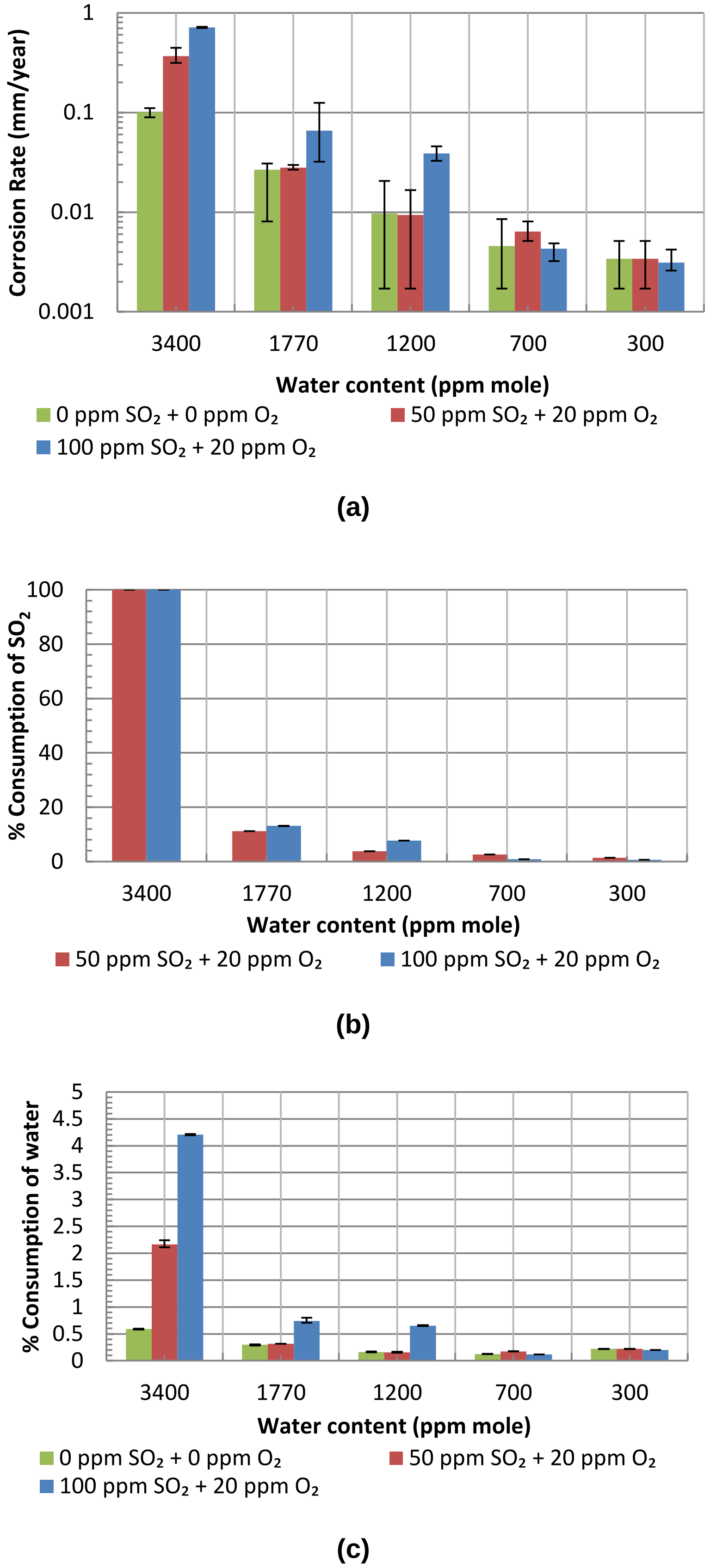

Figure 8.25: (a) General corrosion rate and rate of consumption of (b) SO_2 and (c) water under different conditions at 80 bar and 35°C.

Chapter 9 Overall Discussion

9.1 Summary

This thesis has presented an investigation into the degradation mechanisms occurring within water-containing supercritical CO_2 in the presence or absence of different levels of impurities such as SO_2 and O_2. The results highlight the importance of understanding and quantifying the general and localised corrosion rates in these systems to ensure pipeline integrity. The influence of temperature, water content, SO_2 content and surface film deposition on the general and localised corrosion have been investigated. This chapter presents an appraisal of the experimental findings in an effort to highlight the contribution of the thesis has made to the research gaps in the literature.

9.2 Nature of Corrosion Products

9.2.1 In the absence of SO_2 and O_2 environment: water as an impurity

An important finding from this work relates to the fact that not only can localised corrosion rates in supercritical CO_2 systems be more than an order of magnitude greater that general corrosion rates, but the volume of condensed water on the surface (in Figure 9.1b and 9.1c) can play a significant role in influencing the corrosion product morphology (through changing the precipitation kinetics). This appears to influence the propensity of the surface to undergo continued localised attack.

The experimental findings complement the work done by Choi et al.,[76] who presented one mechanism of corrosion attack and film formation at the surface in Figure 9.1 (a) at 50°C and 80 bar. This study has demonstrated that one similar mechanism of corrosion attack and film formation can be observed on the surface of the carbon steel samples exposed to water-saturated CO_2 at 80 bar and 50°C (Figure 9.1b). While, this work also complements that two different regions can be observed on the surface at 35°C and 80 bar in Figure 9.1c and 9.1d. This work also has investigated further to relate the corrosion product chemistry and morphology produced at each precipitation to the extent of surface attack (localised) as shown in Figure 7.6-7.9.

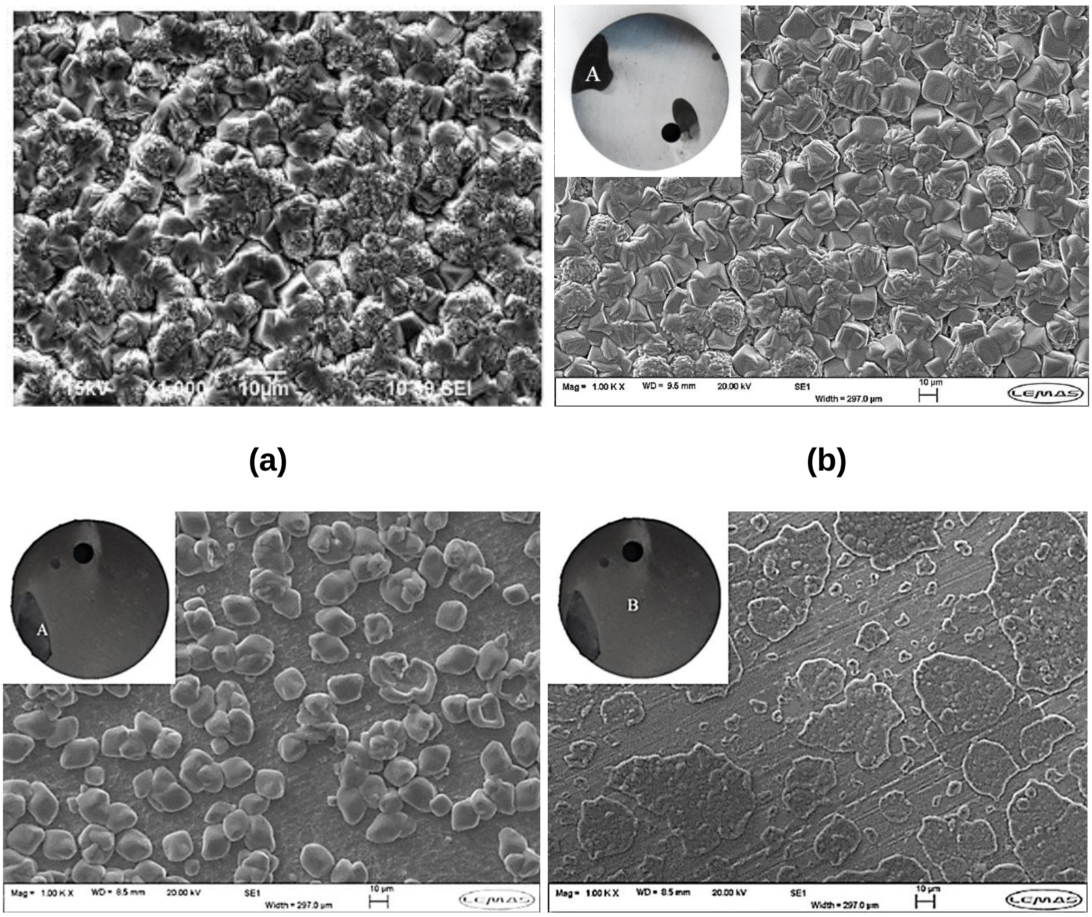

(a) **(b)**

(c) **(d)**

Figure 9.1: SEM images of the corroded samples exposed to water-saturated CO_2 at 50°C and 80 bar for (a) from Choi et al.,[2] (b) from Hua et al.,[92, 93, 94] 35°C and 80 bar for (c) – Region A (d) – Region B from Hua et al.,[92]

9.2.2 In the presence of SO_2 and O_2 environment

One of the main observations from this thesis is that whether the same corrosion product morphology and composition are produced when the SO_2 and O_2 contents are much lower than those generally reviewed in literature[14, 56, 78, 80, 90] as summarised in Table 9.1 (This work complements the literature already conducted in this area by systematically reviewing the level of localised attack in comparison to general corrosion rate measurements, reviewing the behavior of SO_2 at low concentrations (realistic in the field) similar to those recommended by DYNAMIS[7] and Alstom[91] from a health and safety perspective (i.e. from 2 ppm to 100 ppm SO_2). The finding is that not only was the combination of SO_2 and O_2 shown to influence pitting severity, the pitting rates recorded were nearly one order of magnitude greater than the uniform corrosion rate determined from mass loss measurements as shown in Figure 8.13.

9.2.2.1 Discussion of reaction mechanisms

A systematic study on the formation of the corrosion products on the surface has been investigated in this project. Both $FeCO_3$ and $FeSO_3{\cdot}3H_2O$ were both identified on the surface of the carbon steel samples exposed to the environments containing between 2 and 100 ppm SO_2 and 20 ppm O_2, whilst only $FeCO_3$ was detected on the surface without SO_2 and O_2.

As discussed by Cole et al.,[6], three series of reactions are capable within steel pipelines which transport supercritical CO_2 when water condenses onto the steel surface. These reactions are:

a) The saturation of the condensed water with CO_2, its association to produce carbonic acid and its subsequent partial homogenous dissociation in two steps to form bicarbonate and carbonate ions:

$$\mathrm{CO_{2(g)}} \leftrightarrow \mathrm{CO_{2(aq)}} \qquad (2)$$

$$\mathrm{CO_{2(g)}} + \mathrm{H_2O_{(l)}} \leftrightarrow \mathrm{H_2CO_{3(aq)}} \qquad (3)$$

$$\mathrm{H_2CO_3} \leftrightarrow \mathrm{H^+} + \mathrm{HCO_3^-} \qquad (4)$$

$$\mathrm{HCO_3^-} \leftrightarrow \mathrm{H^+} + \mathrm{CO_3^{2-}} \qquad (5)$$

a) In the next stage of reactions, the cathodic reaction can occur either by direct reduction of hydrogen ions, or the reduction of carbonic acid or carbonate ions:

$$2H^+ + 2e^- \leftrightarrow H_2 \quad (6)$$

$$2H_2CO_3 + \ 2e^- \rightarrow H_2 + 2HCO_3^- \quad (7)$$

$$2HCO_3^- + \ 2e^- \rightarrow H_2 + 2CO_3^{2-} \quad (8)$$

b) The final stage is the anodic dissolution of iron:

$$Fe \rightarrow Fe^{2+} + 2e^- \quad (9)$$

Which can be followed by the precipitation of $FeCO_3$ via a one stage reaction with carbonates, or via a two stage reaction with bicarbonates:

$$Fe^{2+} + CO_3^{2-} \rightarrow FeCO_3 \quad (10)$$

$$Fe^{2+} + 2HCO_3^- \rightarrow Fe(HCO_3)_2 \quad (11)$$

$$Fe(HCO_3)_2 \rightarrow FeCO_3 + CO_2 + H_2O \quad (12)$$

As can be observed from the XRD analysis of the steel samples, SO_2 is capable of playing a key role in the corrosion mechanisms. The formation of $FeSO_3$ can be described by the following reactions[15, 80, 95]:

a) Firstly, SO_2 is believed[15, 80, 95] to dissolve into the condensed water film on the surface and subsequently becomes ionized:

$$H_2O + SO_2 \rightarrow H^+ + HSO_3^{2-} \quad (13)$$

$$HSO_3^{2-} \rightarrow H^+ + SO_3^{2-} \quad (14)$$

b) The cathodic reaction then occurs through the direct reduction of hydrogen ions:

$$2H^+ + 2e^- \leftrightarrow H_2 \quad (15)$$

c) The formation of $FeSO_3$ then occurs via a precipitation process:

$$Fe^{2+} + SO_3^{2-} \rightarrow FeSO_3 \tag{16}$$

$FeSO_3{\cdot}3H_2O$ was observed by both Choi et al.,[15] and Xiang et al.,[80] in SO_2 containing dense phase CO_2. Additionally, both these authors detected the presence of $FeSO_4$ on the steel surface, when O_2 was introduced into the system. Choi et al.,[15] performed tests at 80 bar and 50°C in water-saturated CO_2 containing 0.8 bar SO_2 and 3.3 bar O_2 whilst Xiang et al.,[80] conducted tests at 100 bar and 50°C in water-saturated CO_2 with the addition of 0.2-2 bar SO_2 and 1000 ppm O_2. In both instances $FeSO_4$ was detected on the steel surface.

It was suggested that the addition of O_2 not only results in an additional cathodic reaction (Equation 17), but it also enables the oxidation of sulphate ions to sulphate ions (Equation 18):

$$O_2 + 4H^{+} + 4e^{-} \rightarrow H_2O \tag{17}$$

$$2SO_3^{2-} + O_2 \rightarrow 2SO_4^{2-} \tag{18}$$

$FeSO_4$ then forms via the following reaction:

$$Fe^{2+} + SO_4^{2-} \rightarrow FeSO_4 \tag{19}$$

$FeSO_4$ was the believed by Choi et al.,[15] to undergo further oxidation to become FeOOH in the presence of O_2 in an acid regeneration process:

$$4\,FeSO_4 + 6H_2O + O_2 \rightarrow 4\,FeOOH + 4H_2SO_4 \tag{20}$$

Table 9.1: Comparison of corrosion rates of sample exposed to water-saturated CO_2 phase with SO_2/O_2 as impurity in this work with that in literature

	CO_2 pressure (bar)	**O_2 content**	**SO_2 content**	**Temp (°C)**	**Test period**	**Water content (ppm in mole)**	**Corrosion Rate (mm/year)**	
							general	**Localised**
Choi et al.,[15]	80	3.3 bar	0.8 bar	50	24 h	0 ppm	No attack	
		0	0			Water-saturated CO_2 (~3400 ppm) – 10 g water added to autoclave to ensure saturation	~0.4	Not quantify
		3.3 bar	0				~1.0	
		0	0.8 bar (1%)				~5.6	
		3.3 bar	0.8 bar (1%)				~7.0	
Xiang et al.,[80]	100 bar	1000 ppm	0.2 bar (0.2%)	50	288 h	Water-saturated CO_2 (~4600 ppm) – 6 g water added to autoclave to ensure saturation	0.2	
			0.7 bar (0.7%)				0.7	
			1.4 bar (1.4%)				0.85	
			2 bar (2%)				0.9	
Xiang et al.,[90]	100 bar	1000 ppm	2 bar (2%)	50	24 h	Water-saturated CO_2 (~4600 ppm) – 3 g water added to autoclave to ensure saturation	2.0	
					72 h		1.8	
					120 h		1.4	
					192 h		0.7	
Yong Hua et al.,[96]	**80 bar**	**0**	**0 ppm**	**35**	**48**	**Water-saturated CO_2 ~34000 ppm water added to autoclave to ensure saturation**	**0.1**	**0.92**
			2 ppm				**0.14**	**1.31**
			50 ppm				**0.38**	**1.48**
			100 ppm				**0.70**	**1.72**
		20 ppm	**2 ppm**				**0.12**	**1.26**
			50 ppm				**0.37**	**1.66**
			100 ppm				**0.72**	**1.72**

Note: 1% ≈ 10000 ppm

It is apparent that the low concentration of 20 ppm O_2 administered in these tests was not sufficient enough to form an appreciable amounts (if any) of crystalline $FeSO_4$. It has been suggested that $FeSO_3$ and $FeSO_4$ are hygroscopic salts, capable of enhancing the ability of a sample surface to retain water[80]. Such a process could potentially influence the corrosion of the steel surface, particularly if the aforementioned acid regeneration process is capable of occurring and further increases the corrosion rate.

9.3 Critical Concentration of Water

9.3.1 In the absence of SO_2 and O_2 environment

This work complements the fact that there is no general consensus on what allowable water content can be in CO_2 transported pipeline without risk of integrity issues.

The temperature plays an important role that it is important to note is that the lower temperature experiment produces the highest corrosion rate. Such a feature may be at least partially attributed to the increased quantity of water in the system as a result of the increased compressibility of CO_2 at the lower temperature. As stated previously, there is approximately double the mass of water in the CO_2 phase within the autoclave at 35°C in comparison to the test at 50°C, despite both environments containing similar molar (3437 and 3400 ppm, respectively), concentrations of water in CO_2.

Another finding is that if the water content is at or below 1600 ppm at 50^oC, then no corrosion (general or localised) will be observed. The reduction in temperature from 50 to 35^oC resulted in general corrosion being observed at a much lower water concentration of 300 ppm, but no localised attack was detected on the surface. This suggests that the current requirement for water content to be below 500 and 650 ppm in the CO_2 pipeline would be sufficient for the prevention of corrosion in the supercritical CO_2 environment that a much higher water content could be tolerated at this specific temperature (50 ^oC) and reduce the relative cost for 500 and 650 ppm should be much higher than 1500 ppm. While, the tests at 35^oC shown that when the water content is close to the maximum set in the US of between 500 and 650 ppm[5, 7] (i.e.

at 700 ppm), pitting rates can reach 0.3 mm/year. From this perspective, the water concentration limit would not be sufficient to completely prevent corrosion in the system at 35°C, although general corrosion rates would be very small in such environments (i.e. below 0.004 mm/year). A comparison of corrosion rates of samples in this work with that in literature are summarised in Table 9.2.

Table 9.2: Comparison of corrosion rates of sample exposed to water - containing CO_2 phase in this work with that in literature

	CO_2 pressure (bar)	**Temp (°C)**	**Test period**	**Water content (ppm in mole)**	**Corrosion Rate (mm/year)**	
					general	**Localised**
Choi and Nesic[76]	80	50	24 h	650 ppm	< 0.01	Not quantify
				2000 ppm		
				3000 ppm		
Dugstad et al.,[8]	100	20	30 days	(~1220 ppm)	No attack	
Dugstad et al.,[56]	100	20	14 days	488 ppm	No attack (3 rpm)	
				1220 ppm	No attack (3 rpm)	
Sim et al.,[75]	80	40	7 days	900 ppm	~0.08	~0.22
				1800 ppm	~0.07	~0.30
				2600 ppm	~0.06	~0.22
				3500 ppm	~0.08	~0.22
				Water-saturated CO_2	~0.08	~0.19
Yong Hua et al.,[92]	**80**	**35**	**48 h**	**300 ppm**	**~0.003**	**0**
				700 ppm	**~0.005**	**~0.29**
				1200 ppm	**~0.01**	**~0.36**
				1770 ppm	**~0.03**	**~0.62**
				2800 ppm	**~0.07**	**~0.85**
				Water-saturated CO_2	**~0.10**	**~0.92**
		50		**700 ppm**	**0**	**0**
				1600 ppm	**0**	**0**
				2650 ppm	**~0.014**	**~0.20**
				Water-saturated CO_2	**~0.02**	**~1.99**

Note: 1% ≈ 10000 ppm

It is worthy noting that the level of localised attack on the steel surface is over an order of magnitude greater than the general corrosion rate, showing that localised corrosion represents a real threat to the integrity of carbon steel pipelines involved in transporting water-containing supercritical CO_2 if the water content is substantial enough. In Table 9.2, Sim et al.,[75] also reviewed the influence of water content on both the general and localised corrosion rate of carbon steel in water-containing CO_2 at 80 bar and 40°C. While, a higher water contents from 900 ppm (mole) water up to water-saturated CO_2 were considered. Dugstad et al.,[91] also presented a much higher water content of 1220 ppm at 100 bar and 20°C and no corrosion attack has been observed.

9.3.2 In the presence of SO_2 and O_2 environment

Later, the critical water content was determined by adding different levels of SO_2 and O_2 with H_2O. A summary of a handful of researchers (for example, Xiang et al.,[14, 80, 90] Dugstad et al.,[56] Farelas et al.,[78] and this work) has shown in Table 9.3. The table shows that in the past no systematic study has been conducted currently in literature to attempted to establish whether the same behaviour observed (in terms of the critical water content required to induce corrosion) extends to lower impurity systems, nor has the corrosion rate been quantified through localised corrosion measurements in such environments. This study (Table 9.3) has demonstrated and compared that in literature the influence of low level of SO_2 contents (up to 100 ppm) on the susceptibility of carbon steel pipeline to both general and localised corrosion in supercritical environment with water. One important finding is that even when water content is at 300 ppm, corrosion is still recorded in all three environments containing different concentrations of SO_2. However, at this level of water content, the general corrosion rate never exceeded 0.004 mm/year based on mass loss measurements. From this perspective, the molar concentration limit of 500 or 650 ppm[5, 7] would not be sufficient to completely prevent corrosion in the system at 35^{o}C, although general corrosion rates are very small in such circumstances (i.e. approx. 0.004 mm/year).

In Table 9.3, localised corrosion has been generally neglected by other researchers; one important finding from this work is that the general corrosion rates calculated from mass loss data are not an accurate reflection that may provide inaccurate information for pipeline integrity. This study has shown that localised corrosion rates can become appreciably high (in excess of 1 mm/year) if enough water is present in the system, even in the absence of SO_2/O_2. In all three environments evaluated, the localised corrosion rates exceeded 0.1 mm/year at a water content of 700 ppm. Only tests performed at 0 and 300 ppm water produce no measureable localised attack on the steel surface. These observations suggest that the minimum water content to produce acceptable levels of general corrosion differs dramatically from that required to prevent significant localised attack.

Dugstad et al.,[56] performed long durations experiments (14 days) to evaluate the susceptibility of X-65 steel to corrosion in the presence of SO_2 (0, 100, 344 ppm) with 488 ppm and 1222 ppm of water at 100 bar and 25°C. Their findings indicated that the presence of SO_2 at concentrations as low as 100 ppm induced small levels of corrosion (~0.005 mm/year) at water contents of 488 ppm, Xiang et al.,[14] have performed a handful of key studies which have considered the influence of SO_2 content (2000-20000 ppm) on the corrosion rate of X-70 carbon steel in water-saturated supercritical CO_2 condition[14] as well as the influence of exposure time[90] and water content[80], whilst the localised corrosion was not recorded in their work as shown in table 9.3.

9.3.3 Summary

Figure 9.2(a and b) presents the extent of general and localised corrosion rates as a function of SO_2 and water content. The results show each region of attack was systematically fixed according carbon steel exposed to water-containing supercritical CO_2 environments mixed with different levels of SO_2 and O_2. The most aggressively attacked regions show in red, bad in yellow, poor in green and safe in blue were used to determine the extent of general, and localised corrosion rate through consideration of mass loss and localised depths. Both plots clearly indicate that increasing concentration of both impurities results in an increase in degradation rates. It is also clear that adhering to a maximum critical water content over a range of SO_2 concentration is more effective than limiting SO_2 content as degradation rates can still be excessive in high water contents without the presence of any SO_2.

Both Figures 9.2 (a) and 9.2 (b) show that a critical water content does exist, below which no substantial level of corrosion exists. However, it is obvious that the critical water content required to minimise localised attack is considerably lower than that to reduce general corrosion to acceptable levels.

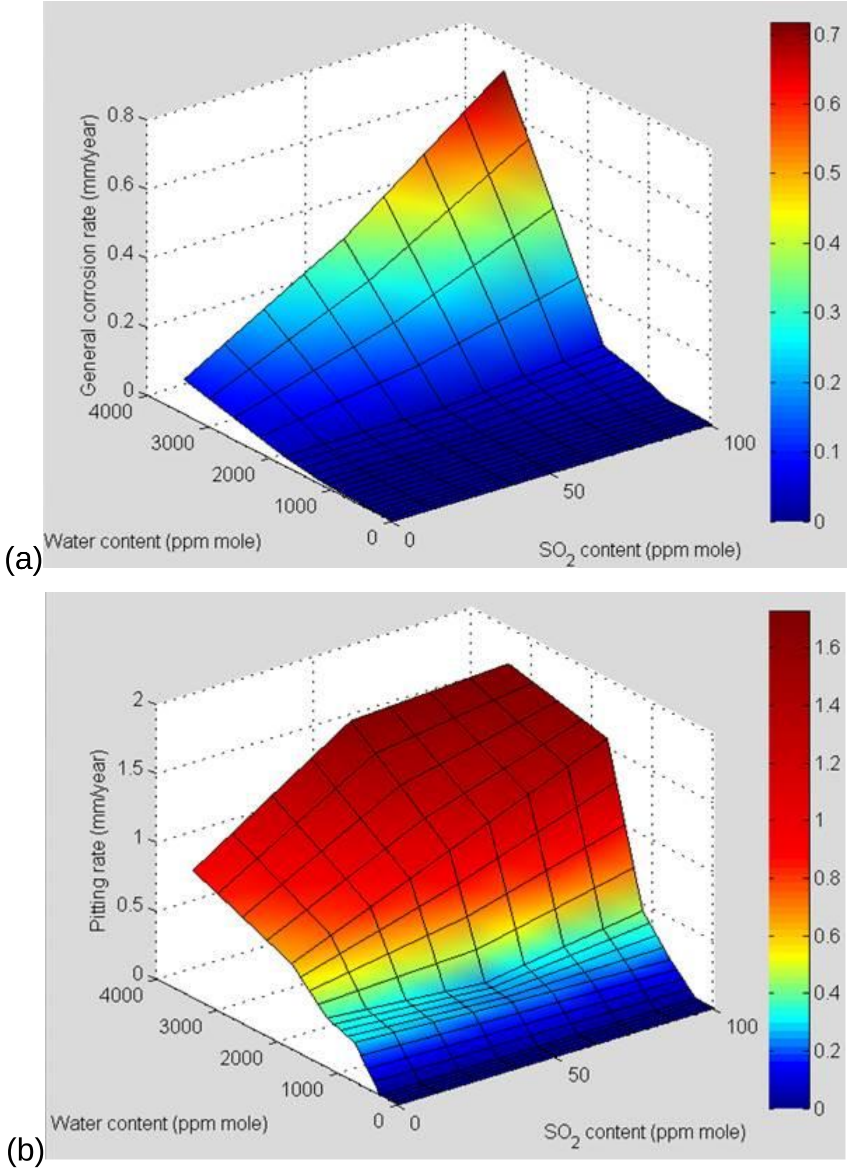

Figure 9.2: Mapping images of carbon steel from water-saturated supercritical CO_2 to under-saturated supercritical CO_2 at 35°C and 80 bar with 0, 50 100 ppm of SO_2 and 20 ppm O_2 for 48 hours presented. (a) general corrosion rates, (b) localised corrosion rates.

Table 9.3: Comparison of corrosion rates of sample exposed to water-containing CO_2 phase with SO_2/O_2 as impurity in this work with that in literature

	CO_2 pressure (bar)	**O_2 content**	**SO_2 content**	**Temp (°C)**	**Test period**	**Water content (ppm in mole)**	**Corrosion Rate (mm/year)**	
							general	**Localised**
Farelas et al.,[78]	80	0	0	50	24 h	650 ppm	0	Not quantify
			0.08 bar (0.1%)				0.03	
			0.04 bar (0.05%)				0.05	
			0.08 bar (0.1%)	25 (Liquid CO_2)			0.1	6.8
			0.04 bar (0.05%)				~0	2.4
			0.08 bar (0.1%)				~0.019	Not quantify
			0.08 bar (0.1%)				~0.013	
Xiang et al.,[14]	100 bar	1000 ppm	2 bar (2%)	50	120 h	414 ppm	~0	Not quantify
						2300 ppm	~0.04	
						2760 ppm	~0.08	
						3220 ppm	~0.35	
						4048 ppm	~0.9	
						Water saturated CO_2 (~4600 ppm)	~1.5	
Dugstad et al.,[56]	100	0	100	20	14 days	488 ppm	< 0.005	Not quantify
			344			488 ppm	< 0.005	
			344			1220 ppm	0.02	
Hua et al.,[97]	**80**	**0**	**0**	**35**	**48**	**300 ppm**	**~0.003**	**0**
						700 ppm	**~0.005**	**~0.29**
						1200 ppm	**~0.01**	**~0.36**
						1770 ppm	**~0.03**	**~0.62**
						Water saturated CO_2 (~3437 ppm)	**~0.10**	**~0.92**
		20	**50**			**300 ppm**	**~0.003**	**0**
						700 ppm	**~0.006**	**~0.22**
						1200 ppm	**~0.01**	**~0.26**

		1770 ppm	~0.03	~1.09
		Water saturated CO_2 (~3437 ppm)	~0.37	~1.66
	100	300 ppm	~0.003	0
		700 ppm	~0.004	~0.18
		1200 ppm	~0.04	~0.44
		1770 ppm	~0.07	~1.55
		Water saturated CO_2 (~3437 ppm)	~0.72	~1.72

Note: 1% ≈ 10000 ppm

Generally a corrosion rate below 0.1 mm/year tends to be quoted by industry as an acceptable level of degradation, although this is for CO_2-containing bines and for oil and gas production pipelines. Figure 9.3 considers the water content required to reduce general and localised corrosion to below 0.1 mm/year based on the trends observed on the surface plots. These values were obtained through linear interpolation between the two measurements either side of 0.1 mm/year and as such, should not be used as exact values. Nonetheless, they illustrate an important point. The critical water content required to minimise localised corrosion is significantly lower than that for general corrosion, demonstrating that evaluating pitting rates in crucial in determining the safe conditions for CO_2 transport.

Irrespective of the SO_2 concentration, the water content required to prevent significant localised attack was established at below 700 ppm. However, the critical water content to reduce general corrosion to 0.1 mm/year varied and reduced significantly from 3400 to 1850 ppm as SO_2 content was increased from 0 to 100 ppm.

It is believed that for metals in corrosive environments, a critical relative humidity exists[95, 98], above which metal corrosion rate would experience a dramatic increase. The value of the critical humidity at atmospheric pressure is believed to be around 60-70%[14] and potentially the reason behind some experts recommending an upper humidity level of 60% for supercritical CO_2 as a worst scenario[7].

The only study to consider this critical humidity in high pressure CO_2 is that performed by Xiang et al.,[14] who identified the critical relative humidity for the corrosion of X70 carbon steel in supercritical CO_2 at 100 bar and 50°C over 5 days experiments. These experiments were performed in the presence of 2% (20000 ppm) SO_2 and 1000 ppm O_2 at a rotation speed of 120 rpm. From mass loss measurements, Xiang et al.,[14] determined the corrosion rate of X70 as a function of humidity and established a very similar trend to that observed in Figure 8.19 consisting of low corrosion rates at low humidity, followed by a rapid rise once a critical water content was reached. Xiang et al.,[14] reported that the critical humidity was approximately 50-60%

based on the general corrosion rates determined from mass loss measurements. Referring back to Figure 8.19, the general corrosion rate measurements tend to agree with the observation of Xiang et al.,[14] very well, whereas the localised corrosion rates in this work investigate further and present a difference perspective by suggesting a considerably lower critical humidity (~ 15%) and Xiang et al.,[14] were not recorded in their work.

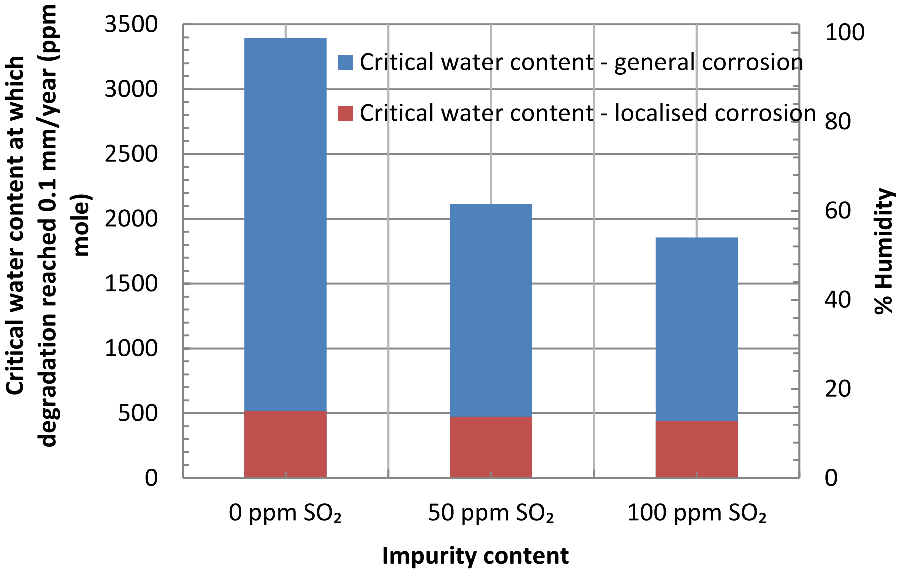

Figure 9.3: Critical water content at which 0.1 mm/year corrosion rate is reached from the perspective of general and localised corrosion for X65 steel. Conditions are 35°C and 80 bar in supercritical CO_2 for 48 hours.

9.3.4 Consumption of impurities

The validity of the results and the limitations of the test procedure are considered by performing additional tests involving the replenishment of the process fluid. Such an approach provides an appreciation for the influence of SO_2/O_2 consumption throughout the experiment. This study has suggested that the consumption of impurities influence the corrosion rates if there is enough water in the system. In the case of water-saturated environment, one of the points outlined from this is the ability for the corrosion products to offer protection to the steel substrate. It is well known from literature and proved in chapter 6 and 7 shown that $FeCO_3$ is capable of blocking active sites on the steel surface and acting as a diffusion barrier to electrochemically active species involved in the charge-transfer corrosion reaction. The ability of $FeSO_3.3H_2O$ to offer similar protection to the steel surface was suggested by Xiang et al.,[80] from their work. However, because of the gradual consumption of SO_2 and O_2 throughout the 192 hour experiment, it is difficult to ascertain whether the reduction in corrosion rate was attributed to a protective film formation. Interestingly, comparing the general corrosion rates provided in Figure 8.13 (50 and 100 ppm SO_2 over 48 hours) and Figure 8.17 (replenished tests for 50 and 100 ppm SO_2 over 96 hours), there is no observed reduction in the corrosion rate of X65 steel. These results strongly suggest that the $FeSO_3.3H_2O/FeCO_3$ corrosion products formed in this instance resulted in no significant reduction in corrosion rate. It is worth noting that longer duration tests were performed by Xiang et al.,[80] which may have enabled a thicker, more substantial, a potentially protective corrosion product to be developed.

In the case of under-saturated with water, the important finding is that no significant corrosion took place as water content is reduced (below ~500 ppm), the consumption of impurities was below 3% as shown in Figure 8.24. Therefore, confidence can be held in the accuracy of the critical water content established to minimise localised corrosion as at low water contents, the level of depletion of impurities is considerably lower. Similar work had done by Dugstad et al.,[91] the consumption of less than 5% impurities was sufficient to influence the corrosion rates. Therefore, measuring the consumption of impurities in a closed systems or flow loops is necessary in order to define acceptable CO_2 specifications with the utmost confidence.

Chapter 10 Final Conclusions and Recommendations for Future Work

The thesis presented has established a link between scientific research and an engineering issue for both general and localised corrosion rates in CO_2 transportation involve in carbon capture and storage. Based on the findings of this project, the following conclusions can be summarised chapter by chapter:

10.1 Supercritical CO_2 -Saturated Water Phase Conclusions

The corrosion behaviour of X65 carbon steel was evaluated in SC-CO_2-saturated water at 80 bar and 35, 50 and 60°C respectively, to simulate conditions of CO_2 transportation when significant amount of water enter into the pipeline. From this study, the following conclusions can be made:

- In the SC-CO_2-saturated water experiments, corrosion rates of X65 were initially high (~10 mm/year). A reduction in corrosion rate was observed with time, coinciding with the formation of an amorphous film on the steel surface and then subsequently a crystalline $FeCO_3$ film on top.

- The corrosion processes accelerate with increasing the temperature.

- The formation of the thin (~5 µm) amorphous film on the surface of the steel coincided with a reduction of the general corrosion rate.

- The formation of crystalline $FeCO_3$ observed faster at higher temperature (60°C) than that at 50 or 35°C. This dense and compact crystal layer (after 48 hours) can protect the surface to reduce the corrosion take place further.

- The results highlight the important of determining levels of localised corrosion in environments representative of CO_2 transport in CCS applications, showing that only mass loss measurements can be misleading in determining the threat posed to carbon steel transportation lines when significant water enter into the pipelines.

10.2 Water-Containing Supercritical CO_2 Phase Conclusions

The research presented has focused towards understanding the extent of both general and localised corrosion in water-containing CO_2 environments representative of CO_2 transport in CCS. Tests were conducted at a pressure of 80 bar and temperatures of 35^oC and 50^oC in both the under-saturated and saturated CO_2 phase for 48 hours to understand the effect of temperature changes on the critical water content required for corrosion to initiate. The main conclusions which can be drawn from this study are:

- In the water-saturated CO_2 environment, two very different types of corrosion behaviour were observed at temperatures of 35 and 50^oC. At 50^oC, the level attack was localised, with approximately 90% of the surface showing no signs of corrosion after 48 hours. In localised regions where corrosion occurred, precipitation of crystalline $FeCO_3$ occurred quickly, producing a compact film covering the corroded areas and reducing the rate of dissolution of the material over the exposure time. The average corrosion rate over 168 hours was recorded at just over 0.03 mm/year.

- Region A consisted of areas where comparatively larger volumes of water had condensed onto the steel surface, resulting in cubic $FeCO_3$ crystals (10 µm in diameter) forming on the steel surface, which offered little or no protection to the propagation of pits over the 168 hour test duration, despite this layer reaching a thickness of ~10 µm. Pitting corrosion rates remained constant at ~1.0 mm/year

- Conversely, Region B consisted of areas on the steel surface that were visibly discoloured, but not as dark as Region A. These areas were covered with ‘patches’ of agglomerated $FeCO_3$ crystal platelets which were stacked on top of one another in a compact structure of 2-3 µm thickness. Consequently, over the 168 hour test, a significant reduction in localised pitting rate from 0.8 to 0.3 mm/year was observed.

- It was hypothesised that the quantity of water condensed in Region B was significantly less, resulting in Fe^{2+} super-saturation of the surface droplet being exceeded faster, resulting in faster surface precipitation, and smaller crystals.
- It was also suggested from TEM images that the propagation of the $FeCO_3$ crystals in Region B initiated from a small Nano-polycrystalline region on the steel surface.
- The general corrosion rate on the steel surface was an order of magnitude less than the rate of surface pitting and reduced from 0.11 to 0.03 mm/year over the 168 hour experiment. It was suggested that the precipitation of the $FeCO_3$ onto the steel surface was responsible for the reduction in general corrosion rate on the steel surface, but it was not clear which crystal morphology/morphologies were responsible for this.
- In contrast, for water-saturated tests at 35^{o}C after 48 hours, the entire carbon steel surface was corroded and regions of more significant localised attack were visible. The precipitated crystals were less compact, offering less protection to the surface and resulting in an average corrosion rate of 0.1 mm/year over 48 hours, five times higher than that recorded at 50^{o}C.
- In under-saturated tests at 50^{o}C, no corrosion was observed at a water content of 1600 ppm and below, whilst a measureable corrosion rate was recorded for 300 ppm water addition at 35^{o}C (0.005 mm/year).
- In all tests performed, the level of localised attack was over an order of magnitude higher than the general corrosion rate calculated. The rate of pitting became more severe with increasing water content for both temperatures.

- Average pitting rates of 0.2 and 1.4 mm/year were recorded for water contents of 2650 and 3400 ppm (water-saturated) at 50^{o}C whilst average pit rates between 0.5 and 0.9 mm/year were determined between 700 and 3437 ppm (water-saturated) at 35^{o}C.

- The results reflect that the temperature drop from 50 to 35°C within the system can promote corrosion at lower water concentrations (on a molar basis) and that the level of localised corrosion can be over an order of magnitude greater than that determined as an average corrosion rate from mass loss measurements.

10.3 Water-Containing Supercritical CO_2 with Different Levels of SO_2 Phase Conclusions

This research presented has focused towards understanding the extent of both general and localised corrosion in water-containing supercritical CO_2 environments containing various concentrations of SO_2 (0-100 ppm) and O_2 (0-20 ppm) representative of CO_2 transport in CCS, paying particular attention to the influence of the different levels of SO_2 and O_2 on the corrosion behaviour. Tests were conducted at a pressure of 80 bar and temperatures of 35^{o}C for 48 hours (also, with and without replenishment of the test fluid, and different sample sizes are considered). The main conclusions which can be drawn from this study are:

- The presence of oxygen did not significantly change the degradation rate in all the tests considered, but did influence the surface morphology in the presence of 50 ppm SO_2. Introducing O_2 saw the formation of crystalline $FeSO_3$ on the steel surface. However, a seemingly amorphous sulphur-containing product was observed on the steel surface in all tests in the presence of SO_2.
- Very small quantities of SO_2 (as low as 2 ppm) are capable of influencing the degradation process and increasing corrosion kinetics.

- The quantity of O_2 in the system was not substantial enough to cause the formation of $FeSO_4$ through further oxidation of $FeSO_3$.

- Addition of 2-100 ppm SO_2 with 20 ppm O_2 resulted in presence of $FeSO_3$ on the steel surface in conjunction with $FeCO_3$. As SO_2 concentration increased, the ratio of $FeSO_3$ to $FeCO_3$ also increased. The quantity of O_2 in the system was not substantial enough to cause an appreciable level of formation of $FeSO_4$.

- Profilometry measurements indicated significant levels of localised attack on the steel surface, predominantly in the form of pitting. The attack became more prominent with increasing SO_2 and water content.
- The general corrosion rate on the steel surface was an order of magnitude smaller than the rate of surface pitting and localised attack was shown to be a fundamental consideration in the CO_2 transport systems. The extent of localised attack became more severe with increasing SO_2 content, but failed to change significantly when O_2 was introduced into the system.

- Additional tests involving changing the surface area to volume ratio indicated that the general and localised corrosion rates in the closed system tests may not reflect a worst scenario of the damage caused to CO_2 transportation pipelines.

- Additional tests involving the replenishment of the process fluid indicated that the general and localised corrosion rates in the closed system tests may not reflect a worst scenario of the damage caused to CO_2 transportation pipelines.

- In under-saturated tests at 35^oC, a measureable general corrosion rate was recorded for 300 ppm water addition at 35^oC (0.003 mm/year) in the presence of SO_2 up to 100 ppm. Average general corrosion rates of 0.004 and 0.07 mm/year were recorded for water contents of 700 and 1770 ppm at 100 ppm of SO_2, whilst average general corrosion rates between 0.005 and 0.03 mm/year were determined between 700 and 1770 ppm at 50ppm of SO_2.

- In under-saturated tests at 35^oC, no localised corrosion was observed at a water content of 300 ppm and below. Average pitting rates of 0.2 and 1.6 mm/year were recorded for water contents of 700 and 1770 ppm at 100 ppm of SO_2, whilst average pit rates between 0.2 and 1.09 mm/year were determined between 700 and 1770 ppm at 50 ppm of SO_2.

- The results also reflect that the SO_2 and O_2 concentration from 50 to 100 ppm within a closed system can increase corrosion rate at water concentrations above 1200 ppm (on a molar basis) and that the level of localised corrosion can be over an order of magnitude greater than that determined as an average corrosion rate from mass loss measurements.

10.4 Recommendation for Future Work

What is clear is that the precipitation of the compact $FeCO_3$ stacked platelets in Region B in Figure 7.5 appears to be responsible for reducing the susceptibility of the surface to localised corrosion. A reduction in pitting rate from 0.8 to 0.3 mm/year was observed between 48 and 168 hours. Conversely, the larger crystals produced in Region A appear to have no effect on the pitting rate over this part of the surface as no change in pitting rate was recorded over the 168 hours, remaining stable between 0.9 and 1.0 mm/year on average as shown in Figure 7.5. However, it is not clear whether the two different $FeCO_3$ precipitating is responsible for the reduction in general corrosion rate.

Currently, the kinetics of $FeSO_3.3H_2O$ precipitation has not been verified. More study on kinetics of $FeSO_3.3H_2O$ together with $FeCO_3$ growth and precipitation need to be conducted and how these link to the corrosion kinetics on the both general and localised scale in supercritical/liquid CO_2 environment.

This study has mainly focused on studying the SO_2/O_2/H_2O as impurities. NO_2, H_2S are also important impurities in CO_2 transport pipelines. Currently, experiments data is needed to support the variation of both general and localised corrosion rates when the presence of different level of H_2S and furthermore, to determine the minimum water concentration is required for safe CO_2 transport.

Further adjustment of the model will be done as more wide condition ranges on the corrosion rate in the presence of SO_2, O_2, H_2O, H_2S and NO_2 from water-saturated to under-saturated conditions.

This study has mainly been focused on the degradation of carbon steel (X65). It is important to conduct similar experiments on different materials such as 1Cr, 3Cr, 5Cr and 13Cr as well as analysis of the degradation and the relative to the formation of corrosion product.

Also, corrosion is one of the major issues observed in the acid gas remove involving in CO_2 capture process (for example, using amines). Absorber, trays, valves and short pipelines can be damages due to high concentration acid gas such as SO_2, NO_2, O_2, and H_2S with water. It needs more experimental data to support the industry to understand the corrosion mechanisms at the surface with different materials.

Wellbore integrity and corrosion issues with material selections in CO_2 geologic storages or enhanced oil recovery environments are also necessary.

References:

1. E. Rubin and H.D. Coninck, IPCC special report on carbon dioxide capture and storage. Prepared by working group III of the intergovernmental panel on climate change Intergovernmental Panel on Climate Change. Cambridge, UK. 2005, Cambridge, UK.
2. Y.-S. Choi and S. Nešić, Determining the corrosive potential of CO_2 transport pipeline in high pCO_2–water environments. International Journal of Greenhouse Gas Control, 2011. 5(4): p. 788-797.
3. J.D. Figueroa, T. Fout, S. Plasynski, H. McIlvried, and R.D. Srivastava, Advances in CO_2 capture technology—The US Department of Energy's Carbon Sequestration Program. International Journal of Greenhouse Gas Control, 2008. 2(1): p. 9-20.
4. A. Oosterkamp and J. Ramsen, State-of-the-art overview of CO_2 pipeline transport with relevance to offshore pipelines. Polytech Report No: POL-O-2007-138-A, 2008.
5. J. Gale and J. Davison, Transmission of CO_2—safety and economic considerations. Energy, 2004. 29(9–10): p. 1319-1328.
6. I.S. Cole, P. Corrigan, S. Sim, and N. Birbilis, Corrosion of pipelines used for CO_2 transport in CCS: Is it a real problem? International Journal of Greenhouse Gas Control, 2011. 5(4): p. 749-756.
7. E.D. Visser, C. Hendriks, M. Barrio, M.J. Mølnvik, G.D. Koeijer, S. Liljemark, and Y.L. Gallo, Dynamis CO_2 quality recommendations. International Journal of Greenhouse Gas Control, 2008. 2(4): p. 478-484.
8. A. Dugstad, S. Clausen, and B. Morland, "Transport of dense phase CO_2 in C-steel pipelines - when is corrosion an issue?", in CORROSION 2011. 2011: Houston, TX:NACE.
9. G. Heddle, H. Herzog, and M. Klett, The economics of CO_2 storage. Massachusetts Institute of Technology, Laboratory for Energy and the Environment, 2003.
10. J.M. West, "Design And Operation Of A Supercritical CO_2 Pipeline-Compression System Sacroc Unit, Scurry County, Texas". 1974.
11. T. Maldal and I.M. Tappel, CO_2 underground storage for Snøhvit gas field development. Energy, 2004. 29(9): p. 1403-1411.
12. R. Svensson, M. Odenberger, F. Johnsson, and L. StrÖmberg, Transportation systems for CO_2—application to carbon capture and storage. Energy Conversion and Management, 2004. 45(15): p. 2343-2353.
13. S.T. McCoy and E.S. Rubin, An engineering-economic model of pipeline transport of CO_2 with application to carbon capture and storage. International Journal of Greenhouse Gas Control, 2008. 2(2): p. 219-229.
14. Y. Xiang, Z. Wang, X.X. Yang, Z. Li, and W.D. Ni, The upper limit of moisture content for supercritical CO_2 pipeline transport. The Journal of Supercritical Fluids, 2012. 67: p. 14-21.
15. Y.-S. Choi, S. Nešić, and D. Young, Effect of impurities on the corrosion behavior of CO_2 transmission pipeline steel in supercritical

CO_2−water environments. Environmental Science & Technology, 2010. 44(23): p. 9233-9238.

16. P.R. Roberge, Handbook of corrosion engineering. Vol. 1128. 2000: McGraw-Hill New York.
17. K. Oldham and J. Myland, Fundamentals of electrochemical science. 1993: Elsevier.
18. J.O.M. Bockris, D. Drazic, and A.R. Despic, The electrode kinetics of the deposition and dissolution of iron. Electrochimica Acta, 1961. 4(2): p. 325-361.
19. D.C. Waard and D.E. Milliams, Carbonic acid corrosion of steel. Corrosion, 1975. 31(5): p. 177-181.
20. Y.H. Sun and S. Nesic, A parametric study and modeling on localized CO_2 corrosion in horizontal wet gas flow. CORROSION/2004, paper, 2004(380).
21. C. Lee, M. Billingham, C. Barrraclough, and D. Milanovi, "Corrosion and selection of material carbon capture and storage". 2009: UK: Intetech Ltd. p. pp. 12-50.
22. H.P. Leckie and H.H. Uhlig, Environmental factors affecting the critical potential for pitting in 18–8 stainless steel. Journal of the Electrochemical Society, 1966. 113(12): p. 1262-1267.
23. G.S. Frankel, Pitting corrosion of metals a review of the critical factors. Journal of the Electrochemical Society, 1998. 145(6): p. 2186-2198.
24. ASTM. Standard G46-94, Standard guide for examination and evaluation of pitting corrosion. ASTM International: West Conshohocken, PA, 2003.
25. S. Nešic and K.L.J. Lee, A mechanistic model for carbon dioxide corrosion of mild steel in the presence of protective iron carbonate films-Part 3: Film growth model. Corrosion, 2003. 59(7): p. 616-628.
26. N. Spycher, K. Pruess, and J. Ennis-King, CO_2-H_2O mixtures in the geological sequestration of CO_2. I. Assessment and calculation of mutual solubilities from 12 to 100°C and up to 600 bar. Geochimica et Cosmochimica Acta, 2003. 67(16): p. 3015-3031.
27. V.R. Eldik and D.A. Palmer, Effects of pressure on the kinetics of the dehydration of carbonic acid and the hydrolysis of CO_2 in aqueous solution. Journal of Solution Chemistry, 1982. 11(5): p. 339-346.
28. J. Li and Z.H. Duan, A thermodynamic model for the prediction of phase equilibria and speciation in the H_2O–CO_2–NaCl–$CaCO_3$–$CaSO_4$ system from 0 to 250 C, 1 to 1000 bar with NaCl concentrations up to halite saturation. Geochimica et Cosmochimica Acta, 2011. 75(15): p. 4351.
29. E. Van Hunnik, E.L.J.A. Hendriksen, and B.F.M. Pots, "The formation of protective $FeCO_3$ corrosion product layers in CO_2 corrosion", in CORROSION 96. 1996: Denver, CO:NACE.
30. A. Dugstad, The importance of $FeCO_3$ supersaturation on the CO_2 corrosion of mild steels. CORROSION/92, paper, 1992(14).
31. Y.M. Gunaltun, Combining Research And Field Data For beorrosion Rate Prediction. CORROSION 96, 1996.
32. A.M. Halvorsen and T. Sontvedt, CO_2 Corrosion Model for Carbon Steel Including Wall Shear Stress Model for Multiphase Flow and

Limits for Production Rate to Avoid Mesa Attack. CORROSION 99, 1999.

33. R.C. John, K.G. Jordan, S.D. Kapusta, A.L. Young, and W.T. Thompson, SweetCor: an information system for the analysis of corrosion of steels by water and carbon dioxide. CORROSION 98, 1998.
34. P.O. Gartland and J.E. Salomonsen, A Pipeline Integrity Management Strategy Based on Multiphase Fluid Flow & Corrosion Modelling. CORROSION 99, 1999.
35. R.C. Woollam and S. Hernandez. Assessment and comparison of CO_2 corrosion predicition models. in SPE International Oilfield Corrosion Symposium. 2006: Society of Petroleum Engineers.
36. S. Olsen, CO_2 Corrosion Prediction by Use of the NORSOK M-506 Model-Guidelines and Limitations. CORROSION 2003, 2003.
37. S. Nešić, Key issues related to modelling of internal corrosion of oil and gas pipelines–A review. Corrosion Science, 2007. 49(12): p. 4308-4338.
38. S. Nesic, J. Postlethwaite, and S. Olsen, An electrochemical model for prediction of corrosion of mild steel in aqueous carbon dioxide solutions. Corrosion, 1996. 52(4): p. 280-294.
39. W. Sun and S. Nesic, Basics revisited: kinetics of iron carbonate scale precipitation in CO_2 corrosion. Corrosion/2006, paper, 2006(06365).
40. D.C. Waard, U. Lotz, and D.E. Milliams, Predictive Model for CO_2 Corrosion Engineering in Wet Natural Gas Pipelines. Corrosion, 1991. 47(12): p. 976-985.
41. S. Nesic and L. Lunde, Carbon dioxide corrosion of carbon steel in two-phase flow. Corrosion, 1994. 50(9): p. 717-727.
42. J.L. Crolet and M.R. Bonis. Prediction of the risks of CO_2 corrosion in oil and gas wells. SPE production Engineering 1991 [cited 6 04]; 449-453].
43. S. Linae and D. Waard, "Corrosion Prediction and materials selections for oil and gas producing environments", in NACE INTERNATIONAL. 2005: Houston, Texas, U.S.A. p. 648.
44. F. Vitse, S. Nešic, Y. Gunaltun, D.L. de Torreben, and D.S. Pierre, "Mechanistic model for the prediction of top-of-the-line corrosion risk", in NACE INTERNATIONAL. 2003: Houston Texas, U.S.A. p. 1075-1084.
45. H.W. Wang, .Y. Cai, and W.P. Jepson, CO_2 corrosion mechanistic modeling and prediction in horizontal slug flow. CORROSION 2002, 2002.
46. M. Nordsveen, S. Nešic, R. Nyborg, and A. Stangeland, A mechanistic model for carbon dioxide corrosion of mild steel in the presence of protective iron carbonate films-Part 1: Theory and verification. Corrosion, 2003. 59(5): p. 443-456.
47. R. Zhang, M. Gopal, and W.P. Jepson, "Development of a mechanistic model for predicting corrosion rate in multiphase oil/water/gas flows", in NACE INTERNATIONAL. 1997: Houston, Texas, U.S.A.

48. A. Anderko. Simulation of $FeCO_3/FeS$ scale formation using thermodynamic and electrochemical models. in Corrosion-National association of corrosion engineers annual conference. 2000: NACE.
49. M.S. High, J. Wagner, and S. Natarajan, "Mechanistic modeling of mass transfer in the laminar sublayer in downhole systems", in NACE INTERNAITONAL 2000: Orlando, Florida
50. J. Fritz, "A mechanistic modeling of CO_2 corrosion of mild steel in the presence of H_2S". 2004, Ohio University.
51. S. Nešić, H. Li, J. Huang, and D. Sormaz, "An open source mechanistic model for CO_2/H_2S corrosion of carbon steel", in NACE INTERTIONAL. 2009: Houston, Texas, U.S.A.
52. I.S. Cole, D.A. Paterson, P. Corrigan, S. Sim, and N. Birbilis, State of the aqueous phase in liquid and supercritical CO_2 as relevant to CCS pipelines. International Journal of Greenhouse Gas Control, 2012. 7(0): p. 82-88.
53. E.W. McAllister, Pipeline Rules of Thumb Handbook: A Manual of Quick, Accurate Solutions to Everyday Pipeline Engineering Problems. 2013: Gulf Professional Publishing.
54. L. Buit, M. Ahmad, W. Mallon, and F. Hage, CO_2 EuroPipe study of the occurrence of free water in dense phase CO_2 transport. Energy Procedia, 2011. 4: p. 3056-3062.
55. F. Eldevik, B. Graver, L.E. Torbergsen, and O.T. Saugerud, Development of a Guideline for Safe, Reliable and Cost Efficient Transmission of CO_2 in Pipelines. Energy Procedia, 2009. 1(1): p. 1579-1585.
56. A. Dugstad, M. Halseid, and B. Morland, Effect of SO_2 and NO_2 on corrosion and solid formation in dense phase CO_2 pipelines. Energy Procedia, 2013. 37: p. 2877-2887.
57. M.E. Boot-Handford, J.C. Abanades, E.J. Anthony, M.J. Blunt, S. Brandani, N. Mac Dowell, J.R. Fernandez, M.-C. Ferrari, R. Gross, J.P. Hallett, R.S. Haszeldine, P. Heptonstall, A. Lyngfelt, Z. Makuch, E. Mangano, R.T.J. Porter, M. Pourkashanian, G.T. Rochelle, N. Shah, J.G. Yao, and P.S. Fennell, Carbon capture and storage update. Energy & Environmental Science, 2014. 7(1): p. 130-189.
58. H. Kruse and M. Tekiela, Calculating the consequences of a CO_2-pipeline rupture. Energy Conversion and Management, 1996. 37(6–8): p. 1013-1018.
59. F.W. Schremp and R.G. Roberson, "Effect of Supercritical Carbon Dioxide (CO_2) on Construction Materials".
60. D.E. McCollough and R.L. Stiles, "Operation of the Central Basin CO_2 Pipeline System", Society of Petroleum Engineers.
61. J.-Y. Lee, T.C. Keener, and Y.J. Yang, Potential flue gas impurities in carbon dioxide streams separated from coal-fired power plants. Journal of the Air & Waste Management Association, 2009. 59(6): p. 725-732.
62. Z. Abbas, T. Mezher, and M.R.M.A. Zahra, CO_2 purification. Part I: Purification requirement review and the selection of impurities deep removal technologies. International Journal of Greenhouse Gas Control, 2013. 16: p. 324-334.
63. R. Anantharaman, O. Bolland, N. Booth, E. van Dorst, C. Ekstrom, E. Sanchez Fernandes, F. Franco, E. Macchi, G. Manzolini, and D.

Nikolic, European best practice guidelines for assessment of CO_2 capture technologies. CAESAR Project, FP7—ENERGY, 2007. 1.

64. L. Basava-Reddi, N. Wildgust, and D. Ryan. Effects of Impurities on Geological Storage of Carbon Dioxide. in 1st Sustainable Earth Sciences Conference & Exhibition (SES2011). 2011.
65. M. Anheden, A. Andersson, C. Bernstone, S. Eriksson, J. Yan, S. Liljemark, and C. Wall. CO_2 quality requirement for a system with CO_2 capture, transport and storage. in Proceedings of the 7th International Conference on Greenhouse Gas Technologies (GHGT-7). 2004.
66. J.S. Wang, D.A. Ryan, E.J. Anthony, N. Wildgust, and T. Aiken, Effects of impurities on CO_2 transport, injection and storage. Energy Procedia, 2011. 4(0): p. 3071-3078.
67. P. Lako, A.J. van der Welle, M. Harmelink, M.D.C. van der Kuip, A. Haan-Kamminga, F. Blank, D.J. Wolff, and M. Nepveu, Issues concerning the implementation of the CCS Directive in the Netherlands. Energy Procedia, 2011. 4: p. 5479-5486.
68. S.L. Wu, Z.D. Cui, G.X. Zhao, M.L. Yan, S.L. Zhu, and X.J. Yang, EIS Study of the Surface Film on the Surface of Carbon Steel from Supercritical Carbon Dioxide Corrosion. Applied Surface Science, 2004. 228(1): p. 17-25.
69. Y.-S. Choi, D. Young, S. Nešić, and L.G.S. Gray, Wellbore integrity and corrosion of carbon steel in CO_2 geologic storage environments: A literature review. International Journal of Greenhouse Gas Control, 2013. 16(0): p. 70-77.
70. Z.D. Cui, S.L. Wu, C.F. Li, S.L. Zhu, and X.J. Yang, Corrosion behavior of oil tube steels under conditions of multiphase flow saturated with super-critical carbon dioxide. Materials letters, 2004. 58(6): p. 1035-1040.
71. Z.D. Cui, S.L. Wu, S.L. Zhu, and X.J. Yang, Study on corrosion properties of pipelines in simulated produced water saturated with supercritical CO_2. Applied Surface Science, 2006. 252(6): p. 2368-2374.
72. S.L. Wu, Z.D. Cui, F. He, Z.Q. Bai, S.L. Zhu, and X.J. Yang, Characterization of the surface film formed from carbon dioxide corrosion on N80 steel. Materials Letters, 2004. 58(6): p. 1076-1081.
73. G. Lin, M. Zheng, Z. Bai, and X. Zhao, Effect of temperature and pressure on the morphology of carbon dioxide corrosion scales. Corrosion, 2006. 62(6): p. 501-507.
74. E.M. Russick, G.A. Poulter, C.L.J. Adkins, and N.R. Sorensen, Corrosive effects of supercritical carbon dioxide and cosolvents on metals. The Journal of Supercritical Fluids, 1996. 9(1): p. 43-50.
75. S. Sim, F. Bocher, I.S. Cole, X.B. Chen, and N. Birbilis, Investigating the effect of water content in supercritical CO_2 as relevant to the corrosion of carbon capture and storage pipelines. Corrosion, 2014. 70(2): p. 185-195.
76. Y.-S. Choi and S. Nesic, "Effect of water content on the corrosion behavior of carbon steel in supercritical CO_2 phase with impurities", in CORROSION 2011. 2011: Houston, TX:NACE.
77. F. Farelas, Y.-S. Choi, and S. Nešić, Corrosion Behavior of API 5L X65 Carbon Steel under Supercritical and Liquid Carbon Dioxide

Phases in the Presence of Water and Sulfur Dioxide. Corrosion, 2012. 69(3): p. 243-250.

78. F. Farelas, Y.-S. Choi, and S. Nesic, "Effects of CO_2 phase change, SO_2 content and flow on the corrosion of CO_2 transmission pipeline steel", in CORROSION 2012. 2012: Salt Lake City, UT:NACE.
79. A. Dugstad and M. Halseid, Internal corrosion in dense phase CO_2 transport pipelines-state of the art and the need for further R&D. CORROSION 2012, 2012.
80. Y. Xiang, Z. Wang, C. Xu, C.C. Zhou, Z. Li, and W.D. Ni, Impact of SO_2 concentration on the corrosion rate of X70 steel and iron in water-saturated supercritical CO_2 mixed with SO_2. The Journal of Supercritical Fluids, 2011. 58(2): p. 286-294.
81. B.P. McGrail, H.T. Schaef, V.A. Glezakou, L.X. Dang, and A.T. Owen, Water reactivity in the liquid and supercritical CO_2 phase: Has half the story been neglected? Energy Procedia, 2009. 1: p. 3415-3419.
82. F. Ayello, K. Evans, R. Thodla, and N. Sridhar, "Effect of impurities on corrosion of steel in supercritical CO_2", in CORROSION 2010. 2010: San Antonio, TX:NACE.
83. M.B. Kermani and A. Morshed, Carbon Dioxide Corrosion in Oil and Gas Production - A Compendium. Corrosion, 2003. 59(8): p. 659-683.
84. ASTM. Standard G1-03, Standard practice for preparing, cleaning, and evaluating corrosion test specimens. ASTM International: West Conshohocken, PA, 2003.
85. Y.C. Zhang, X.L. Pang, S.P. Qu, X. Li, and K.W. Gao, Discussion of the CO_2 corrosion mechanism between low partial pressure and supercritical condition. Corrosion Science, 2012. 59: p. 186-197.
86. S.Q. Guo, L.N. Xu, L. Zhang, W. Chang, and M.X. Lu, Corrosion of Alloy Steels Containing 2% Chromium in CO_2 Environments. Corrosion Science, 2012. 63: p. 246-258.
87. J.B. Sun, W. Liu, W. Chang, Z.H. Zhang, Z.T. Li, T. Yu, and M.X. Lu, Characteristics and formation mechanism of corrosion scales on low-chromium X65 steels in CO_2 environment. Acta Metall Sin, 2009. 45(1): p. 84.
88. A. Dugstad, "Fundamental Aspects of CO_2 Metal Loss Corrosion - Part 1: Mechanism", in CORROSION 2006. 2006: San Diego, CA:NACE.
89. V. Ruzic, M. Veidt, and S. Nešić, Protective iron carbonate films-Part 1: Mechanical removal in single-phase aqueous flow. Corrosion, 2006. 62(5): p. 419-432.
90. Y. Xiang, Z. Wang, Z. Li, and W.D. Ni, Effect of Exposure Time on the Corrosion Rates of X70 Steel in Supercritical $CO_2/SO_2/O_2/H_2O$ Environments. Corrosion, 2012. 69(3): p. 251-258.
91. A. Dugstad, B. Morland, and S. Clausen, Corrosion of transport pipelines for CO_2–Effect of water ingress. Energy Procedia, 2011. 4: p. 3063-3070.
92. Y. Hua, R. Barker, and A. Neville, Effect of temperautre on the critical water content for general and localised corrosion of X65 carbon steel in the transport of supercritical CO_2. The International Journal of Greenhouse Gas Control, 2014. 31: p. 48-60.
93. Y. Hua, R. Barker, and A. Neville, Comparison of corrosion behaviour for X-65 carbon steel in supercritical CO_2-saturated water and water-

saturated/unsaturated supercritical CO_2 The Journal of Supercritical Fluids, 2015. 97: p. 224-237.

94. Y. Hua, R. Barker, C. T, M. Ward, and A. Neville, Relating Iron Carbonate Morphology to Corrosion Characteristics for Water-Saturated Supercritical CO_2 Systems. The Journal of Supercritical Fluids, 2015. vol. 98: p. 183-193.
95. W.H.J. Vernon, A laboratory study of the atmospheric corrosion of metals. Part I.—The Corrosion of copper in certain synthetic atmospheres, with particular reference to the influence of sulphur dioxide in air of various relative humidities. Transactions of the Faraday Society, 1931. 27: p. 255-277.
96. Y. Hua, R. Barker, and A. Neville, Understanding the Influence of SO_2 and O_2 on the Corrosion of Carbon Steel in Water-Saturated Supercritical CO_2. Corrosion, 2015. vol. 71: p. 667-683.
97. Y. Hua, R. Barker, and A. Neville, The influence of SO_2 on the tolerable water content to avoid pipeline corrosion during the transportation of supercritical CO_2. International Journal of Greenhouse Gas Control, 2015. 37: p. 412-423.
98. W.H.J. Vernon, A laboratory study of the atmospheric corrosion of metals. Part II.—Iron: the primary oxide film. Part III.—The secondary product or rust (influence of sulphur dioxide, carbon dioxide, and suspended particles on the rusting of iron). Transactions of the Faraday Society, 1935. 31: p. 1668-1700.